Spring 2018

Investigation of the hydrodynamics and scale-up of advanced TRISO nuclear fuel manufacturing using sophisticated measurement techniques

Thaar M. Aljuwaya

Department: Mining and Nuclear Engineering

INVESTIGATION OF THE HYDRODYNAMICS AND SCALE-UP OF ADVANCED TRISO NUCLEAR FUEL MANUFACTURING USING SOPHISTICATED MEASUREMENT TECHNIQUES

by

THAAR M. ALJUWAYA

A DISSERTATION

Presented to the Faculty of the Graduate School of the

MISSOURI UNIVERSITY OF SCIENCE AND TECHNOLOGY

In Partial Fulfillment of the Requirements for the Degree

DOCTOR OF PHILOSOPHY

in

NUCLEAR ENGINEERING

2018

Approved by:

Muthanna Al-Dahhan, Advisor
Hyoung K. Lee
Xin Liu
Joshua P. Schlegel
Xinhua Liang

ABSTRACT

The successful performance and safety of the Very-High-Temperature Nuclear Reactors (VHTR) extremely depend on the quality of the TRISO nuclear fuel coated particles. However, the coating of the TRISO particles is delicate process and impacted by the hydrodynamics of spouted beds. Therefore, in this work, we applied advanced non-invasive measurement techniques which are gamma-ray computed tomography (CT) and radioactive particle tracking (RPT), to investigate foremost the local parameters to advance the fundamental understanding of the hydrodynamics and scale-up of gas-solid spouted beds. The CT technique has been applied to study the effects of particle density, particle size, bed size, and superficial gas velocity on the gas-solid cross-sectional distributions of spouted beds. The CT results demonstrated that the summation that operating spouted beds at stable spouting state would lead to achieving proper coating layers of the particles in the TRISO fuel coating process is not adequate. On the other hand, the RPT technique has been applied to evaluate the hydrodynamics, and mixing and segregation behavior of binary solids mixture spouted beds with particles of same size but different densities encountered in the TRISO nuclear fuel particles manufacturing process. The RPT results demonstrated that for the hydrodynamics of binary solids mixture spouted beds having particles of similar size but different densities, particle collisions by the particle-particle interaction plays an important role. At last, we evaluated the new mechanistic scale-up methodology that has been developed in our laboratory based on matching the radial profile of gas holdup at the region of the developed flow since the gas dynamics dictate the hydrodynamics of the gas-solid spouted beds. The measured local parameters obtained in this part confirm the validation of our new methodology of scale-up of gas-solid spouted beds.

ACKNOWLEDGMENTS

First of all, praise belongs to God (ALLAH) who created the heavens and the earth, who sends down the rain from the skies, and who revives therewith the earth after its death, for his kindness and so many blessings in my life.

I express gratitude from the depth of my heart to my advisor, Professor Muthanna H. Al-Dahhan who guided me diligently and patiently through my PhD studies. I have learned a lot from him. I will continue to be inspired by and has some of his energy and enthusiasm before graduating. I would also like to acknowledge the members of my committee, Dr. Hyoung K. Lee, Dr. Xin Liu, Dr. Joshua P. Schlegel, and Dr. Xinhua Liang for their support, co-operation and valuable inputs which helped me in shaping my research work. Also, I would like to thank the US Department of Energy - Nuclear Energy Research Initiative (DOE-NERI) grant (NERI DEFC07-07ID14822) for financial support to carry out this work. I must thank the King Abdulaziz City for Science and Technology (KACST) for sponsoring his Ph.D. studies at Missouri S&T. I thank my closest friends Marwan Alobaidi, Thaqal Alhuzaymi, and Meshari Alqahtani for sincerity and for all the moments we've shared. I would like to thank the secretary's office of the Departments of Nuclear, and Chemical and Biochemical Engineering, Graduate Studies, International Affairs and Curtis laws Wilson Library for helping and guiding me throughout my stay.

This journey would not have been possible without the support of my family. Thank you to my family for encouraging me in all of my pursuits and inspiring me to follow my dreams. I am especially grateful to my parents, who supported me and believed in me and wanted the best for me.

TABLE OF CONTENTS

Page

LIST OF ILLUSTRATIONS

Page

LIST OF TABLES

Page

NOMENCLATURE

Symbols		Description
an-sp, sp-fo, fo-an	:	tracer particle transition, respectively, out from the annulus into the spout, out from the spout into the fountain, out from the fountain into the annulus.
d_p	:	particle diameter, m
D_c	:	inner column diameter, m
D_i	:	inlet orifice diameter, m
D_s	:	mean value of the spout diameter, m
D_{rr}	:	radial turbulent diffusivity, cm^2/s^2
D_{zz}	:	axial turbulent diffusivity, cm^2/s^2
e_{ss}	:	restitution coefficient of the particles
Fr	:	Froude number
g	:	acceleration of gravity, m s^{-2}
H	:	static bed height, m
H_F	:	fountain height, m
H_m	:	maximum spoutable bed depth, m
(i,j)	:	coordinates of a given compartment in the defined 2-D domain.
(i,j,k)	:	coordinates of a given compartment in the defined 3-D domain.
L	:	column length, m
$\boldsymbol{M}$	:	matrix of the transition occurrences in each compartment in the of the defined z-r domain
N_v	:	is the total number of occurrences per compartment
N_t		is the total number of cycles over a given experiment
N_θ	:	is the number of compartments in the direction.
$\widetilde{N}_{v(i,k)}$	:	is the average number of velocity occurrences for a given two-dimensional compartment (i,k)
P	:	bed pressure, Pa
$\boldsymbol{P}$	:	vector of the cumulative probability distribution of the solids particles penetration into the spout along the spout height.

qth	:	cycle number during an experiment.
$\boldsymbol{R}$	:	vector of the mean radius of the solid particles penetration into the spout.
Re	:	Reynolds number
R	:	column radius, cm
r		radial position from the axis of the column, cm
r/R		dimensionless radius
T	:	bed temperature, K
$T_{an-sp,q}$	:	time of particle transition out from the annulus into the spout during qth cycle of an experiment, second
$T_{sp-fo,q}$	:	time of particle transition out from the spout into the fountain during qth cycle of an experiment, second
$T_{fo-an,q}$	:	time of particle transition out from the fountain into the annulus during qth cycle of an experiment, second
$\bar{T}_{sp}$, $\bar{T}_{an}$, $\bar{T}_{fo}$	:	mean residence time of solids in the spout region, in the annulus region, in the fountain region, respectively, second.
$\bar{T}_{cycle}$,	:	mean cycle time of the solids in the spouted beds, second.
t	:	time, second
TKE	:	turbulent kinetic energy (per unit bulk density), $cm^2\ s^{-2}$
U	:	superficial gas velocity, $m\ s^{-1}$
U_{mf}	:	minimums fluidization velocity, $m\ s^{-1}$
U_{ms}	:	minimums pouting velocity, $m\ s^{-1}$
U	:	axially averaged of the mean particle velocity ($\bar{u}$), $m\ s^{-1}$
$U_{P\text{-}RMS}$	:	axially averaged of the root man square velocity, $cm\ s^{-1}$
u	:	instantaneous local particle velocity, cm/s
$\bar{u}$	:	azimuthally-averaged particle velocity, cm/s
u'	:	fluctuating particle velocity, cm/s
u_{RMS}	:	root mean square particle velocity, cm/s
$\boldsymbol{V}$	:	*vector of the r-coordinate of the center of the compartment of the defined domain.*
Y		tracer particle displacement, cm
z	:	axial distance form inlet orifice, m

Greek letters Description

β : fluid-particle interaction coefficient, kg m^3 s^{-1}.

ρ_s : particle density, Kg m^{-3}.

ρ_f : fluid density, Kg m^{-3}.

μ : fluid viscosity, Kg m^{-1} s^{-1}.

ϕ_s : sphericity of particles.

φ : inertial friction angle of particle, deg.

ε_{mf} : bed voidage at minimum fluidization.

e_{ss} : restitution coefficient of the particles

ε_o : voidage at packed bed state

ε_s : solids fraction (or solids holdup).

ε_g : gas fraction (or gas holdup).

Δ : size of the side of square discretization element in the 2-D domain, mm

Subscripts Description

′ : Dimensionless parameter.

1. INTRODUCTION

This Section presents the background information of this research. It covers energy demands, generation IV nuclear reactors, TRISO nuclear fuel particles, gas-solid spouted beds, research motivation, and research objectives.

1.1. ENERGY DEMANDS AND THE NUCLEAR ERA

The demand for more energy became one of the most important elements of the 21st century. Industrialized countries' demands for energy are steadily growing, along with policies and regulations that drive usage efficiency and sustainability. Moreover, underdeveloped and developing countries with booming industrial sectors (i.e., India and China) witnessed ever higher demands for energy and actively work to secure energy sources. This will unquestionably affect political decision-making on the local, regional, and international governing levels since energy resource renewability and distribution are issues to require intergovernmental coordination and cooperation. There are many types of energy sources used today, including: fossil sources (i.e., non-renewable sources) such as coal, oil, and natural gas; and renewable sources such as biomass, hydro, geothermal, wind, solar, and nuclear energy. Among these mentioned energy sources, the most important, when considering level of power production and reasonable prices, is natural gas. However, oil and natural gas are not abundant enough to cover global demands, and some of the oil-producing and -exporting countries have become oil-consuming and -importing ones. There is also the challenge of environmental pollution, which accompanies the processing of and use of most fossil energy sources. As such, concerns have been raised about what has to be done or what could be done to address this challenge of fossil energy source

depletion in the near future. Some sources of energy, like oil, continue to be economically worthwhile to extract. Some others are highly productive and provide a substantial amount of energy for a long period of time, like nuclear energy.

All energy sources possess negative and positive implications on people's lives and the surrounding environment. For example, combustion of coal will emits massive amounts of carbon dioxide (CO2) to the atmosphere. Such emissions have been shown to raise the greenhouse impact in the atmosphere and bring on global warming. This also applies, albeit to a lesser degree, to natural-gas-operated plants, which burn much cleaner than coal-operated ones. Globally, miners are decreasingly hired to mine coal and many face greater restrictions, regulations, and rules regarding future coal extraction and usage. The CO_2 emissions coming out of coal-operated power plants are at least twice the volume of those coming from gas-operated power plants. Recent studies indicate that world demands for electricity are increasing, even though that increase is steady and controllable through campaigns on efficient usage in the US and some other Western countries. Currently, the production of energy is downgrading due to power plant aging; many are likely to be shut down within the next 25 years, including plants that work with atomic energy. For these reasons, it is vital that states cooperatively start looking for the most sustainable, safe, and environmentally benign energy sources to provide for these growing energy demands.

Even with the ongoing research and development of alternative energy sources, it is important to note that the dependence on traditional energy sources, mainly oil and gas, will continue. However, states with successful research and development efforts will depend less on oil and gas. This developmental pattern is more likely to occur in developed countries rather than developing countries due to the latter's lack of interest in developing

or finding alternative energy sources for their energy demands and the high initial cost these countries would be required to bear, something they may not have means or desire to pay for at the moment. China and India are two examples of developing states with the greatest output of carbon emissions into the environment. When this is criticized, they argue that the pollution magnitude and the harm they are doing to the environment is on par with that of the UK, of France, and of other developed states during the 18th and 19th centuries.

Taking the lead in addressing this climate change challenge resulting from high environmental pollution from carbon emissions, the United Nations hosted a Climate Summit that took place on September 23, 2014, at the UN headquarters in New York. The former UN Secretary-General Ban Ki-moon pledged to all heads of state, private sector investors, and civil society leaders to take action by developing a low carbon economic growth model and by addressing climate change on five fronts: pricing of carbon, cutting of emissions, strengthening resilience, mobilizing money and markets, and mobilizing new coalitions. At the Climate Summit, world leaders agreed that climate change is a reality and that there is no quick-fix way to resolve it; such a challenge's solution must be found through adherence to a long-term vision based on a gradual reduction of emissions and the building up of resilience.

These days, most international efforts are aimed at finding an alternative solution to the question of energy production. Ideally, this alternative energy source would emit less carbon, be economically reliable, and be more sustainable than fossil fuels. The answer to this challenge has been found in atomic energy—a clean, reliable, and sustainable source of energy. Atomic energy is now considered one of the most promising sources of energy

with the least harmful impact on the environment. It is also very reliable in terms of pricing and safety control. As President Obama said in his (A New Foundation for American Economy) speech given at Northwestern University in Evanson, Illinois on October 2, 2014, one of the most important cornerstones of building this new foundation is to rely on clean energy production—atomic energy is an excellent candidate!

Atomic energy production is simply a controlled nuclear explosion under certain circumstances that produces an enormous amount of heat. The energy from the heat is then transferred into water to create a high-pressure steam, which is directed into steam turbine electricity generators to generate electricity. Despite its promise as the energy source of the future, its developmental course still needs further research regarding how to best use the nuclear fuel and, more importantly, how to make atomic energy production safer. Given the horrific nuclear reactor incidents that have occurred in the past, it is very important to build reactors to be more sturdy and secure in design. Many kinds of research were conducted to design safer and more effective reactors, and these efforts have produced good results theoretically as well as on a lab level.

1.2. GENERATION IV NUCLEAR REACTORS

Nuclear reactors are characterized by generation. As of today, there are four generations (I, II, III, III+, and IV) of nuclear reactor designs, but only two of them are currently in use within the energy production field. The Generation I nuclear reactor design was developed between the 1950s and 1970s and almost no reactors with this design are currently in commercial operation. Generation II nuclear reactors were constructed up until the end of the last century and includes some of the existing system designs, such as the BWR, PWR, CANDU, VVER, and RBMK. Most of these designs are currently in

operation. However, after the Chernobyl disaster in 1986 (i.e., Chernobyl. Chernobyl, Ukraine (former Soviet Union), April 26, 1986), calls for enhancing the security and safety of nuclear reactors led to the development of the Generation III nuclear reactor designs. Generation III and III+ designs of nuclear reactors can be considered as more advanced than Generation II, which brings us to Generation IV, the result of major strides to improve nuclear reactor designs. In the year 2000, the Generation IV International Forum (GIF) was established to design and develop Generator IV nuclear reactors for commercial use. Compared to the Generation III designs, Generation IV designs showed marked improvements and address problems that came to light when the Fukushima accident happened in 2011. With the progress and development currently reached, commercial deployment of the Generator IV nuclear reactors is expected to occur by 2020–2030 (Liu et al., 2012). Fourteen members in the the Generation IV International Forum - Argentina, Australia, Brazil, Canada, Euratom, France, Japan, the Republic of Korea, the People's Republic of China, Russia, South Africa, Switzerland, the United Kingdom, and the United States - have signed the GIF Charter for international cooperation in research and development (R&D) of Generation IV nuclear energy systems (GIF, 2016). Regarding the development of Generation IV system designs, the GIF established certain goals, which are summarized in Table 1.1 (below). As a result, we are seeing a trend as of late, where many states are considering ordering or building one or two of these new reactors, which possess new security-focused designs based on the concept of passive safety. Passive safety, as it would be implemented, simply means that the engineered components of the reactors would, in the case of an emergency, cool and eventually shut down the nuclear reaction instead of accelerating it, as seen in the older, yet still common reactor designs.

Newly-designed reactors use simple physics approaches that allow the core to shut down automatically in the case of an emergency and without the need for sophisticated engineered safety tools, rotary mechanisms, or human intervention. This new safety technology was applied, to a certain degree, to some of the existing reactors, but not all. The crucial characteristic of Generation IV designs, is that passive safety is a standard feature applied to all Generation IV reactors, as demonstrated in Table 1.1 (below). However, passive safety does not mean that any given reactor is completely safe. Other elements and components must still be in place and functional for the safety mechanism to work appropriately. For this reason, modern reactor designs incorporate both active and passive safety systems, making them safer than older designs.

With serious focus on the goals mentioned above, the members of the GIF identified six candidate reactor system designs among more than 100 proposals of new reactor designs. These six technologies have either been developed or are currently under development for the fourth generation of nuclear reactors. All six technologies operate at a temperature higher than existing Generation III reactors and are identified by the GIF (GIF, 2002) as being aligned with the Generation IV goals (Table 1.1). The six candidate designs/technologies are:

1. Very high-temperature gas-cooled reactor (VHTR);
2. Gas-cooled fast reactor (GFR);
3. Sodium-cooled fast reactor (SFR);
4. Lead-cooled fast reactor (LFR);
5. Molten salt reactor (MSR);
6. Super-critical water-cooled reactor (SCWR).

In the next sub-sections, the design of each one of the above systems is briefly discussed.

Table 1.1. Goals identified by the GIF for the Generation IV Nuclear Energy Systems (Abram and Ion, 2008; GIF, 2002).

Field of goal	Goal
Sustainability–1	The Generation IV nuclear energy systems should meet the objectives of sustainable energy generation, clear air, long-term availability, and effective utilization of fuel.
Sustainability–2	The Generation IV nuclear energy systems should be incorporated with effective minimization and management of nuclear waste, and reduce the burden of the long-term stewardship, and thus enhancing the protection for the environmental surroundings.
Economics–1	The Generation IV nuclear energy systems should be incorporated with a clear life-cycle cost advantage more than other sources of energy.
Economics–2	The Generation IV nuclear energy systems should have a financial risk level that is comparable to other energy projects.
Safety and Reliability–3	The Generation IV nuclear energy systems operations should excel in reliability and safety.
Safety and Reliability–2	The Generation IV nuclear energy systems should have an extremely low likelihood and level of reactor core damage.
Safety and Reliability–3	The Generation IV nuclear energy systems will eliminate the need for offsite emergency response.
Proliferation Resistance and Physical Protection–1	The Generation IV nuclear energy systems operations Generation IV nuclear energy systems will increase the assurance that they are a very unattractive and the least desirable route for diversion or theft of weapons-usable materials, and provide increased.

1.2.1. Very-High-Temperature Reactor (VHTR). The VHTR is the next phase of development for high-temperature gas-cooled reactor. The VHTR (shown in Figure 1.1) was identified as a candidate in 2002 since it had the potential to fulfill the GIF goals for the Generation VI nuclear reactors (Fütterer et al., 2014). In addition to that, much interest has been given to this candidate due to their high hydrogen production efficiency, safety, and reliability (Fütterer et al., 2014; Ge et al., 2015; Heath et al., 2013; Lee et al., 2008; López-Honorato et al., 2009; Verfondern et al., 2007; Yang et al., 2013). The VHTR relies on a once-through uranium cycle – although closed cycles using thorium fuel are possible as well – along with a thermal neutron spectrum. With a graphite moderator and helium coolant, this system can deliver outstanding heat for industry and electricity production, ranging between 700℃ and 950℃. In the future, this type of nuclear reactor design is expected to be capable of reaching temperatures of over 1000℃. The design of the VHTR is intended to provide high-temperature heat to industries with intensive energy consumption, like hydrogen production and petrochemical industry refining processes. Within the same plant, it can also incorporate electricity production. Due to the high temperatures that can be produced from this design, high-temperature-efficient materials and an advanced fuel for high performance are required. For fuel requirements, the VHTR uses coated fuel particles, well known as TRISO (i.e., Tristructural-isometric) fuel, as the fundamental unit in the core. The reactor core can be either a prismatic block fuel type, like the one used in Japan (HTTR), or a pebble-bed fuel type, like the one being built in China (HTR-10). The system is also flexible in adopting both U/Pu fuel cycles, which can result in enhanced waste reduction. What makes the VHTR a good source of heat for heavy industries like refineries and petrochemical industries, is its outstanding safety. The

excellence in safety found in both prismatic-block and pebble-bed concepts is evident in the high temperature capacity of their graphite cores, the powerful temperature coefficient of reactivity, and the vigorousness of TRISO fuel, all of which enable a reactor to survive accidental or natural-disaster-caused failures without the need for off-site power. The reliance on off-site power to prevent a reactor meltdown and the inability to access this power at the time of the meltdown is what led to the disaster of the Fukushima Daiichi station in Japan (GIF, 2014).

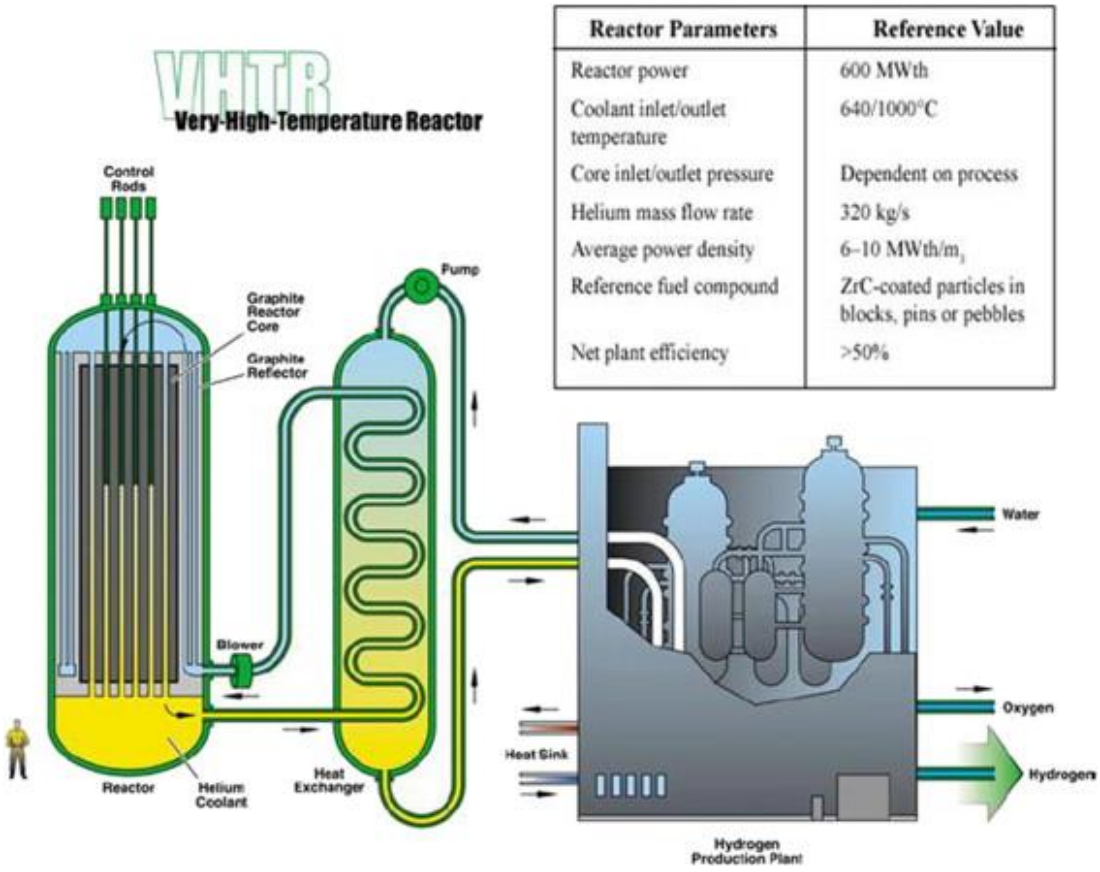

Reactor Parameters	Reference Value
Reactor power	600 MWth
Coolant inlet/outlet temperature	640/1000°C
Core inlet/outlet pressure	Dependent on process
Helium mass flow rate	320 kg/s
Average power density	6–10 MWth/m_3
Reference fuel compound	ZrC-coated particles in blocks, pins or pebbles
Net plant efficiency	>50%

Figure 1.1. Very high-temperature reactor (VHTR) NPP concept (GIF, 2002).

1.2.2. Gas-Cooled Fast Reactor (GFR). The gas-cooled fast reactor (GFR) is a high-temperature reactor (shown in Figure 1.2) that relies on helium coolant and fast neutron spectrum along with a closed fuel cycle. The design of this reactor has the advantage of fast-spectrum systems, which enhances the sustainability of long-term uranium resource use and creates minimal radioactive wastes. The configuration of the GFR core could be based on plate- or pin-based fuel assemblies or even prismatic blocks design, which enables for much better coolant circulation than traditional fuel assemblies. Different fuel forms have been taken into consideration in the design of the GFR to operate at very high temperatures and also to retain the release of the fission products: composite ceramic fuel, TRISO nuclear fuel particles, or ceramic clad elements of actinide compounds. The disadvantage of this reactor is its reliance on gas coolant since it does not possess the graphite reactor core found in VHTR reactor designs (GIF, 2014).

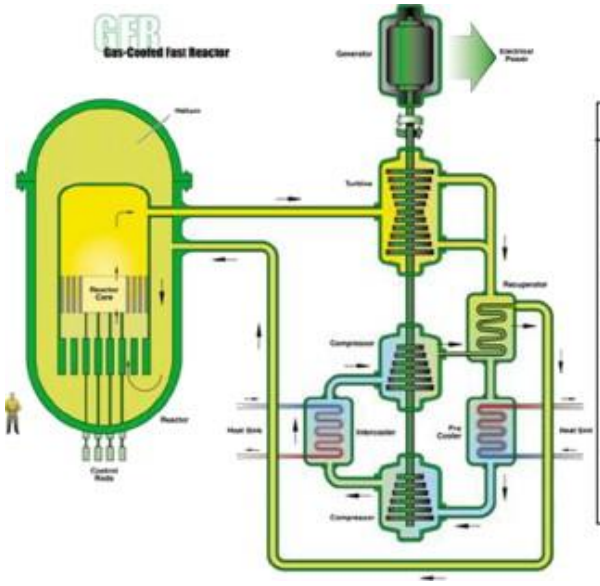

Reactor Parameters	Reference Value
Reactor power	600 MWth
Net plant efficiency (direct cycle helium)	48%
Coolant inlet/outlet temperature and pressure	490°C/850°C at 90 bar
Average power density	100 MWth/m3
Reference fuel compound	UPuC/SiC (70/30%) with about 20% Pu content
Volume fraction, Fuel/Gas/SiC	50/40/10%
Conversion ratio	Self-sufficient
Burnup, Damage	5% FIMA; 60 dpa

Figure 1.2. Gas-cooled fast reactor (GFR) NPP concept (GIF, 2002).

1.2.3. Sodium-Cooled Fast Reactor (SFR). The design for the Sodium-Cooled Fast Reactor System (SFR) (shown in Figure 1.3) features a closed fuel cycle and a fast neutron spectrum, which highly reduce the risk of nuclear material proliferation. By using liquid sodium as the reactor coolant in this system, many advantages can be found. The sodium coolant system is sealed and an oxygen-free environment, thus preventing corrosion. In addition, only a low fraction of the coolant is allowed within the reactor core. Despite its advantages, further research on creating an effective passive safety system in this design is still required and its performance still needs to be validated. The SFR is expected to be in operation by the year 2022. States that are interested in and starting to develop their own national SFR designs include: France, the Russian Federation, China, the Republic of Korea, Japan, and India. The plant options for this type of reactor range between small, 50-300 MWe modular reactors, and large plants with a maximum capacity of 1500 MWe. The degree to which SFRs heat up to sits between 500-550 ℃ for all sizes.

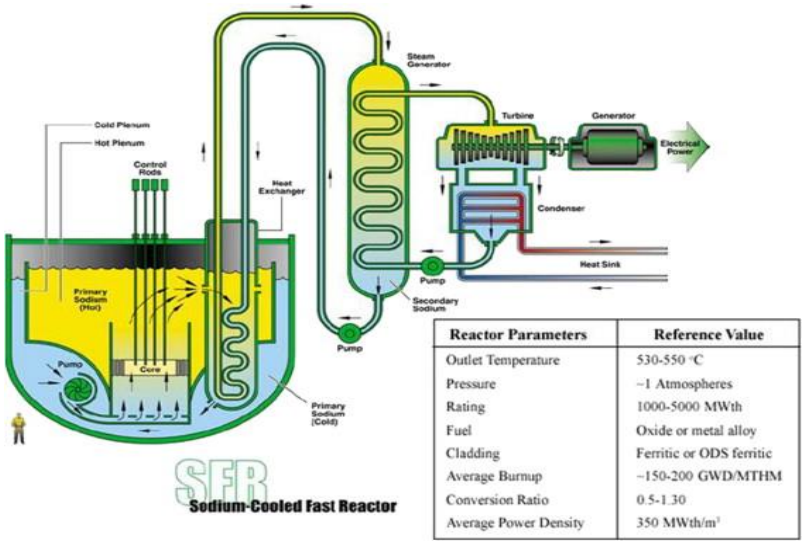

Reactor Parameters	Reference Value
Outlet Temperature	530-550 °C
Pressure	~1 Atmospheres
Rating	1000-5000 MWth
Fuel	Oxide or metal alloy
Cladding	Ferritic or ODS ferritic
Average Burnup	~150-200 GWD/MTHM
Conversion Ratio	0.5-1.30
Average Power Density	350 MWth/m³

Figure 1.3. Sodium-cooled fast reactor (SFR) NPP concept (GIF, 2002).

1.2.4. Lead-Cooled Fast Reactor (LFR). The Lead-cooled fast reactor (LFR) is another high-temperature reactor (shown in Figure 1.4) that operates at atmospheric pressure and at a very high temperature due to the high boiling point of its coolant, lead, which boils at 1743 °C. The core of this reactor is distinguished from other reactors possessing a fast-neutron spectrum because of the scattering properties of lead. The challenge with the LFR design surrounds its lead-coolant system, which possesses drawbacks of its own, especially the potential for lead erosion-corrosion.

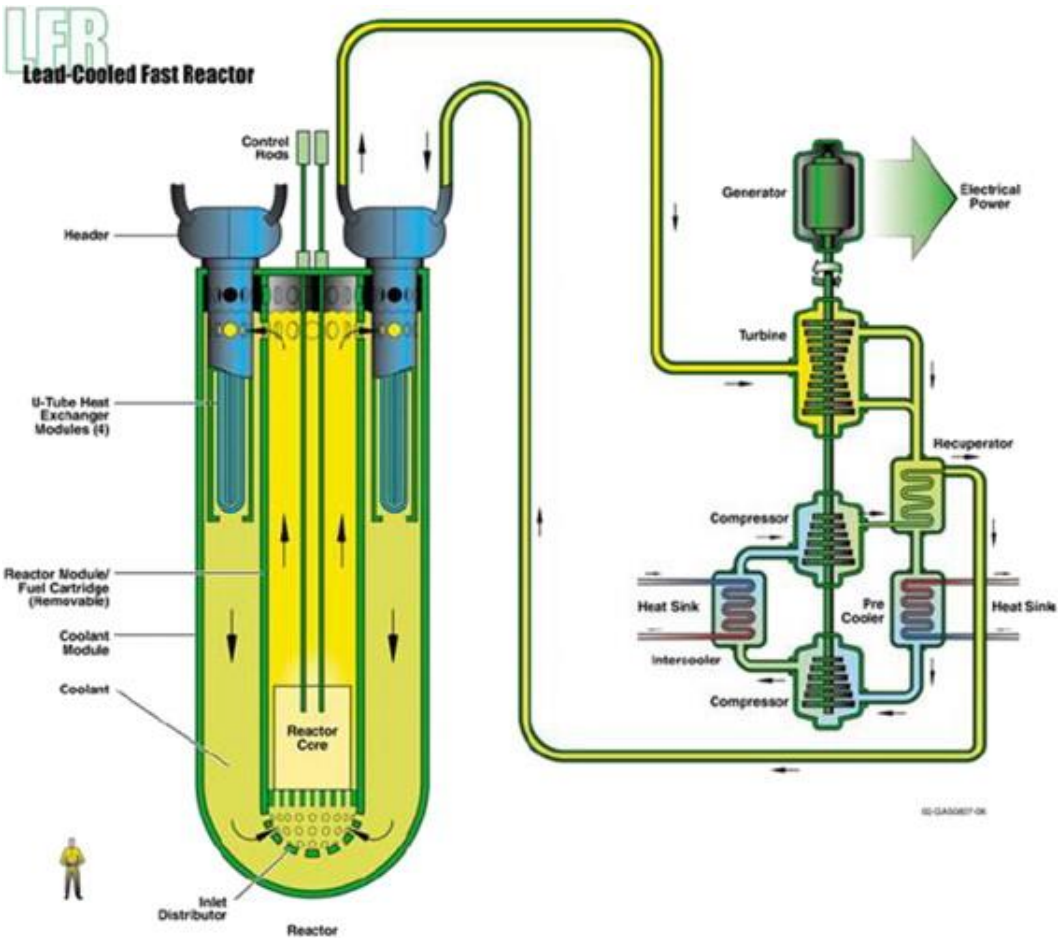

Figure 1.4. Lead-cooled fast reactor (LFR) NPP concept (GIF, 2002).

1.2.5. Molten Salt Reactor (MSR). The Molten salt reactor (MSR) was first developed in the United States between 1950 and 1976. The MSR (shown in Figure 1.5) is classified as a fast reactor and was named after the fuel type used in it. This reactor uses a liquid fuel mixture of sodium, uranium fluorides, and zirconium. This molten salt fuel flows in graphite channels within the reactor's core, producing the desired thermal spectrum and generating a very high temperature that is efficient for electricity production of about 1000 MWe and for industrial-level use. The MSR designs are divided into two subclasses according to the way the fuel is used. Both subclasses use molten salt fluoride. The difference is that in the first subclass, the fissile material is dissolved in the molten fluoride salt to serve as the fuel to the reactor. In the second subclass, the molten salt fluoride is deployed as a coolant of a coated particle-fueled core, known as a fluoride salt cooled high-temperature reactor (FHR) to distinguish it from the very-high-temperature reactors (VHTR). The MSR system is rated good for safety and neutral for economic impact due to the large number of subsystems it uses. The Russian Federation expects to deploy the MSRs in 2025.

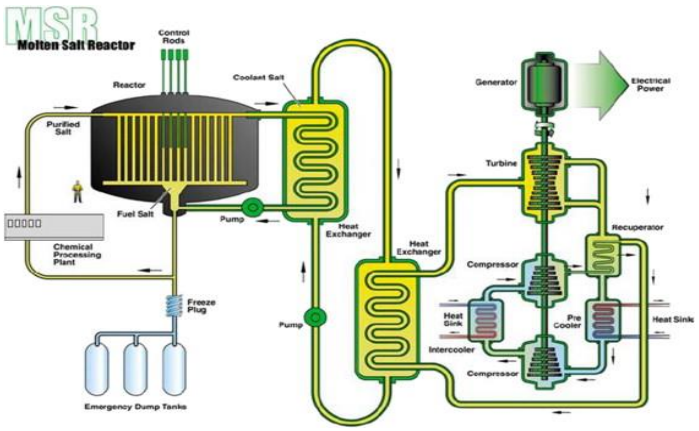

Figure 1.5. Molten salt reactor (MSR) NPP concept (GIF, 2002).

1.2.6. Supercritical-Water-Cooled Reactor (SCWR). This design uses two fuel cycle options: the first is an open-fuel cycle along with a thermal neutron spectrum reactor, and the second is a closed-fuel cycle along with a fast neutron spectrum reactor and complete actinide fuel cycling. Both options work with high pressure, high temperatures, and light water reactors that operate above the thermodynamic critical state (i.e., critical point) of water (374 ℃, 22.1 MPa). The SCWR (shown in Figure 1.6) may also use a light or heavy water moderator depending on the cooling system used. Contrasted with existing water-cooled reactors, the coolant in the SCWR may encounter a substantially higher enthalpy within the core, which cuts down on the mass flow of the core for a given thermal power and raises the outlet enthalpy of the core to superheated conditions. The design of the SCWR has two baseline concept reactors: pressure-vessel-based and pressure-tube-based. Both have a thermal efficiency that can be increased by 44%, unlike the current water-cooled reactors whose thermal efficiencies can only be increased by 34-36%. The other feature of SCWR designs is that a reactor coolant pump is not required. It also has a containment feature designed with pressure suppression pools, which are good for the proliferation level needed. The higher steam enthalpy decreases the size of the turbine system and will eventually reduce the cost of building the conventional island. The challenges facing SCWR designs are almost identical to those faced by current water-cooled reactors, except for a few details. Their passive safety systems have yet to be demonstrated and their transient heat transfer models, which allow for transformation from a supercritical stage to a sub-critical one, need to be validated. SCWR designs also require special, qualified materials like advanced steel are needed for cladding. Due to non-uniformities of local power and of coolant mass flow rate, which are caused by a larger

enthalpy rise of the coolant, hot spots may occur in the reactor. The higher coolant temperature results in higher fuel cladding temperatures and this, in turn, will affect the fuel burnup and the peak cladding temperature. This Generation IV design is expected to be deployed in the next decade. Canada and Japan are among the countries most interested in deploying the SCWR design.

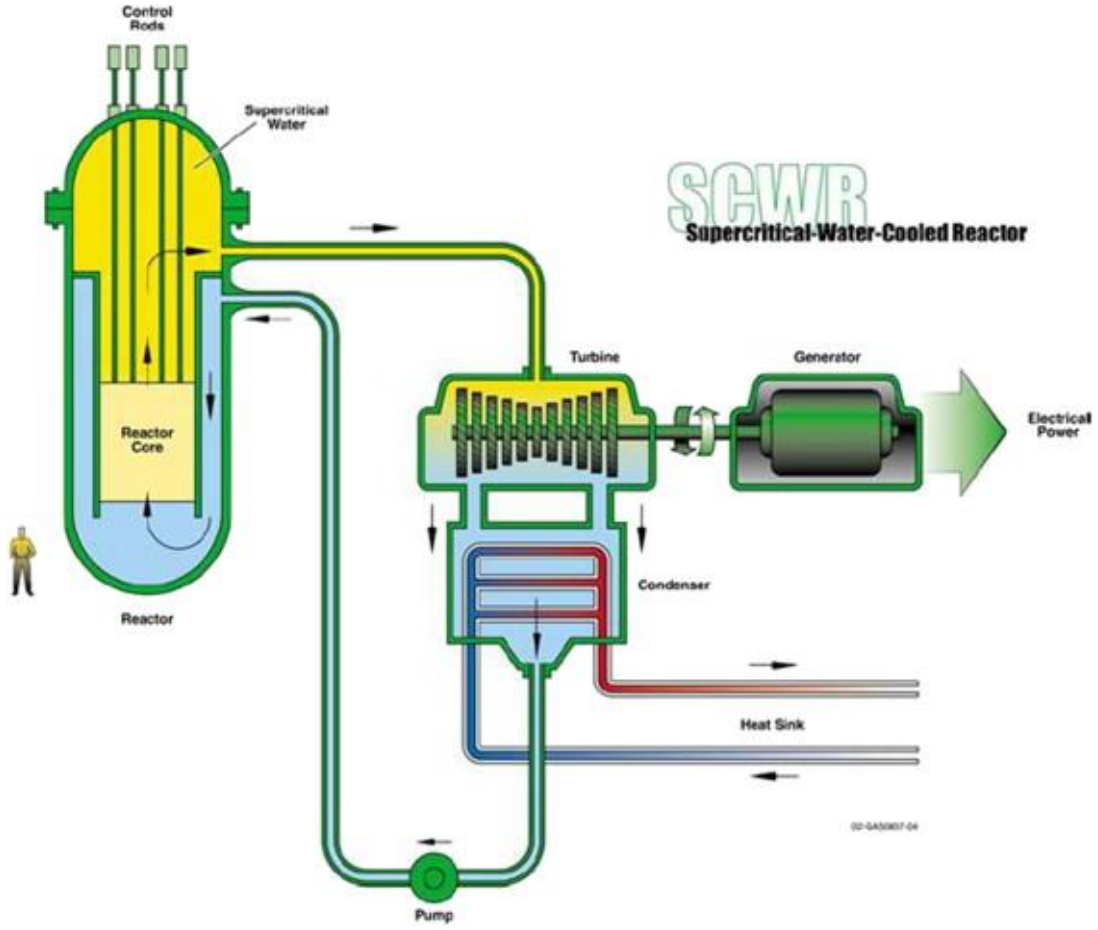

Figure 1.6. Super-critical water-cooled reactor (SCWR) NPP concept (GIF, 2002).

1.3. TRISO NUCLEAR FUEL PARTICLES

TRISO is an acronym of TRIstructural-ISOtropic. The TRISO-coated fuel particle was initially invented in the United Kingdom during the Dragon reactor project (Huddle et al., 1969). The TRISO particle fuel consists of a fuel kernel coated with four layers of isotropic materials. The fuel kernels are usually made from uranium dioxide (UO2) and, in some cases, uranium carbide (UC) or uranium oxicarbide (UCO; combines both uranium carbide and uranium oxide to minimize oxygen stoichiometry). As mentioned earlier, the fuel element, or the TRISO nuclear fuel particles, is the crucial unit in the core of the VHTR design of Generation VI nuclear reactors. The TRISO fuel particles are dispersed into the hexagonal graphite blocks in the form of fuel rods/compacts or pebbles. Individual TRISO-coated fuel particles can withstand very high temperatures of up to 1600ºC to achieve high burnup and to retain fuel during severe accidents. The coating process of TRISO fuel is very delicate and must meet certain production requirements to be accepted for use. The technique used in the coating process is chemical vapor deposition (CVD) administered within gas-solid spouted beds. Figure 1.7 illustrates the structure of the TRISO fuel particle, which consists of the following:

- Fuel kernel: The fuel kernel is usually made up of UO_2 (~ 350 µm to 500 µm diameter).
- Porous carbon buffer layer: This layer is made of pyrolytic carbon (with a thickness of about 95 µm). This layer functions as an attenuation layer for the released fission products created from the fuel kernel and provides space for the storage of the gaseous fission products. The buffer layer is also designed to contain fuel kernel swelling, reduce stress on the following coating layers, and prevent the damage of

the inner pyrocarbon (IPyC) layer by recoil resulting from released fission fragments. At last, the inclusion of the buffer layer in TRISO fuel enables the attainment of higher fuel burnup.

- Inner pyrocarbon (IPyC) layer: This layer is made up of pyrocarbon (IPyC) (with a thickness of about 40 µm). The IPyC layer is designed to retain gaseous fission products within the TRISO particle and helps to protect the kernel from chlorine or corrosion produced during the fabrication of the SiC layer. In addition to that, the IPyC layer can withstand high internal pressure at very high temperatures in the TRISO particle.
- Silicon carbide (SiC) layer: This layer is made up of silicon carbide (with a thickness of about 35 µm). This layer provides mechanical strength for the TRISO-coated fuel particle and is the strongest among the four layers. In addition to that, it works as a barrier to prevent the release of metallic fission products (for example, Ag, Cs, and Sr) because of the lower diffusion rate it permits compared to the IPyC layer.
- Outer pyrocarbon (OPyC) layer: The OPyC layer (with a thickness of about 40 µm) is the outermost layer of the TRISO fuel particle and is made of pyrocarbon. The OPyC protects the SiC layer from the surrounding environment during fuel particle handling and compresses the SiC layer in place.

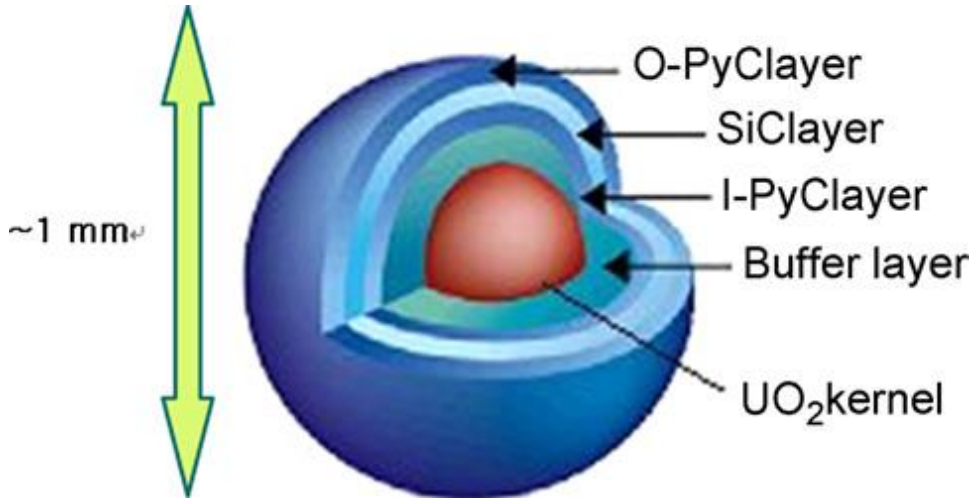

Figure 1.7. TRISO fuel particle used in Generation IV nuclear reactor (Kim et al., 2008).

1.4. GAS-SOLID SPOUTED BEDS

Spouted beds are gas-solid contactors widely used for applications within the chemical engineering and mining processes, such as gasification, polymerization, granulation, coating, and drying (Gryczka et al., 2008; Mathur and Epstein, 1974c; Olazar et al., 2003; Olazar et al., 1992). The spouted bed was originally developed in 1954 at the National Research Council of Canada by Mathur and Gishler (Mathur and Epstein, 1974a; Mathur and Gishler, 1955) to overcome some of the limitations in fluidized beds in handling heavy, coarse, and unevenly-sized particles. Key features of spouted beds consist of: capability to provide uniform thermal distribution, good particles mixing, and efficient contact between the solid and fluid phases. The spouted bed consists of a vertical inlet that directs gas upwards through the base center of a conical, cylindrical, or cylindrical-conical reactor, which contains a bed of particles. If the velocity of gas introduced into the bed of particles is sufficiently high, the gas carries the particles up rapidly through the bed axis and, thus, forms a hollowed region in the center of the bed. The particles carried somewhat

above the bed surface then fall freely back to the bottom of the bed, establishing continuous circulation. The established systematic, cyclic movement of the solids creates three distinct regions, each with their own specific flow behavior: a spout in the center of the column where the particles are carried up by the gas to the top of the bed surface; an annulus surrounding the spout where the particles fall back to the bottom of the bed; and a fountain above the top of the spout-annulus regions in which the particles transition from the spout to the annulus. Figure 1.8 shows a simple schematic diagram of a spouted bed (inspired from the work of Olazar et al. (Olazar et al., 2003)) and illustrates the three regions: the spout, the annulus, and the fountain. It is clear that such a flow pattern in spouted beds creates complex recirculation, which engenders strong gas-particle interactions allowing for many applications.

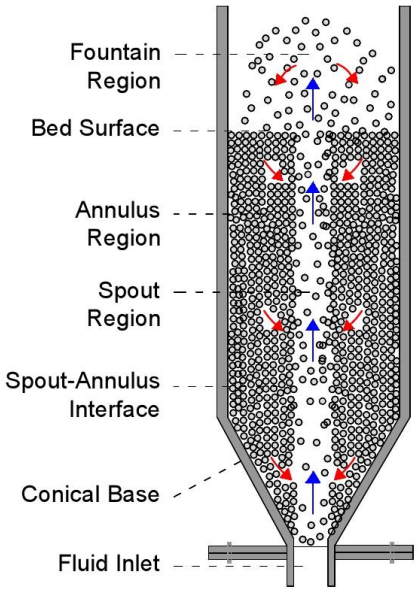

Figure 1.8. Schematic diagram of gas-solid spouted beds illustrating the three regions; the spout, the annulus, and the fountain.

1.5. MOTIVATION

As mentioned earlier, the very-high-temperature reactors (VHTRs) are the most suitable candidate for meeting the GIF goals of Generation VI nuclear reactors. Passive safety is one of the most important features that characterizes the VHTRs (Juhn et al., 2000). The fundamental design and safety of VHTRs rely heavily on the quality of the TRISO-coated particle fuels (Heath et al., 2013; Lee et al., 2008; Liu et al., 2012; Miller et al., 2004; Miller et al., 2006; Nickel et al., 2002; Porter et al., 2013; Sawa, 2012) and, as a natural extension, the fuel-coating technology and other related processes. In the coating process, the fuel kernel is coated with four layers: a porous buffer pyrolytic carbon layer (buffer PyC), an inner dense pyrolytic carbon layer (IPyC), a silicon carbide layer (SiC) and an outer dense pyrocarbon layer (OPyC) (Verfondern et al., 2007). The TRIOS-coated fuel particles are coated in gas-solid spouted beds via a chemical vapor deposition (CVD) process. However, the TRISO fuel coating process is very delicate and must meet certain production requirements before it can be accepted. For one, the particles' coating must contain uniform layers with absolutely no defects. The current standard of TRISO fuel production requires that there should be no more than 1 in 10^5 coating failures on individual particles (Pannala et al., 2007). The quality of the TRISO nuclear fuel particles produced, whether uniformly or non-uniformly coated, is strongly impacted by the hydrodynamics of the gas-solid spouted beds, and the solids flow field (Lee et al., 2008; Liu et al., 2012; Miller et al., 2006; Porter et al., 2013; Şentürk Lüle et al., 2015; Tang et al., 2002). To obtain proper coating of layers, efficient contact must be achieved between the particles and the active gas (López-Honorato et al., 2008). Accordingly, understanding the hydrodynamics of the spouted bed TRISO coater using advanced measurement techniques

is essential to properly assessing the fabrication process of TRISO-coated nuclear fuel particles.

In the coating process of the fuel particles, the sizes of the kernels, the densities of the kernels, and the coating layers are of prime interest when analyzing the hydrodynamics of spouted beds. The density of the UO_2 kernels ($\rho_p \sim 10.80$ g/cm^3) is much larger than that of general particles used in chemical engineering, one example being glass beads ($\rho_p \sim 2.60$ g/cm^3). Figure 1.9 shows the change in particle density and size during the coating process of the TRISO-coated nuclear fuel particles. Since the layers compact together to form a non-homogenous mixture of multiple materials, the size and density of the particles during the coating process are not constant, varying with and during each layer deposition. The density of the kernel is approximately 10.8 g/cm^{3,} and the diameter is 0.5 mm. The average density of the particle is then reduced substantially to 4.1 g/cm^3 when the particle is coated with just the first layer (low-density pyrolytic carbon), and the diameter increases to 0.68 mm. This process takes place for all the coating layers, resulting in a final particle density of about 2.65 g/cm^3 and a diameter of about 1 mm. Without a doubt, the changing particle properties during the coating process will significantly affect the hydrodynamics of the spouted bed and the performance of the said coating process. In addition, the large density difference of the two components after the first coating layer ($\rho_{kernel\text{-}Uo2}$ /$\rho_{kernel\text{-}coated\text{-}PyC} \sim$ 2.63) subject them to unlike behavior and particle segregation phenomena. Once again, it is for these reasons that the kernel sizes, kernel densities, and the coating layers at each stage of the coating process are of prime interest when it comes to optimizing the hydrodynamics of gas-solid spouted beds for each stage. These factors should be investigated systematically (Liu et al., 2015a; Takeda and Yamamoto, 1976). However, the

issue becomes more complex when we take into account the fact that the probability of success for one coating also depends on the success of the preceding coating. Accordingly, this demands an investigation on the hydrodynamics of gas-solid spouted beds with binary mixtures. What is more, process development on large-scale spouted beds is needed to sustain commercialization of the VHTRs; the use of spouted beds to fabricate TRISO-coated fuel particles have only been carried out at a laboratory-scale up until now. For commercial implementation of VHTRs, large-scale spouted beds need to be able to fabricate TRISO-coated particles of high quality, and of large quantities. The spouted bed scale-up required to meet the fuel demands VHTRs is considered one of the main challenges faced by the TRISO spouted bed coater, or spouted beds in general. This investigation will significantly help in the development of reliable and safe scale-up methodology and design, and ensure desired performance and operation of TRISO fuel spouted beds.

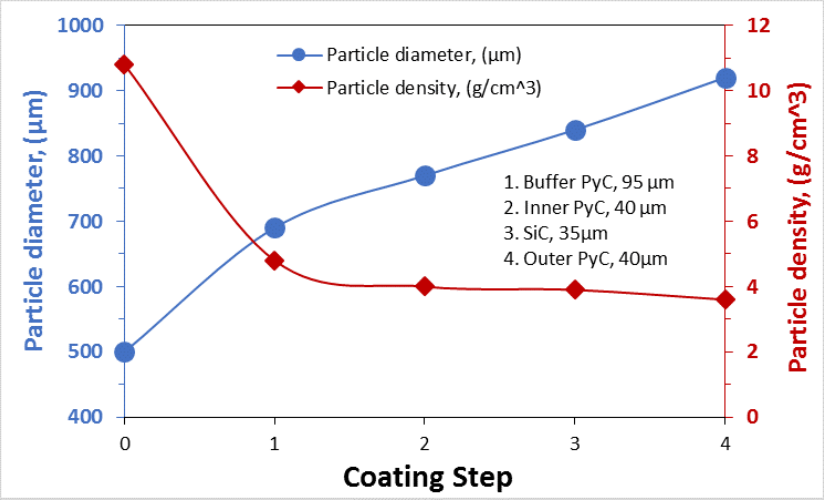

Figure 1.9. Thee change in particle density and size during the coating process of the TRISO particle.

Despite the fact that spouted beds have actually been employed for coating the TRISO fuel particle for a long time already, selecting the design, operating conditions, and scale of the bed appears to be largely empirical. In the literature, many experimental and computational studies have been performed in general about the hydrodynamics of gas-solid spouted beds (Benkrid and Caram, 1989; Du et al., 2006b; Guoxin et al., 2008; He et al., 1994a; Huilin et al., 2004; Larachi et al., 2003; Matsen, 1968; San José et al., 2006; San José et al., 1998; San José et al., 2005b; Sari et al., 2012; Shuyan et al., 2009; Shuyan et al., 2010; Takeuchi et al., 2008; Thanit et al., 2005; Wang et al., 2006; Zhu et al., 2011). Unfortunately, the literature is lacking data regarding the key parameters that characterize the gas-solid flow of spouted beds. Even though a number of published results containing indirect deductions from invasive local measurement techniques or variation in experiment conditions have been reported, this is insufficient. The solids flow fields in gas-solid spouted beds are not yet fully understood (Duarte et al., 2009; Larachi et al., 2003). Having a fundamental understanding of the gas and solids dynamics is critical for evaluating gas-solid contact efficiencies in spouted beds (Takeuchi et al., 2008). Most of the experimental studies reported in the literature that focus on the characterization of hydrodynamics within gas-solid spouted beds were carried out using invasive techniques of local point measurement (e.g., pressure probes, optical and capacitance probes). These types of invasive techniques have several limitations, the main limitation being the local disturbance of the gas-solid flow caused by the probes (Liu et al., 2008). Studies on important parameters that characterize the hydrodynamics of gas-solids spouted beds, such as those looking at the cross-sectional phases' distributions, the holdups radial profiles along the bed height, the 3-D solid velocity fields, the turbulent parameters, the gas

dispersion, and the mixing behavior are extremely rare in the open literature. In addition to that, most of the reported studies mentioned above have findings that cannot be directly employed to optimize actual spouted bed nuclear fuel coaters.

Indeed, the outlook for future fuel-coating technologies and applications are further complicated by the fact that many new concepts will involve fuel kernels of various sizes, compositions, and densities. An example of this can be found in the growing interest to include new coating materials such as zirconium-carbide (ZrC), which would provide greater resistance against chemical attack by the fission product palladium and which would permit an increase in the power density and size of the VHTRs. It is then necessary to acquire accurate knowledge on the crucial parameters that characterize the hydrodynamics of gas-solid spouted beds, such as cross-sectional phases' distributions, holdups radial profiles along the bed height, 3-D solid velocity fields, turbulent parameters, gas dispersion, mixing behavior, and others. It can be possible to assess these key parameters and to improve well-developed models and correlations for spouted beds using advanced non-invasive velocimetry or tomography techniques. This assessment can be achieved using two advanced non-invasive techniques available in our laboratory: gamma-ray computed tomography (CT) and radioactive particles tracking (RPT) techniques. It has been proven through practical experimentation and research studies that CT and RPT are the most promising technologies for visualizing multi-phase flow systems (i.e. gas-liquid, gas-solid, gas-liquid-solid phase) (Al Mesfer et al., 2016, 2017; Bhusarapu et al., 2004; Duduković, 2003; Karim et al., 2004; Larachi et al., 1997; Luo et al., 2003; Rados et al., 2003; Shaikh and Al-Dahhan, 2003; Wu et al., 2001). With that perspective already mentioned, this was the primary motivation behind the initiation of the current study.

1.6. OBJECTIVES

The focus of this work is to conduct an experimental study on the hydrodynamics of gas-solids spouted beds using advanced measurement techniques. The overall objective is to advance the fundamental understanding of gas-solids spouted bed hydrodynamics and mixing behavior, related to the gas/solids holdups and 3-D solids flow fields, and to assess the scale-up methodologies of spouted beds. The obtained data are valuable as benchmarking data for the validation and evaluation of computational fluid dynamics (CFD) models. The specific objectives to be accomplished in this work are to:

I. Experimentally investigate the effects of gas velocity, bed size (3-inch and 6-inch ID), particle size, and particle density on the radial or diameter profile and cross-sectional distributions of gas and solids holdups in gas-solid spouted beds using gamma-ray computed tomography (CT).

II. Experimentally investigate the hydrodynamics and mixing behavior of binary solids mixtures (same size, but differing densities) within 6-inch spouted beds using the radioactive particle tracking (RPT) technique. This will allow us to study solid velocity fields and turbulence parameters (Reynolds stresses, turbulent kinetic energy, and turbulent eddy diffusivities).

III. Assess the scale-up methodologies of gas-solid spouted beds using radioactive particle tracking (RPT) based on the solids fluctuation velocity, solids turbulent diffusivity, and the 3-D trajectory time series analysis. Dynamical tests will be applied on the RPT data to determine residence time distribution (RTD), distribution/average cycle time of the solids, and probability of solids transition between adjacent regions of the bed.

2. LITERATURE REVIEW

Section 2 presents a comprehensive review of all relevant literature. It covers the hydrodynamics of gas-solid spouted beds operated with particles of heavy density, hydrodynamics and segregation of binary solids mixture spouted beds, and the scale-up of gas-solid spouted beds.

2.1. SPOUTED BEDS OPERATED WITH HEAVY PARTICLES

In the literature, only few studies on spouted beds operating with heavy particles of density above 5 g/cm^3, mostly encountered in the TRISO coating process were, so far, reported (Sari et al., 2012; Zhou and Bruns, 2012). Zhou and Bruns (Zhou and Bruns, 2012) experimentally studied the minimum spouting gas velocity of zirconia particles (ZrO_2, ρ_p = 5.89 g/cm^3) in shallow spouted beds, with the help of pressure drop sensors. They established new correlations for estimating the minimum spouting velocity based on experimental data. In addition, Sari et al. (Sari et al., 2012) investigated the minimum spouting gas velocity of ZrO_2 particles (ρ_p = 6.05 g/cm^3, d_p = 0.5, 1 mm) by means of pressure drop measurements in spouted beds with a diameter of 150 mm and cone angles of 30°, 45°, and 60°. The investigation indicated that the steady spouting state exists in the range of $1.2U_{ms}$–$2.1U_{ms}$, beyond which jet spouting begins; U_{ms} is the minimum spouting velocity. The above studies only focused on the minimum spouting velocity and one type of high-density particles. So far, no detailed studies on the effects of high-density particles on local hydrodynamic parameters of spouted beds have been reported. Pannala et al. (Pannala et al., 2007) used the Multiphase Flow with Interphase eXchanges (MFIX) computer code to simulate the spouting process of zirconia particles in 2-dimensional

rectangular and conical-bottomed spouted beds. This model treats phases as continuous and interpenetrating, yielding a granular layer pseudo-fluid, which requires the definition of some properties such as viscosity bulk, shear the granular phase and pressure granular stage properties present in the momentum balance equation. Absence or unavailability of advanced measurement techniques for experimental validation were the reasons for why they simulated 2-dimensional spouted beds instead of fully 3-dimensional spouted beds. They pointed out that experimental studies are essential for better optimization and validation of more accurate computational modeling of spouted beds. Furthermore, Liu et al. (Liu et al., 2012) used pressure sensors at both ends of the spouted beds to establish a relationship between the pressure drop change prior and following the coating process of each layer in the real TRISO fuel-coating process. The authors found that the pressure drop change occurred simultaneously with the change of particle properties during the successive coating of each layer. They also pointed out that experimental investigations are needed to quantify specific influences of key parameters on local spouted bed hydrodynamics. Liu et al. (Liu et al., 2015a) used the CFD–DEM (Computational Fluid Dynamics–Discrete Element Model) coupling simulation method to examine the fluidization behavior of particles with different densities in the spouted bed. The simulation results revealed that the spouting behavior of the particles is incoherent and periodic when the spouting state is stable. They reported that the stable spouting range expands with particle density increases.

Taking into account the complexity of the two-phase flow through a spouted bed, a comprehensive knowledge of the hydrodynamics involved has not been achieved to date. Many experimental and computational works on the hydrodynamics and flow field of gas-

solid spouted beds, in general, have been reported (Bahramian and Olazar, 2011; Benkrid and Caram, 1989; Du et al., 2006b; Du et al., 2015a; Duarte et al., 2009; Guoxin et al., 2008; He et al., 1998; He et al., 1994a; He et al., 2000; Lan et al., 2012; Lim and Grace, 1987; Madonna, 1966; Piskova and Mörl, 2008; San José et al., 2005a; San José et al., 1998; San José et al., 2005b, c; Shuyan et al., 2009; Wang et al., 2014; Zhonghua and Mujumdar, 2008). The reported studies used various techniques, such as direct visualization, pressure measurements, and various probes to measure global dynamic parameters (e.g., spout diameter, spout shape, spoutable height, fountain height, etc.). Furthermore, some of them employed intrusive techniques such as optical and capacitance probes for local point measurement. Both optical fiber and static pressure probes have been widely used for hydrodynamic characterization of the spouted bed systems. However, these techniques have several limitations, a major one being the local disturbance of the gas-solid flow caused by the probe (Liu et al., 2008). Moreover, the conditions in all of these studies focus on low-density particles (ρ_p < 3.0 g/cm^3). It is then necessary to acquire accurate knowledge on the crucial parameters that characterize the hydrodynamics behavior of spouted beds, such as cross-sectional phases' distributions, holdups radial profiles along the bed height, 3-D solid velocity fields, turbulent parameters, gas dispersion, mixing behavior, and others. Recently, it has become possible to assess these key parameters and to improve well-developed models and correlations for spouted beds using advanced non-invasive velocimetry or tomography techniques. In our laboratory, the mentioned assessment has been achieved using advanced non-invasive techniques: Gamma-ray computed tomography (CT) and Radioactive particles tracking (RPT) techniques. With these techniques, we were able to address important issues related to the

scale-up of spouted beds (Ali et al., 2016a, 2017a). It has been proven through practical experimentation and research studies, that CT and RPT are the most promising technologies for visualizing multi-phase flow systems (i.e., gas-liquid, gas-solid, gas-liquid-solid phase) (Duduković, 2003; Larachi et al., 1997).

For this part of the study, we aim to provide an experimental investigation of the hydrodynamics of gas-solid spouted beds at cold conditions using advance non-invasive technique; gamma-ray computed tomography (CT). The gas-solid distribution and its variations have a strong impact on the performance of the spouted beds. Assessment of phase (gas or solids) distributions in spouted beds is of primary concern for accurate design and control of the TRISO fuel-coating process. For example, knowledge of the gas and solids holdup distributions would define parameters such as the spouting conditions, the coating gas composition, and the coating temperature, which will, in turn, result in a higher probability of coating success. The coating layers deposited on the particles depend on how and where the particles are present in the bed. In spouted beds, the solids holdup distributions (or gas holdup) differ from region to region and these differences cause changes in gas-solid interactions and, above all, changes in the value of the absorption and the conversion of gaseous reactants. In this part of the study, the effects of the particle properties and operating parameters on the gas-solid distribution of spouted beds are the focus. It is hoped that the originality of the results and the analysis of them presented here will provide the basis for assessing design and control processes of TRISO fuel coaters, and contribute to other spouted bed applications. This part of the study will provide reliable and valuable benchmark data for the assessment and validation of CFD models and their closures. Improved validation of CFD models for reliable and safe design, scale-up, and

process optimization will ensure proper performance and operation of TRISO fuel coaters. Finally, successful implementation of the CT as a non-invasive technique on the cold-flow coater will lay the ground for its implementation in hot pilot plants and industrial units.

2.2. HYDRODYNAMICS AND MIXING BEHAVIOR OF BINARY SOLIDS MIXTURE GAS-SOLID SPOUTED BEDS

In literature, several studies have been reported in general about the hydrodynamics of binary solids in conventional spouted beds, also known as conical-cylindrical spouted beds (Cook and Bridgwater, 1978; Du et al., 2016; Du et al., 2015a; Du et al., 2015b; Ishikura et al., 1983; Kutluoglu et al., 1983; Liu et al., 2015b; Piccinini, 1980; Piccinini et al., 1977; Robinson and Waldie, 1978; Takeda and Yamamoto, 1976). Some studies were reported for the hydrodynamics of binary solids but different types of spouted beds such as the conical spouted beds (i.e. made with fully conical geometry) (José, 2013; Olazar et al., 1993; San José et al., 2006; Santos et al., 2012), and the flat-bottom spout-fluid bed, (Zhang et al., 2011; Zhang et al., 2012, 2013). Earlier experimental studies with systems of both continuous solids flow (Kutluoglu et al., 1983; Piccinini, 1980; Piccinini et al., 1977) and batch solids (Cook and Bridgwater, 1978; Robinson and Waldie, 1978) revealed that the particles of larger size and density usually tend to go through comparatively short cycle within the three distinct regions of spouted beds (i.e., the spout, the fountain, and the annulus) in comparison to the particles of smaller size and density. Consequently, the particles of the larger size and density congregate in the inner upper area of the annulus region, the region where the particles move slowly and downward and spend most of their time in the bed (Robinson and Waldie, 1978). (Olazar et al., 1993) used probe-based techniques (i.e., pressure probe, optical probe, and sampling suction probe) to investigate

bed stability and bed segregation of conical spouted beds for binary mixtures with particles of different sizes but similar densities. The effects of the stagnant bed height, of the geometrical dimensions of the bed (inlet diameter, cone angle), of the height of the stagnant bed, of the gas velocity, and of the mixture composition on bed segregation and bed stability have been reported. They concluded that conical spouted beds could present more effective stability when operating with a binary mixture of particles of varied sizes rather than uniform ones at certain operating conditions. However, the pressure probe, optical probe, and sampling suction probe techniques have been largely used for hydrodynamic characterization of the above mentioned spouted bed systems where such techniques have several limitations, a major one being the local disturbance of the gas-solid flow caused by the probe (Liu et al., 2008). (Zhang et al., 2012, 2013) investigated the mixing and segregation behavior of a binary mixture in a flat-bottom spout-fluid bed. They used pressure taps and high-speed digital CCD camera for measuring flow regimes, and concentration profiles, receptively. The effects of the size and density of the particles on spouting stability have been examined in terms of mixing index, flow regimes, and concentration profile using pressure taps. (Ren et al., 2012) studied the mixing behavior of binary mixtures of particles having equally size and different density in conventional spouted beds, conical-cylindrical spouted beds, using three-dimensional computational fluid dynamics (CFD) coupled with the discrete element method (DEM) and determined that the mixture of the binary particles go through/experience three stages of mixing process: macro-mixing, micro-mixing, and stable-mixing stages. (Du et al., 2015a) used measurements of pressure drop and it's fluctuation analysis to determine the transitions mechanisms of the flow regime in spouted beds of fine particles mixed with coarse particles

of different density, or size, or both. Similar to what is reported earlier in conical spouted beds, they found effective improving spouting stability in spouted beds of fine particles when mixed with particles of coarse size. Almost the same group, later on, reported flow regime transitions maps for spouted beds of fine particles mixed with coarse particles (Du et al., 2015b). The effects of the size and density of the particle, the ratio of mixing, gas velocity and diameter of inlet orifice on minimum spouting velocity and transition of flow regime in spouted beds of fine particles have been reported. They concluded that more experimental investigation is needed to quantify key parameters on the flow field and local hydrodynamics of binary spouted beds. Recently, (Du et al., 2016) studied the segregation phenomena and the mixing of the particles in spouted beds of binary mixtures of fine and coarse particles using CFD coupled with a multi-fluid model (MFM). The simulation results showed that the mixing and segregation of the particles in the binary mixture spouted bed are rather impacted by the density than the size of the coarse particles. In addition to that, the simulation showed that increasing the applied spouting velocity of the bed can contribute to the reduction in the segregation extent of particles. They concluded that in spouted beds of a binary mixture, the segregation of the particles exists in a region in which the difference in the gas-solid drags of different solids is significant.

Although the insights on the effects of varying the size, density, shape, and collision properties given by the previously mentioned studies, understanding the hydrodynamics of gas-solid spouted beds of binary mixture are still not satisfactory from a fundamental level. Indeed, almost no experimental results that have been reported in the literature so far on the solids holdups distributions, 3-D solids velocity field, fluctuation velocity, turbulent parameters (stresses, kinetic energy, granular temperature, eddy diffusivity), particle-

particle interactions, circulation time, local residence time, and stagnant zones, and many other parameters in binary spouted beds. In addition to that, most of the experimental investigations of segregation in binary spouted beds are through invasive withdrawal of samples and their analysis, a measurement protocol which may itself change the segregation pattern. Computational fluid dynamic (CFD) models, such as the work of (Du et al., 2016) have been moderately successful in tracking the mechanisms of mixing and segregation, even though they often depend on *ad hoc* treatment of particle collisions through the concept of distinct granular temperature for each solids phase. Discrete element models (DEM), such as the work of (Ren et al., 2012), probes much deeper into the mechanism of segregation and also identify the relevant time scales. However, both k-fluid CFD (Euler-Euler) and DEM CFD (Euler-Lagrange) models suffer from the essential drawback of the lacking of the reliable experimental data for local velocities and volume fraction distribution. In addition, the sensitivity of such models when multiple solids present to different conditions such as gas holdup distribution or different distribution functions such as the radial distribution is far from being reported in the literature. Global validations (such as overall bed expansion, pressure drop) even when applied to these sophisticated mechanistic models, do not do justice to them since the underlying local gradients of velocities and phase fractions are never verified or validated. Moreover, models found in the literature, such as the multi-fluid model (MFM) used to describe gas-solid-solid flow, impose several assumptions and coefficients that are usually adopted for the two-fluid model (TFM) used for gas-solid two-phase flow because of a lack of experimental data. Clearly, there is a strong need for such reliable experimental data before these models can be further extended or be expected to make realistic predictions.

Moreover, in the above literature, only one study on binary solids in gas-solids spouted beds operating with heavy particles of density above 5 g/cm^3, mostly encountered in the TRISO coating process were, so far, reported (Piccinini et al., 1977). However, only qualitative information was given about the effect of particle density on the segregation phenomenon using glass ballotini (ρ_p ~ 2.56 g/cm^3) and steel ball bearings (ρ_p ~ 7.92 g/cm^3) of the same diameter.

As aforementioned, the hydrodynamic behavior of gas-solid flow in binary spouted beds demands an investigation. Therefore, for this part of the study, we aim to provide an experimental investigation on the hydrodynamics of gas-solid spouted bed of binary mixture having particles of a same size and different densities by means of advance non-invasive; Radioactive Particle Tracking (RPT) technique. A binary mixture consists of glass beads and steel particles of densities 2500 and 7400 kg/m^3, respectively are used in the experiments. The glass and steel particles were intentionally selected to obtain density ratio (ρ_{steel} /ρ_{glass} ~ 2.96) between the two materials close to that acquired in the actual spouted bed nuclear fuel coaters after the coating of the first layer ($\rho_{kernel\text{-}Uo2}$/$\rho_{kernel\text{-}coated\text{-}PyC}$ ~ 2.63). In the RPT technique, a single radioactive tracer particle similar in density, size, and shape of the tracked solids phase is employed to track the recirculating of the representing solids phase. The RPT had already proved, through practical experimentation and research studies, its capability to track solids and liquid dynamics in different multiphase flow systems such as gas-solid spouted beds (Ali et al., 2017a), gas-liquid bubble columns (Al Mesfer et al., 2017), gas-solid raiser (Bhusarapu et al., 2006), gas-solid fluidized beds, gas-solid pebble bed (Khane et al., 2016a). In our previous works, we used the same technique to evaluate scale-up approaches of spouted beds (Ali et al., 2017a).

In this part of the work, the RPT experiments have been performed for binary mixtures of different compositions at different superficial gas velocities to evaluate the effect of compositions on the flow filed of spouted beds of binary mixture. Since the flow behavior of the gas-solid spouted beds is chaotic, the RPT experiments were carried out for each one of the solids phases on an individual basis, and then the statistical averages of each flow fields are combined together to formulate the entire picture of the binary mixture flow field. The same method using the RPT technique was adopted to investigate solids mixing in gas-liquid-solid fluidized beds (Cassanello et al., 1996) and gas-solid-solid fluidized beds (Upadhyay and Roy, 2010). Thus, for this part of the study, the RPT technique is used for the first time to investigate hydrodynamics behavior of gas-solid flow in binary spouted beds. The finding of this work will help to advance the understanding of the gas-solid spouted beds for advanced nuclear fuel particle manufacturing where the four coating layers occur in series and hence binary mixtures of solids could occur. Similar conditions could be encountered in any industrial applications of spouted beds where binary mixture of solids present such as drying, coating, granulation, polymerization, and gasification (Gryczka et al., 2008; Mathur and Epstein, 1974c; Olazar et al., 2003; Olazar et al., 1992).

2.3. SCALE-UP OF GAS-SOLID SPOUTED BEDS

The scaling up of the gas-solids spouted-beds from the laboratory sizes to larger commercial unites is a challenging task. In the literature, different studies on the scale-up of gas-solids spouted beds were so far reported (Al-Juwaya et al., 2017; Ali et al., 2016a, 2017a, b; Aradhya et al., 2016, 2017; Béttega et al., 2009; Du et al., 2009; He et al., 1997; Konduri et al., 1999). (He et al., 1997) proposed the first scaling up methodology of gas-

solids spouted beds that is based on matching dimensionless groups. The dimensionless groups derived by (He et al., 1997) are:

$$\left\{\begin{matrix}\frac{gd_p}{U^2}, \frac{\rho_s d_p U}{\mu}, \frac{\rho_f}{\rho_s}, \frac{H}{d_p}, \frac{D_c}{d_p}, \phi_s, \varphi, \varepsilon_o, dimensionless\ particle\ size \\ distribuation\ and\ dimensionless\ bed\ geometry\end{matrix}\right\} \quad (1)$$

In their work, (He et al., 1997) adapted the scaling rules proposed by Glicksman (Glicksman, 1984) for gas-solid fluidized beds which are derived for the most part from non-dimensionalizing the equations of motion for fluid and particles which leads to dimensionless hydrodynamic numbers (e.g. Froude (Fr) and Reynolds (Re) numbers). However, this was despite the differences in the dynamic behaviors of solids particles between the spouted beds and fluidized beds. In fluidized beds, air is introduced via a multiorifice distributor/plate to penetrate the bed particles where the bed is divided into two distinct regions; bubble and emulsion. On the other hand, the gas in spouted beds is introduced as a jet via a single orifice located in the center of a conical base creating three distinct regions inside the bed and establishing a systematic cyclic pattern of solid movement. These differences made the scale-up of spouted beds is distinct than that in fluidized beds, due to the complex interaction between the phases (particle-particle, fluid-particle interaction) and the existence of the three distinct regions in spouted beds. (He et al., 1997) evaluated the above set of dimensionless groups experimentally in two different sizes of spouted beds at ambient and elevated pressure. They designed a series of experiments with varied operating conditions where the dimensionless groups are matched and mismatched between the two beds. (Du et al., 2009) added the restitution coefficient

parameter (e_{ss}) that accounts for the effects of particle-particle collisions in the spout to the dimensionless groups of (He et al., 1997). Subsequently, the full set of the scale-up groups have become to be:

$$\left\{ \frac{g d_p}{U^2}, \frac{\rho_s d_p U}{\mu}, \frac{\rho_f}{\rho_s}, \frac{H}{d_p}, \frac{D_c}{d_p}, \phi_s, \varphi, \varepsilon_o, e_{ss}, \begin{array}{c} dimensionless\ particle\ size \\ distribuation\ and\ dimensionless\ bed\ geometry \end{array} \right\} \quad (2)$$

However, the aforementioned studies of (He et al., 1997) and (Du et al., 2009) only met with limited success since the hydrodynamic similarity on these studies was demonstrated based on measurements of global parameters such as dimensionless fountain height, pressure along the annulus, and dimensionless spout diameters. Recently, (Aradhya et al., 2017) and (Ali et al., 2016a, 2017a) confirmed that (He et al., 1997)'s approach of matching dimensionless groups for scale up of spouted beds is not sufficient for attining hydrodynamics similarity according to measurments of local hydrodynamics parameters using optical fiber probe (Aradhya et al., 2017), gamma-ray computed tomography (CT) (Ali et al., 2016a), and radioactive particle tracking (RPT) techniques (Ali et al., 2017a). This drove (Al-Dahhan et al., 2014) and (Aradhya et al., 2016) to propose a new scale-up methodology based on a mechanistic approach that requires the knowledge of the radial gas holdup profiles since the gas phase dictates the flow dynamics of the gas-solid spouted beds.

The new mechanistic scale-up methodology of gas-solid spouted beds has been proposed as follow (Al-Dahhan et al., 2014; Aradhya et al., 2016):

"*when spouted beds with different sizes and/or conditions are geometrically similar and have closer (which is called matched) gas phase holdup radial profiles at a desired bed height within the developed flow region, the local dimensionless values of the hydrodynamic parameters and their trends are similarity or closer to each other in these two spouted beds at corresponding bed heights*"

Consequently, by attaining similar gas holdup profiles between two different sizes spouted beds, a successful scale-up is achieved. (Aradhya et al., 2016) with the help of computational fluid dynamics (CFD) defined operating conditions that provide similar and dissimilar gas holdup profiles between two spouted beds of different sizes. They demonstrated the validity of the new scale-up methodology based on measurements of limited local solids holdup and solids axial velocity using optical probe technique. Further validation of the scale-up methodology was established based on measurements of the cross-sectional distribution of solids and gas holdups at selected dimensionless height and their radial profiles (Ali et al., 2018). (Ali et al., 2018) concluded that when the radial profiles of gas holdup are matched or close to each other for two beds of different sizes and conditions, the similarity in local solids and gas holdups is attained in all three regions of the spouted bed; the spout, the annulus and the fountain. More recently, we demonstrated the hydrodynamics similarity in terms of the dimensionless values and radial profiles of the components of the particles velocities, normal stresses, shear stresses and turbulent kinetic energy (Ali et al., 2017c). In this part of study, the new scale-up methodology of spouted beds is further validated by evaluating other key solid particles flow parameters such as the spout diameter, cumulative probability distribution of the solids particles penetration into the spout, fraction of cycle time in each region of the bed, the radial profiles

of the dimensionless values of the root-mean-square particle velocities and solids eddy diffusivity using radioactive particle tracking (RPT) technique. At a minimum, this part of the study is anticipated to advance the fundamental understanding of spouted beds hydrodynamics and scale-up processes and minimize time and cost of the related development. Additionally, it is expected that the further validation of the new scale-up methodology will provide opportunities to apply this method in control and process design of spouted beds nuclear fuel manufacturing than might ever before accomplished empirically. Also, this part of the study would lead to improvement in other applications of CVD coating process of gas-solid spouted beds such as encapsulation of high-temperature phase change materials (PCMs) (Zhang et al., 2017), and coating of pharmaceutical particles (Pissinati and Oliveira, 2003).

3. EXPERIMENTAL SET-UP AND MEASUREMENTS TECHNIQUES

This section is devoted to the description of the experimental set-up, the design of the spouting facility, the materials used, the experimental procedures, the measurement techniques, and the reconstruction algorithms of the techniques employed.

3.1. EXPERIMENTAL SET-UP OF SPOUTED BEDS

In the present study, the experimental works were carried out in two conical base spouted bed columns made of Plexiglas with an inner diameter of 0.076 m (3-inch) and a 0.152 m (6-inch). The schematic diagrams of the two spouted beds used are shown in Figure 3.1. Both columns were designed to be geometrically similar, with 1.14m height and conical base of a 60-degree angle. The two columns were designed without any ports or connections on the wall to eliminate the possibility of any non-symmetric problems on the columns, which complicates the CT and RPT data reconstructions process. Each column consists of one-piece column attached to a conical base. At the bottom of the conical base, a gas distributor made of stainless steel was placed to pass through the gas flow inside the column. The diameter of the inlet orifice is 9.5 mm, and 19.1 mm for 3-inch and 6-inch spouted beds respectively. Figure 3.2 shows gas distributor made of stainless steel and used for the 6-inch spouted bed. The gas used was dry compressed air supplied from an industrial compressor with capacity up to 735 CFM and 200 Psig. After the flow pass through the piping components of the compressor, the rate of the flow is regulated, using a pressure regulator and rotameter setup consisting of two rotameters connected in parallel. The gas flow rates were measured using the two rotameters and were introduced into the spouted beds through the inlet orifice (gas distributor).

For all the objectives and experimental conditions investigated, three standard conditions were applied in the operation of spouted beds to sustain stable spouting in each one of the spouted bed setups mentioned above. This first condition is based on the ratio of the column diameter and the particle diameter Di /d_P < 25~ 30 and was submitted proposed by (Chandnani and Epestein, 1986) submitted the first standard condition by the following equation Di /d_P < 25~ 30 through experimental works were achieved on a small column and fine particles. (Mathur and Epstein, 1974b) Proposed the second standard condition by the following equation D_c/Di > 3~12 by evaluating experimentally small columns. Finally the third standard condition (He et al., 1992) was based on equation H < H_m. Whereas, D_i is diameter of the gas inlet, d_p is the diameter of the particle, D_c is the diameter of the column, H is the height of the static bed, and H_m is the height of the maximum spoutable bed.

3.2. DUAL SOURCE GAMMA RAY COMPUTED TOMOGRAPHY (DSCT)

The Dual Source Gamma-ray Computed Tomography (DSCT) is a systemized technique used to obtain measurements of cross-sectional phase distribution of two-phase or three-phase flow systems (gas-liquid, gas-solid, and gas-liquid-solids). The CT has been employed for visualization of different multiphase flow systems (Al-Dahhan, 2009; Al-Dahhan et al., 2007; Al Mesfer et al., 2016; Bhusarapu et al., 2006; Chen et al., 1999; Kemoun et al., 2001; Kumar et al., 1995; Liu et al., 2011; Luo and Al-Dahhan, 2010; Prasser et al., 2003; Rados et al., 2005; Roy and Al-Dahhan, 2005; Roy et al., 2005; Shaikh and Al-Dahhan, 2005; Varma et al., 2008). The details of the hardware and software information of the DSCT have already been elaborated in detail by Varma et al. (Varma et al., 2008). The DSCT setup consists of a selection of collimated detectors and opposing

sources present on a platform that can rotate 360° around the column that needs to be scanned.

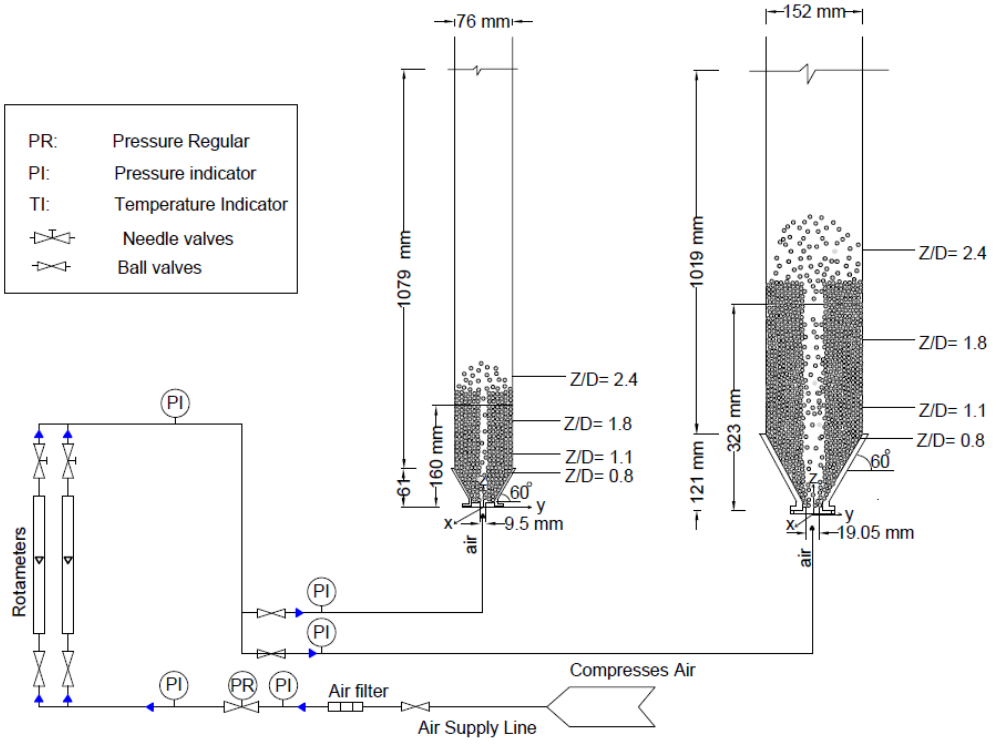

Figure 3.1. Schematic diagram of 6-inch and 3-inch spouted beds setups used for CT and RPT measurements. z/D represents the dimensionless highest used in CT experiments.

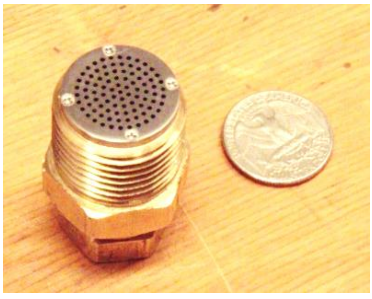

Figure 3.2. Gas distributor (stainless steel) used for 6-inch spouted bed to pass through the gas flow inside spouted bed.

It provides 197 views in each scan and 21 projections in each view. Figure 3.3 shows a typical 3-dimentional (3D) model of the DSCT technique's platform. This platform can move up and down to capture the vertical view of the column to generate 2-dimentional (2D) and 3-dimentional (3D) images. The DSCT setup consists of two sealed gamma ray sources. Each source is housed on a collimated device in such a way to provide a fan-beam shape with a thickness of about 3 mm and a fan angle of 40°. The radioactive isotopes used in the DSCT are Cs-137 and Co-60 with initial activity of about, 200 and 300 mCi (millicurie), respectively. The Cesium (Cs-137) and Cobalt (Co-60) were the most frequently used isotopes as gamma-ray sources. The Cs-137 is commonly used in nuclear gauging applications in industries because it has a long half-life, it does not scatter interference of photons of other energies and emits single clear photo peak. Co-60 is also widely used because of its small scatter interference of signals. Based on the number of sources used in the DSCT system, it can be called as a single source in a case it is one or a dual source in a case the two sources are used. In this work, only Cs-137 was used to distinguish between the solid and gas phases of spouted beds and the technique called CT.

Opposite to each source, an array of 15 sodium iodide (NaI) scintillation detectors is located on an arch plate to collect the unattenuated gamma rays passing through the column. The detectors are 802 Canberra model where each detector consists of 2 × 2 inches of cylindrical NaI scintillation crystal, a photomultiplier tube (PMT), an internal magnetic/ light shield, aluminum housing, and a 14-pin connector. Each detector is followed by a Canberra preamplifier and excited at 900V provided from a high power supply. The detected signal, the signal from the preamplifier, is then amplified using timing amplifier, and processed, recorded, using multilevel discriminator and a scaler. The detectors are

collimated by a 2 mm slit width lead collimator, attached on the crystal of each detector. The CT has a connection to a power supply that provides the charge to excite the detectors. The detectors absorb the fallen radiation and release it as light photons that hit photo-sensitive cathodes and multiplier tubes. The free electrons that arise in the process are multiplied and sent to the output as current. The signals from the detectors are amplified by a timing amplifier to increase the amplitude from the detectors. The NaI detectors used were Canberra Model 802 scintillation detectors. Each detector in the system consist of NaI (TI) scintillation crystal (2 × 2 inches), a photomultiplier tube (PMT), a light shield, aluminum housing, and a 14 connections pins. The High voltage (HV) applied for the PMT of each detector was 900V. The detected signals coming from the detectors were discriminated from background radiation and recorded by a fast-timing multilevel discriminator and a scaler respectively.

The detectors arrays are used to collect the unattenuated photons of the gamma rays that pass through the multiphase experimental setup. Figure 3.4 shows a detailed top view of the setup, with the dimensions and angles that are used in the image reconstruction process. The sources and the detectors arrays are both mounted on a rotational plate that moves them together 360° around the investigated column, offering 197 views in each scan and 21 projections in each view. This rotational plate is connected to another plate that moves axially to selected level position to take the scan. In this work, only Cs-137 (gamma photon energy of 0.662 MeV) source was used for spouted beds experiments with an activity of about 200 mCi at the time of the experiments. The counts for each projection were collected for 60 samples at 20 Hz to improve accuracy. However, a total of 62055

(197 views × 315 projections) projection measurements were taken across the domain of the spouted bed column in each scan.

Figure 3.3. The platform of the DSCT technique and 6-inch gas-solid spouted bed inside the setup for the scan.

Quantitative measurements of the phase volume holdups were made for the gas-solid spouted beds. Before scans are taken, the gas flow rate introduced into the column and the bed pressure are set at the desired operating conditions, and time is given for at least 30 minutes for the entire system to allow stabilizing the flow inside the spouted bed.

Once the desired operating condition is obtained, The CT system is employed to take the scan at different vertical locations. For convince of comparison between the two beds, those vertical locations were nondimensionalized heights (z/D) and shown in Figure 3.1, where z refers to the actual height of measurement from the gas distribution and D refers to the column diameter of spouted beds. The z/D levels of scan for the two beds were, at the cone section (z/D=0.8), above the cone section (z/D=1.1), at the middle section and below the bed surface (z/D=1.8), and finally at the fountain region (z/D=2.4). Note that the dimensionless levels (z/D) between the two beds are matched. Figure 3.5. Shows a photograph of the DSCT setup and the 6-inch spouted bed inside for scan.

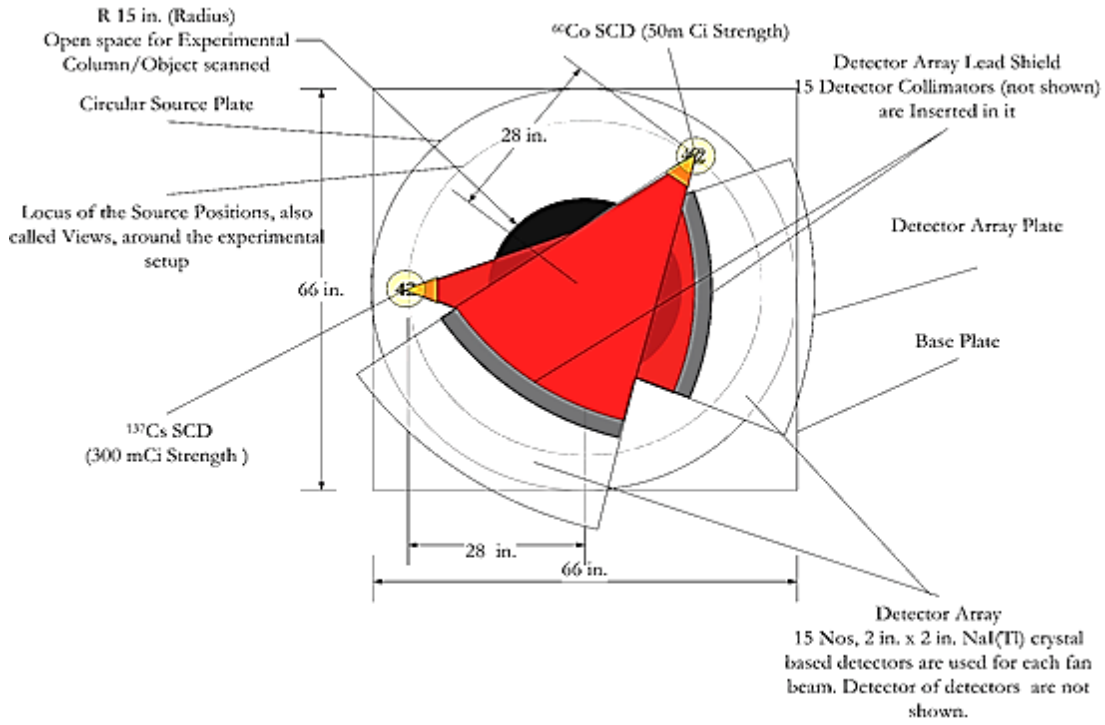

Figure 3.4. Schematic diagram showing the top view of the DSCT technique the red region between the source and the detectors represents the γ ray beam (physically not visible) (Varma, 2008).

Figure 3.5. Photograph of the DSCT technique, and 6-inch spouted bed inside the setup for scan.

3.2.1. Implementation of Alternating Minimization (AM) Reconstruction Algorithm for CT Experiments.

Prior to discussing the algorithm implemented here, note that in reconstruction, data obtained during CT scans are interpreted in terms of Beer-Lambert's law.

$$I = I_o . \exp(-\mu . l) \tag{3}$$

Where, in general, I and I_o are incident and radiation intensity after passing through length l [cm] of object whose linear gamma-ray attenuation coefficient is μ [cm^{-1}]. Note that the linear attenuation coefficient μ differs from the mass attenuation coefficient μ/ρ.

As illustrated in equation (3), to obtain the attenuation coefficient values, a part from the transmission ratio, the chord lengths l for each pixel should be identified. In the next step the purpose is obtain l.

The value of l is calculated based on the geometry of CT scan and the dimensions of spouted bed column. The first step in the reconstruction process is to define the size of the pixels or the dimensions of the matrix used for the discretization of the reconstruction domain. Cross, circular, section of spouted bed column is encompassed by a square matrix with dimensions (n) raws x (m) columns, as shown in Figure 3.6.

The size of the pixels also depends on the achievable spatial resolution of the CT scanner, (i.e., the detector collimator width. An even number of pixels is needed on each side of the matrix, and hence a suitable number of pixels were selected). Hence, the corresponding size of the pixels is then calculated to represent the diameter of spouted bed column. To obtain that, a FORTRAN code "*fanmat.f*" available in our laboratory is used to calculate the following necessary information:

1. The identity of the pixels through which the projection pass through.
2. The length of the intersection of each pixel (l) in each view and the projection ray passing through it (21 projections per view for one detector, 197 views per one completed CT scan).
3. The identity of all the rays that pass through any given pixel and the length of intersection of each of those rays with that pixel.

Summary of user inputs in "*fanmat.f*", for the 6-inch spouted bed are listed below:

• M: The number of views (197)
• N: The number of pixels on one side of the matrix (even number, 80). For example, if N=80, then the domain will be divided into 80x80 pixels. Note that in this case (DCOL = 6", N=80) pixel size is 2 mm, which is exactly the resolution limit or the detector collimator width.
• ND: The number of detectors (15)
• NB: The number of projections in one view (ND x NP, 315)
• DCOL: The diameter of the test section (the diameter of 6-inch spouted bed column, 15.24), given in cm
• R: The distance between the source and the center of the spouted bed column (71.12 cm), in cm
• FANANG: The angle subtended by the spouted bed column on the source, in degrees (DCOL=15.24, FANANG =12.3). The *fanangle* is simply calculated as illustrated in the figure below (Figure 3.7).

For a given spouted bed column (3-inch or 6-inch ID), number of views, number of projections per view, and the matrix discretization, this process needs to be carried out just one time. Hence, the length l is known, the counts values I_o and I are measured in the absence and presence of the spouted bed column respectively. The next step is to assign initial values for the Alternating Minimization (AM) reconstruction algorithm.

Algorithmically, the AM is an iterative process, and should start with some initial values in each pixel, and then iteratively adjust them to explore for μ values. The initial

guess values were assigned equal to the linear attenuation coefficient of water (0.08, unit [cm^{-1}]) to all the pixels in the square matrix, within or on the boundary of spouted bed column as shown in Figure 3.6. However, selecting these values can be randomly or heuristically if there was any information about where the μ value might be, only affects the number of iterations during the reconstruction process. Finally, for the pixels outside the spouted bed domain, zero is assigned.

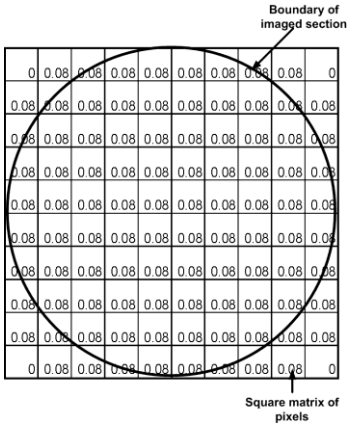

Figure 3.6. The computational domain is discretized into cells of size x.

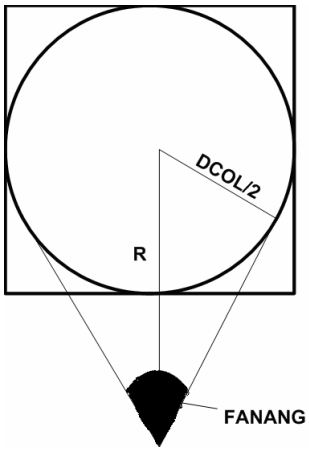

Figure 3.7. Geometrical features of fan-angle subtended by spouted bed column.

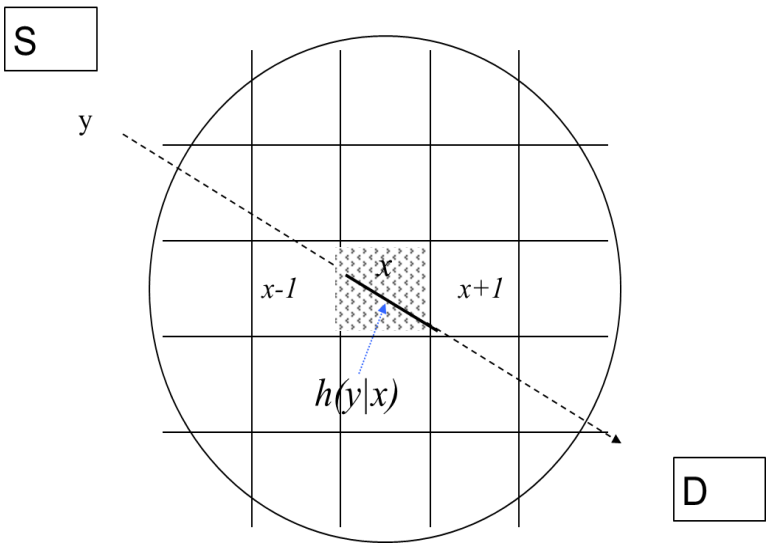

Figure 3.8. Schematic of the representation of a transmission tomography domain (Varma, 2008).

For image reconstruction, an Alternating Minimization (AM) algorithm has been applied to determine the phase holdup distribution in gas-solid spouted beds. The AM has been developed by (O'Sullivan and Benac, 2007) and implemented by (Varma, 2008; Varma et al., 2008) for imaging two-phase systems in case of single gamma source is used. The target throughout the AM algorithm will be to reformulate the maximum likelihood estimation problems into the minimum Kullback-Leibler divergence (I-divergence or information divergence) (Csiszár, 1975) and tackle it by means of AM algorithm. Prior to discussing the AM method, the notations used are listed below (see Figure 3.8 to understand these notation):

- x : Indices of pixel (image coordinate).
- $\mu(x,E)$: Attenuation coefficient of each pixel x (cm^{-1}) for a photon of energy E (KeV).
- $\varepsilon_i(x)$: Holdup of phase i in pixel x.

- *y*: Indices of source detector pair (projection).
- *d(y)*: Transmission data for a given *y*. This is a Poisson random number
- *d(y,E)*: Energy tagged transmission data *d(y)*.
- *h(y|x)*: Length of the segment of the projection *y* that is within the pixel *x* (cm).
- $I_o(y)$: Incident photon counts (source intensity).

The image reconstruction algorithm is based on Beer-Lambert's law and relatively realistic reconstruction model for known length of projection (*l*).

$$I = I_o . \exp(-\mu . l) \tag{4}$$

If $q(y:\mu)$ is defined as the model for the transmission of gamma photons per Beer-Lambert's law (Varma, 2008), hence

$$q(y:\mu) = I_o(y) \exp\left[\sum_{x \in X} -h(y \mid x)\mu(x)\right] \tag{5}$$

It is clear that $q(y:\mu)$ is a function of the attenuation $\mu(x)$ and the Length of the segment of the projection *y*, where x is the pixel space index. Csiszar's I-divergence is actually a discrepancy evaluate between two non-negative functions, a(y) and b(y) (Csiszar, 1991) that is provided as:

$$I(\mathrm{a} \,||\, \mathrm{b}) = \sum_{y \in Y}\left[a(y) \ln\left(\frac{a(y)}{b(y)}\right) - (a(y) - b(y))\right] \tag{6}$$

Where y is a finite dimensional space.

If we assume (Counts received by the detectors) $a(y) \to d(y)$. Then the I-divergence equation (6) will become:

$$I(d \,||\, q) = \sum_{y \in Y} \left[d(y) \ln \left(\frac{d(y)}{q(y:\mu)} \right) - (d(y) - q(y:\mu)) \right] \tag{7}$$

This algorithm criteria minimizes the I-divergence between the two functions (d and q), the first is linear (the measured data established) as well as the second is exponential (q). Minimizing equation (7) as $\min_{q \in \mu} I(d \,||\, q)$ with respect to $\mu(x)$ will yield equation (8) to obtain μ :

$$\hat{\mu}^{(k+1)}(x) = \hat{\mu}^{(k)}(x) - \frac{1}{z(x)} \ln \left(\frac{\tilde{b}(x)}{\tilde{b}^{(k)}(x)} \right) \tag{8}$$

Where:

$\hat{b}^{(k)}(x)$ and $\tilde{b}(x)$ are the back projections of d and the current estimates of q (the back projections of the measured data d and the Beer's model q above).

$$\tilde{b}(x) = \sum_{y \in Y} h(y \,|\, x) d(y) \tag{9}$$

$$\hat{b}^{(k)}(x) = \sum_{y \in Y} h(y \,|\, x) \hat{q}^{(k)}(y) \tag{10}$$

$$\hat{q}^{(k)}(y) = I_o(y)\exp\left(\sum_{x\in X} h(y \mid x)\hat{\mu}^{(k)}(x)\right) \tag{11}$$

The iterative process throughout the AM algorithm will work in reverse from equation (11) to equation (8), to provide us with a re-estimate of each and every possibility of the $\mu(x)$ values throughout the AM algorithm.

Where:

$\hat{\mu}^{(k=0)}(x)$: Initial guess values (used to calculate $\hat{q}^{(k)}(y)$ in equation (11).

$\hat{q}^{(k)}(y)$: used to to receive $\hat{b}^{(k)}(x)$ in equation (10).

$\tilde{b}(x)$: computed once based on the measured data $d(y)$.

$\hat{\mu}^{(k+1)}(x)$: acquired from equation (8) in alternating means (k = k+1).

$\hat{\mu}^{(k+1)}(x)$: cannot be negative. If $\hat{\mu}^{(k+1)}(x) < 0$ it is over written as $\hat{\mu}^{(k+1)}(x) = 0$.

Z(x): an appropriate scaling accustomed for the x^{th} pixel.

Hence, $\mu(x)$ is obtained by reconstructing the image from the entire set of projection measurements and the next step is to calculate the phase volume fraction or phase holdups for gas/solid spouted bed.

3.2.2. Calculating the Phases Holdups. For two-phase system, gas-solid spouted bed in this case, $\mu(x)$ In equation (12) represents the attenuation value, and ε represents the holdup fraction for each phase. Recall, the goal of using CT is to acquire ε (phase holdup for gas/solids). The total mass attenuation coefficient in eaquation (12) equals to the sum of the individual phase mass attenuation coefficients weighted by the respective volume fraction. Consequently,

$$\hat{\mu}_{s-g}(x) = \hat{\mu}_s(x)\varepsilon_s(x) + \hat{\mu}_g(x)\varepsilon_g(x) \quad (12)$$

Where:

$\hat{\mu}_{s-g}(x)$: is the attenuation value for the gas-solids when the system is dynamic at the desired operating condtion.

$\hat{\mu}_s(x)$: is the attenuation value for pure solids phase.

$\hat{\mu}_g(x)$: is the attenuation value for pure gas phase (empty column).

$\varepsilon_s(x)$: is the solids phase fraction (or solids holdup).

$\varepsilon_g(x)$: is the gas holdup fraction (or gas holdups).

Then if we assume $\hat{\mu}_g(x)$ is neglected (attenuation for gas is very small). Hence, equation (12) will become,

$$\hat{\mu}_{s-g}(x) = \hat{\mu}_s(x)\varepsilon_s(x) \quad (13)$$

The sum of the phase holdups is equal to unity ($\varepsilon_s + \varepsilon_g = 1$). if we replace ε_s by $1-\varepsilon_g$, equation (13) becomes,

$$\hat{\mu}_{s-g}(x) = \hat{\mu}_s(x)(1-\varepsilon_s(x)) \quad (14)$$

Hence, the gas holdup is equal to

$$\varepsilon_g(x) = \frac{\hat{\mu}_s(x) - \hat{\mu}_{s-g}(x)}{\hat{\mu}_s(x)} \quad (15)$$

And the solid holdup is equal to

$$\varepsilon_s(x) = 1 - \frac{\hat{\mu}_s(x) - \hat{\mu}_{s-g}(x)}{\hat{\mu}_s(x)} \quad (16)$$

Finally, to acquire the data needed to reconstruct the phase volume fraction for gas-solid spouted beds, the CT scans are excuted for 3 different conditions:

1. **Empty column** (column containing gas only) to measure I_o. Another option is **column at packed bed state** (column containing packed bed of solids only)
2. **Solids only** to measure I
3. **Gas and solids** (actual two phase flow operation at the desired conditions) to measure I.

3.3. RADIOACTIVE PARTICLE TRACKING (RPT)

Radioactive Particle Tracking (RPT) is a non-invasive technique used to track a single radioactive tracer particle that emits gamma ray radiation in order to monitor the recirculating phase dynamics whose velocity field shall be monitored. The RPT dates back to the year 1964 when its use was first employed by Kondukov and colleagues, where six scintillation detectors were used to track a radioactive tracer particle in fluidized beds. Further, in 1985, Lin et al were the developers of a unique computer-automated radioactive particle tracking (CARPT) facility. The compound noun and adjective “Computer-automated” refers to the automated calibration device found in this technique. The RPT has been successfully applied using a single radioactive tracer particle to measure the 3D

flow fields and turbulent parameters in different multiphase flow systems (Bhusarapu et al., 2004; Chen et al., 1999; Larachi et al., 2003; Rados et al., 2005; Rammohan et al., 2001a; Roy et al., 1994). The RPT is the promising technique for visualization of multiphase flow system and can truly allow to obtain the velocity fields profile and turbulent parameters for gas solids spouted beds (Al-Dahhan, 2009). The tracer particle flows along with the recirculating phase, and its gamma radiation is detected using an array of detectors placed strategically around the column that to be investigated. The system converts the gamma rays emitted by the tracer particle into voltage pulses. The position of the tracer is determined by the number of the pulses recorded from each detector with the help of mathematical algorithm programs developed for such purpose. The frequency or intensity of the gamma rays that arrives at each detector decreases as the distance between the detector and the tracer particle increases. The intensity recorded at each detector is converted to the related distance between the detector and the tracer using a distance-intensity relationship that is obtained through prior calibration experiment conducted before the actual RPT experiment. The calibration map is established by placing the tracer particle at different known positions of the spouted bed column using automated calibration device. The actual RPT experiment should be run for sufficient time while recording the appearance of the tracer particle to reach plateau time averaged at each location inside the spouted bed. As a result, the Lagrangian trace of the tracer particle is employed for deciphering the instantaneous positions of the tracked solid phase after which this information is used to acquire the instantaneous ensembled velocity time series. Hence, determining the instantaneous positions of the tracer particle yields an abundant information of the tagged solids flow fields like the 3D mean velocity fields, turbulence

kinetic energies, shear stresses, dispersion coefficients, along with other parameters that depict the flow regimes and characteristics of the tagged solid phase (Al-Dahhan, 2009).

In the RPT experiments, the gamma rays emitted by the tracer particle were collected using twenty-eight non-collimated (2 in x 2 inch) NaI (TI) detectors arranged strategically around the spouted bed column in a spider manner. The positions of these detectors were carefully adjusted to have efficient tracking by the detectors, and homogenous solid angle subtended by the crystal of each detector from any point in the spouted bed column. In addition, these detectors provide high efficiency, uniform response, and have a proven record of long-term reliability and stability according to Canberra Industries. Figure 3.9 and Table 3.1 provide the configuration and positions consisting of 28 detectors located at 14 axial levels with four detectors in each level, each two detectors facing one another (i.e. at 180-degree angle to each other). The accuracy of the results obtained increases with increase in the number of detectors. The detectors were mounted on movable horizontal aluminum structures that are in turn held by four vertical Unistrut bars sited at equal distance from the column and 90-degree interval around the column. Each Unistrut supporter had seven detectors placed at different axial levels. The detectors were positioned vertically with respect to the expected bed dynamic, as well as each detector was radially arranged at 12.7 cm with respect to the symmetrical axis of the column. The detectors are horizontally leveled using a leveling device and twin laser-equipped aluminum fake detectors facing one another. The detectors were aligned both in the axial and azimuthal directions using the laser-equipped aluminum fake detector.

The tracer particle for each RPT experiment was made in case it should has as closely as possible the same size, density, and shape of the tagged solid phase. The tracer

particle is embedded with Co-60 (d_p = 600 µm) with initial activity of about 500 µci (micro curie). The RPT experiment comprises two steps:

I. RPT calibration process.

II. RPT actual experiment process.

In order to estimate the position of the tracer particle, calibration was performed before to the actual RPT experiment by placing the tracer particle at various known locations, which yield a calibration map relating counts and particle positions for each detector. In the calibration process: A fully automatic calibration device was used to provide highly accurate RPT measurements. This device can automatically move a calibration rod with the tracer particle attached to its tip to visit hundred or thousand known locations inside the spouted bed column. Hence, the positions of the tracer particle during the actual run can be found by relating that counts in the actual run to the counts in the calibration process where the positions already were known.

The time of tracking was important for each bed in order to have sufficient number of occurrences of the tracer particle in each sampling compartment. The more tracking time conducted; the local properties more acquired and the close averaged velocity obtained to the tracer particle velocity. The local statistical characteristics were assessed with approximately two million data points obtained from exactly fourteen hours of particle tracking in 6-inch spouted beds, and one million data points obtained from six hours of particle tracking in 3-inch spouted beds. For both beds, the counting acquisition frequency was acquired at 50 Hz. The 3D instantaneous particle positions were reconstructed from the count rate of the tracer particle using cross correlation based position algorithm coupled

with a semi-empirical model used to provide further calibration points based on relating the count rate of the tracer particle to the positions of the particle.

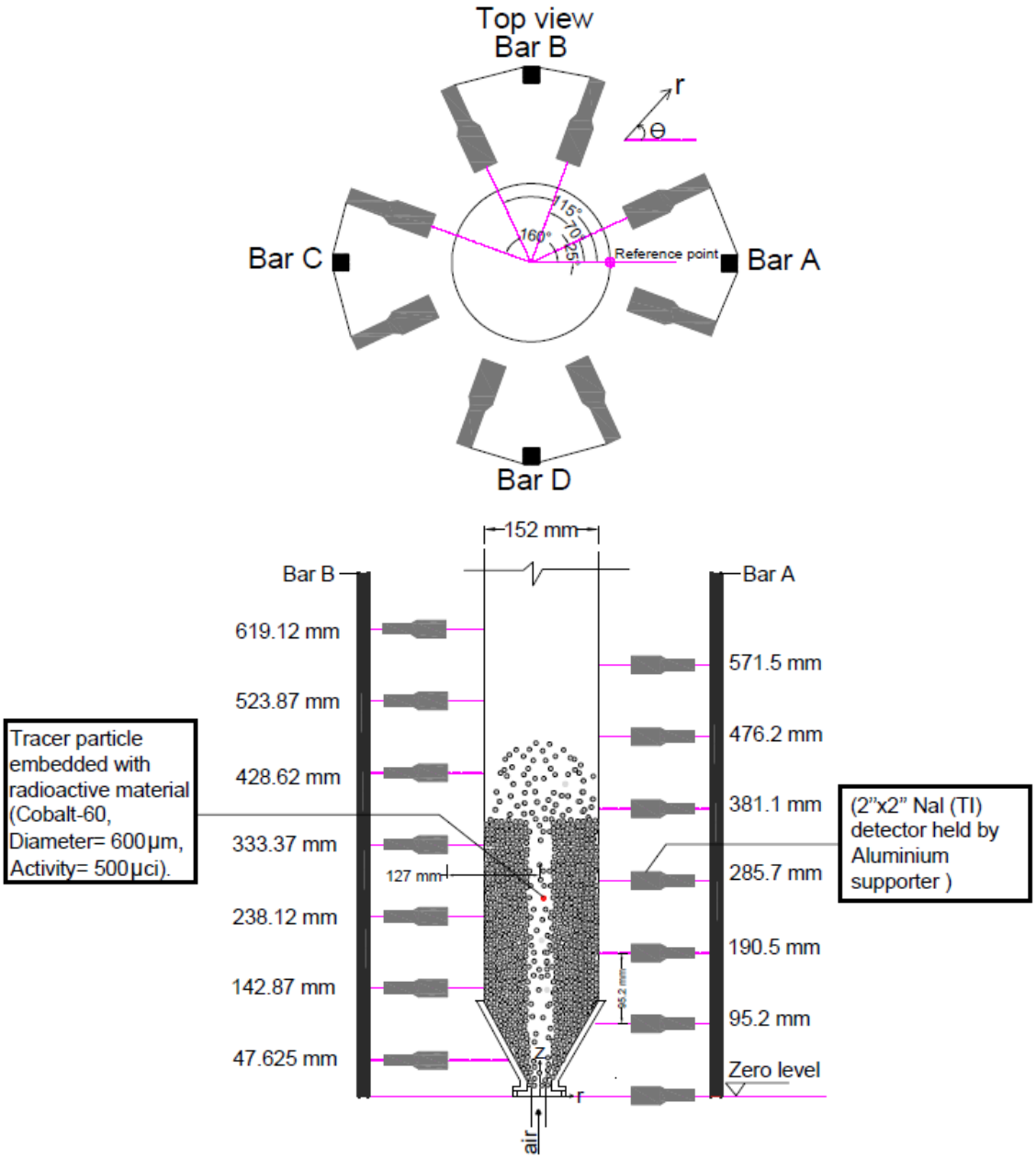

Figure 3.9. Schematic diagram showing the positions of 14-detecors arranged around the 0.152 m spouted bed.

Table 3.1. Polar coordinates of each detector with respect to the axis of the spouted bed column and the height from the gas distributor (Z).

Detector #	r, cm	θ, °	Z, cm	Detector #	r, cm	θ, °	Z, cm
1	12.7	115	4.76	**15**	12.7	295	4.76
2	12.7	70	14.28	**16**	12.7	250	14.28
3	12.7	115	23.81	**17**	12.7	295	23.81
4	12.7	70	33.33	**18**	12.7	250	33.33
5	12.7	115	42.86	**19**	12.7	295	42.86
6	12.7	70	52.38	**20**	12.7	250	52.38
7	12.7	115	61.91	**21**	12.7	295	61.91
8	12.7	25	0	**22**	12.7	205	0
9	12.7	340	9.52	**23**	12.7	160	9.52
10	12.7	25	19.05	**24**	12.7	205	19.05
11	12.7	340	28.57	**25**	12.7	160	28.57
12	12.7	25	38.1	**26**	12.7	205	38.1
13	12.7	340	47.62	**27**	12.7	160	47.62
14	12.7	25	57.15	**28**	12.7	205	57.15

3.3.1. Implementation of Cross-Correlation Based Position Reconstruction Algorithm for Spouted Beds RPT Experiments.

In radioactive processes, when a nucleus becomes energized and reaches an excited state, the nucleus will release its excess energy in order to return to its ground state by emitting particles or electromagnetic radiation. The common types of these radiations are classified as alpha, beta, and gamma

radiation. Both alpha and beta particles are not very penetrative and can easily be absorbed by materials. Gamma radiation, however, is very penetrative and can travel considerable distances through many substances. In gamma ray detection, dealing with distance is of much importance. Photons energies detected by a detector substantially depends on the distance between the source and that detector. For a point source, the relation between the counts measured by a detector and the location of that source in a space (x,y,z) requires the attention of different parameters. In RPT technique, this relation is applied. To understand this relation, consider a point source placed in a position (x,y,z) inside a cylindrical column Figure 3.10 (below).

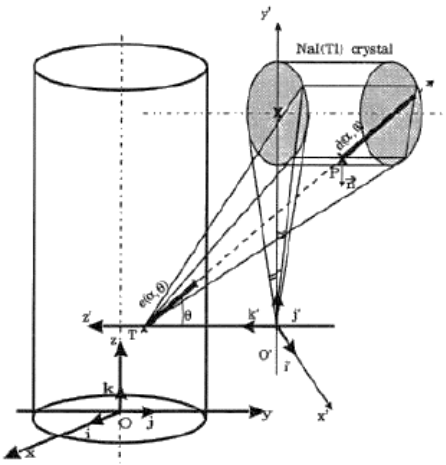

Figure 3.10. Geometrical construction of the path between the point source (tracer) and the NaI (TI) detector in a column under investigation (from (Larachi et al., 1997)).

Theoretically, the number of counts C that would be detected by a detector with energy source activity A, and in count time T with respect to the detection efficiency (ε) is given by (Tsoulfanidis, 2010), as follows:

$$\left\{ \begin{array}{c} C = \dfrac{T\upsilon A\phi\varepsilon}{1 + \tau\upsilon A\phi\varepsilon} \\ where \\ \varepsilon = \oiint_{\Omega} \dfrac{\underline{r}.\underline{n}}{r^3} \underbrace{\exp(-\mu_R e_R - \mu_w e_w)}_{f_a} \underbrace{(1 - \exp(-\mu_D d))d\Sigma}_{f_D} \end{array} \right\} \quad (17)$$

Where,

A - Strength of point radioactive source inside a dense medium.

υ - Number of γ-rays emitted per disintegration ($\upsilon = 2$ for Co-60).

ϕ - Photo-peak ratio.

τ - Detector dead time per recorded pulse.

ε - Total efficiency (i.e., the probability that un-scattered γ-rays emerging from the source will interact with the detector material).

Ω - Solid angle subtended by the detector surface area at the source position.

n - An external unit vector normally perpendicular to $d\Sigma$.

$d\Sigma$ - Infinitesimal surface area element of the detector.

r - Separation distance between the source and the point on the surface of the detector ($d\Sigma$).

f_a - Probability that gamma-rays travelling within solid angle Ω will not interact with the medium inside the reactor and the wall of reactor given by:

$$\exp(-\mu_R e_R - \mu_w e_w) \quad (18)$$

f_D - Probability that gamma-rays traveling distance d will interact in the crystal material is given by:

$$(1 - \exp(-\mu_D d))d\Sigma \quad (19)$$

μ_R, μ_w, μ_d - Total linear attenuation coefficients of the reactor inventory, reactor wall, and detector material, respectively. The linear attenuation coefficient μ is the product of mass attenuation coefficient (μ/ρ) times the absorber density of material (ρ).

e_R, e_w, d- Gamma-rays path length through the medium inside the reactor, reactor wall, and the thickness of crystal inside the detector, respectively.

Hence, equation (17) provides the mathematical description of the relation between the counts detected by the detector and the location of the point source. Further details about factors that contribute to equation (17) are given by (Larachi et al., 1997). Indeed, in RPT experiments, to overcome the problem of the location of the particle, approximate methods are required to reconstruct the positions of the particle from the counts recorded by the detectors. Four methods/algorithms have been used by different research groups for the RPT experiments to determine the instantaneous particle positions from the counts recorded by the detector:

- Data Reduction Scheme (Chen et al., 1999; Lin et al., 1985; Rammohan et al., 2001b).
- Monte-Carlo Based Search Method (Chen et al., 1994; Larachi et al., 1997)
- Neural Network Based Method (Godfroy et al., 1997)
- Cross-Correlation Based Search Method involving Semi-Empirical Model (used in this work) (Bhusarapu et al., 2004).

In this sub-section, the cross-correlation based position reconstruction algorithm is implemented to determine the instantaneous particle positions (x,y,z) for the RPT experiments. The usage of the present method will help to assess the definition of the instantaneous positions of the tracer particle, as well as the obtained parameters from the RPT experiments. This method was originally developed and used for processing the RPT data by (Bhusarapu et al., 2006) on gas-solid risers. The method was also used in our laboratory for a pebble bed reactor study (Khane et al., 2016a; Khane et al., 2016b). In this process, the 3D particle positions are reconstructed from the count rate of the tracer particle using cross correlation-based position algorithm. In addition, a semi-empirical model is used to provide further calibration points based on relating the count rate of the tracer particle to the positions of the particle. Figure 3.11 shows calibration points positions along the 6-inch spouted beds column obtained using the RPT calibration device. The working principle of the present method as detailed in (Bhusarapu et al., 2006) involves the next two steps below. The cross correlation based position method was originally developed and used for processing the RPT data by (Bhusarapu, 2005) on gas-solid risers. The method was also used in our laboratory for a pebble bed reactor study (Khane, 2014). For further details about the technique and algorithms used to reconstruct the particle positions, the reader can refer to recent works of our group (Khane, 2014; Mesfer, 2013).

3.3.1.1 Step I - finding cross-correlation coefficient. In this step, the cross correlation function of the two series count rate obtained from the calibration process and the actual run is used to calculate the cross-correlation coefficient (R) of the two series. The aim of this step is to find the initial best-estimated position of the particle by determining the correlation between the count rate from the calibration and the actual run.

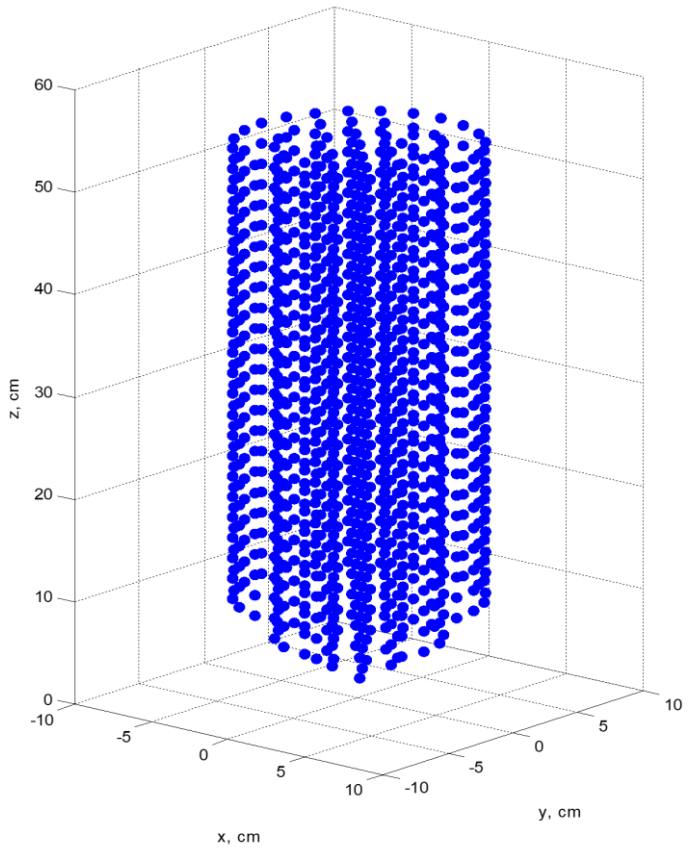

(a)

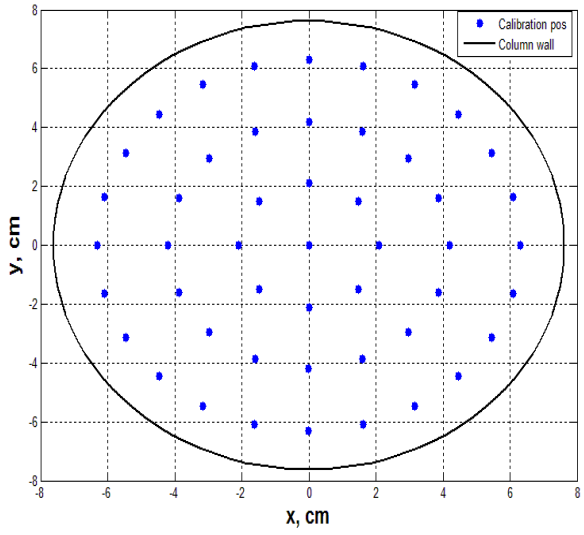

(b)

Figure 3.11. Calibration points positions along the 6-inch spouted beds column; (b) top view of (a) showing 3 rings of calibration points in r-direction (0 cm, 2.1 cm, 4.2 and 6.3 cm) with different azimuthal positions.

Note that in the calibration process, the counts were taken at known positions. Unlike in the calibration process, in the actual run the positions of the particle were unknown, and only the counts were taken. The cross-correlation coefficient (*R*) refers to the correlation of the two series and the normalized correlation of the two series can be defined as:

$$R_{run,calib_k}(0) = \sum_{i}^{N_d} \frac{C_{calib}(i)}{\sqrt{\sum_{j}^{N_d} C_{calib}^2(j)}} \cdot \frac{C_{run}(i)}{\sqrt{\sum_{j}^{N_d} C_{run}^2(j)}} \tag{20}$$

Where,

C_{calib} - count rate recorded during the calibration process at known position.

C_{run} - count rate recorded during the tracking process at unknown position.

N_d - total number of detectors used to track the tracer particle.

Hence, the positions of the tracer particle during the actual run can be found by relating that counts in the actual run to the counts in the calibration process where the positions already were known. Indeed, this is the basic idea that is implemented by the RPT technique to track the tracer particle. The maximum value of the cross-correlation coefficient (*R*) is one. If the value of R equals one, this indicates that the two series counts for the 28 detectors are matched. If the value of *R* is close to one, this indicates the best estimation of the tracer particle position. In practice, when this normalization is applied, a good match is achieved when the value of *R* is greater than 0.995. Figure 3.12 shows an example of calculated initial best estimation of tracer particle specific position point along with R-values. Once the values of *R* are calculated for all raw data sets in the actual run

and the calibration process, the initial best estimate positions of the tracer particle can be defined and the next step will be to search around these positions.

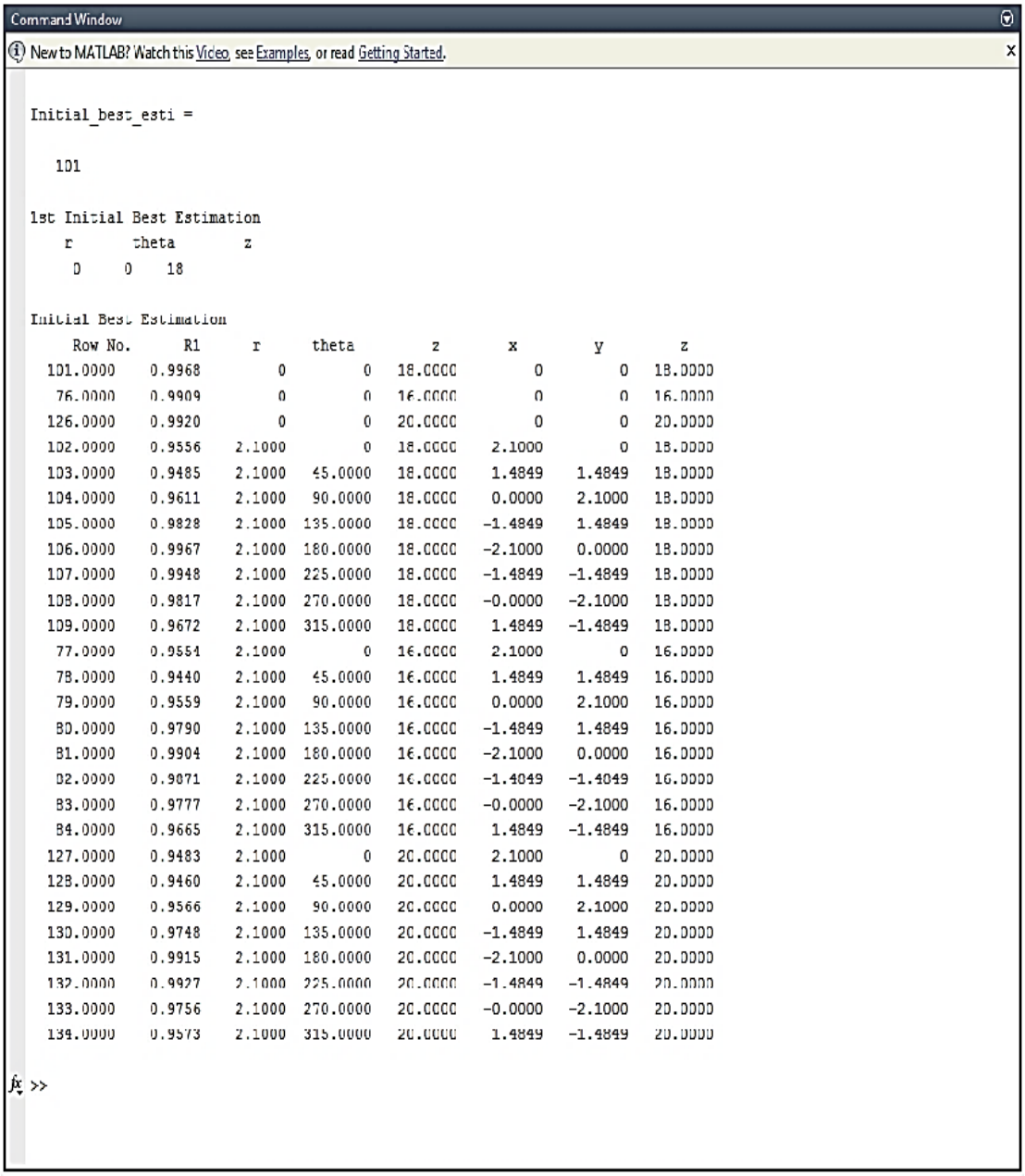

Figure 3.12. Screenshot of the command window showing the initial best estimation positions with R-values and the Row No. of these positions in the calibration.

3.3.1.2 Using semi-empirical model to provides additional calibration datasets at refined mesh level.

In this step, the best initial estimation position of the tracer particle will be used to provide the nearest neighboring positions around that position. The initial best estimate position will be at the center, and the neighboring positions are around it in all the three directions (x,y,z). Once the adjacent positions are calculated, the next step is to use the semi-empirical model to calculate the counts recorded for these positions with respect to each detector. The aim of this model is to refine the mesh level and provide a new calibration dataset. The calibration process of the RPT is both time-consuming and labor intensive. Establishing new calibration dataset can overcome the limited numbers of the calibration points especially when it comes to dense flow (see Figure 3.13). The semi-empirical mathematical model is given by:

$$C = \underbrace{\frac{k_1}{d^2}}_{f_1} \cdot \underbrace{\exp\left(-k_2 d_x - k_3 d_y - k_4 d_z\right)}_{f_2} \cdot \underbrace{\left(1 - \exp\left(-\mu_d k_5\right)\right)}_{f_3} \tag{21}$$

In equation (26), *C* is the counts recorded by the detector, *dx, dy, and dz* are the x, y, and z components of the tracer particle position from the center of the crystal detector, *d* is the distance between the tracer position and the center of the detector crystal, μ_d is the mass attenuation coefficient of the detector crystal, and $K_{1,\,2,3,4,5}$ are model constants. Solid angle subtended by the detector in the detection system is represented in the model by the term $f_1 = \frac{k_1}{d^2}$ .The inverse-square law (applicable only for point source) shows that the counts recorded by the detector are directly proportional to the solid angle subtended by

the detector from that position and inversely to the square of the distance between the source and the detector. The attenuation medium traveled by the γ-rays in x, y, and z directions from the source to the detector is represented by the exponential term $f_2 = \exp\left(-k_2 d_x - k_3 d_y - k_4 d_z\right)$, where $k_{2,3,4}$ are effective mass attenuation coefficients in the three directions. The term $f_3 = \left(1 - \exp\left(-\mu_d k_5\right)\right)$ is corresponding to the probability that the γ-rays emitted from the system will interact with the scintillator crystal of the detector, where k_5 is corresponding to the path length of the photon through thickness of the crystal material. Hence, the advantage of this model is that it will record the count rate by each detector within the spouted beds geometry. This can be accomplished by including the attenuation medium traveled by the γ-rays and the probability of interaction between these γ-rays and the detectors, and not just the distance between the tracer position and the center of crystal detector.

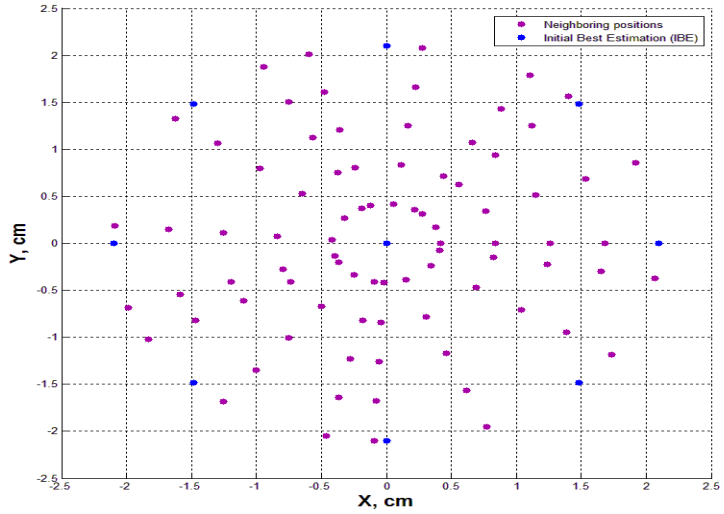

Figure 3.13. Top view of the Initial Best Estimation (IBE) (Step I) and nearest neighbors positions (Step II).

3.3.2. Data Treatment. The measurements of the RPT allow the determination of the three coordinates (r, θ, z) of the instantaneous tracer particle positions (i.e. the Lagrangian trajectory of the tracer particle) at selected sampling rate. Figure 3.14 shows 40-s representative example of the time-series of the z-coordinate of the tracer particle positions in the industrial-scale spouted bed at the condition of reference case. As can be seen in Figure 3.14, fast upwards movements of the tracer are detected periodically (every 5-7 s) in the spout as the gas in this region carries the particles up. The tracer often accelerates up near the axis of the spout, and starts its journey from the comical part of the bed to end it in the fountain region. In the fountain, the tracer disengages from the gas phase to fall down over the annulus region where particle vertical movement changes from upwards to downwards. Hence, the time of transition of the tracer particle between the adjacent regions of the spouted bed (spout, annulus, and fountain) in the course of each and every cycle of an experimentation, are recognized in each qth cycle as the following (To illustrate on how these times of transitions between regions are determined, see Figure 3.14):

- Time of tracer particle transition out from the annulus into the spout in the qth cycle ($T_{an-sp,q}$): the moment at which the axial position of the tracer particle is minimal in one-cycle (i.e. the z-coordinate of the tracer approaches its lowest value in one particular cycle);
- Time of tracer particle transition out from the spout into the fountain during qth cycle ($T_{sp-fo,q}$): the moment, after ($T_{an-sp,q}$), at which the axial position of the tracer is the same as the mean height of the bed surface in one particular cycle

(i.e. the z-coordinate value of the tracer particle approaches the value of the mean bed height/annulus surface ($z = H$));

- Time of tracer particle transition out from the fountain into the annulus during the qth cycle ($T_{fo-an,q}$): the moment, after ($T_{sp-fo,q}$), at which the tracer particle penetrates the bed surface at $z = H$ during one particular cycle.

Accordingly, tracer particle positions, transitions and times of transitions between adjacent regions (the spout, the annulus, and the fountain), were analyzed to calculate the following key parameters of solids flow in the spouted beds:

- Cumulative probability distribution of the solids particles penetration into the spout ($\boldsymbol{P}$): this distribution illustrates, for each $z - coordinate$ along the spout height, the probability of the solids particles being entrained into spout from the annulus at a height below or equal to the corresponding $z - coordinate$.
- Cumulative probability of the landing position of the solid particles at the annulus surface: this distribution illustrates, for each $r - coordinate$ at the bed surface, the probability of the solids particles being entrained into the annulus from the fountain at a radial position, from the boundary of the spout region, equal or less than the corresponding $r - coordinate$.
- Cumulative probability of the penetration of the solid particles into the base of the fountain region: this distribution illustrates, for each $r - coordinate$ at the spout region ends (i.e. z = H), the probability of the solids particles being entrained into fountain from the spout at a radial position, from the spout axis, equal or less than the corresponding $r - coordinate$.

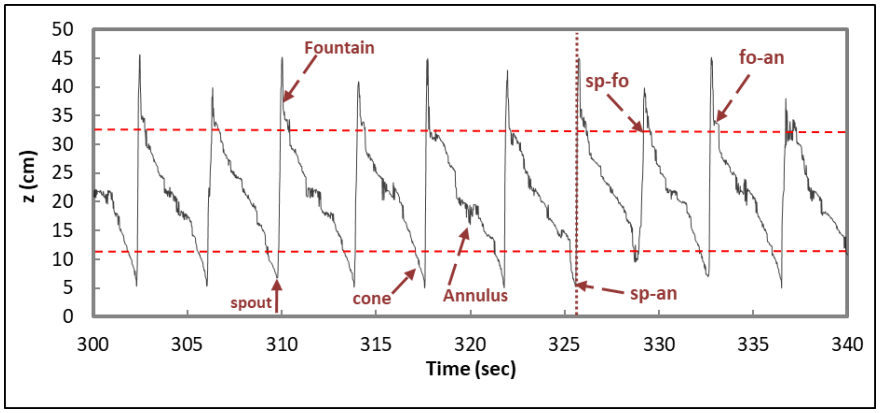

Figure 3.14. Representative example of time series of the z-coordinate of the tracer particle during a typical experiment in the industrial-scale spouted beds.

To calculate the penetration of the solids from the annulus into the spout, only the 2-D z-r domain is considered. In another word, single population were extracted from combining the data of both sides of the axis of symmetry of the bed. Assigning compartment (i, j) of the defined domain whose side is Δ and centered at $z = \Delta(i - \frac{1}{2})$ and $r = \Delta(j - \frac{1}{2})$. Then, let a vector $\boldsymbol{V}$ whose entries V_j is defined as:

$$V_j = \Delta\left(j - \frac{1}{2}\right), \quad \forall j, 1 \le j \le n \tag{22}$$

Hence, V_j in equation (22) represents the r-coordinate of the middle position of the compartment (i, j) within the domain $(\forall i,\ 1 \le i \le m)$. A square matrix (m, n) $\boldsymbol{M}$ is then introduced and starting with initial value $M_{i,j} = 0$, and incremented by one for each time tracer particle transit out from the annulus into the spout region $T_{an-sp,k}$ $(1 \le k \le N_t,$ where N_t is the total number of cycles over a given experiment). This increment

is only performed when the tracer particle is in the compartment (i, j) of the z-r domain at the time of the transition (i.e. the z and r coordinates of the tracer particle position are within the intervals [$i\Delta$, $i\Delta$] and [$j\Delta$, $j\Delta$], respectively). Therefore, $M_{i,j}$ stands for the number of transitions that tracer undertaken from the annulus to the spout over a given experiment and at a location contained in the compartment (i, j) within the z-r domain.

Let a column vector $\boldsymbol{R}$ whose entries m is defined as follows:

$$R_i = \frac{1}{\sum_{j=1}^{n} M_{i,j}} \sum_{j=1}^{n} M_{i,j}\, V_j \tag{23}$$

Hence, the $\boldsymbol{R_i}$ in equation (23) gives us the mean r-coordinate of the tracer position whenever the tracer penetrates the spout at a z-coordinate within the length [$i\Delta$, $i\Delta$]. In another word, $\boldsymbol{R_i}$ characterizes the spout shape of the bed along the spout height. The vertical cumulative probability distribution of the penetration of solid particles into the spout was calculated as follows:

$$P_i = \frac{1}{N_t} \sum_{l=1}^{i} \sum_{j=1}^{n} M_{i,j} \tag{24}$$

Hence, $\boldsymbol{P_i}$ gives us the cumulative probability of the solids particles being entrained from the annulus into the spout region. A similar methodology was carried out to determine the cumulative probability of the landing position of the solid particles at the annulus surface and the penetration of the solid particles into the base of the fountain region.

In order to obtain the time-averaged velocity and turbulent parameters, it is required to identify the initial coordinates of the particles in the spouted beds column. To accomplish that, cylindrical mesh compartments were defined to represent the entire column of spouted beds. Two important points were considered when determining the sampling compartments: the sufficient occurrences of the particle per compartment and a good radial profile description for each bed height level. The sampling compartments were evaluated, and the column was divided into 1127 and 735 compartments respectively for 6-inch and 3-inch spouted beds, while maintaining eight radial points for profile description. The cylindrical sampling compartments used and the assignment of these compartments for the RPT data processing are shown in Figure 3.15 (below) and Table 3.2 (below) respectively.

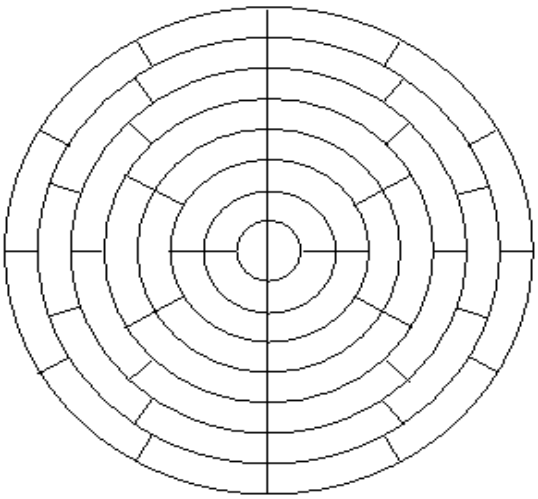

Figure 3.15. Sampling Compartments Describing the Spouted beds column.

Table 3.2. Assignment of Compartment for RPT Data Processing.

N_r^*	Δr, cm	N_z^*	Δz, cm	N_θ^*
8	0.952	23	2	2,4,4,6,6,8,10,12

Once the instantaneous positions of the tracer particle and its Lagrangian trajectory were defined, the next step was to calculate the instantaneous particle velocity (r, θ, and z) and the turbulence parameters in each compartment. Simple algebra in equation (25) (below) is sufficient to understand how this can be calculated, the distance traveled by the particle between two successive positions divided by the time interval needed to travel that distance, will yield its velocity.

$$\begin{pmatrix} u_r \\ u_\theta \\ u_z \end{pmatrix} = \frac{1}{T}\begin{pmatrix} r_{k+1} - r_k \\ r_m(\theta_{k+1} - \theta_k) \\ z_{k+1} - z_k \end{pmatrix} where \begin{cases} T = t_{k+1} + t_{k+1} \\ r_m = (r_{k+1} + r_k)/2 \end{cases} \quad (25)$$

Undoubtedly, the instantaneous particle velocities will not be constant in each compartment. To overcome this, taking the average of the instantaneous particle velocities for each compartment is required. Then, based on the ensembled particle total number of occurrences per compartment (N_v), the time-averaged (mean) velocity fields in each compartment (i, j, k) were calculated as follows:

$$\bar{u}_{p(i,j,k)} = \frac{1}{N_v}\sum_{k=1}^{N_v} u_{p(i,j,k),k} \quad p = r, \theta, z \quad (26)$$

For data presentation, the circular azimuthal averaging was performed for each (r,z) level to calculate the azimuthally-averaged velocity ($\bar{u}_{p(i,j,k)}$) for the axial and radial components, where N_θ is the number of compartments in the azimuthal direction. As a result, eight positions of the profile description were obtained along the radial direction for each (z) level:

$$\bar{u}_{(i,k)} = \frac{1}{N_\theta \widetilde{N}_{v(i,k)}} \sum_{j=1}^{N_\theta} \bar{u}_{(i,j,k)}\, N_{v(i,j,k)} \tag{27}$$

$$\widetilde{N}_{v(i,k)} = \frac{1}{N_\theta} \sum_{j=1}^{N_\theta} N_{(i,j,k)} \tag{28}$$

In the above equations, $\widetilde{N}_{v(i,k)}$ is the average number of velocity occurrences for a given two-dimensional compartment (i, k). Hence, from the instantaneous velocities and ensemble average velocities in each compartment, the fluctuation velocities were conventionally calculated by subtracting the mean velocity from the instantaneous velocities ensembled as follows:

$$\acute{u}_{p(i,j,k)} = u_{p(i,j,k)} - \bar{u}_{p(i,j,k)} \tag{29}$$

Once the fluctuation velocities were obtained, the root mean square velocities, turbulent stresses, and turbulent kinetic energy per unit mass were calculated as follows:

$$u_{p-RMS(i,j,k)} = \sqrt{\overline{(\acute{u}_{p(\imath,J,k)})^2}} \qquad p = r, \theta, z \tag{30}$$

$$\tau_{pq} = \overline{\acute{u}_{p(\imath,J,k)} \acute{u}_{p(\imath,J,k)}} \qquad p, q = r, \theta, z \tag{31}$$

$$TKE = \frac{1}{2}(\tau_{rr} + \tau_{\theta\theta} + \tau_{zz}) \tag{32}$$

3.4. EXPERIMENTAL CONDITIONS OF OBJECTIVE I

This subsection is devoted for the experimental conditions employed in Objective I to investigate the effects of gas velocity, bed size (3 and 6 inch diameter), particle size, and density on the radial or diameter profile and cross-sectional distributions of gas and solids holdups in gas-solid spouted beds using gamma-ray computed tomography (CT).

The actual experimental works in this part are similar to that used by Ali et al. (Ali et al., 2016a, 2017a), and consist of two different size of fully cylindrical-conical base spouted beds with inner diameter of 0.076 m and 0.152 m. The deployed spouted beds were fabricated from Plexiglas material and each unit consisted of one-piece column attached to a conical base. The schematic diagrams of the two spouted beds employed are shown in Figure 3.16. Both columns were specified and designed to be geometrically similar with 1.14 m height and conical base of 60-degree angle. The two columns were constructed without having any ports or connections on the wall surface to avoid the possibility of any non-symmetric issues for the columns, which in turn mess and complicate the CT reconstructions procedure. At the bottom of the conical base, a gas distributor made of stainless steel was placed to pass through the gas flow inside the column. The diameters of the inlet orifice are 9.5 mm and 19.1 mm for the 0.072 m and 0.152 m spouted beds respectively. The gas used was dry compressed air supplied from an industrial compressor with capacity up to 735 CFM and 200 Psig. The air was filtered before being passed through into the column at ambient temperature (T= 20°C). After the flow pass through the piping components of the compressor, the rate of the flow is regulated, using a pressure regulator and rotameter setup made by parallel connecting of two rotameters. The gas flow rates were maintained at the desired operating condition with the aid of the rotameters and a set of gauge valves and were introduced into the spouted beds through the inlet orifice

(gas distributor). All the experiments were carried out at the ambient temperature and the atmospheric pressure. The design of the operating conditions for spouting stability was described in detail in previous paper (Ali et al., 2016a), and was based on the findings of (Chandnani and Epestein, 1986; He et al., 1992; Lim and Grace, 1987; Mathur and Epstein, 1974c).

$$U_{ms} = \left(\frac{d_p}{D_c}\right)\left(\frac{D_i}{D_c}\right)^{\frac{1}{3}}\sqrt{\frac{2gH_o(\rho_p - \rho_g)}{\rho_g}} \tag{33}$$

Table 3.3. Properties of the materials used.

Material	d_p (mm)	ρ_p (g/cm^3)	ϕ_p	ε_o
Glass beads	1	2.4	1	0.413
	2	2.5	1	0.411
Steel particles	1	7.4	0.98	0.412
	2	7.4	0.98	0.411

Four different particulate materials, nearly spherical in shape with narrow size distribution, were employed in the experiments: steel particles of mean diameter 1 mm and 2 mm and glass beads of mean diameter 1 mm and 2 mm. The advantage of using steel particles is their high density allows the determination of the hydrodynamics of spouted beds of heavy particles and the way they differ from relatively spouted beds of light

particles. The glass particles were chosen to enable the comparison of the results of this study with those reported in the literature where glass beds are largely used for fluidization studies. Another reason why we selected the steel and glass particles is the density ratio between the two materials (ρ_{steel} /ρ_{glass} ~ 2.96). This ratio made the two materials excellent choices, since in the actual spouted bed nuclear fuel coaters a close ratio is obtained after the coating of the first layer ($\rho_{kernel\text{-}Uo2}$ /$\rho_{coated\text{-}kernel}$ ~ 2.63). Therefore, the results of the two materials will be valuable for designing and understanding, and can be linked to the spouted bed nuclear fuel coaters. The relevant properties of the particulate materials are listed in Table 3.3.

The stagnant bed heights range from 0.14 m to 0.32 m. The superficial gas velocities vary from $1.1U_{ms}$ to $1.4U_{ms}$, where U_{ms} is the minimum superficial gas velocity required to obtain the onset external spouting state in spouted beds. Below this velocity, solids circulation is absent, and, consequently, all the three regions in spouted beds are not fully created. The minimum spouting velocity can be obtained experimentally or theoretically, and it is a function of the physical properties of the particles used (density, size, shape), bed geometry (column diameter, inlet diameter, cone angle), static bed height, and gas properties (density, viscosity). The minimum spouting velocities were measured experimentally and compared with the well-known correlation available in the literature by Mathur and Gishler for deep spouted beds ($H_o/D_c > 1$) (Eq.(1)) (Mathur and Gishler, 1955). The measured values are found close to the estimayed ones by the correlation with average percentage increase of 7.31%.

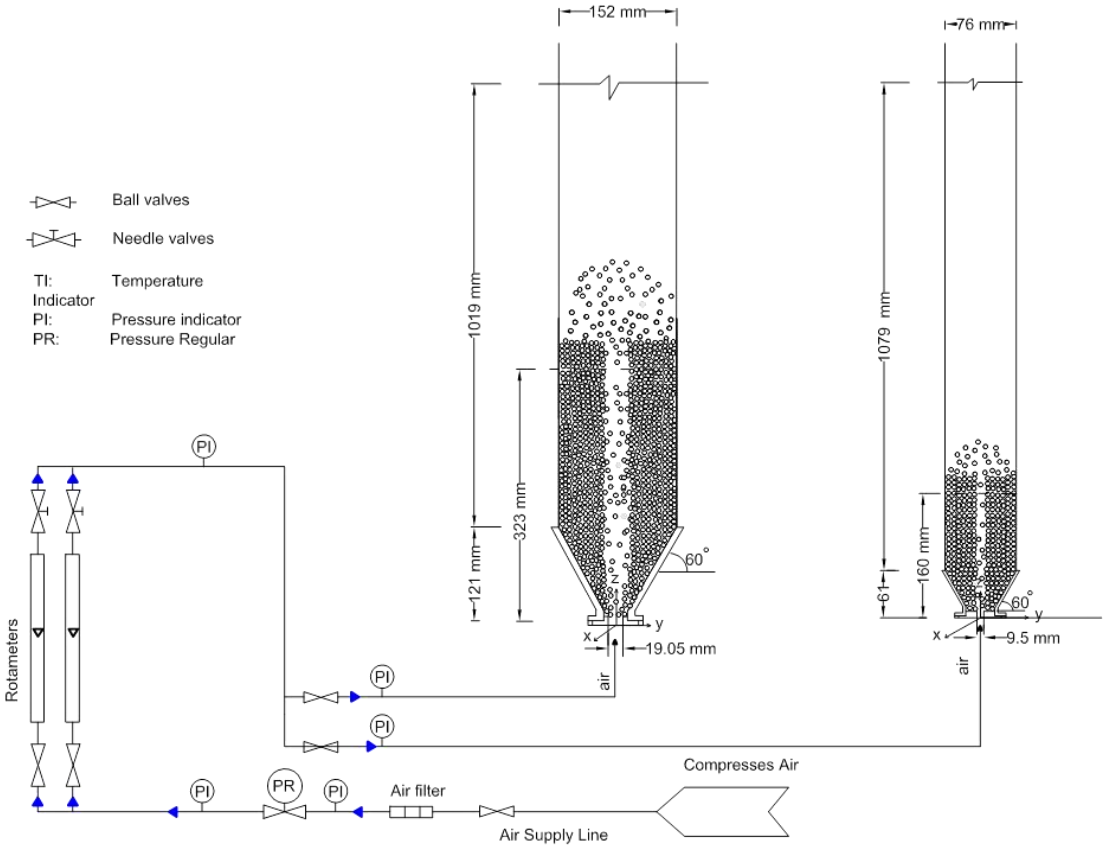

Figure 3.16. Schematic diagram of the 0.076 m and 0.152 m spouted beds.

3.5. EXPERIMENTAL CONDITIONS OF OBJECTIVE II

This subsection is devoted for the experimental conditions employed in Objective II to investigate the hydrodynamics and mixing behavior of binary particles of the same size and different densities in 6-inch spouted beds using RPT by studying the solid velocity fields, and turbulence parameters (Reynolds stresses, turbulent kinetic energy, and turbulent eddy diffusivities).

In this part of the study, all the experiments were carried out in 0.152 m inner-dimeter (6-inch) spouted bed. This spouted bed setup is the same used in our previous studies (Ali et al., 2016a, 2017a) and has similar configures to those reported in the literature for example (Djeridane et al., 1998; He et al., 1994b). The conical base is angled by 60-degree while the height of the column is 1.14 m. The cylindrical column attached to the conical base was one-piece fabricated and was made without any ports or connections at the wall to avoid any non-symmetric issue could raise at the reconstruction process of the RPT. Having one-piece column helps the stabilization of the bed at operation. At the bottom of the conical base, a gas distributor of stainless steel having diameter of 19.1 mm was placed to pass through the gas flow inside the column and to prevent the particles to fall. The ratio of the inlet orifice diameter to the particle diameter (D_i/d_s) is 9.55. This ration value meets the criterion reported by (Chandnani and Epestein, 1986) to sustain stable spouting in the bed, where the D_i/d_s should be smaller than (<) 25 ~ 30. The gas used in the experiments is dry compressed air supplied from a large air compressor that features a capacity up to 735 CFM and 200 Psig. The gas flow rate was regulated with the help of pressure regulator and two rotameters connected in parallel. All the experiments were carried out at ambient temperature and atmospheric pressure. A binary mixture consists of glass beads and steel particles of densities 2500 and 7400 kg/m^3, respectively are used in the experiments. The glass and steel particles were intentionally selected to obtain density ratio (ρ_{steel} /ρ_{glass} ~ 2.96) between the two materials close to that acquired in the actual spouted bed nuclear fuel coaters after the coating of the first layer ($\rho_{kernel\text{-}Uo2}$ /$\rho_{coated\text{-}kernel}$ ~ 2.63). Therefore, the results of the binary mixtures will be valuable for designing and understanding of the spouted bed nuclear fuel coaters. The binary particles are of the same

shape and size with mean diameter of 2 mm. The mixtures of the particles are in the ratio (vol. %) of 100:0 (pure component of glass beads), 50:50, and 0:100 (pure component of steel particles). The total weight of each one of the mixtures is held constant at 6.39 kg while the intimal bed height was varying from 0.18 m to 0.32 m. The variation in the initial bed weight was strategically selected to maintain constant weight of bed particles between the mixtures and hence obtaining equal or close minimum superficial spouting velocity between the mixtures of particles. Accordingly, acquiring equal or close minimum superficial spouting velocity for all the mixtures will assist the basis comparison and evaluation between the investigated conditions. The superficial spouting gas velocities range from 1.1 U_{ms} to 1.3 U_{ms}, where U_{ms} stands for the minimum superficial spouting velocity of the binary mixture of spouted beds necessary to establish stable external spouting (Mathur and Epstein, 1974c). For all the compositions of the mixture, the RPT experiments were carried out one at time for both glass and steel particles.

In this part, two tracer particles were manufactured for the RPT experiments, one to track the glass particles (density = 2500 kg/m^3) and the other for steel particles (density = 7400 kg/m^3). For the glass tracer particle, a radioactive Cobalt (Co-60) (d_s = 600 µm) of initial activity of about 500 µci (microcurie) was encapsulated in an Aluminum particle to attain the same density (shape and size) of the glass particles. For the steel tracer particle, radioactive Cobalt (Co-60) was encapsulated in a steel particle to attain the same density (shape and size) of the steel particles. All the RPT experiments are carried out, that is, at any experiment, just one single material is (either glass or steel) tracked. Further, each tracking experiment is carried out for sufficient time implying that the assumption of ergodicity can be satisfied. Local statistical characteristics were assessed with

approximately one and a half million instantaneous positions obtained on about six hours of particle tracking in the 0.152 m inner-dimeter spouted bed. The effect of tracking time was evaluated by operating the RPT for 14 hours and then compare the data obtained with those from six hours of particle tracking at identical spouted bed operating condition. The data from the independent experiments was found identical, and hence, the six hours of tracking time was considered sufficient for all the conditions reported in this study including those with relatively high initial bed height.

The positions of the detectors used to track the tracer were carefully adjusted to have efficient tracking by the detectors, and homogenous solid angle subtended by the crystal of these detectors from any point in the spouted bed column. The configuration and positions consisting of 28 detectors located at 14 axial levels with four detectors in each level, each two facing one another (i.e. at 180-degree angle to each other), as shown in Figure 3.9.

These detectors were mounted on movable horizontal aluminum structures that are in turn held by four vertical Unistrut bars sited at equal distance from the column and 90-degree interval around the column. Each one of the vertical bars hold seven detectors placed at selected different vertical levels. The detectors were positioned vertically with respect to bed dynamic from inlet to fountain. Also, each detector was radially arranged at 12.7 cm from with respect to the symmetrical axis of the column. The acquisition was carried out at time intervals of 20 ms and 50 Hz acquisition rate. The accuracy and precision associated with the measurement of the tracer positions through the same RPT technique and setup have previously been evaluated to be within 2 mm (Ali et al., 2017a). Since the uncertainty in the accuracy and precision of the RPT measurements (the mean error and

standard deviation are less than 2 mm) is small in comparison with the spatial results presented in this study, the error bars will not be shown on the for the spatial results. The good precision and accuracy of the current RPT technique is mainly due to the fact that the number of detectors used to track the tracer particle in this study is essentially sufficient to minimize error measurement and more than those used in similar RPT technique found in the literature for spouted beds studies (Cassanello et al., 1999; Djeridane et al., 1998; Larachi et al., 2003; Roy et al., 1994; Spreutels et al., 2016a; Spreutels et al., 2016b). To ensure the reproducibility of the results obtained using the RPT technique and for accurate comparability between the investigated conditions, a repeated set of RPT detection experiments was carried out at the identical operation conditions for each investigated condition. The results obtained from the RPT technique and the reproducibility were found reproducible and not significantly influenced by the measurement errors, respectively. The RPT experiments were carried out in first stage for the pure phases while in the second stage involve studying the hydrodynamics of binary mixture of solids of similar size and different density, and the effect of superficial gas velocity was investigated. The experimental matrix performed is demonstrated in Table 3.4.

Table 3.4. Experimental matrix.

Compositions by volume	d_s (mm)	ρ_s (kg/m^3)	H_o (mm)	U_{ms} (m/s)	U_{ms} (m/s), correlation prediction of (Mathur and Gishler, 1955)	U/U_{ms}		
100% glass	2	2500	320	0.89	0.85	1.1	1.2	
100% steel	2	7400	160	0.91	0.94	1.1	1.2	
50% glass, 50% steel			200	0.88	Does not apply	1.1	1.2	1.3

3.6. EXPERIMENTAL CONDITIONS OF OBJECTIVE III

This subsection is devoted for the experimental conditions employed in Objective III to assess the new scale-up methodology of spouted beds using RPT based on the solids turbulent diffusivity and the 3-D trajectory time series analysis. Dynamical tests will be applied to the RPT data using statistical tools to determine residence time distribution (RTD), circulation time distribution, return length, and distribution/average cycle time of the solid in the spout, the annulus, and the fountain regions.

In this part of study, three set of conditions were systematically designed to examine the validation of the new scale-up methodology of gas-solids spouted beds based on matching gas holdup profiles using the RPT technique. These conditions are summarized in Table 3.5. The first set of conditions were designed for the pilot plant-scale spouted beds and stand here as the reference case. The second set of conditions were designed for the lab-scale spouted beds to provide similar gas holdup profile to that obtained in the reference case. The third set of conditions were designed to provide dissimilar gas holdup profiles to that obtained in the reference case. The conditions of the reference case (Table 3.5) are similar to the conditions of the reference case used by (He et al., 1997). To identify the conditions and the size of the spouted bed that provide similar gas holdup radial profiles of the reference case, (Aradhya et al., 2016) measured the radial profiles of the gas holdup in the bed of the reference case using optical fiber probe. (Aradhya et al., 2016) then used validated computational fluid dynamics (CFD) (Lan et al., 2012) to identify the conditions which provide similar radial profiles of gas holdup to that of the reference case.

Table 3.5. Experimental conditions for similar and dissimilar gas holdup radial profiles for the hydrodynamics similarity of spouted beds identified by (Aradhya et al., 2016).

Condition/Case	**Reference**	**Similar gas-holdup profile**	**Dissimilar gas-holdup profile**
Bed scale	**Pilot plant**	**Lab**	**Lab**
D_c (m)	0.152	0.076	0.076
D_i (mm)	19.1	9.5	9.5
L (m)	1.14	1.14	1.14
H (m)	0.323	0.16	0.16
T (K)	298	298	298
P (kPa)	101	364	101
Particles	Glass	Steel	Glass
d_p (mm)	2.18	1.09	1.09
ρ_s (kg/m^3)	2400	7400	2450
ρ_f (kg/m^3)	1.21	3.71	1.21
μ (x 10^5) (Pa.s)	1.81	1.81	1.81
U (m/s)	1.08	0.64	0.74
U_{ms} (m/s) Experimental Values	0.89 m/s	0.58 m/s	0.68
U_{ms} (m/s) Correlation prediction of (Mathur and Gishler, 1955)	0.85 m/s	0.59 m/s	0.68

The third set of conditions were designed to provide dissimilar gas holdup profiles to that obtained in the reference case. In addition, the third set of conditions (i.e. conditions of dissimilar gas holdup profile) were designed to examine hydrodynamics similarity when simply scaling by matching the solids material and dimensions of beds of different sizes.

All the conditions were performed at room temperature. However, to achieve similar radial profiles of gas holdup, the spouted bed of the similar gas holdup conditions has to be operated at high pressure of 364 kpa using 1.09 mm diameter steel particles.

While the other spouted beds of reference case and the cae of dissimilar used atmospheric pressure and glass beads of 2.18 mm diameter and 1.09 mm diameter, respectively. The spouted bed of the diameter of the reference case was 0.152 m while the diameter of the beds of the other cases was 0.076 m. (Aradhya et al., 2016) used optical fiber probe at three levels (z/D_c =1.1, 1.8, 2.5) but one angular location of the probe for each level to measure the solids and gas holdups radial profile and to confirm the similarity and dissimilarity of these profiles for the conditions listed in Table 3.5. (Ali et al., 2018) confirmed these conditions for matching radial profiles of gas holdup using gamma-ray computed tomography (CT) and furthermore validated the newly developed mechanistic scale up methodology by comparing the cross-sectional distribution and radial profiles of solids and gas holdups at various levels along the bed height of the studied spouted beds. Accordingly, the three sets of conditions of Table 3.5 have been used in this study.

4. RESULTS AND DISCUSSIONS

This section presents the results obtained using the CT and RPT techniques and their analysis for the topic of each part of this study. It covers the results and discussion of (i) Investigation of cross-sectional gas-solid distributions in spouted beds using advanced non-invasive gamma-ray computed tomography (CT), (ii) Investigation of hydrodynamics of binary solids mixture spouted beds using radioactive particle tracking (RPT) technique, (iii) Scale-up and hydrodynamics of spouted beds TRISO nuclear fuel particles coaters using advanced radioactive particle tracking (RPT) technique.

4.1. INVESTIGATION OF CROSS-SECTIONAL GAS-SOLID DISTRIBUTIONS IN SPOUTED BEDS USING ADVANCED NON-INVASIVE GAMMA-RAY COMPUTED TOMOGRAPHY (CT)

For this part of the study, we aim to provide an experimental investigation of the hydrodynamics of gas-solid spouted beds at cold conditions using advance non-invasive technique; gamma-ray computed tomography (CT). The gas-solid distribution and its variations have a strong impact on the performance of the spouted beds. Assessment of phase (gas or solids) distributions in spouted beds is of primary concern for accurate design and control of the TRISO fuel-coating process. For example, knowledge of the gas and solids holdup distributions would define parameters such as the spouting conditions, the coating gas composition, and the coating temperature, which will, in turn, result in a higher probability of coating success. The coating layers deposited on the particles depend on how and where the particles are present in the bed. In spouted beds, the solids holdup distributions (or gas holdup) differ from region to region and these differences cause changes in gas-solid interactions and, above all, changes in the value of the absorption and

the conversion of gaseous reactants. In this study, the effects of the particle properties and operating parameters on the gas-solid distribution of spouted beds are the focus. It is hoped that the originality of the results and the analysis of them presented here will provide the basis for assessing design and control processes of TRISO fuel coaters and contribute to other spouted bed applications. This study will provide reliable and valuable benchmark data for the assessment and validation of CFD models and their closures. Improved validation of CFD models for reliable and safe design, scale-up, and process optimization will ensure proper performance and operation of TRISO fuel coaters. Finally, successful implementation of the CT as a non-invasive technique on the cold-flow coater will lay the ground for its implementation in hot pilot plants and industrial units.

The cross-sectional distribution of the phases' holdups of gas-solid spouted beds was studied by the CT. The aim is the establishment of a map of local bed holdups in the three regions of spouted beds, which allow for assessing the design of the TRISO fuel coating process. More precisely, we investigated the solids holdup distributions for spouted beds of particles of different densities and sizes and beds of different sizes. The results highlight key phenomena governing the gas-solids distributions and prove the significance of the impact of the gas dynamics on the hydrodynamics of spouted beds. The findings will lead to further discussion about the influence of the U/U_{ms} on the gas and solids holdups distributions of spouted beds. The discussion on the results will involve two perspectives points: the spouted beds hydrodynamics in general and the spouted beds hydrodynamics from the TRISO fuel coating viewpoint.

4.1.1. Effects of Particle Density And Size. Figure 4.1 and Figure 4.2 present the measured time averaged cross-sectional distributions of the solids holdups as a function of bed material using the CT. The solids used are high-density steel particles (ρ_p= 7.4 g/cm^3) and glass beads (ρ_p= 2.5 g/cm^3). The scale-bar on the right of the images indicates the fraction of the solids holdup. Red color is an indicator of a higher solids holdup, whereas the blue is an indicator of a lower solids holdup. The color scale used in the figures is kept constant for the convenience of comparison between the images. The color distributions of the images clearly highlight the three regions of spouted beds: the spout, the annulus, and the fountain regions. Overall, the cross-sectional distribution images provide a quantitative picture of the way the solids are distributed in spouted beds. It should be pointed out that the cross-sectional phase distribution reported in this study is the only quantitative study in the literature on the gas-solid spouted beds. Exception is made for recent work of our group (Ali et al., 2016a). The experimental results in Figure 4.1 and Figure 4.2 are qualitatively similar to those corresponding to other examined systems here and exhibit the significant variations of the solids holdup with bed position. The solids holdup distributions of the steel and the glass vary in the same way with respect to the z/D ratio. For each material, the solids holdup increases with increasing the bed height, and the reverse is true for the gas holdup (gas holdup = 1- solids holdup). This increase occurs when some solids enter the spout from the annulus at levels below the bed surface. The variation of the solids holdup with the radial position is pronounced. At each z/D level, solids holdup are seen to be low near the axis of the spout and increase, very slightly near the axis, then very sharply at the spout-annulus interface. In the annulus, the solids holdup distribution is almost unchanged along the bed height. At the column wall, the solids holdup is seen to be

unchanged. It can be observed in Figure 4.1 (D_c= 0.076 m, γ= 60°, D_i= 9.5 mm, d_p= 1 mm; H_o= 160 mm, U/U_{ms}= 1.1), based on the color scale located at the right of the images that as material density increases, solids holdup decreases. Steel particles demonstrate lower solids holdup in the spout than the glass particles at the same U/U_{ms} ratio. This solids holdup decrease is due to the increase in the minimum spouting velocity of the solids when the value of material density increases. It means that at the same U/U_{ms} ratio between the two materials, the glass particles are more existing at a lower superficial gas velocity. The same finding is observed for the 0.152 m spouted bed column in Figure 4.2 (D_c= 0.152 m, γ= 60°, D_i= 19.1 mm, d_p=2 mm; H_o= 160 mm; U/U_{ms}= 1.1).

In order to verify the qualitative observations made between the different bed material densities, quantitative comparisons of solids holdup between materials are also presented in this section. From Figure 4.1 and Figure 4.2, it can be observed that the cross-sectional solids holdup distributions in spouted beds are axis-symmetrical. Therefore, one is justified representing the cross-sectional distribution through azimuthal averaging of the two-dimensional data. The cross-sectional images in Figure 4.1 and Figure 4.2 are azimuthally averaged to obtain the radial profiles in Figure 4.3 and Figure 4.4, respectively. Figure 4.3 shows the comparison of the solids holdup radial profiles of different material studied under selected spouted bed system (D_c= 0.076 m, γ= 60°, D_i= 9.5 mm, d_p=1 mm; H_o= 160 mm, U/U_{ms}= 1.1) at different z/D levels. In the spout, which is characterized as a gas-solid riser the solids holdup is lower near the gas inlet and increase as the height increases along the bed. As pointed out earlier, this increase in solids holdup is due to the entrainment of particles from the annulus along the height of the bed, in agreement with the observations of (He et al., 1994a; Pianarosa et al., 2000; San José et al., 1998; San José

et al., 2005b). (Grbavčíc et al., 1976; Mathur and Epstein, 1974c) stated that the cross-sectional average gas holdup decrease with increasing bed height, and the reverse is true for the solids holdup. Indeed, Roy et al. (Roy et al., 1994) examined a bimodal cycle time distribution of the radioactive tracer. They showed that there are two main solid exchange regions. One at the conical base and the other just below the bed surface. Some authors reported that there is a loss of gas to the annulus at level below the bed surface resulting the increase on the solids holdup (Pianarosa et al., 2000). This loss of gas is not noticed for the investigated conditions shown in Figure 4.3 and Figure 4.4. The variation on the solids holdup profiles is not pronounced along the bed height of the annulus. The solids holdup profiles in the annulus are almost unchanged along the bed height, with an average value of 0.59. Hence, particle-particle contacts and interaction forces cannot be ignored in the annulus. It is also to be noticed that the shape of the solids holdup profiles in the spout region is much closer to a parabolic shape. The profiles show that the solids holdup is low near the axis of the bed and increase radially toward the spout-annulus interface. The experimental results in Figure 4.3 and Figure 4.4 present the great variation of solids holdup in the spout with bed position, either the longitudinal or the radial directions. The profiles obtained here are in excellent agreement with the recent works (Al-Dahhan et al., 2014; Ali et al., 2016a; Aradhya, 2013). Comparison to be made using these results related to correlations prediction of solids holdup are restricted. To the authors' knowledge, it seems that there are no correlations predicting solids holdup in spouted beds available in the literature. The only correlations available in the literature are to predict the gas holdup for conical spouted beds (San José et al., 1998; San José et al., 2005b). However, these correlations of conical beds (made with fully conical geometry) cannot be applied to the

conventional spouted beds, also known as conical-cylindrical spouted bed, due to geometrical differences between the two beds (Olazar et al., 1998; Olazar et al., 1993; San José et al., 1993). In the fountain, the solids holdup profiles differ from those collected in the other regions of spouted bed. The reason is the unique motion of the particles in this region, which can be described as a bridge to redirect the particles from the spout back into the annulus. The solids holdup in the fountain is crucial for the solids distribution from the fountain into the annulus, and the solids circulation in the entire bed. The profiles show the solids holdup is higher near the core of the fountain and decrease radially toward the outer region of the fountain. It has been reported the importance of the fountain in promote the particle segregation in spouted beds (Cook and Bridgwater, 1978; Kutluoglu et al., 1983). Waldie et al. (Waldie et al., 1986) also considered the significance of the fountain when the spouted bed is used as a coater, the interaction of a feed spray with particles in the fountain is impacted by the gas-solids distribution in the fountain. Hence, attention should be paid in future for the fountain in the coating process of TRISO fuel particles using spouted beds.

As shown in Figure 4.3, as the density decreases the solid holdup increases, confirming what is found in the cross-sectional images. The effect of increasing the solids density is a decrease in the solids holdup. Glass beads have higher solids holdup in the spout than steel particles when the two systems are applied at the same U/U_{ms} ratio. The reason is mainly the increase of the minimum spouting velocity of steel particles. This finding about the spout is in agreement with the experimental results of San José et al. (San José et al., 2005b), who used optical probe in conical spouted beds. San José et al. (San José et al., 2005b) reported that the gas holdup increases when the minimum spouting

velocity increases and when the value of the particle density increases. However, the reverse is true for the solids holdup. In Figure 4.3, the average percentage difference between the profiles of the two materials in the spout is 54.62%, 46.96%, 37.39%, respectively, at z/D levels of 0.8, 0.9, and 1.1. The differences in the solids holdup of the two materials can be explained as follows. Since the superficial gas velocity applied to the steel particles is higher than that of glass, the particles with the smaller density will less drag in the spout than the particles of the greater density. As a consequence, they will lag behind the air flow in the spout region and the core of the fountain as well. Thus, the particles with the smaller density are expected to have the lower axial velocity and the longer time to travel through the spout than the particles with the greater density. Accordingly, the particles with the smaller density are more presented into the spout region and solids holdup increases. The results also can give the thought that the glass particles fed more into the spout region than the steel particles. However, no noticeable differences were observed for the solids holdup profiles of the two materials in the annulus region. This is primarily attributed to the very slow movements of the particles in the annulus, where the particles move slowly downward in this region as in moving packed bed. The average percentage difference between the profiles in the annulus is small. The results indicate that the solids holdup distributions in the annulus region are less dependent on the material density. In the fountain, the glass particles demonstrated higher solids holdup than steel particles. The average percentage difference between the profiles of the two materials in the fountain is 34.44%. The results presented in Figure 4.4 demonstrate the same findings as in Figure 4.3, despite the differences in the bed size and the spouting conditions. In Figure 4.4, the glass particles show higher solids holdup values than the steel particles,

both in the spout or the fountain. The average percentage difference between the profiles of the two materials in the spout is 25.09%, 28.9%, 21.9%, respectively, at z/D levels of 0.8, 0.9, and 1.1. The radial profiles of the two materials compared in the annulus region have small or no deviations. The average percentage difference between the profiles of the two materials in the fountain is 18.99%.

The particle size has an essential role in gas-solids spouted beds and, therefore, in the coating process of TRISO particles. For example, the heat transfer from the wall-to-the bed, from solid-to-solid surface, and from the gas phase-to-the solids in spouted beds largely depend on the distribution of the solids holdup and increase with increasing the particle size. In addition, the amount of the coating layers captured by the particles and quality of that layers are also dependent on the size of the particles (i.e., Surface area of the particles). The size of the particles varies during the coating process of the TRISO particles. Thus, additional information on the solids holdup distributions were obtained by examining the effect of the particle size. Figure 4.5 and Figure 4.6 show the comparisons of the solids holdup radial profiles of material of different sizes and same density under selected spouted bed systems. The results concerning the impact of the particle size in the annulus are found less accentuated and not shown in the figures. The influence of the particle size on the solids holdup is quite evident in the spout region. In Figure 4.5, the average percentage difference between the profiles of the different sizes particles in the spout is 9.74%, 5.85%, 7.37%, respectively, at z/D levels of 0.8, 0.9, and 1.1. The results suggest that increasing the particles size leads to a decrease in the solids holdup in the spout at the same U/U_{ms}. This decrease is caused by the increase of the minimum spouting velocity when the particle size increases. The particles with the smaller size are expected to be present more in the

spout and, therefore, have a longer contact with the gas phase. In Figure 4.6, the average percentage difference between the profiles of particles of different sizes in the spout is 9.53%, 7.54%, 6.41%, respectively, at z/D levels of 0.8, 0.9, and 1.1. Comparing the deviations here with those for the different densities, we found that the particle size has less impact on the solids holdup distributions than the particle density for the range investigated.

The results discussed above demonstrate that the changes in the properties of the particles must be accompanied by appropriate changes in the input process of the spouting conditions to produce particles with uniform coating layers. The assumption that stable spouting mode would result in uniform coating layers for the particles is not adequate. The results show that even though the particles were operated at the stable spouting state and same U/U_{ms}, differences were obtained in the solids holdup distributions in the spout and the fountain regions. The coating formation of particles in a spouted bed is ultimately a function, but not limited to the solids holdup distributions of the particles. Recently, Liu et al. (Liu et al., 2015a) used the CFD–DEM coupling simulation method to study the fluidization behavior of particle with different densities in the spouted bed. Liu et al. (Liu et al., 2015a) reported that the stable spouting range expands when the particle density increases. Hence, there is a larger velocity adjust range to be selected from initial spouting to the end of the stable spouting state. Furthermore, the authors determined the power spectral density distribution of the time domain signal of the axial instantaneous particle velocity under different U/U_{ms} ratio for various material densities. They reported that the dominant frequency of the particle spouting process and the particle residence time distribution of various densities would be almost the same in the spout region, even if the

particle density increases, as long as U/U_{ms} is not changed. In addition, they stated that with the consistent residence time of all the particles in the spout region, the layers would uniformly deposit on the surface of all particles. The results reported in our work do not comply with the findings of Liu et al. (Liu et al., 2015a). As shown in the figures, when two materials are operated at the same U/U_{ms}, solid holdup distributions of the two materials are different. Therefore, the mass of materials deposited on the particles will be varied due to the variation in the number of particles present in the spout and in the fountain at a given time. Recently, the preference has been to move towards coating the TRISO layers continuously, without unloading the particles after each coating step to avoid smooth and sharp interface between the layers and to avoid mechanical shocks caused by unloading procedure of the particles (Minato et al., 1997). Therefore, it is necessary to optimize the spouting conditions of the particles in the intermediate coating process of each layer due to the change of the properties of the particles, in agreement with the findings of Minato et al. (Minato et al., 1997). The results reported here also demonstrate that the solids flow is strongly influenced by the forces exerted by the gas on the solid particles. Indeed, Al-Dahhan et al. (Al-Dahhan et al., 2014; Ali et al., 2016b; Aradhya, 2013) considered the significance of the gas dynamics in gas-solids spouted beds. (Al-Dahhan et al., 2014; Ali et al., 2016b; Aradhya, 2013) stated that the gas dynamic dictates the hydrodynamic of gas-solid spouted beds, and they used this assumption to develop a new mechanistic scale-up approach based on matching gas holdup profiles between two different sizes of beds. This is also evident in the results reported here, since the deviations between the profiles of the two materials are prominent in the spout region, as the spout region is predominantly dominated by the gas phase.

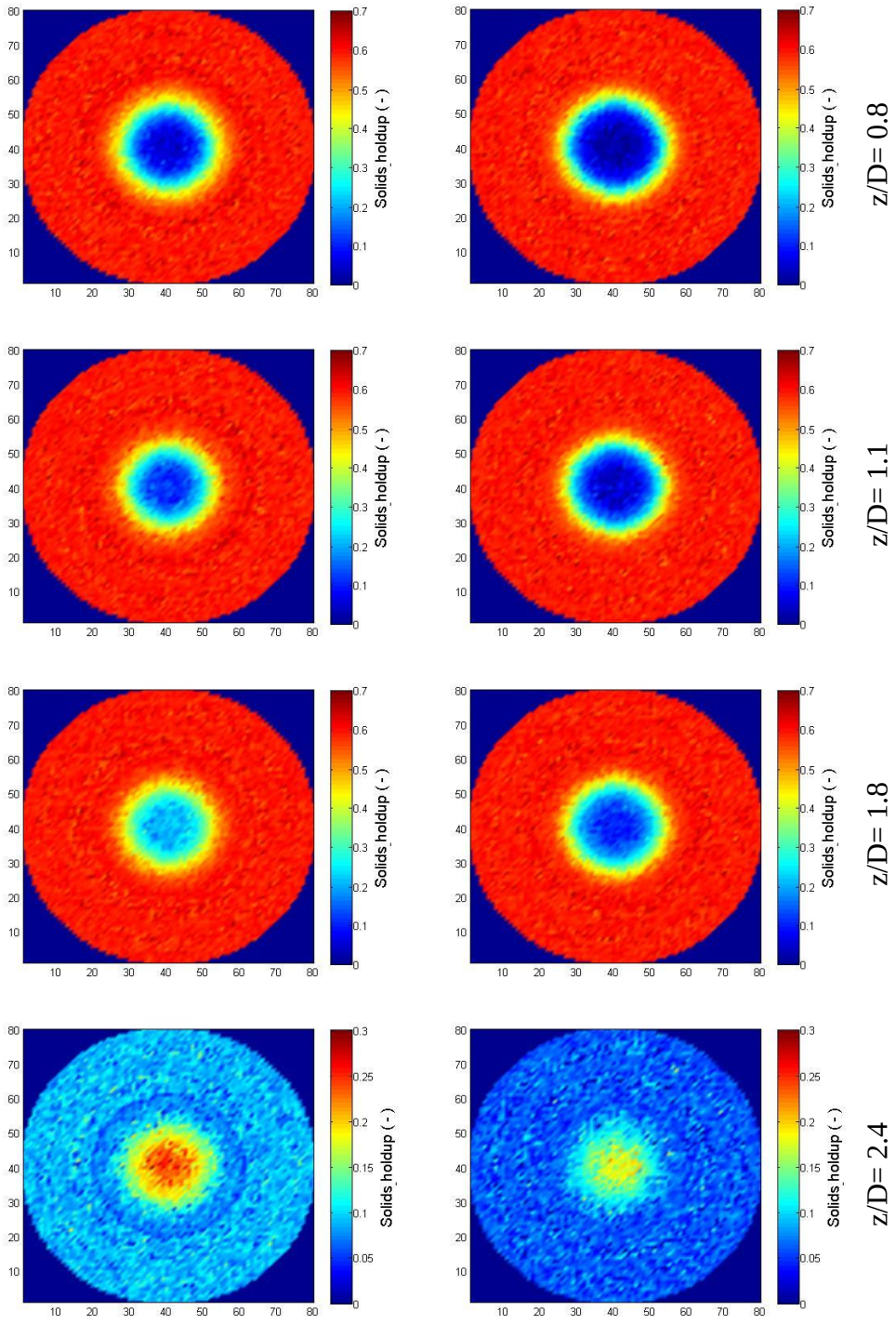

Figure 4.1. Cross sectional distribution of time-averaged solids holdup of spouted beds of different material (a) glass and (b) steel. Conditions: (D_c= 0.076 mm, γ= 60˚, D_i= 9.75 mm, d_p=1 mm; H_o= 160 mm; U/U_{ms}= 1.1).

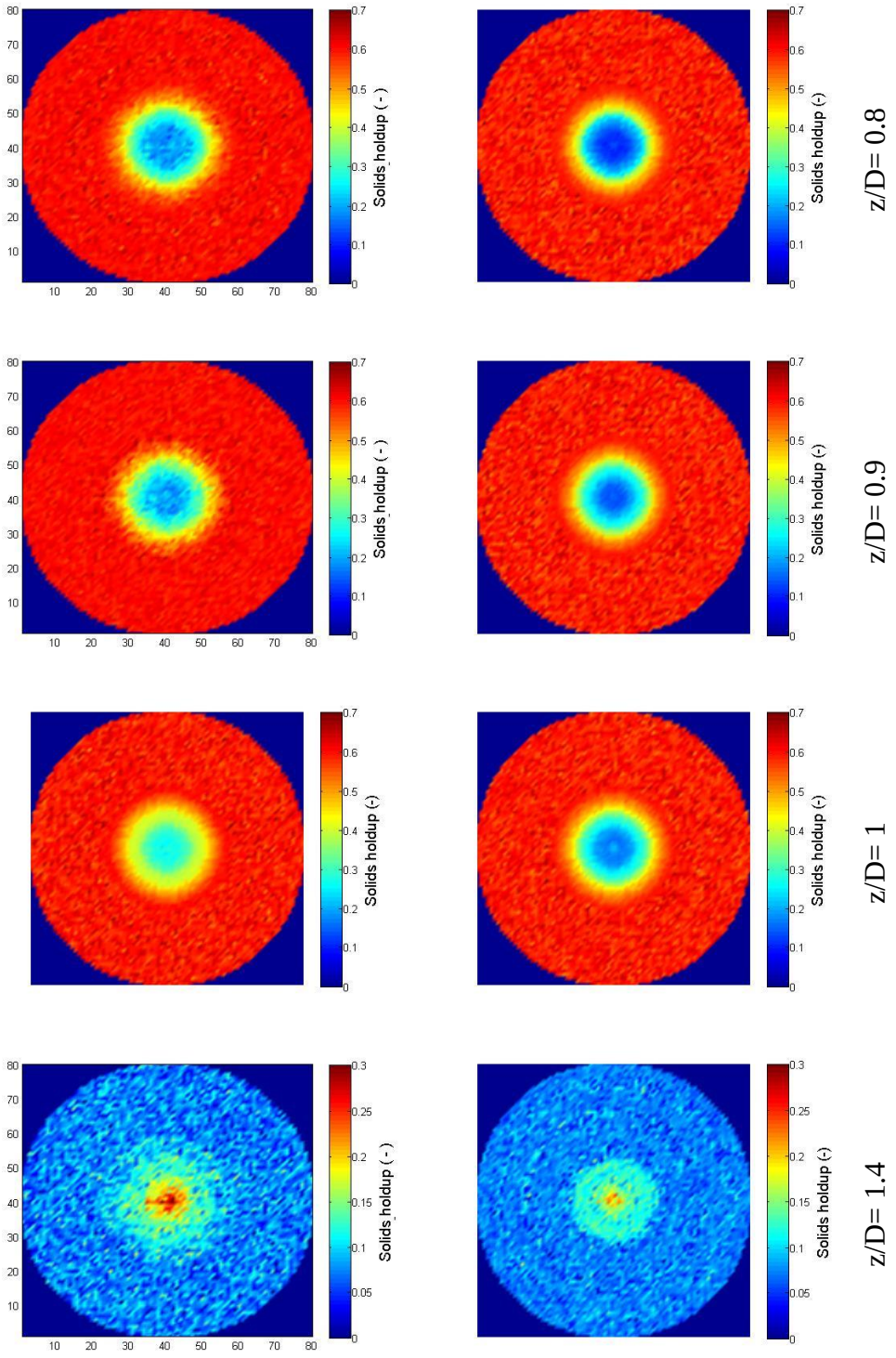

Figure 4.2. Cross sectional distribution of time-averaged solids holdup of spouted beds of different material (a) glass and (b) steel. Conditions: (D_c= 0.152 m, γ= 60˚, D_i= 19.1 mm, d_p=2 mm; H_o= 160 mm; U/U_{ms}= 1.1).

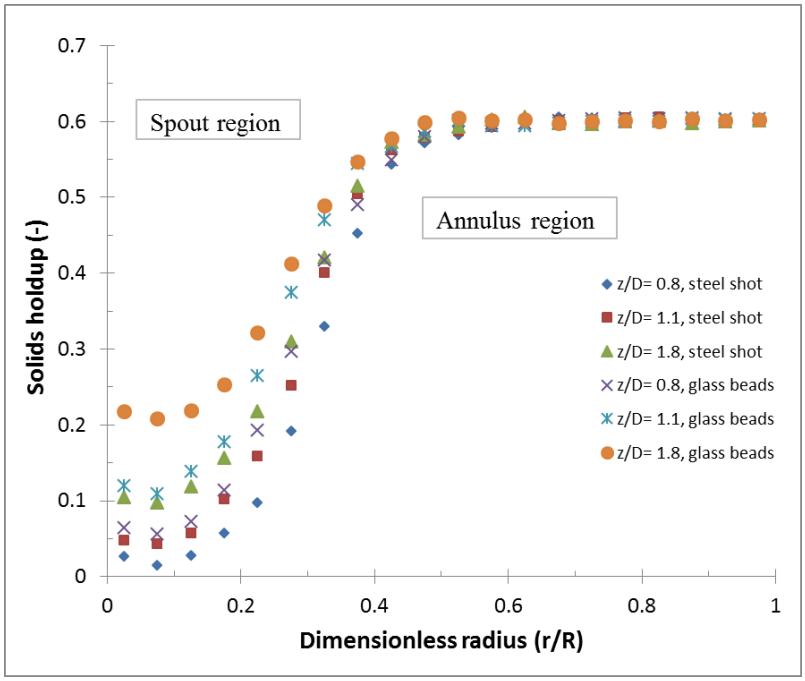

(a)

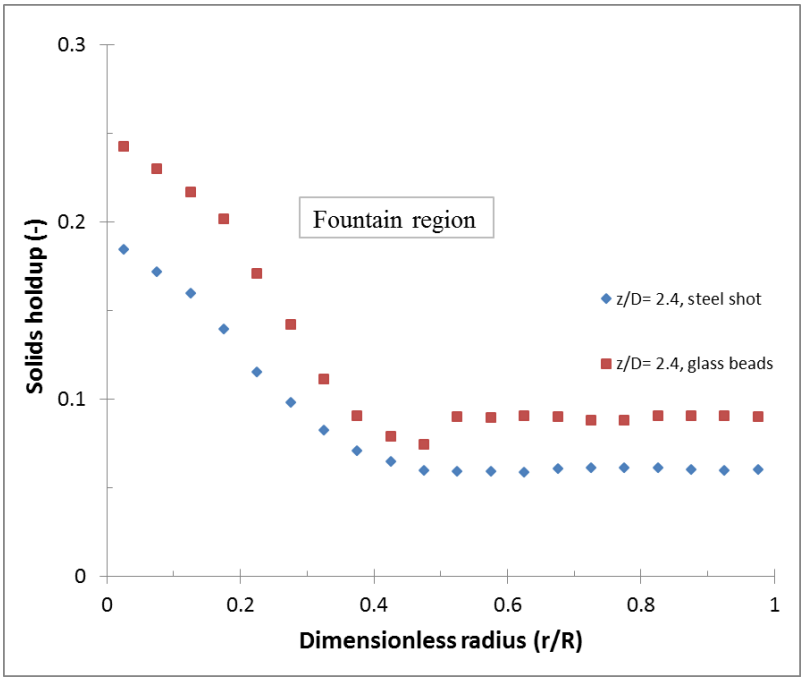

(b)

Figure 4.3. Effect of solids density on the radial profiles of solids holdup. Conditions: (D_c= 0.076 m, γ= 60°, D_i= 9.75 mm, d_p=1 mm; H_o= 160 mm; U/U_{ms}= 1.1).

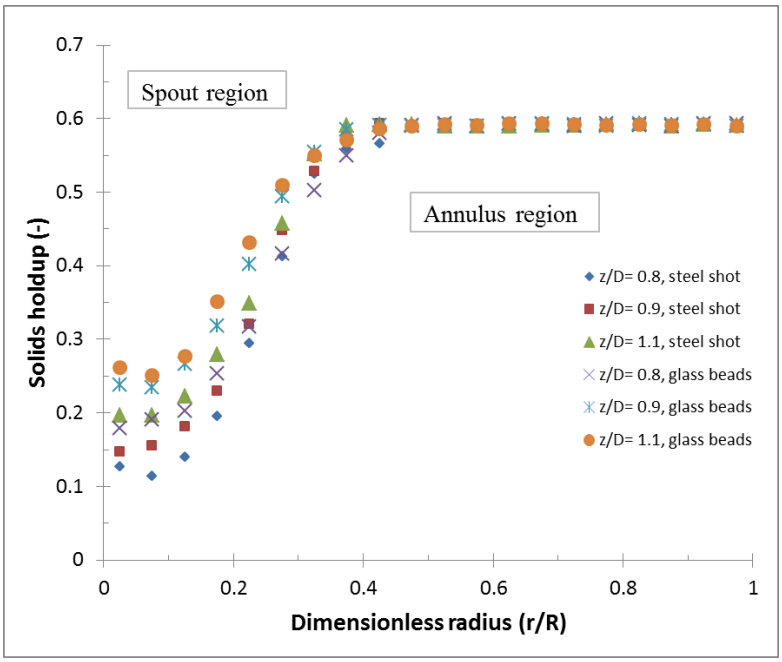

(a)

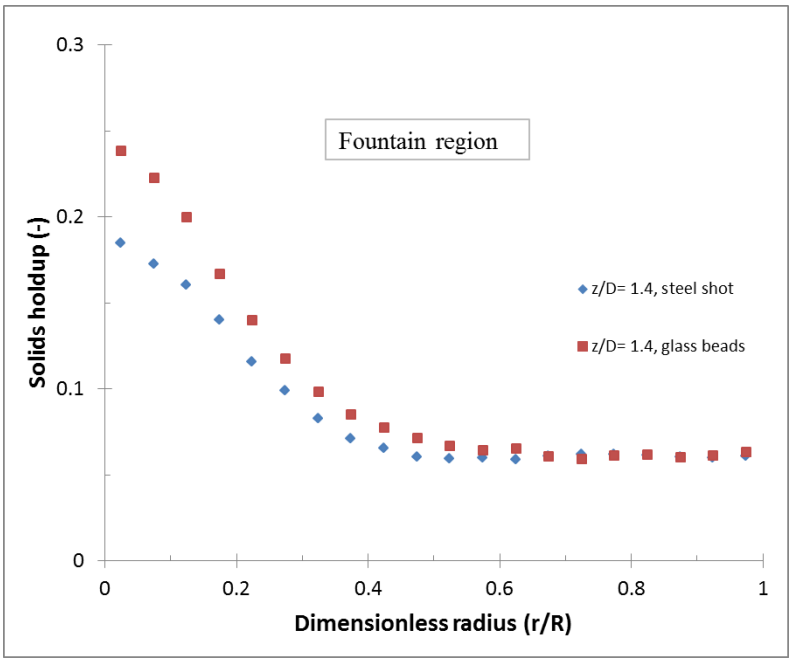

(b)

Figure 4.4. Effect of solids density on the radial profiles of solids holdup. Conditions: (D_c= 0.152 m, γ= 60°, D_i= 19.1 mm, d_p=2 mm; H_o= 160 mm; U/U_{ms}= 1.1).

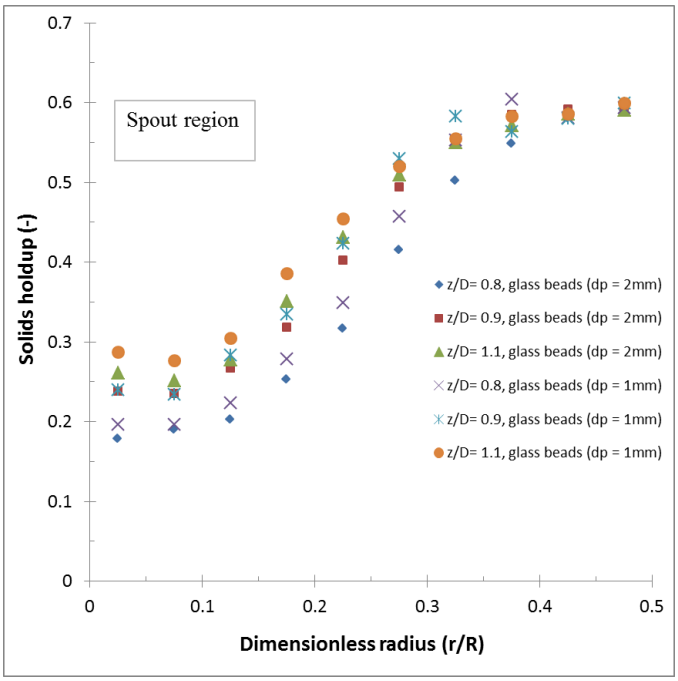

Figure 4.5. Effect of particle diameter on the solids holdup radial profiles in the spout region Conditions: (D_c= 0.152 m, γ= 60°, D_i= 19.1 mm, H_o= 160 mm; U/U_{ms}=1.1).

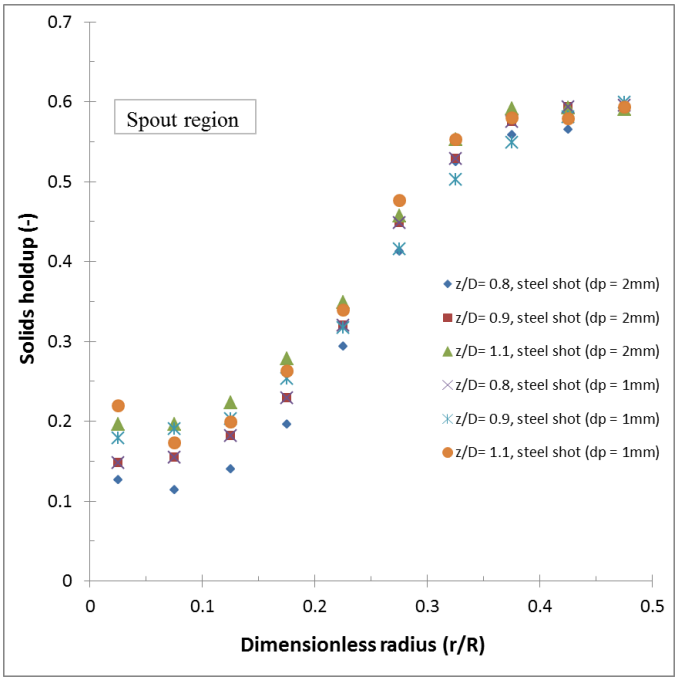

Figure 4.6. Effect of particle diameter on the solids holdup radial profiles in the spout region Conditions: (D_c= 0.152 m, γ= 60°, D_i= 19.1 mm, H_o= 160 mm; U/U_{ms}= 1.1).

4.1.2. Effect of Bed Size. The hydrodynamics behavior of spouted beds varies with scale. Hence, it is challenging to predict the hydrodynamics of large-scale reactors, based on the information of smaller scales. More precisely, it means that if one parameter is changed (e.g., bed diameter) most of the other parameters will change concordantly. Only a few works have addressed the scale-up spouted beds (Ali et al., 2016a, 2017a; Aradhya, 2013; Du et al., 2009; He et al., 1997). The last works have given a qualitative and quantitive studies on the scale-up of spouted beds. These studies make it apparent that the effect of the bed diameter needs further investigation. Therefore, it is important to obtain further fundamental insights into the effect of the bed diameter to formulate precise hypotheses on their behavior of spouted beds reactors. Figure 4.7 and Figure 4.8 show the measured time averaged cross-sectional distributions of the solids holdup as a function of bed size. The beds sizes used are 0.076 m, and 0.152 m ID (inner diameter) spouted beds. The first observation inferred from the images is that the spouting structure of both sizes of the beds is qualitatively similar, with the agreement with the results of (Ali et al., 2016a; Aradhya, 2013) for scale-up of spouted beds at different conditions. However, based on the color distributions of the images, the solids holdup increases as the bed size increases. The 0.152 m ID spouted bed has higher solids holdup than the 0.076 m ID spouted beds when the two beds are applied at the same U/U_{ms} and H_o. The solids holdup is higher in the 0.152 m ID spouted bed because the U_{ms} value for the 0.152 m ID spouted bed is lower than that for the 0.076 m ID spouted bed. (Ali et al., 2016a) reported higher solids holdup for bed of large size at different operating conditions. Figure 4.9 and Figure 4.10 show the comparisons of the solids holdup radial profiles for beds of different sizes under selected spouted bed conditions.

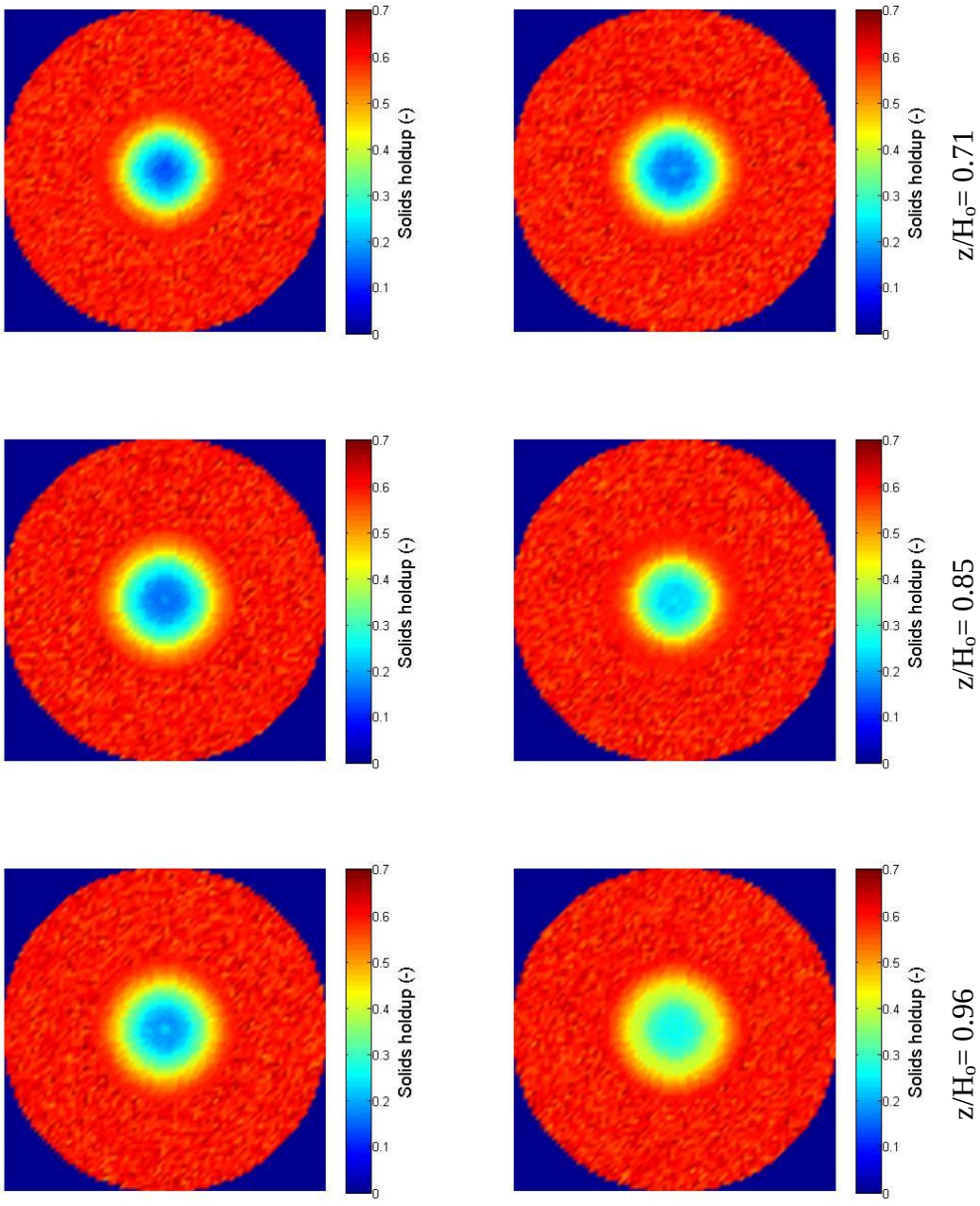

Figure 4.7. Cross sectional distribution of time-averaged solids holdup of spouted beds of different bed sizes (a) 0.076 m and (b) 0.152 m. Conditions: (glass, d_p= 1 mm; H_o= 140 mm; U/U_{ms}= 1.1).

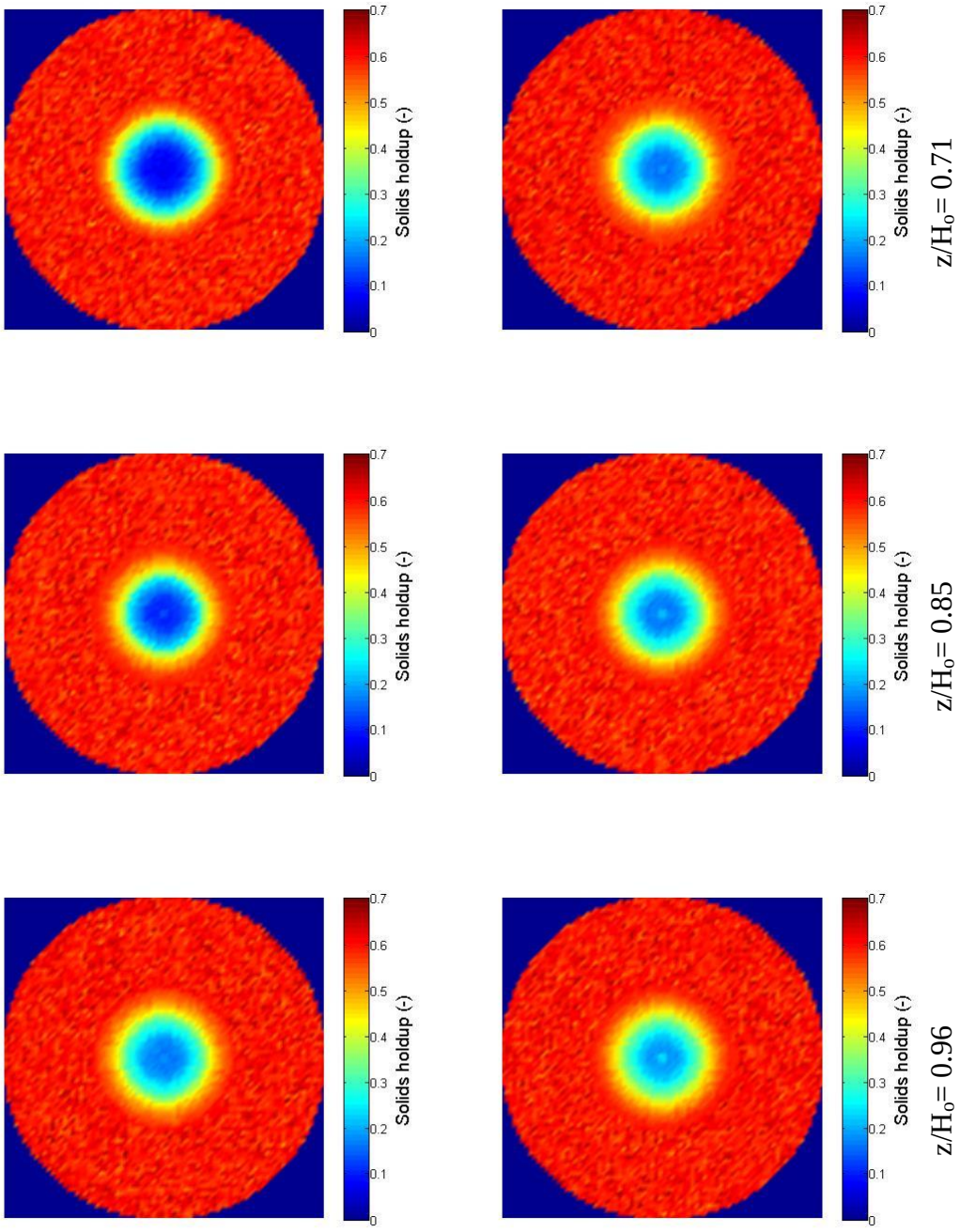

Figure 4.8. Cross sectional distribution of time-averaged solids holdup of spouted beds of different bed sizes (a) 0.076 m and (b) 0.152 m. Conditions: (steel particle, d_p= 1 mm; H_o= 140 mm; U/U_{ms}= 1.1).

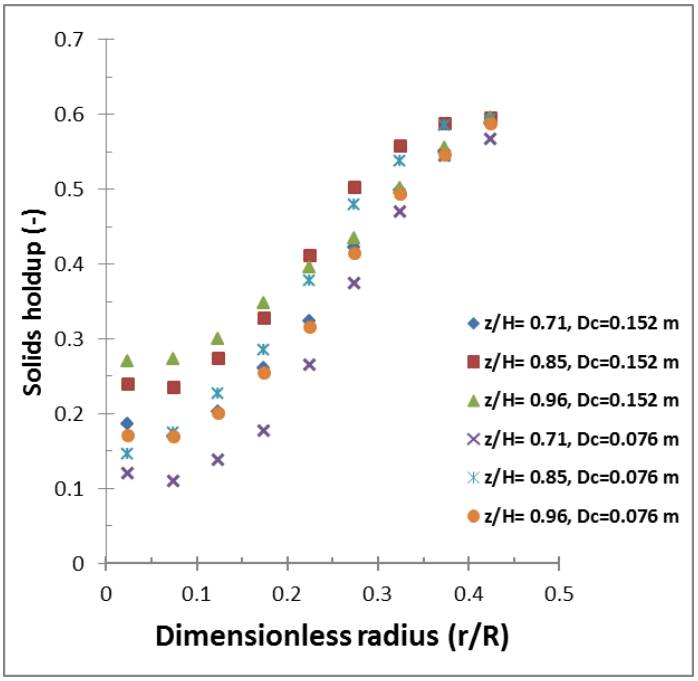

(a)

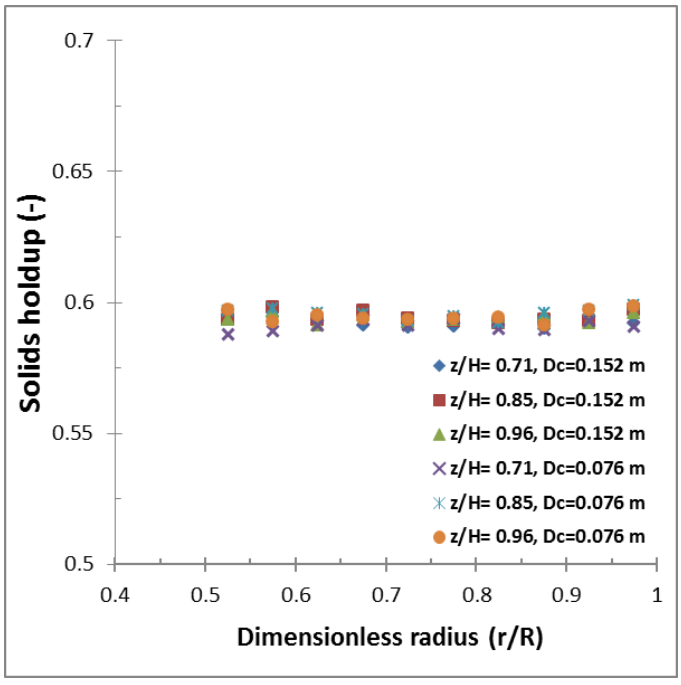

(b)

Figure 4.9. Effect of bed diameter on the solids holdup radial profiles in (a) the spout and (b) the annulus regions. Conditions: (glass particle, d_p= 1 mm; H_o= 140 mm; U/U_{ms}= 1.1).

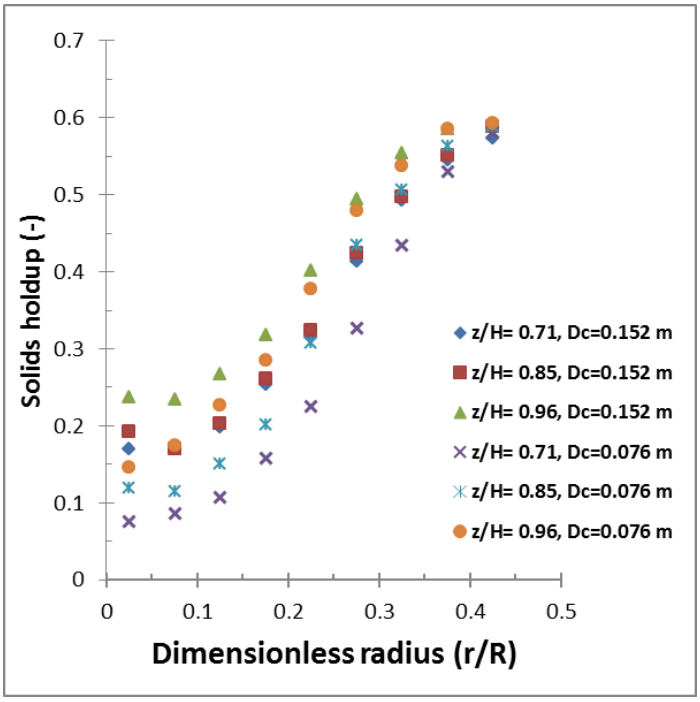

(a)

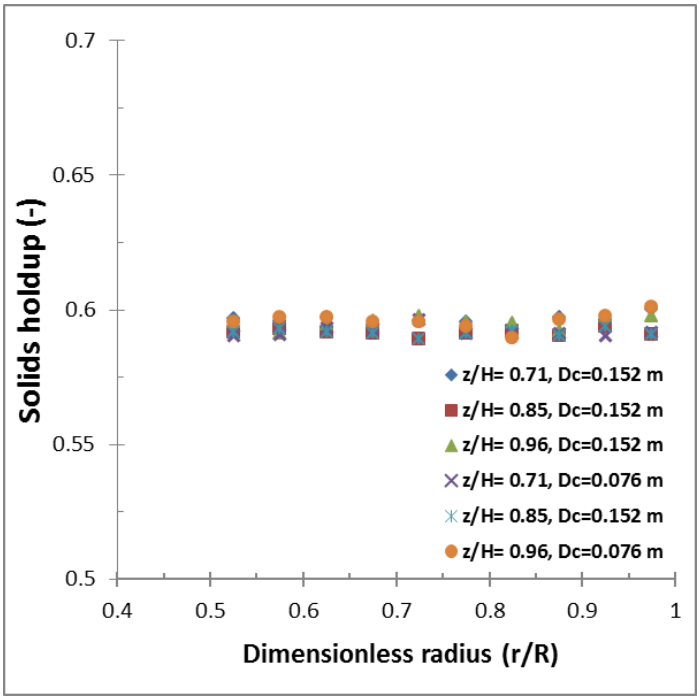

(b)

Figure 4.10. Effect of bed diameter on the solids holdup radial profiles in (a) the spout and (b) the annulus regions. Conditions: (steel particle, d_p= 1 mm; H_o= 140 mm; U/U_{ms}= 1.1).

The comparison of solid holdup profiles in 0.076 m, and 0.152 m spouted beds demonstrates that the solids holdup in 0.152 m spouted bed is higher than that in 0.076 m spouted bed. From the result, the only deviation of the solids holdup profiles between the two beds was observed in the spout. However, in the annulus region, unchanged profiles are achieved for both beds. The movement of the particles in the annulus of both beds is the same; the particles move slowly and downward as in moving packed bed. In Figure 4.9, the average percentage difference between the profiles of the different beds sizes in the spout is 24.34%, 16.17%, and 23.91%, respectively, at z/D levels of 0.8, 0.9, and 1.1. The average percentage difference between the profiles in the annulus is small. In Figure 4.10, the average percentage difference between the profiles of the different beds sizes in the spout is 37.68%, 19.12%, and 15.06%, respectively, at z/D levels of 0.8, 0.9, and 1.1.

4.1.3. Effect of Superficial Gas Velocity. In the literature, it is commonly assumed that the gas holdup in the annulus region of spouted beds is constant along the bed height and equal to the gas holdup value at loose-packed bed state (ε_o = 0.411), where there are particles but the gas flows through the voids between the particles without disturbing them significantly (Epstein et al., 1978; Mathur and Epstein, 1974a; Mathur and Gishler, 1955; Matsen, 1968; Thorley et al., 1955). Accordingly, different measurements techniques, CFD models, and closures for simulating spouted beds, including studies targeting TRISO fuel coating, were based on this assumption. However, the question whether there are variations in the gas holdup in the annulus or not is not completely covered. Hence, further investigation was conducted to resolve this question, along with the influence of the U/U_{ms} on the spout and annulus regions, taking into consideration the advantage of the non-invasive measurements of the CT technique without disturbing the flows in spouted beds.

Figure 4.11 show the time-averaged cross-sectional distribution and the corresponding frequency distribution for gas holdup of selected spouted bed system (D_c= 0.152 m, γ= 60°, D_i= 19.5 mm, solids: glass beads, d_p= 2 mm; H_o= 325 mm) at z/D level of 1.1 and different U/Ums ratios. At no time during the experiments, the annulus appeared to be fluidized. The images show the effect of the U/U_{ms} ratio on the gas holdup distributions, as the gas holdup at many local positions in the spout and the annulus (in strict sense) regions increased with increasing the U/U_{ms} ratio. A more detailed view of the gas holdup measurements can be obtained from the statistical analysis. Pixels outside the spouted bed diameter (i.e., pixels with gas holdup equal to one) were not considered in the normalized frequency distribution for a case of comparison. The mean and the mode of the distribution are only affected by the magnitude of the gas holdup values in the spout and the annulus regions. The normalized frequency distribution is predominant at the gas holdup value in the annulus and skews to the right where the frequency distributions are small in the spout. The skewness distribution (non-symmetric) is expected for spouted beds due to lower and upper gas holdup values on the data. Also, the skewness distribution of the peaks further confirms the divergence between the spout and the annulus regions in spouted beds. The mean values of the frequency distribution below the images disclose that the gas holdup increases in the entire bed. As the U/U_{ms} ratio increases, the mean value of the gas holdup cross-sectional distributions increases. At U/U_{ms} = 1.1, the mean of gas hold-up values is 0.429, above to the mean gas holdup value at the loose-packed bed sate (ε_o= 0.411). However, this value increased sustainably from 0.429 to 0.473 when the U/U_{ms} ratio increased from 1.1 to 1.4. Increasing the U/U_{ms} ratio changes the frequency distribution to higher values and shifts the peak plateau to the right past the gas holdup value at the loose-packed bed state. This

phenomenon is more obvious when one compares the peak plateau at U/U_{ms}= 1.1 and U/U_{ms}= 1.4. In addition, the standard deviation increases monotonically with increasing the U/U_{ms} ratio. Nevertheless, one can argue that the gas holdup cross-sectional distributions in the annulus remained non-fluidized for the investigated U/U_{ms} ratios. Therefore, diverting the flow of air to the annulus should only have contributed to increasing the gas holdup, with little effect on the structure of the annulus.

For further comparison of the results, the results of solids holdup cross-sectional distributions are also presented here. The effect of the U/U_{ms} ratio on the cross-sectional distribution of the solids holdup at z/D level of 1.1 is shown in Figure 4.12. The images demonstrate that the solids holdup distribution is nearly symmetrical around the bed axis. Such symmetry exists at U/U_{ms}= 1.1 and even at the higher U/U_{ms} ratio. Nonetheless, it is evident from the images that increasing the U/U_{ms} shifts the solids holdup to decrease whether in the spout or the annulus. The images also show the spout size increase with increasing the $U/U_{ms,}$ in qualitative agreement with (Bridgwater and Mathur, 1972; He et al., 1998; McNab, 1972). The effect of increasing the U/U_{ms} ratio in spouted beds can be explained by observing it as a decrease in the solids holdup due to the increase in the gas holdup whether in the spout or in the annulus when the superficial gas velocity is increased. In the annulus, the voids between the particles at many local positions increase with increasing the U/U_{ms} ratio, confirming what is presented in Figure 4.11. This finding is more pronounced at U/U_{ms}= 1.4, where pixels with yellow colors increased in the annulus region. The mean of the solids holdup cross-sectional distribution is 0.571, 0. 565, 0.547, and 0.526, respectively at U/U_{ms} ratio equals to 1.1, 1.2, 1.3, and 1.4. The mean of the solids holdup distribution is affected by the magnitude of the phase holdup values in both

regions (the spout and the annulus). Consequently, in order to properly analyze the results, the data of each region in spouted bed must be excluded from the other and analyzed separately. We will restrict the following discussions on the gas holdup profiles.

Figure 4.13 shows the radial profiles of the gas holdup in the annulus region along the bed height at different U/Ums ratios for selected spouted bed system (D_c= 0.152 m, γ= 60°, D_i= 19.5 mm, solids: glass beads, d_p= 2 mm; H_o= 325 mm) at different z/D levels. At z/D=1.1, the average gas holdup in the annulus is 0.414 at U/U_{ms}= 1.1, is 0.413 at U/U_{ms}= 1.2, is 0.431, at U/U_{ms}= 1.3, and 0.441 at U/U_{ms}= 1.4. For only one level, (z/D = 1.1), the average gas holdup in the annulus increased by 4.87%, and 7.56%, respectively, for U/U_{ms} equal to 1.3, and 1.4, above loose-packed bed value. The results show that the gas holdup in the annulus increases with increasing the ratio of U/U_{ms} despite the rise in the level of the bed height; increasing the U/U_{ms} ratio allows for additional gas flowing between the particles. The results demonstrate that the conventional assumption that the gas holdup in the annulus is constant and equals to the loose-packed bed value is not completely accurate. This finding is in line with the finding reported in the literature (He et al., 1994a) and contradicts the common spread assumption that the gas holdup in the annulus equals to the loose-packed bed value. (He et al., 1994a) measured the gas holdup in the annulus using optical probe for conical-cylindrical spouted bed under comparable conditions (D_c= 0.152 m, γ= 60°, D_i= 19.5 mm, solids: glass beads, d_p= 1.14 mm; H_o= 325 mm, U/U_{ms}= 1.1, 1.2, and 1.3) similar to the ones presented in Figure 4.13. They reported that the gas holdup in most of the annulus is above the loose-packed bed value. In their work, the mean of the gas holdup values in the annulus increased by 2.5%, 4.9%, and 11.6% higher than the loose-packed bed value of 0.412, respectively, at U/U_{ms}= 1.1, 1.2, and 1.3. It should be noted that

the increase in the gas holdup values in their work was observed starting from U/U_{ms}= 1.1, while in this work it was observed at U/U_{ms}= 1.2. The disturbance of the optical probe may have contributed to this difference. The above assumption, in fact, simplifies the actual process occurring in the annulus of spouted beds. The annulus does not remain at the loose-packed bed gas holdup. Rather, it can include additional gas flowing between the particles, therefore resulting in the dynamic distribution of the two phases of spouted beds. This distribution potentially impacts reactions and transfer rates of the mass and heat in spouted beds. Hence, findings, measurements techniques, CFD models, and the reported closures for simulating spouted beds based on this assumption can be challenged due to the accuracy. The fluid dynamic in spouted beds is highly sensitive to the variations of the gas holdup. Thus, simulations of different conditions of gas holdup distribution can lead to different fluid dynamic profiles. So far, despite the attempts to apply the CFD models (Béttega et al., 2009; Du et al., 2006a, b; Duarte et al., 2005; Duarte et al., 2009; Hosseini et al., 2013; Lan et al., 2012; Liu et al., 2015a; Ren et al., 2011; Shuyan et al., 2009; Wang et al., 2014; Zhonghua and Mujumdar, 2008) on simulating spouted beds, detailed validations of these models and closures against detailed local hydrodynamics of the annulus has not yet been covered. Accordingly, future models are required to pay attention to the annulus of spouted beds and prove that they captured the interplay phenomena and parameters. From the TRISO fuel coating point of view, the results suggest that the higher the U/U_{ms} applied on the spouted beds, the more of reactive gas will escape from the spout to the annulus or vice versa from the annulus to the spout. Thus, contact between the particles and the reactants gaseous may take place in the annulus, whereas typically it is assumed to be in the spout.

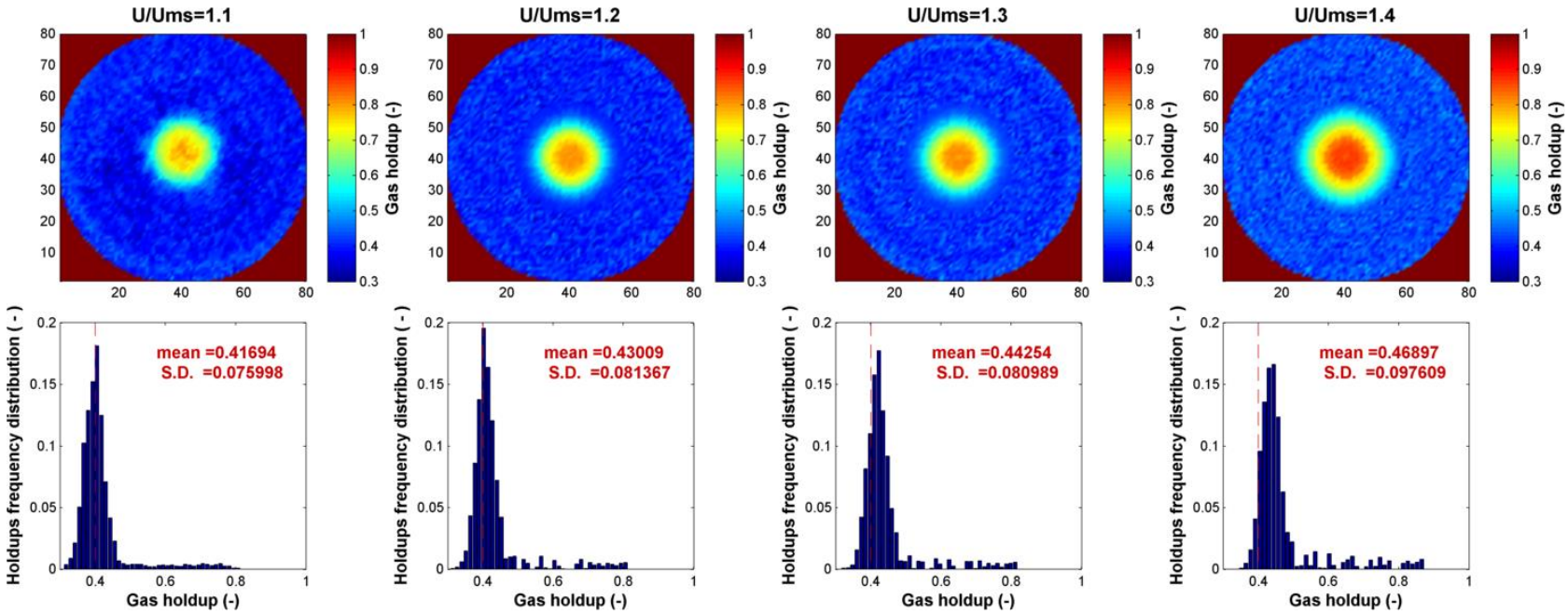

Figure 4.11. Effect of superficial gas velocity on the cross-sectional distribution and the corresponding frequency distribution of the local gas holdup for selected spouted bed system (D_c= 0.152 m, γ= 60°, D_i= 19.5 mm, solids: glass beads, d_p= 2 mm; H_o= 325 mm) at z/D level of 1.1 and different U/U_{ms} ratio.

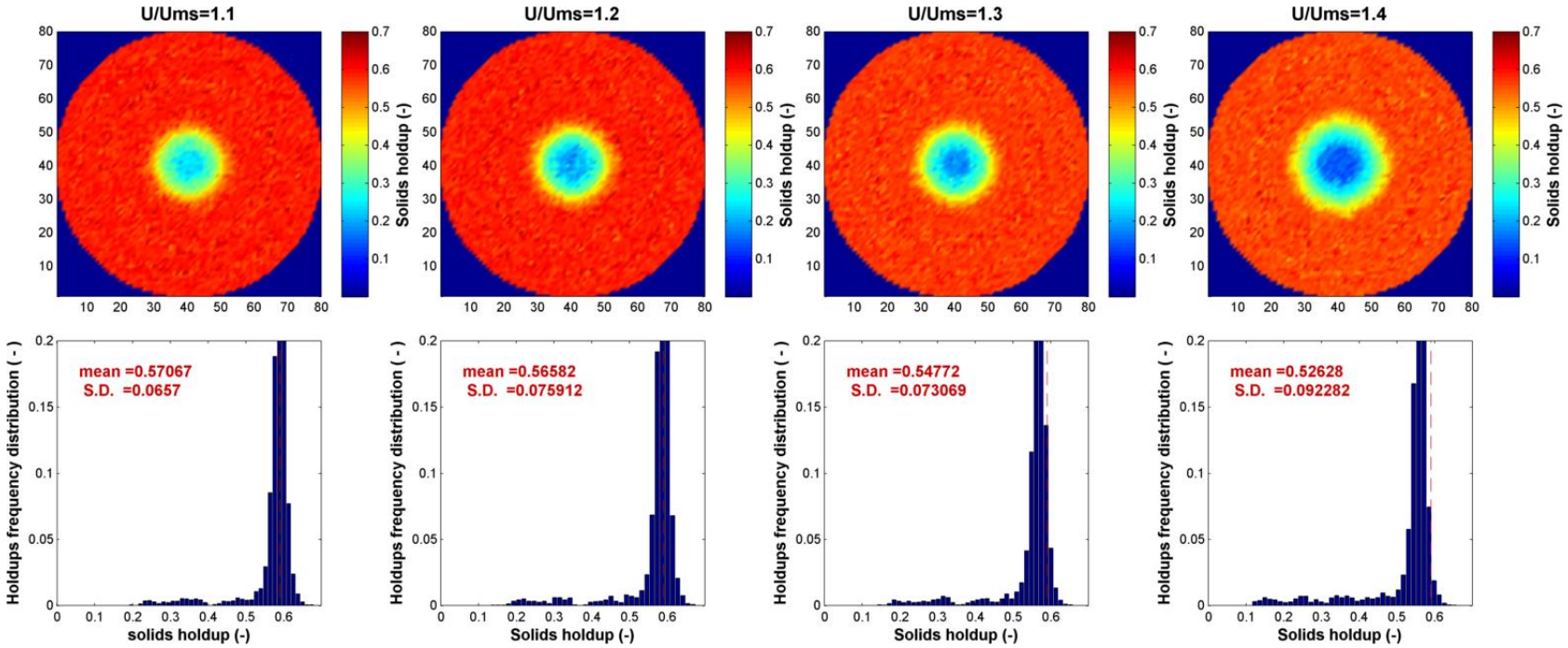

Figure 4.12. Effect of superficial gas velocity on the cross-sectional distribution and the corresponding frequency distribution of the local solids holdup for selected spouted bed system (D_c= 0.152 m, γ= 60°, D_i= 19.5 mm, solids: glass beads, d_p= 2 mm; H_o= 325 mm) at z/D level of 1.1 and different U/U_{ms} ratio.

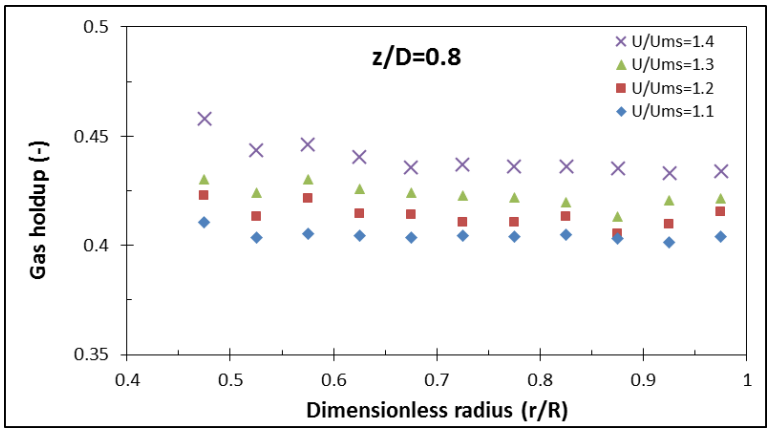

(a)

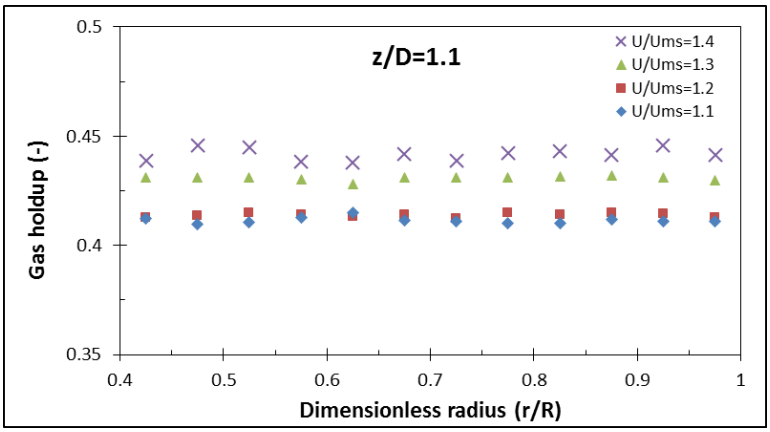

(b)

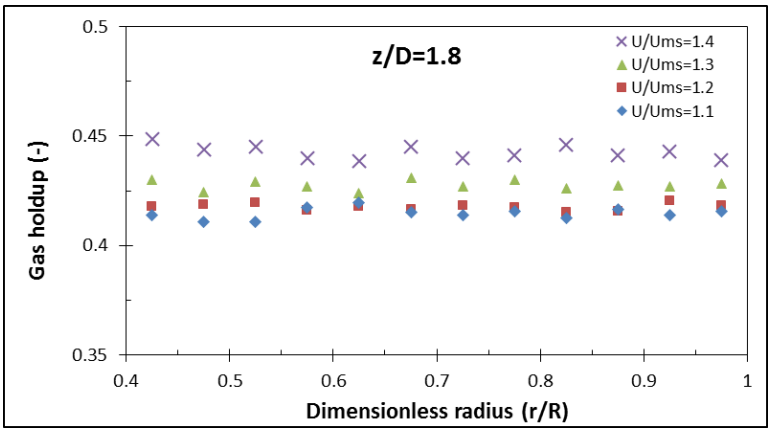

(c)

Figure 4.13. Effect of gas velocity on the radial profiles of gas holdup in the annulus region for selected spouted bed system (D_c= 0.152 m, γ= 60°, D_i= 19.5 mm, solids: glass beads, d_p= 2 mm; H_o= 325 mm) at different U/U_{ms} ratios.

The effect of the U/U_{ms} on the gas holdup profiles in the spout for selected spouted bed system (D_c= 152.4 mm, γ= 60˚, D_i= 19.5 mm, solids: glass beads, d_p= 2 mm; H_o= 325 mm) is shown in Figure 4.14. For z/D= 1.1, the deviation between the profiles increased by 8.32%, 10.13%, and 22.13% with increasing the U/U_{ms} ratio from 1.1 to 1.2, 1.3, and 1.4, respectively. However, the deviation between the profiles decreases with increasing the z/D levels and becomes less at z/D= 1.8.

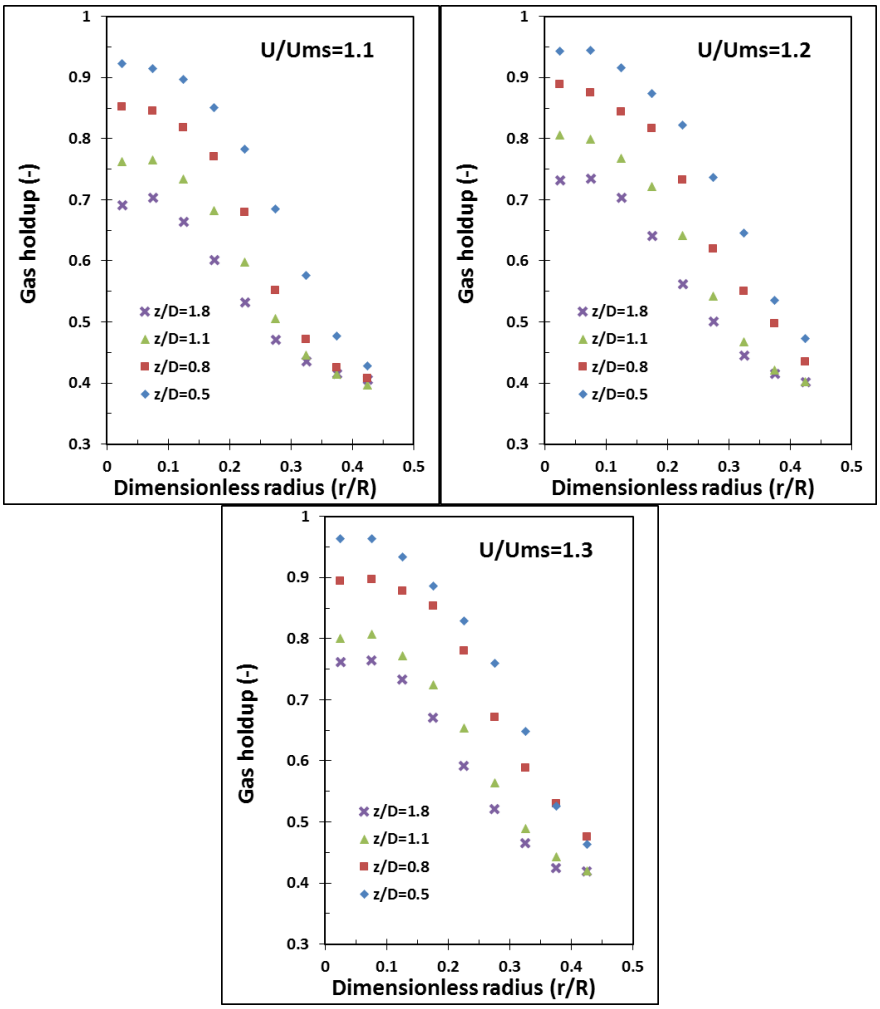

Figure 4.14. Effect of gas velocity on the radial profiles of gas holdup in the spout region for selected spouted bed system (D_c= 0.152 m, γ= 60°, D_i= 19.5 mm, solids: glass beads, d_p= 2 mm; H_o= 325 mm) at different U/U_{ms} ratios.

The deviations between the profiles at z/D=1.8 were 10.57%, 15.52% and 23.96% for U/U_{ms} equals to 1.2, 1.3, and 1.4, respectively. For each U/U_{ms} ratio, the gas holdup decreases with the increase in the bed height and decreases radially towards the spout-annulus interface, where the maximum gas holdup was obtained at the axis of the spout. The results clearly show the effect of the U/U_{ms} ratio on the gas holdup in the spout. Increasing the U/U_{ms} causes the gas holdup values to increase substantially in the entire spout. This implies that applying spouted beds at higher U/U_{ms} ratios, even when these ratios are within stable range of operation, will cause the spout to become bigger and more dilute (see Figure 4.11 and Figure 4.12). Thus, particles in the spout will have less chance to contact with the reactive gas due to the violent spouting caused by the large energy transferred from the gas (see Figure 4.15).

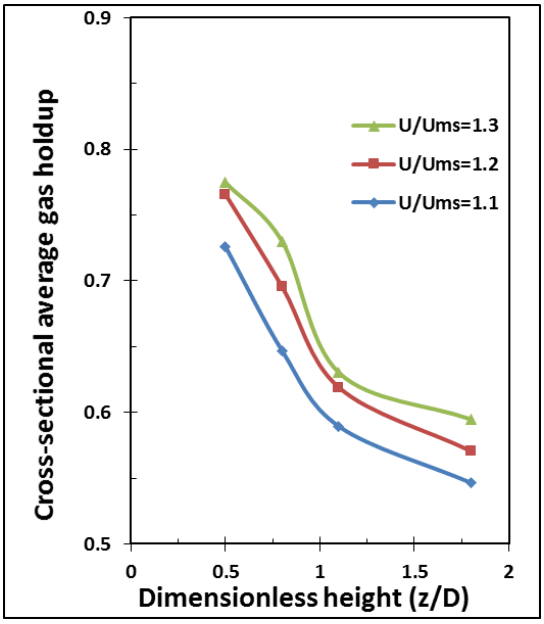

Figure 4.15. Vertical profile of the cross-sectional average gas holdup in the spout region for selected spouted bed system (D_c= 0.152 m, γ= 60°, D_i= 19.5 mm, solids: glass beads, d_p= 2 mm; H_o= 325 mm) at different U/U_{ms} ratios

4.2. INVESTIGATION OF HYDRODYNAMICS OF BINARY SOLIDS MIXTURE SPOUTED BEDS USING RADIOACTIVE PARTICLE TRACKING (RPT) TECHNIQUE

To monitor the trace of both glass and steel solids in the binary mixture, two tracer particles have been prepared and used where each tracer particle is embedded with radioactive material and has size and density similar to those of the tagged solid phase. The tracking experiments of the tracer particles have been carried out separately (one by one) for each mixture composition and applied superficial gas velocity. This means that for one particular experiment, just one particular tracer particle is existing inside the spouted bed of the binary mixture. Hence, since reliability, reproducibility, and ergodicity are inherent in the measurement of the RPT technique, the same postulates will still be taking into account in this work and therefore we conclude that the time-averaged solid flow field obtained from one particular tracking experiment using one particular tracer particle, is equivalent to that might be obtained if both solid phases could be tracked simultaneously. In an ergodic system, a specific time-averaged quantity acquired from an adequately time series data should be equal to the corresponding ensemble mean of that quantity, where sufficient statistics is obtained o reach plateau time-averaged at each location inside the spouted bed in either experiment (Burov et al., 2011). In order to derive conclusions from all the obtained experimental results, we have chosen four levels of heights in the column for the different cases (note that initial bed height is different in each case). For a fair comparison, these levels of heights were normalized as z/H_o (i.e., normalized axial height) where the z refers to the axial distance from the gas distributor of the bed and H_o corresponds to the initial bed height. For all the profiles plotted for each investigated condition, the lowermost level corresponds to the conical-cylindrical conjunction, the second level corresponds to the plane that is in the middle of the cylindrical part of the bed,

the third level corresponds to the plane that is just below the bed surface, and the highest level corresponds to the fountain region. One has to keep this in mind these levels when analyzing the presented profiles.

4.2.1. Solids Flow Filed of Gas-Solid Spouted Beds with Particles of Same Size and Densities. This subsection is devoted for the RPT results obtained for gas-solid spouted beds operated with particles of same size and densities.

4.2.1.1 Mean solids velocity field. In spouted beds, three distinct regions exist a and each one has a specific flow behavior. The solids are carried up by the gas phase in the spout region, which functions as a gas-solid riser until the solids reach the top of the bed surface. Here, the solids are disengaged from the gas phase and are in the fountain region. The solids fall down freely, due to gravity, onto the annulus region. During such solids circulation, the three known regions of spouted beds are created; the spout in the center of the column, the annulus surrounding the spout, and the fountain on the top of the spout-annulus regions. Figure 4.16 illustrates the azimuthally averaged radial profiles of the mean axial velocity of only glass and steel in gas-solid spouted beds with particles of same size and densities measured in each experiment at different z/H_o levels for different U/U_{ms}. The results show the magnitude and pattern of the azimuthally averaged radial profiles of the axial velocity of the particles in each region of the spouted beds. In the spout, the particles move upwards (i.e., $U_z > 0$) with a higher axial velocity near the center zone of the spout, where the particles are carried up by the gas phase. The velocity of the solids decreases radially out from the axis (i.e., center of the spout) toward the spout-annulus interface. This is consistent with the results of solids velocity obtained by the RPT technique (Ali et al., 2017a, b) and of solids holdup obtained by the CT technique (Ali et al., 2016a) where weak

divergence in the solids holdup profile is observed at the spout-annulus interface. When the particles reach the fountain, the axial velocity is at a maximum near the axis but becomes negative (i.e., downward, $U_z < 0$) as particles fall in the outer region of the fountain. The results indicate that the mean axial solids velocity of either glass or steel particles is higher when the z/H_o levels are low, as well as increases along with increasing the U/U_{ms}. In addition, our findings indicated that the solid axial velocity in the spout region reduces with the height of the bed. This is due to insertion of solid from the annulus region to the spout region along the height of the bed. This is in agreement with our gamma-ray computed tomography (CT) technique results (Al-Juwaya et al., 2017; Ali et al., 2016c). Which showed higher solids holdups in the spout region at higher bed levels. More solids to be carried by the gas phase reduces the velocity of the particle where the transferred energy and the imparted momentum on the particles are dissipated to more particles at the upper levels compared to the lower levels of the spout region. The particles velocity in the spout region should be higher than that in the fountain region since the fountain region is a disengagement region between the solids particles and the up flow of the gas phase. The mass velocity of the gas is lower in the fountain region as compared to the spout region due to the larger cross-sectional area of the fountain region. Hence, the momentum that is imparted on the particles is lower in the fountain region making the particles velocity lower in the fountain region as compared to those in the spout region, which facilitate the disengagement of the particles from the gas phase, and hence they fall down back to the annulus region. The profiles show that for glass particles of lower density the mean axial velocity is higher compared to that of higher density steel particles at same U/U_{ms} and all levels. The disparity is as a result of the level of inertia which affects the particle motion

in each region of the beds. The motion of the steel particle is restricted more than that of the glass particles, due to the higher density and inertia of the steel particles. In another word, the glass particles dragged easier than the steel particles through the gas phase.

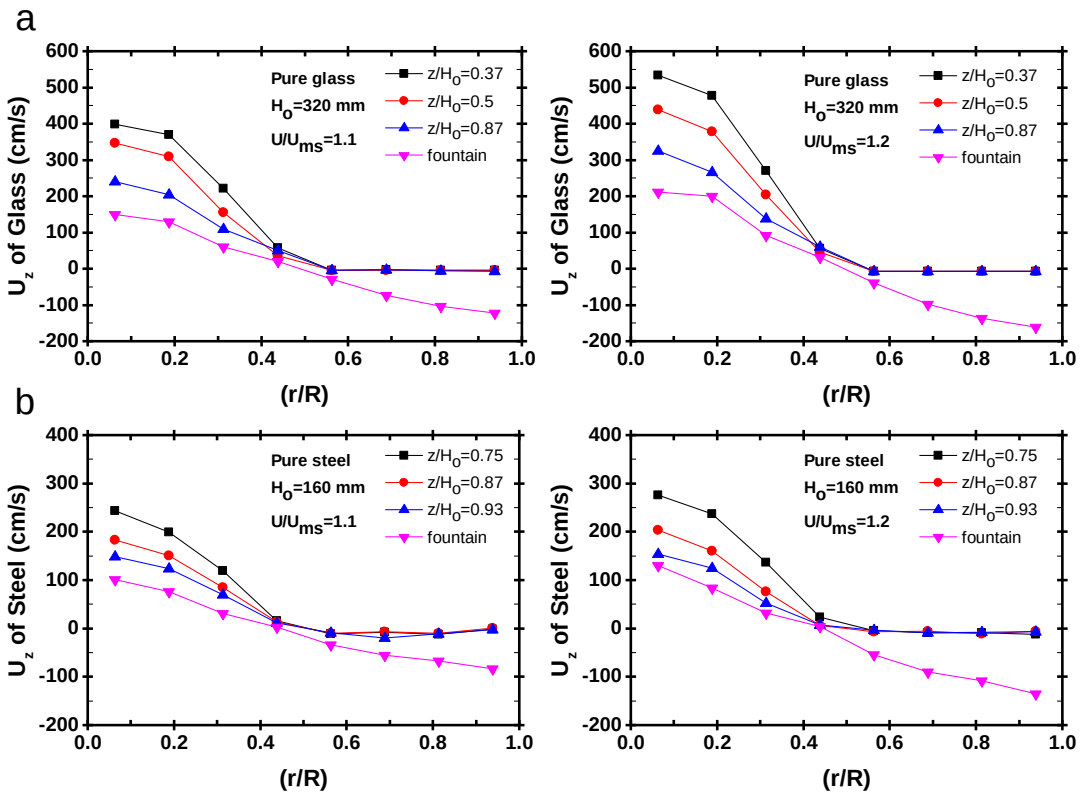

Figure 4.16. Azimuthally averaged radial profiles of the Axial mean solids velocity fields of (a) glass and (b) steel particles in gas-solid spouted beds with particles of same size and densities at different levels for different U/U_{ms}.

Figure 4.17 shows the azimuthally averaged radial profiles of the mean radial velocity of glass and steel in gas-solid spouted beds with particles of same size and densities at different z/H_o levels for different U/U_{ms}. The negative and positive value of the solid radial velocity refers to the inward and outward motion of the solids, correspondingly.

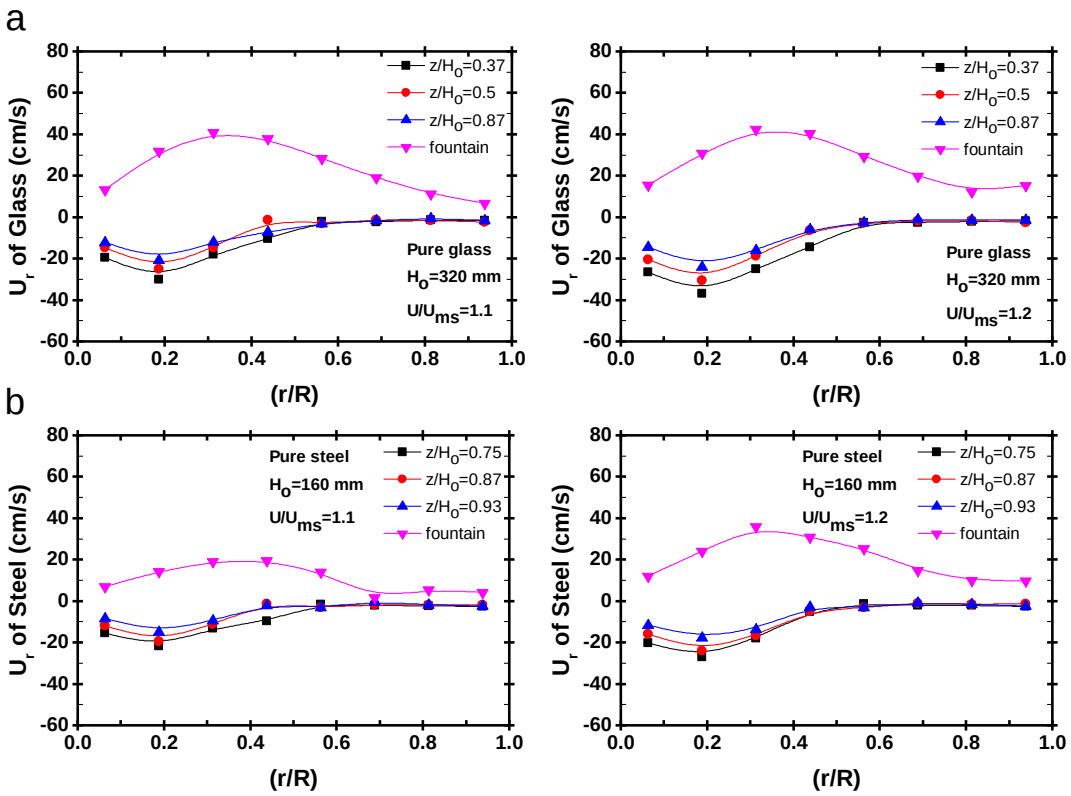

Figure 4.17. Azimuthally averaged radial profiles of the Radial mean solids velocity fields of (a) glass and (b) steel particles in gas-solid spouted beds with particles of same size and densities at different levels for different U/U_{ms}.

Results concerning the radial profiles of the mean azimuthal particle velocity are of the order of magnitude of the radial results components or less and not shown here. In the spout region, the particles are mostly moved towards the axis of the spout (i.e., inward, $U_r < 0$) with higher intensities at the conical base. The radial velocity after that decreases gradually with increasing the bed height and becomes positive (i.e., outward, $U_r > 0$) in the fountain region. However, a large radial dispersion is observed in the fountain which depicts the behavior of such region.

In general, for all U/U_{ms}, the time-averaged radial solids velocities are small in comparison with the corresponding time-averaged axial velocities, which is expected as a result of the absence of net solids motion (time-averaged) in the radial direction of the bed. This, however, does not mean that the fluctuations in the radial direction are also negligible. This can be seen in the radial RMS velocities that are comparable to those in the axial direction especially in the fountain region, as discussed in the following section. When the U/U_{ms} is increased, the convection of the particles inwards to the axis of the spout region, and outworlds the core of the fountain is increased. In comparison to the mean axial solids velocity data, there is a lack of the measurements of the mean radial solids velocity in the literature of spouted beds. This lack is crucial, especially for the evaluation of the CFD models because, even the radial velocity intensities are not even close to the mean axial solids velocity, the term $(\partial \varepsilon_s U_r/\partial_r + \varepsilon_s U_r/r)$ is the corresponding balance of the gradient term $(\partial \varepsilon_s U_z/\partial_z)$ in the continuity equation that is employed in the two-fluid modeling approaches for the spout (Djeridane et al., 1998; Huilin et al., 2004; Krzywanski et al., 1992).

4.2.1.2 Root mean square (rms) solids velocity. Figure 4.18, Figure 4.19, and Figure 4.20, respectively, illustrate the azimuthally averaged radial profiles of the axial (U_{z_RMS}), radial (U_{r_RMS}), and azimuthal (U_{θ_RMS}) RMS solids velocity for glass and steel particle in gas-solid spouted beds with particles of same size and densities at different z/H_o levels for different U/U_{ms}. The results show the pattern and magnitude of the three components of the RMS velocities for the glass and steel in each region of the spouted beds. The results show that the fluctuation movements of the particles that are to some extent in charge for the local mixing of the solids are mainly controlled in the axial

component of the fluctuation movements. In the spout, the magnitude of the axial RMS velocity is much larger than in the other regions.

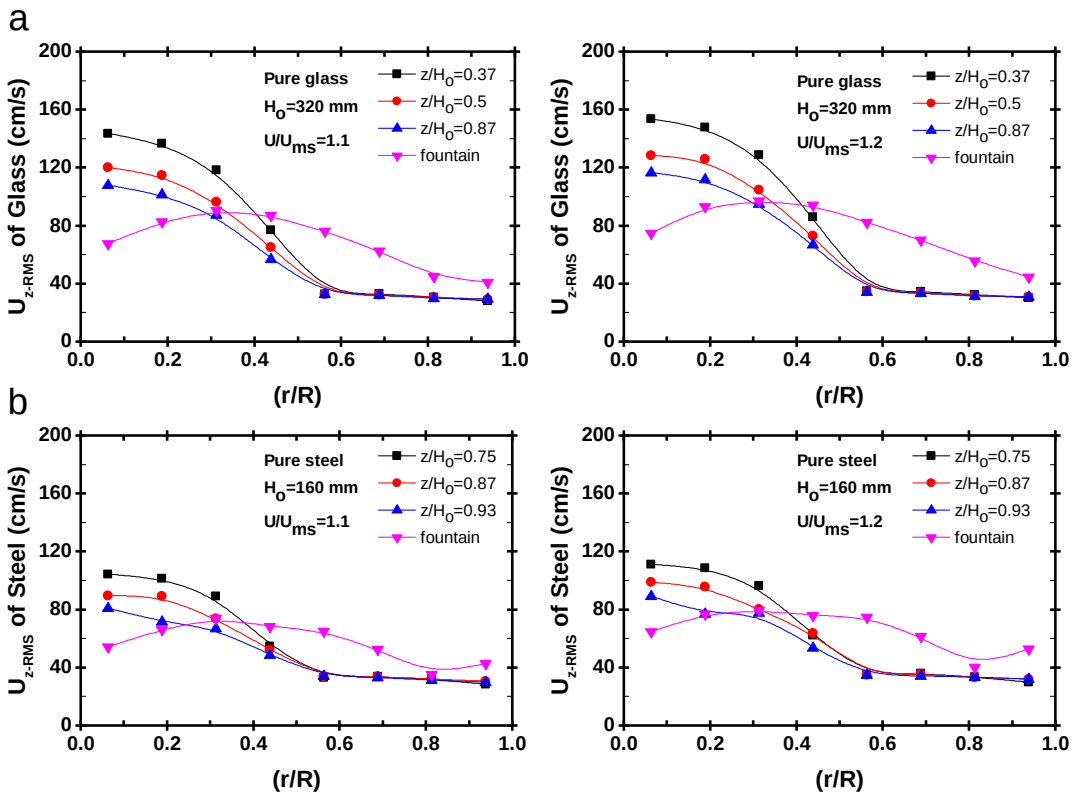

Figure 4.18. Azimuthally averaged radial profiles of the Axial RMS velocity fields of (a) glass and (b) steel particles in gas-solid spouted bed of solids of similar density and size at different levels for different U/U_{ms}.

The fluctuation velocity of the particle is high wherever there is a great deal of motion of particles. The maximum value is detected at the center zone of the spout region. This is because the axial particle velocities and its fluctuations velocities are also maximal in the central zone of the spout. Since the particle velocities and its fluctuations velocities

in the spout reduce radially outwards to the annulus region, the same trends are found for the U_{z_RMS} and U_{r_RMS}.

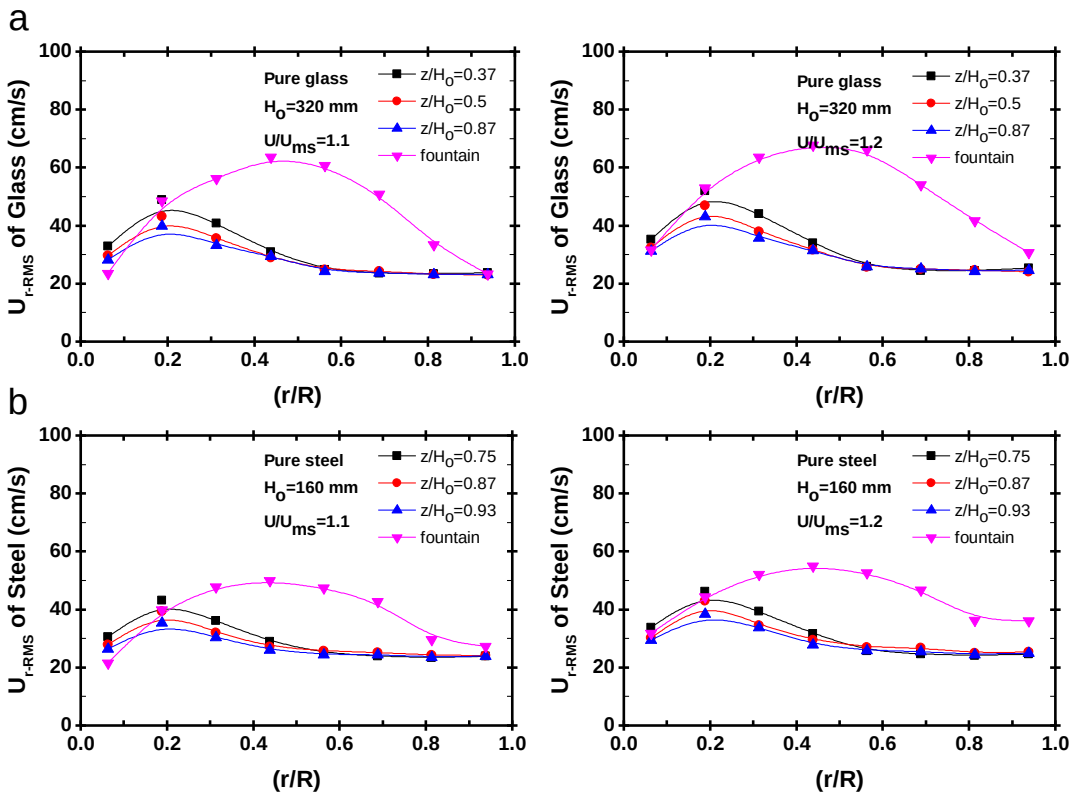

Figure 4.19. Azimuthally averaged radial profiles of the Radial RMS velocity fields of (a) glass and (b) steel particles in gas-solid spouted beds with particles of same size and densities at different levels for different U/U_{ms}.

Even when the annulus appears as a downward flow, the radial profiles of U_{z_RMS} and U_{r_RMS} demonstrate that the fluctuation velocities in the annulus are not necessarily negligible. However, the profiles of the axial and radial components reveal that turbulence is fairly homogeneous on the annulus. When approaching the fountain, the U_{z_RMS}, the

U_{r_RMS}, and the U_{θ_RMS} are increased due to the absence of the confinement effect of the annulus region.

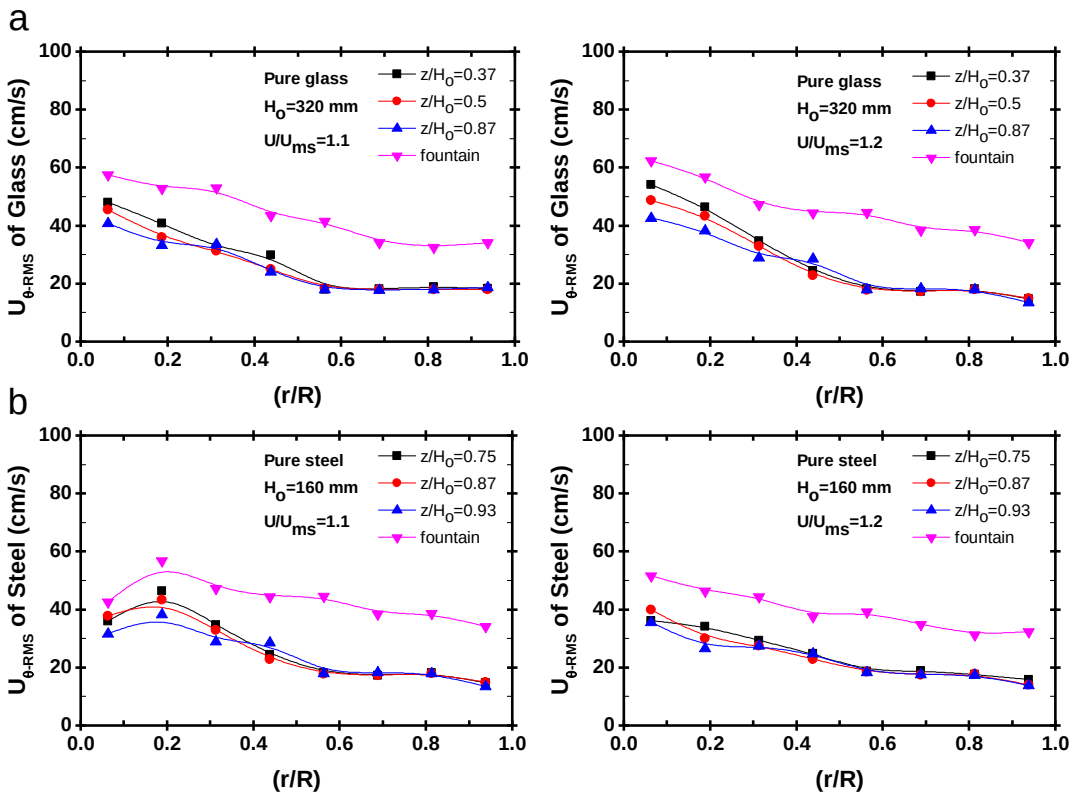

Figure 4.20. Azimuthally averaged radial profiles of the Azimuthal RMS velocity fields of (a) glass and (b) steel particles in gas-solid spouted beds with particles of same size and densities at different levels for different U/U_{ms}.

The profiles also demonstrate that turbulent movement of the solids particles is largely developed between the two components the axial and the radial the fluctuations velocity. It is must be noted that the fluctuations movements in the spout, annulus, and annulus are of varying sources. In the spout and the fountain regions (both of them are

dilute regions), the fluctuations movements originate from the turbulence of the gas phase and the particle-particle interaction, but in the annulus (dense region) they are mainly related to the gas holdup in the annulus and particle-particle shear forces. When the profiles of the two materials are compared, the U_{z_RMS} and U_{r_RMS} velocities of glass are higher than those of steel. This indicates that at same superficial gas velocity and U/U_{ms} but different initial bed height, the fluctuation components of the glass particles are higher in comparison with the steel particles due to lower inertia or density.

Unlike the U_{z_RMS}, the U_{r_RMS} and U_{θ_RMS} both for glass and steel do not show much sensitivity in the spout with the increase in U/U_{ms}. The reason being the net motion of solids is through the z-direction of the bed. Therefore, the increment in the U/U_{ms} does not largely affect the solids movements in r and θ-directions, at least in the range of velocities investigated. Also, for the same U/U_{ms}, values of U_{θ_RMS} do not vary much with the axial position along the spout, and these values are lower than those of the U_{z_RMS}, and U_{r_RMS} both for glass and steel. This is to be expected as the net motion is in *z*-direction, therefore, the fluctuation is also higher in the same direction. It is also found that the profile of U_{θ_RMS} indicates slightly higher values at the fountain both for glass and steel. This can be explained by the spiral movement of the particles as they pass through the spout, and rotate in the fountain.

4.2.1.3 Turbulent stresses and kinetic energy. As mentioned earlier, the solids turbulent parameters (normal stress, shear stress, and turbulent kinetic energy) in gas-solid spouted beds can be evaluated using the RPT technique. The time-averaged of these quantities were calculated from the solids fluctuation velocities that were derived through the subtraction of the instantaneous solids velocities from the time-averaged solids

velocities. Figure 4.21, Figure 4.22, and Figure 4.23, respectively, illustrate the azimuthally averaged radial profiles of the axial (τ_{zz}), radial (τ_{rr}), and azimuthal ($\tau_{\theta\theta}$) normal stresses for glass and steel in gas-solid spouted beds with particles of same size and densities at different z/H_o levels for different U/U_{ms}. The results show the pattern and magnitude of the three components normal stresses for the glass and steel in each region of the spouted beds. As can be seen in the figures, the turbulent movement of the particles is mainly controlled in the axial component of the normal stresses.

In the spout, the magnitude of τ_{zz} is much larger than in the other regions. The maximum value is detected near the axis of the spout region. This is because the axial particle velocities and the related fluctuation velocities are also maximal in the central zone of the spout. The τ_{zz} of both glass and steel are higher at lower levels in the spout as a result of the variation in the shear rate imparted from the gas phase and the particle collision and decreases with increasing z/H_o levels. However, when compare the values of the τ_{zz} of both materials, it can be seen that the steel particles give a lower τ_{zz}, while the glass particles have a higher τ_{zz}. This is in line with the RMS velocity fluctuation profiles where the axial RMS values of the glass are found higher than those of the steel. The heavier particle and the lighter particles have unequal fluctuating intensity or normal stresses. However, at the annulus region, due to the nature of the flow structure in this region, the magnitudes of τ_{zz} are much lower than those of the spout region and are the difference is low between the two materials. This is also due to the velocities of solids and the fact that their fluctuations are small in this region.

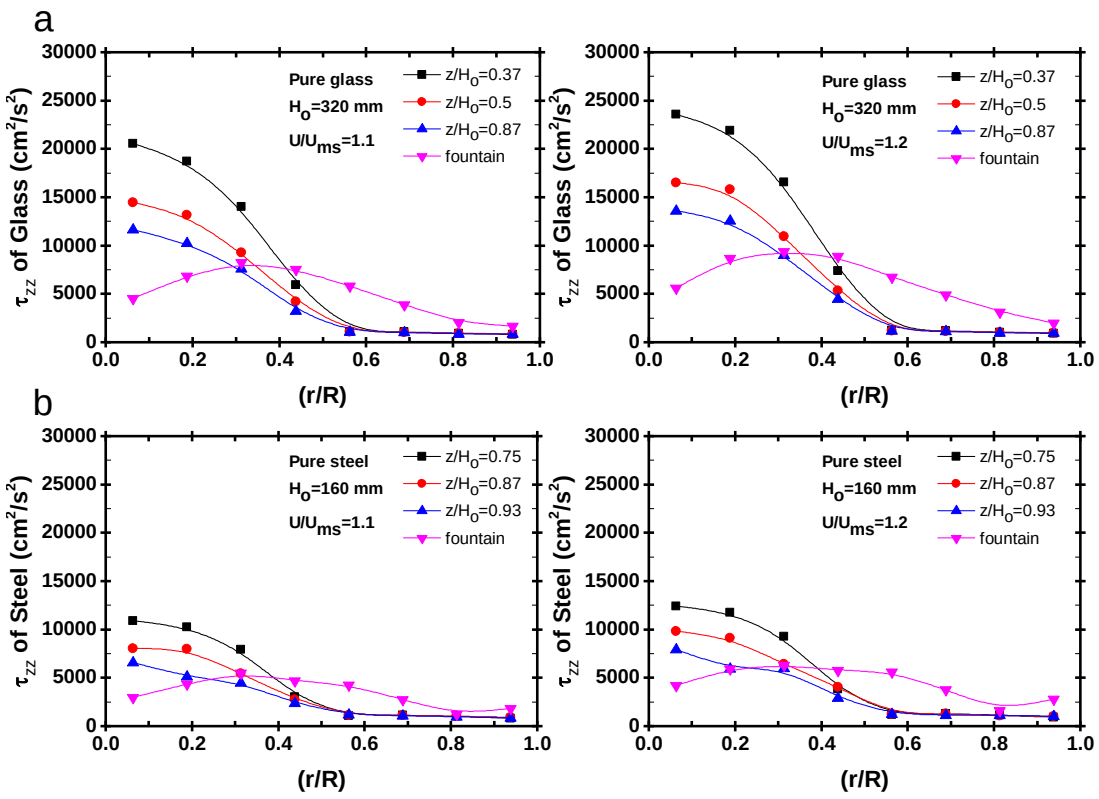

Figure 4.21. Azimuthally averaged radial profiles of the Axial normal stress (τ_{zz}) of (a) glass and (b) steel particles in gas-solid spouted beds with particles of same size and densities at different levels for different U/U_{ms}.

At the fountain region, the τ_{zz} values are smaller near the bed axis and they increase towards a maximum at the zone of about r/R=0.4; and then they decrease towards the bed wall. This trend indicates that the axial particle velocity fluctuations in the core of the fountain are smaller, despite the fact that particle velocities at the core of the fountain are larger. At the zone of about r/R=0.4 as shown in Figure 4.16 the axial particle velocities invert from positive (upward) to negative (downward) values. Therefore, the fluctuations of the axial velocities are larger in this zone of the bed. These fluctuations decrease towards the wall of the bed and hence, τ_{zz} decreases. The same trend is found for the two materials.

When compare the profiles of the τ_{zz} of both particles in the fountain, the results show that the axial normal stress of glass is higher than that of steel in the fountain region. This means glass particles have faced more turbulent movements and deflections in the fountain than steel particles. One should keep in mind differences on initial conditions between the two materials beds when analyzing the results.

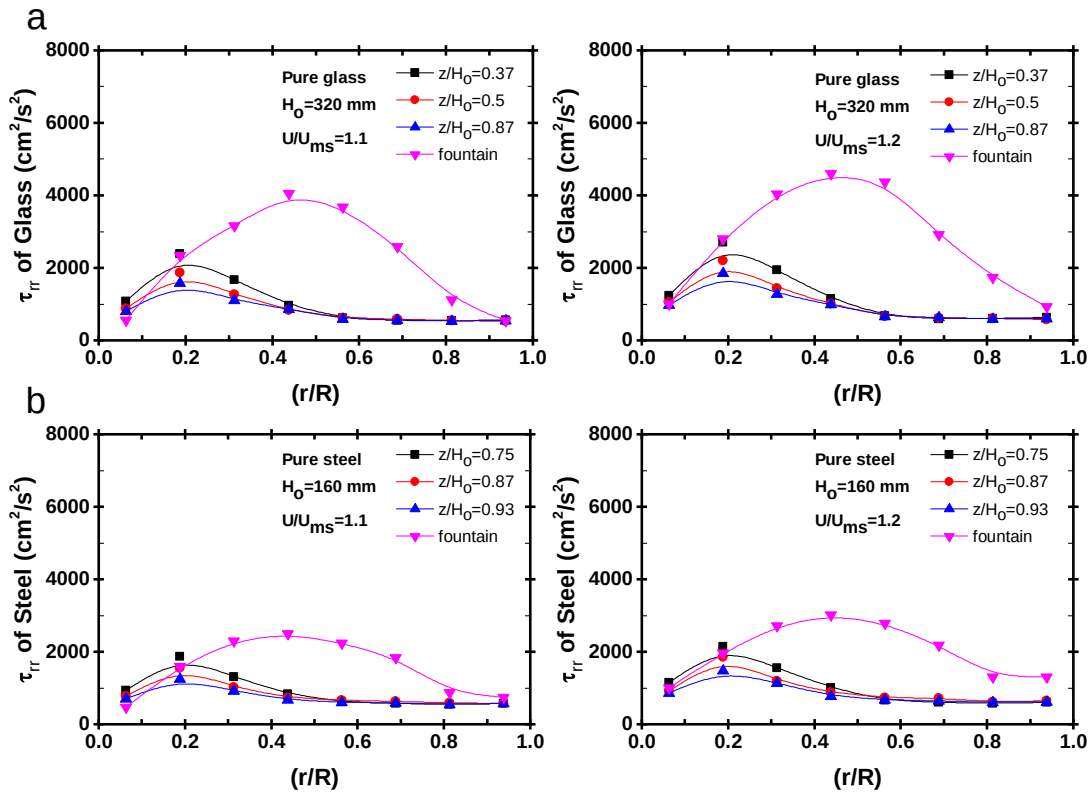

Figure 4.22. Azimuthally averaged radial profiles of the Radial normal stress (τ_{rr}) of (a) glass and (b) steel particles in gas-solid spouted beds with particles of same size and densities at different levels for different U/U_{ms}.

In the annulus, it can be seen that the glass and steel particles share the same pattern of the τ_{zz} in the annulus region, while in the spout and the fountain regions the pattern of

the τ_{zz}, and τ_{rr} of the two materials is different. However, the magnitudes of τ_{rr} are much smaller than those of τ_{zz} in the three regions of the spouted beds. In the spout and annulus regions, the τ_{rr} values are comparable to those of τ_{zz} in the annulus region. This is mainly because of the gradient in the axial solids velocity.

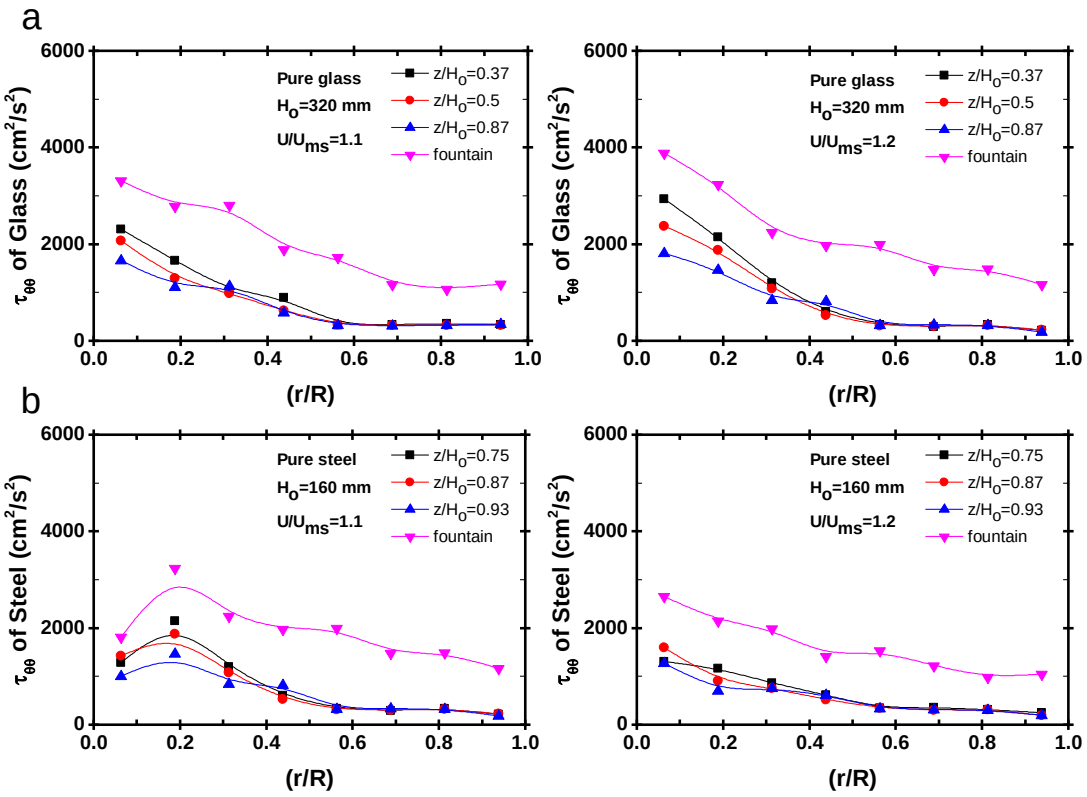

Figure 4.23. Azimuthally averaged radial profiles of the Azimuthal normal stress ($\tau_{\theta\theta}$) of (a) glass and (b) steel particles in gas-solid spouted bed of solids of similar density and size at different levels for different U/U_{ms}.

More so, both the azimuthal and axial solids velocities are small and, therefore, their gradients are as well small. However, in the fountain region, due to the flow structure of the fountain and the freely falling particles, non-negligible particle radial velocities and

their fluctuations exist. Hence, the magnitudes of τ_{rr} are much larger than those in the spout and annulus regions. When compare the values of the τ_{rr} of both particles, the results show that the radial normal stress of glass is higher than that of steel in the fountain region.

Figure 4.24 the azimuthally averaged radial profiles of the Shear stress for both glass and steel particles in gas-solid spouted beds with particles of same size and densities at different levels for different U/U_{ms}. Only the profiles of the shear stress (τ_{rz}) component are presented in this section. The other components of shear stresses, $\tau_{z\theta}$, and $\tau_{r\theta}$, represent the same comparison and therefore they are not reported here. In the spout region, τ_{rz} radial profiles show maxima at the zone between the center of the spout and the spout-annulus interface (~r/R=0.2). This trend reflects the magnitude of the fluctuations in the axial and radial components of the velocities; their multiplication gives the maximum value at ~r/R=0.2. At about the spout-annulus interface, the τ_{rz} values are negative from about r/R=0.35 to about r/R=0.6. In the annulus region, the values of τ_{rz} are small compared to those of the spout region due to the nature of the annulus's flow structure. In the fountain region, however, the maximum value occurs in the zone of about r/R=0.7. Furthermore, particle-particle interaction causes the fluctuations in the particles velocity in the spout and the fountain regions however such interaction is not predominant than the interaction between the fluid and the particles. Therefore, mentioning that the high-velocity fluctuation and high mean velocities are the reasons is like mentioning that the stresses are induced by the gas turbulence and the particle-particle interactions. As mentioned earlier, the fluctuations movements in the spout, annulus, and annulus are of varying sources. In the spout and the fountain regions, the fluctuations movements originate from the turbulence

of the gas phase and the particle-particle interaction, but in the annulus, they are mainly related to the gas holdup in the annulus and particle-particle shear forces.

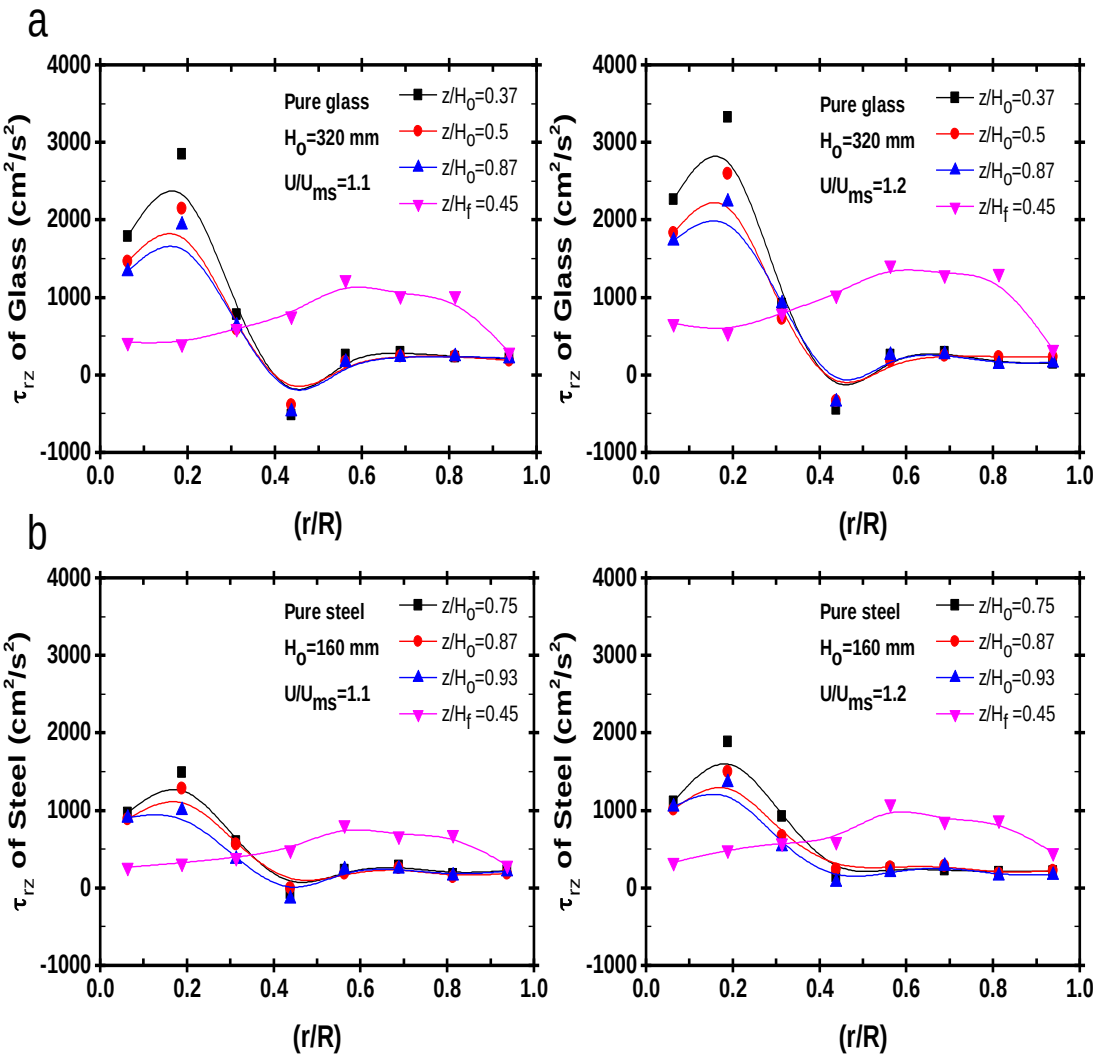

Figure 4.24. Azimuthally averaged radial profiles of the Shear stress (τ_{rz}) of (a) glass and (b) steel particles in gas-solid spouted beds with particles of same size and densities at different levels for different U/U_{ms}.

Therefore, fluctuating movement exist at the spout-annulus interface and in the annulus but cannot be higher than that obtained in the spout. In another word, the contribution of the axial component of particle velocity is very high on the fluctuation intensity of the particle. However, in the fountain region due to the reduction in the mass velocity of the gas phase and hence the momentum imparted on the particles because of the larger cross-sectional area for the gas to flow makes the velocity of the particle lower as compared to the spout region. Also due to the disengagement of the particles and the gas in this region, the particles change the direction of the flow from upward to downward forward the annulus region. These make the nature of the particles fluctuation different from that in the spout region, which make the stress profiles, and magnitude in the fountain region different from those in the spout region. When comparing the profiles of the τ_{rz} of glass and steel particles, the results show that the τ_{rz} of glass is higher than that of steel in the fountain region.

Figure 4.25 demonstrates the azimuthally averaged radial profiles of the turbulent kinetic energy (TKE) of glass and steel in gas-solid spouted beds with particles of same size and densities at different levels for different U/U_{ms} ratio. The turbulent kinetic energies of the particles are larger in the center zone of the spout region for the particles and reduce as the spout-annulus interface is approached. This trend is similar to the trend of the τ_{zz} whose values are significant compared to τ_{rr}. When comparing the values of the turbulent kinetic energies of both materials, it can be seen that the steel particles give a lower TKE, while the glass particles have a higher TKE. This is in line with the RMS velocity fluctuation profiles where the axial RMS values of the glass are found higher than those of the steel.

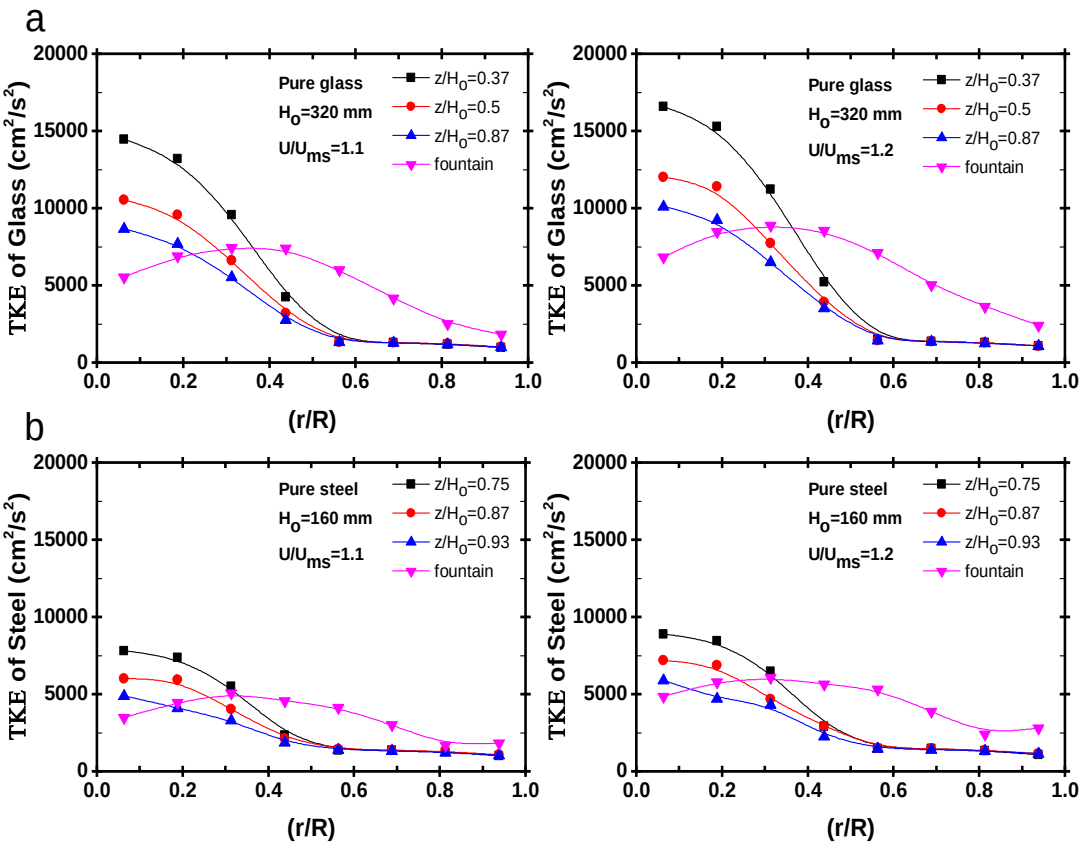

Figure 4.25. Azimuthally averaged radial profiles of the turbulent kinetic energy (TKE) of (a) glass and (b) steel particles in gas-solid spouted beds with particles of same size and densities at different levels for different U/U_{ms}.

At the annulus region, the turbulent kinetic energy levels off and the magnitudes are similar for the two materials. In the fountain region, the turbulent kinetic energy magnitudes are comparable to those of the spout region's central zone; the maximum value exists at the region between about r/R=0.4 to r/R=0.5. This is similar to the trends for τ_{zz} and τ_{rr}, whose values are dominating the estimated values of turbulent kinetic energy. The radial profile values of the turbulent kinetic energies for glass (lighter particle), noticeably differ from those of steel. The glass particles have higher turbulent kinetic energy than steel particles.

4.2.2. Investigation of the Solids Hydrodynamics of Binary Mixture in A Gas-Solid Spouted Bed with Particles of Same Size but Different Densities. In the following the results of the solids hydrodynamics of binary mixture spouted beds consisting of 50% by volume glass particles and 50% by volume steel particles (Table 3.4) are discussed. For each tracking experiment of the RPT technique, the appropriate tracer particle is employed to track the corresponding solid phase of the binary mixture. In this study, tracer particle positions and transition between adjacent regions of the bed were analyzed to calculate the following key solids flow parameters in a binary mixture of solids spouted beds at different U/U_{ms} in addition to the solids flow field in terms of solids velocity and turbulent parameters:

- Cumulative probability distribution of the solids particles penetration into the spout (***P***): this distribution illustrates, for each $z - coordinate$ along the spout height, the probability of the solids particles being entrained into spout from the annulus at a height below or equal to the corresponding $z - coordinate$.
- Cumulative probability of the landing position of the solid particles at the annulus surface: this distribution illustrates, for each $r - coordinate$ at the bed surface, the probability of the solids particles being entrained into the annulus from the fountain at a radial position, from the boundary of the spout region, equal or less than the corresponding $r - coordinate$.
- Cumulative probability of the penetration of the solid particles into the base of the fountain region: this distribution illustrates, for each $r - coordinate$ at the spout region ends (i.e. z = H), the probability of the solids particles being

entrained into fountain from the spout at a radial position, from the spout axis, equal or less than the corresponding $r - coordinate$.

The cumulative probability distributions of the solids are discussed first. The solids velocity fields and turbulent parameters are shown later. Symbiotic and comparative analysis of the results is used to understand the segregation and hydrodynamics of the solids in binary spouted beds with particles of the same size but different densities at different U/U_{ms}.

4.2.2.1 The probability of solids transition between adjacent regions of the bed. Figure 4.26 shows the cumulative distributions for both glass and steel at U/U_{ms} = 1.1. The value of U/U_{ms} corresponds to an underdeveloped fountain. The behavior of the fountain is important as explained by (McNab, 1972). (McNab, 1972) stated that a fountain is described as underdeveloped, developed, or overdeveloped, depending whether it covers only part of the bed surface, covers all the bed surface, or hit the column wall, respectively. (Kutluoglu et al., 1983) reported a relation between the radial position of particles at the fountain-entry and the height achieved by the particles in the fountain region, regardless the scatter caused by collisions of the particles. (Kutluoglu et al., 1983) reported that when particles originate at the fountain-entry from a position near the axis of the spout, they are more likely to approach the maximum of the height of the fountain. The appropriate distance coordinate in the figures is radial for landing position on the annulus surface, radial for the radial position of particles at the fountain-entry, and vertical for the penetration of the particles from the annulus into the spout region. For convenience, each coordinate was normalized by the corresponding maximum value of the region of interest. First observation can be withdrawn from the results (Figure 4.26 (b)) is that that both glass and

steel distributions are found all the way along the bed height, even when the fountain is at underdeveloped state (U/U_{ms}= 1.1). This means in this case bed never achieves complete segregation. The axial distribution of the binary solids particles along the spout region is a key characteristic of the gas-solid spouted beds and demonstrate a main difference from binary gas-solid fluidized beds. Since in binary fluidized bed, segregation usually take place with heavier or larger particles defluidized in the lower levels of the bed, while the less dens or smaller particles accumulated in the higher levels of the bed (Huilin et al., 2007). However, as can be seen in Figure 4.26, the heavier steel particles, have a tendency to land from the fountain region at the inner region of the annulus surface (Figure 4.26 (a)) and then to enter the spout region at higher levels of the annulus (Figure 4.26 (b)), and then to enter the fountain region from a position near to the spout-annulus interface (Figure 4.26 (c)). These observations are in line with conclusions made by (Cook and Bridgwater, 1978; Kutluoglu et al., 1983; Piccinini et al., 1977; Ren et al., 2012; Robinson and Waldie, 1978). The differences on the penetration behavior of glass and steel particles from one region to another indicates that segregation to a certain extent is present in this case. This extent of segregation can be unveiled when a closer look is paid at the distribution of the particles entry levels into the spout presented in Figure 4.26 (c). As can be seen in Figure 4.26 (c), the particles enters levels into the spout is characterized by two regions one after the other from top to bottom; the cylindrical and conical region. Furthermore, a point sink is observed in the conical part of the bed for the penetrating of the solids into the spout, as reported by (Benkrid and Caram, 1989) found in the range between 4 and 5 mm above the gas distributor (z/H=0.15-0.2). The profiles revealed higher probability for the glass than the steel to enter the spout from the conical region, and the reverse is true for the cylindrical

region. The glass had 31.8% probability higher than the steel to enter the spout from the conical region. Note that the probability distributions of glass and steel is independent of each other. However, when a single population is produced form both particles data combined together, 59.53% of the solids were found to enter the spout from the conical section of the bed. This value is not too far from the 61% value obtained from RPT measurements in a spouted bed dimensions (i.e. geometrical dimensions) similar to the one here by (Roy et al., 1994), and the 67 % value acquired through wall measurements in half column spouted beds by (Thorley et al., 1959). The depths of the beds in the aforementioned studies are relatively larger than the one employed in the current experiments. Hence, the contribution of the glass to the solids entering the spout from the conical region is higher from begin equal to that of steel or vice versa. Should the probability value of glass or steel be close from the 59.53% value, segregation is countered, at least form from the particle entry level factor. In the spout region, particle segregation takes place due to differences in the particle vertical velocities of solid phases, which will be proved later when discussing the solids velocity field results. Therefore, particle segregation in the spout could be encountered by a desegregation tendency to take place in the annulus region. On the other hand, the fountain is found to play an essential part in the mixing process of the bed, and work as a distributor by transporting the particles from the spout region to the annulus and hence sustain the entire circulation of the particles inside the bed. The glass particles have a tendency to reach higher axial levels in the fountain region, and hence end up landing at a radial position not close to the boundary of the spout.

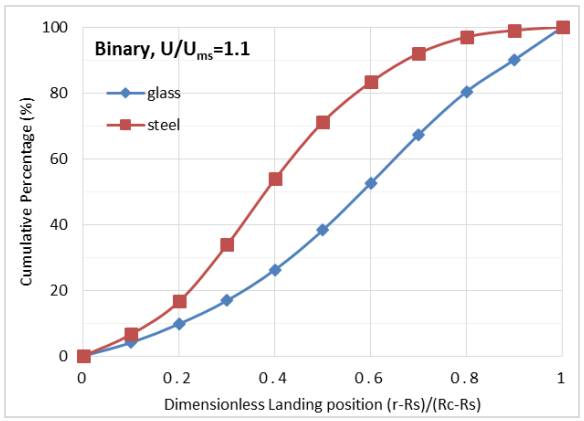

(a)

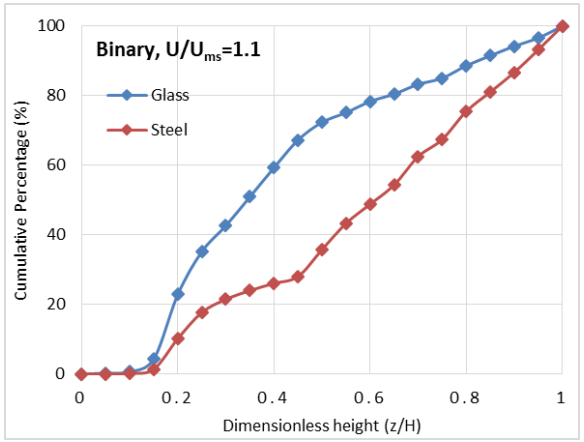

(b)

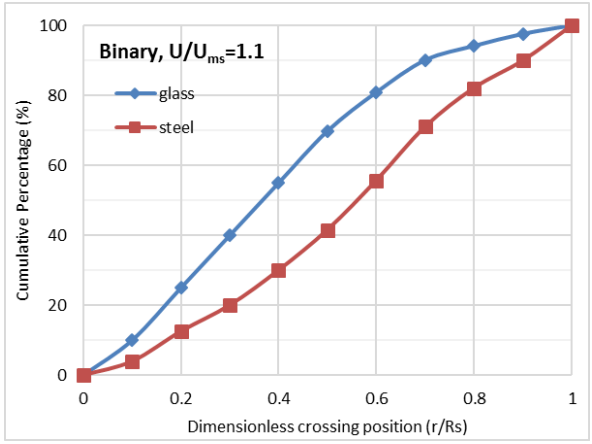

(c)

Figure 4.26. Distribution of cumulative probability of particles transitions between the adjacent regions of the bed in gas-solid spouted bed with particles of same size but different densities at U/U_{ms} =1.1. (a) landing position of the solid particles at the annulus surface; (b) solids particles penetration into the spout from the annulus; (c) Entering position of the solid particles into the base of the fountain region at z = H.

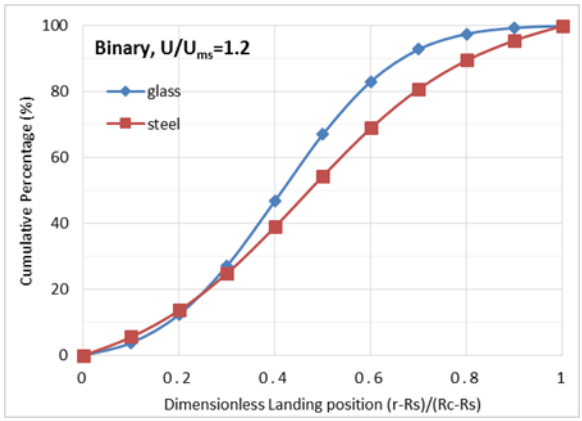

(a)

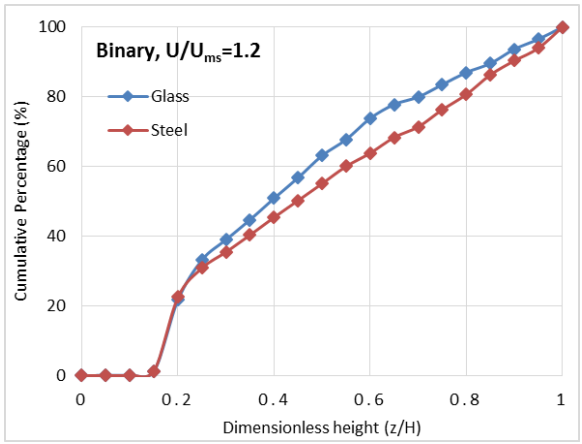

(b)

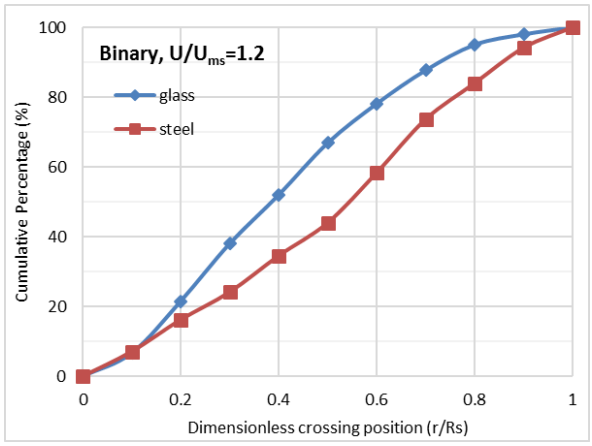

(c)

Figure 4.27. Distribution of cumulative probability of particles transitions between the adjacent regions of the bed in gas-solid spouted bed with particles of same size but different densities at U/U_{ms} =1.2. (a) landing position of the solid particles at the annulus surface; (b) solids particles penetration into the spout from the annulus; (c) Entering position of the solid particles into the base of the fountain region at z = H.

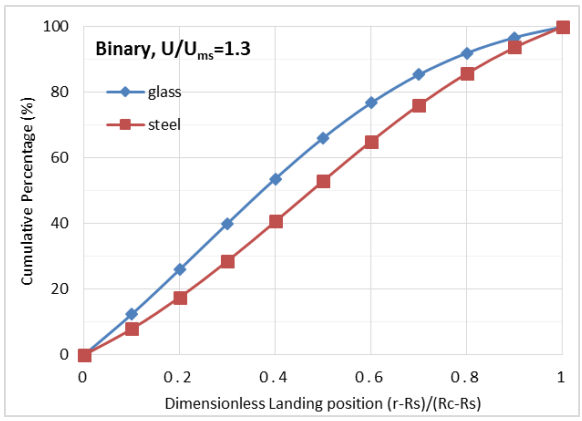

(a)

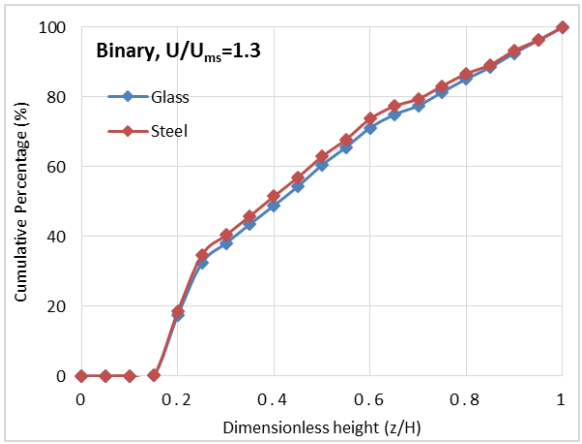

(b)

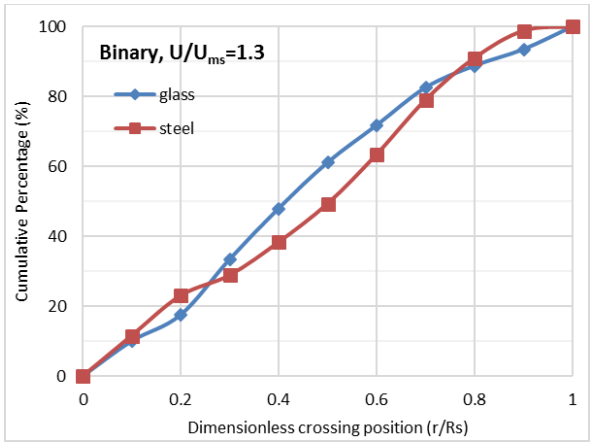

(c)

Figure 4.28. Distribution of cumulative probability of particles transitions between the adjacent regions of the bed in gas-solid spouted bed with particles of same size but different densities at U/U_{ms} =1.3. (a) landing position of the solid particles at the annulus surface; (b) solids particles penetration into the spout from the annulus; (c) Entering position of the solid particles into the base of the fountain region at z = H.

On the other hand, the steel particles are found to elevate lower levels than the glass particle in the fountain region, and hence arrive at a position close the boundary of the spout and congregating in the inner part of the annulus region. The likely explanation why this happens stems from two main reasons. Foremost, particles of dissimilar density are subject to have dissimilar kinetic energy and trajectories in the spout region, in the spout-fountain entry, and in the fountain region and therefore land at varying positions on the annulus surface. Further, even if we assume the particles of dissimilar densities arrive at the same position on the annulus surface, they can have varying trajectories and time of passage in the annulus region. For a developed fountain, the distribution of the cumulative probability for the glass and steel penetrations at U/U_{ms} =1.2 are shown in Figure 4.27. As shown in the profiles, the radial and vertical distributions appear to be influenced by U/U_{ms} for each of the boundaries. It can be seen that steel had more probability in Figure 4.27 (a) to land at a distance further from the spout than what observed in Figure 4.26 (a) and the reverse is true for glass particles. This is an indication of desegregation to take place in the annulus region and contributes to the key role of the fountain in determining particle segregation when multiple solids present. However, the relation between the fountain-entry radial position and position where the solid is landed shown in Figure 4.26 seems to disappeared in Figure 4.27. For the particle entry levels into the spout, it can be seen that the glass almost had a probability equal to that of the steel to enter the spout from the conical region, and the same is true for the cylindrical region. For a single population of the solids, we found that 63.78% of the solids enter the spout from the conical region at U/U_{ms}=1.2, higher from what found at U/U_{ms}=1.1. However, the probability for glass and steel individually is 67.77% and 60.06%, respectively. These probabilities are just about

3% difference from the 63.78%. This finding demonstrates that segregation is countered in the annulus and hence reduce segregation in the spout when the U/U_{ms} increases. Hence, segregation is countered. The same finding is obtained in Figure 4.28 (b) for U/U_{ms}=1.3 where the accumulative probability of glass and steel almost the same. The probability for glass and steel individually is 65.64% and 67.87%, respectively, and is 1% different when a single population is produced from the data of the two solids phases.

4.2.2.2 Mean solids velocity field. Figure 4.29, and Figure 4.30, respectively illustrate the azimuthally averaged radial profiles of the axial, and radial solids velocity for the binary solids mixture in a gas-solid spouted bed with particles of same size but different densities at different z/H_o levels for different U/U_{ms}. For each solid material, the matching tracer particle has been employed in the RPT experiment. As can be seen from the figures, each particle whether glass or steel in the binary case is having similar flow behavior to that obtained in spouted beds with particles of same size and densities. The particles maintained the same flow pattern of that in same size and densities system. The particles flow upward with a high velocity in the spout while traveling with low velocity and downward in the annulus. When the particles reach the fountain, the axial velocity is at a maximum near the axis but becomes negative (i.e., downward, $U_z < 0$) as particles fall in the outer region of the fountain. The results indicate that at the lower levels of the spout, both for glass and steel mean axial velocity is high and at higher levels the axial velocity for both the solids decreases. However, the profiles show that the mean axial velocities of similar size steel (density 7400 kg/m^3) particles are lower than the mean axial velocities of similar size glass (density 2600 kg/m^3) particles. This dissimilarity in the axial particle velocities is unsurprising because of the large difference in the solid density between the

two materials (~ 3 times). In spouted beds of binary solids mixture, the ascending gas flow impart energy (momentum) on the particles of different densities, and therefore resulting in different drag forces exerted on the different solid phases and different particle velocities. Consequently, the dissimilarity in axial solids velocities of glass and steel particles in the spout is in agreement with what has been reported that particles segregation takes place in the spout region (Cook and Bridgwater, 1978; Du et al., 2016; Ishikura et al., 1983; Kutluoglu et al., 1983; Piccinini, 1980; Piccinini et al., 1977; Ren et al., 2012). Segregation in binary spouted beds occurs for the most part as a result of the deviation in the particle velocities of the different phases (Ishikura et al., 1983). However, when comparing the profiles of binary solids spouted bed system with those of only one type of solids spouted bed system at similar U/U_{ms}, it is found that the magnitudes of the particles velocity in binary system are larger in case of steel particles and the opposite is true for the glass particles. This could be due to an increase in particle collisions by particle-particle interaction in the binary system making glass particles to transfer part of their kinetic energy to steel particles. This indicate the fact that in gas-solid-solid spouted beds, particle-particle interaction takes on an important role however it is not necessarily dominating over the fluid-particle interaction. The collisions between the particles contributed to reduce the difference in the axial solid velocity between glass and steel particles but not reverse that difference between them, glass particles remained with higher velocity. One also should keep in mind that though the volume fraction of both the solids is same in the present case (50% glass 50% steel) when the bed is considered as a whole, the total number glass particles in the bed are close to those of steel. Since the spout is the more dilute region with a low volume fraction of solids (holdup) (both glass and steel in volume fraction terms and

number terms), the imparted momentum or kinetic energy between solids is not high. It emphasizes the fact that in binary spouted bed, particle-particle interactions play a role but however they are not-dominating over the fluid-particle interaction. Within the annulus, the axial velocities of glass and steel particles are small and negative, where the particles flow downward as in loosely moving packed bed. The results show that the particle vertical velocities in the annulus are quite similar for the two particle phases and are very close to those obtained in systems with particles of same size and densities. This similar behavior between the two phases in the annulus demonstrates that the annulus plays a minor role in the segregation or desegregation in binary solids mixture spouted beds with particles of the same size but different densities. The radial velocities of both phases in the annulus lead to the same finding. Some phenomena reported in the literature such as the interparticle percolation that could causes deviations on the paths of smaller and larger particles within the annulus should also be considered (Kutluoglu et al., 1983; Scott and Bridgwater, 1975). However, in the present study, this mechanism should be not of importance considering that the binary particles employed are both of equal size. Hence, this may counter segregation in the annulus for the binary mixture of spouted bed. (Kutluoglu et al., 1983) reported two mechanisms that could affect segregation or desegregation at the top of the annulus; rolling and bouncing. However, in deeper beds as in this case (i.e., H_o = 200 mm), the annulus surface is more flat than in shallow beds or that in conical spouted bed where the annulus surface could be sloped by a certain degree. Hence, rolling is expected to has no effect on segregation or desegregation at the annulus surface in this case. However, bouncing in this study could play important role due to significant difference in density between the two materials.

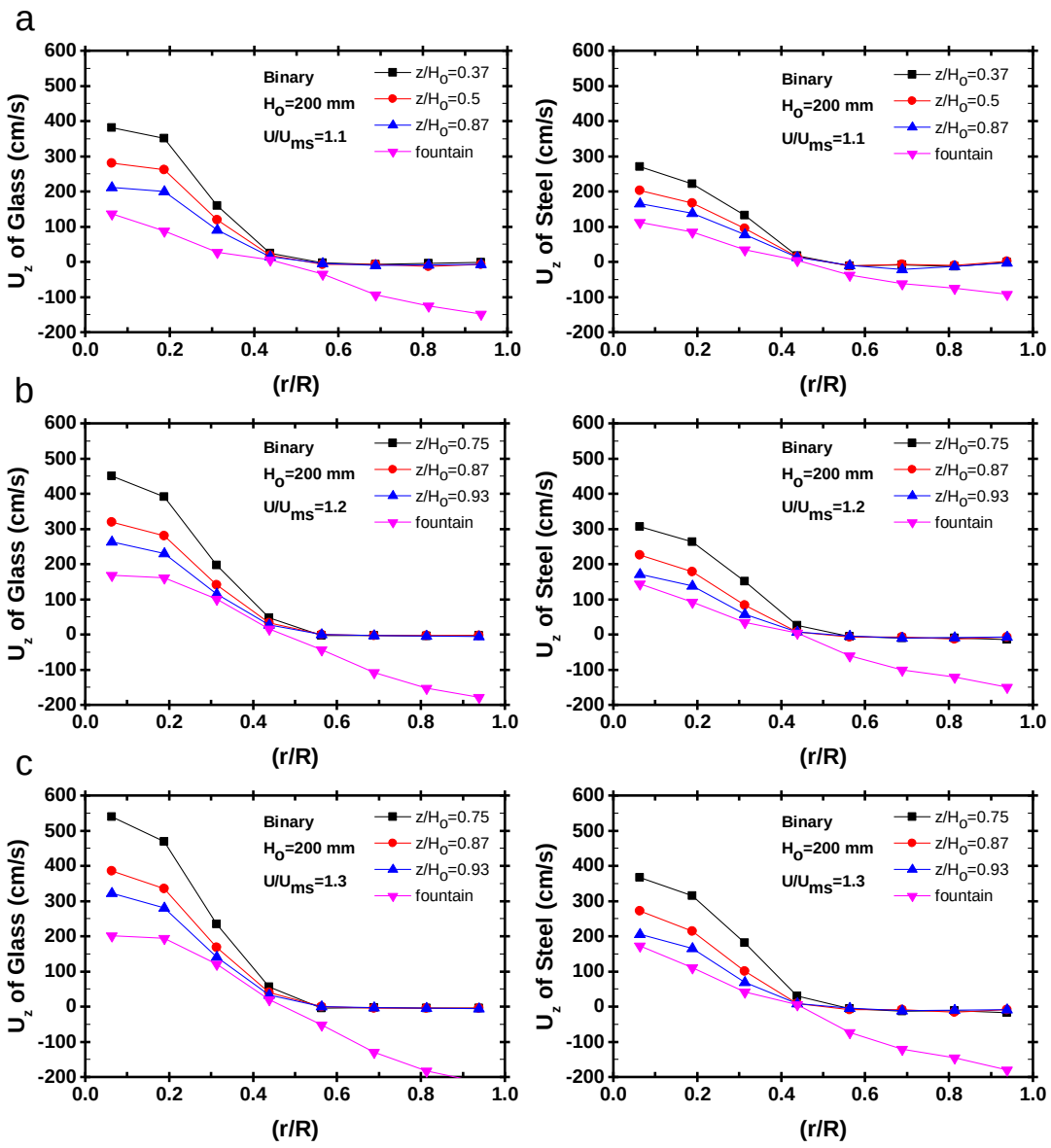

Figure 4.29. Azimuthally averaged radial profiles of the Axial mean solids velocity fields of glass (2 mm) and steel (2 mm) particles in gas-solid spouted bed of binary mixture (50% glass 50% steel) at different levels for different U/U_{ms} ratios: (a)1.1, (b)1.2, and (c) 1.3.

This bouncing mechanism has also been observed visually where glass particles tended to bounce in comparison to steel particles and steel particles tended to insert themselves in the annulus. However, the bouncing of the glass particles was random at the

annulus surface where either inward or outward bouncing were experienced by the particles. Therefore, it is not obvious whether or not the bouncing of the particles enhance segregation.

In the fountain, differences on the mean velocities between the two materials is very pronounced and in line that segregation also takes place in this region (Kutluoglu et al., 1983). The profiles show that in the fountain the mean velocities of same size of glass particles (density 2600 kg/m^3), are larger than the mean velocities of same size of steel particles (density 7400 kg/m^3). The fountain distributors the solids from the spout region back to the annulus region, and plays a key role in the mixing process in either spouted beds of similar solids particles or binary mixture of solids spouted beds with particles of different densities. Indeed, the influence of the fountain on the mixing or segregation process should be more important in binary case due to differences on solids phases. As can been seen in the figures, in the core of the fountain, light particles (glass in this case) have higher axial and radial velocity than the heavy particles (steel in this case). Meanings that the glass particle has larger chance to raise up higher than the steel particles, in a time-averaged sense, and hence land at further radial distance from the spout boundary. The radial solids velocities of glass particles in the fountain is comparatively higher than the steel particles which indicate the circulation of glass in the fountain. And therefore, they have higher chance to move radially outwards in the fountain than steel. This unlike behavior of the two materials in the fountain causes segregation of glass and steel particles to take place at the outer and inner part of the bed surface, respectively. This tendency was especially apparent for underdeveloped fountain.

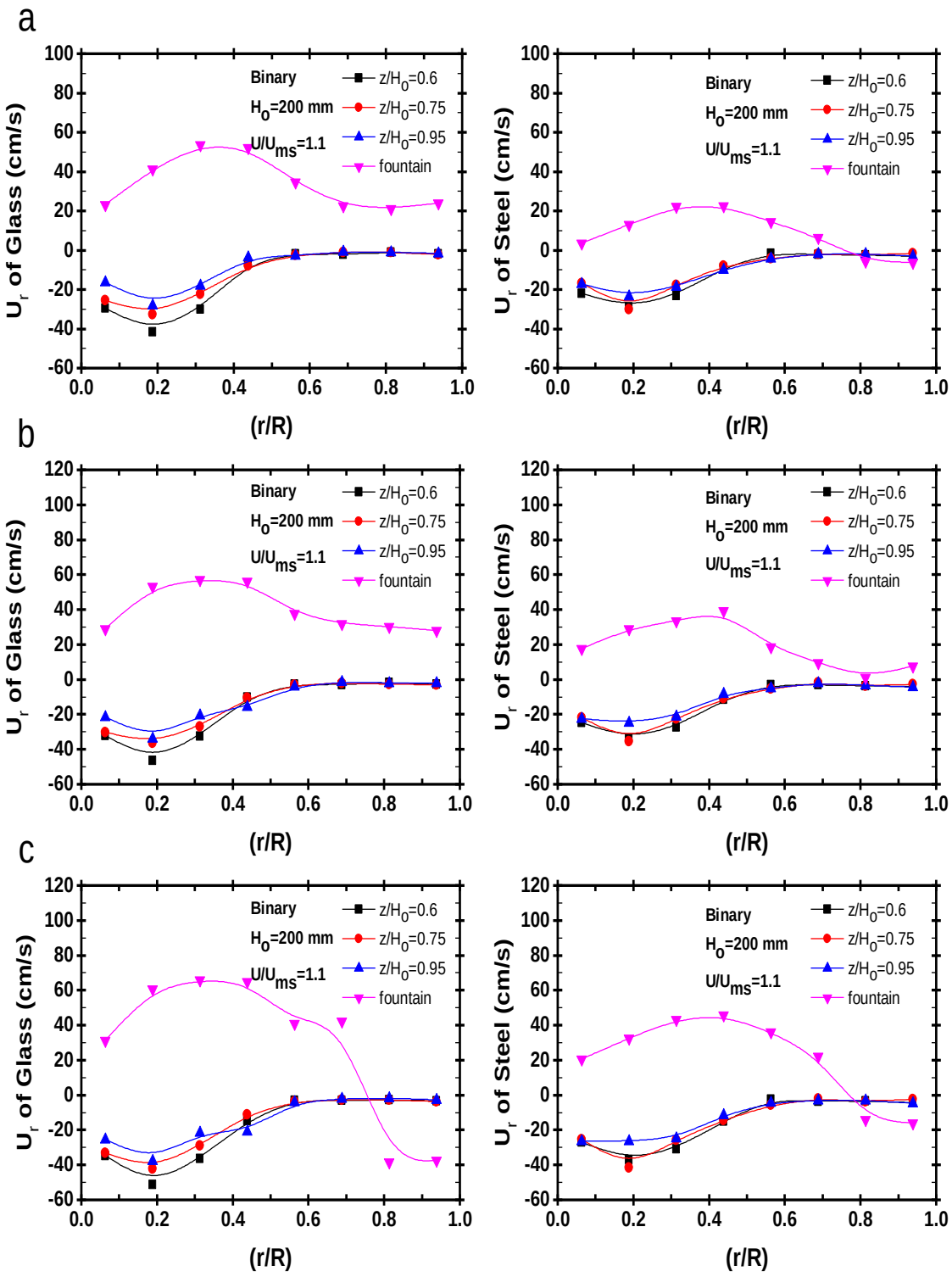

Figure 4.30. Azimuthally averaged radial profiles of the Radial mean solids velocity fields of glass (2 mm) and steel (2 mm) particles in gas-solid spouted bed of binary mixture (50% glass 50% steel) at different levels for different U/U_{ms} ratios: (a)1.1, (b)1.2, and (c) 1.3.

4.2.2.3 Root mean square (rms) solids velocity. Figure 4.31, Figure 4.32, and Figure 4.33, respectively illustrate the azimuthally averaged radial profiles of the axial, radial, and azimuthal RMS velocity for the binary mixture at different z/H_o levels for different U/U_{ms}. The results indicate that the $U_{z\text{-}RMS}$ values for both glass and steel particles increase with the U/U_{ms}, as expected, due to the increase in the kinetic energy of the introduced gas phase which will in return import in further turbulent spouting to the particles in the spout region. The fluctuation velocity of the glass and steel particles are higher in the lower levels of the spout than that at the top, similar to that observed in the in gas-solid spouted beds with particles of same size and densities. In the profiles, it can be seen that the steel particles give a lower axial RMS velocity, while the glass particle have a higher axial RMS velocity for all the U/U_{ms} ratio. Hence, the difference in RMS velocities between glass and steel having the same size, but different density and mass, is in line with the mechanism of particles collisions that contributes to segregation to take place in the spout. The turbulence in the spout region is high, and hence the fluctuation of the particle velocities is also high, and for that reason the impact of the interparticle collisions is evident in the spout region. the higher the fluctuation velocity of the particle the less losing of momentum the particle had, as reflected by the higher particle velocity of glass. However, one also must keep in mind that RMS velocity consists of both kinetic and collision contributions. Therefore, lower density glass dragged more effectively by the gas and hence have higher kinetic energy and thereby increased fluctuation velocity. Some inspection reveals that the RMS velocity of glass in the binary case is lower than the RMS velocity of glass in gas-solid spouted beds with particles of same size and densities case, while the RMS velocity of steel in present case is higher than the RMS velocity of steel in

gas-solid spouted beds with particles of same size and densities case. Thus, it is suggested that glass particles may be transferring some of their kinetic energy to the steel particles. With a system of binary particle, the collision between the particles increases, resulting in the increase of velocity fluctuations. However, as can be seen in the figures, the fluctuations velocity of both particles in the annulus is small and similar to each other. This is mainly due to the nature of the flow in the annulus, where particles move slowly and downward as in a loosely packed bed. As shown in the profiles, the RMS velocities in the annulus are similar for the two materials, hence, the interparticle collisions effect is minimal in the annulus region. Also, RMS velocity results in the annulus corroborates that interparticle percolation plays minor role in the annulus of binary spouted beds of particles of equal size. Therefore, this contributes to the conclusion mentioned earlier that the annulus plays minor role in the segregation or desegregation in binary spouted beds of particles of equally size but different densities. Some inspections also reveal that increasing U/U_{ms} causes minor increase in the fluctuations velocity of both particles in the annulus. This could be due to a minor increase in voids between the particles in the annulus when the bed is operated at high U/U_{ms}, resulting to increase movements of the particles within the annulus (although minor increase). In a recent study (Al-Juwaya et al., 2017), we have showed that gas holdup, voidage, does not remain at the gas holdup value at loose-packed bed state when the U/U_{ms} increases (i.e. $U/U_{ms} = 1.3$). However, the study also showed that diverting the flow of air to the annulus should only have contributed to increase the gas holdup, with no effect on the structure of the annulus.

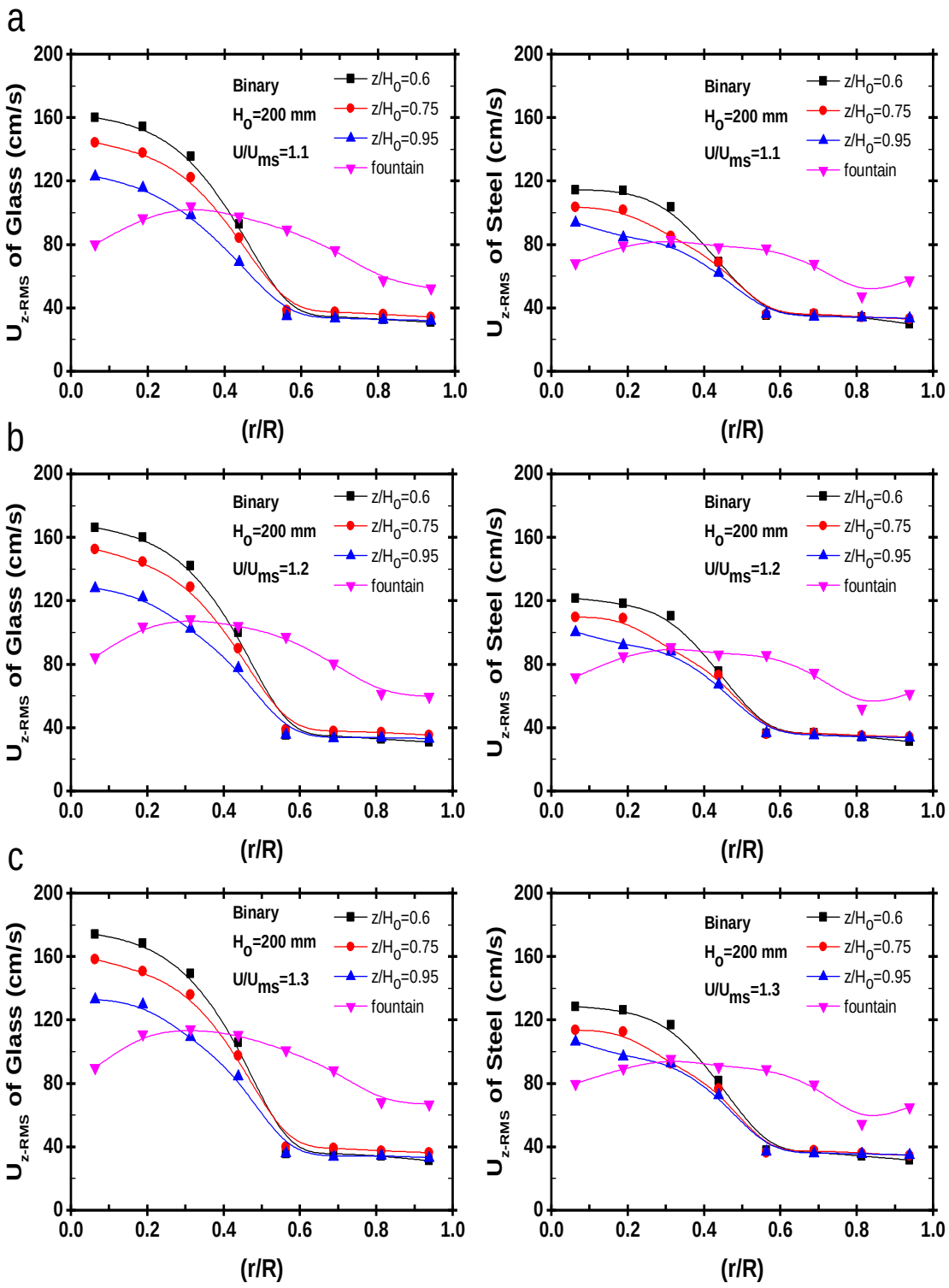

Figure 4.31. Azimuthally averaged radial profiles of the Axial RMS velocity fields of glass (2 mm) and steel (2 mm) particles in gas-solid spouted bed of binary mixture (50% glass 50% steel) at different levels for different U/U_{ms} ratios: (a)1.1, (b)1.2, and (c) 1.3.

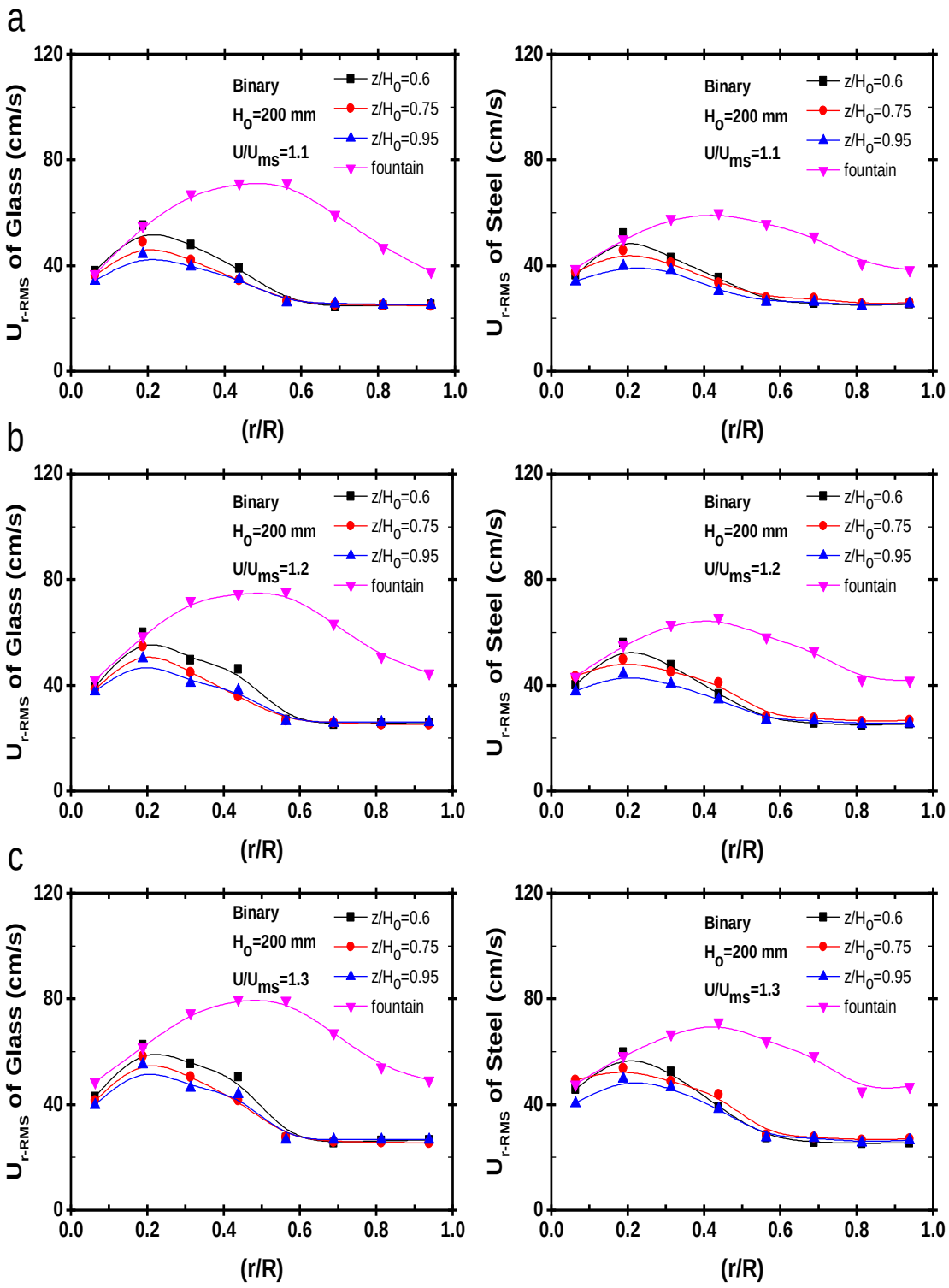

Figure 4.32. Azimuthally averaged radial profiles of the Radial RMS velocity fields of glass (2 mm) and steel (2 mm) particles in gas-solid spouted bed of binary mixture (50% glass 50% steel) at different levels for different U/U_{ms} ratios: (a)1.1, (b)1.2, and (c) 1.3.

Even when the annulus appears as a downward flow, the radial profiles of U_{z_RMS} and U_{r_RMS} in the binary case demonstrate that the fluctuation velocities in the annulus are not negligible in binary solids spouted beds.

In the fountain, the fluctuation velocity of same size of glass (density 2600 kg/m^3), is larger than the fluctuation velocity of same size of steel (density 7400 kg/m^3). This difference indicates that glass particles have faced more deflection due to particle collisions than steel particles especially near the core of the fountain and at higher levels where particle crowding is significant (i.e. solids holdup at the core of fountain increases with height). And therefore, this is in line that glass particles reach higher heights in the fountain to fall at radial positions not close to the boundary of the spout. Note that each steel had a mass which is approximately 3 times greater than glass particle. Therefore, the collisions between particles of the two materials will likely lead to much wider deflection of the glass particle in comparison to the steel particles. The results also indicate a dip in the $U_{r\text{-}RMS}$ at the wall. This occurs because direct impact of solids radially at the wall is brought to rest and the solids are forced to transfer their momentum to the wall. The $U_{\theta\text{-}RMS}$ profiles showed less sensitivity with the increase in U/U_{ms}. This is because the net motion of solids is in *z*-direction. It is also found that the profile $U_{\theta\text{-}RMS}$ indicate slightly higher value at the wall both for glass and steel.

This suggests that in the computational fluid dynamics (CFD) modeling of spouted beds, one should avoid 2D and 2D-axisymmetry simulations. Consequently, the results of the RMS solids velocities also emphasize that particle-particle interaction is essential in binary solids mixture of spouted bed with particles of same size and different densities.

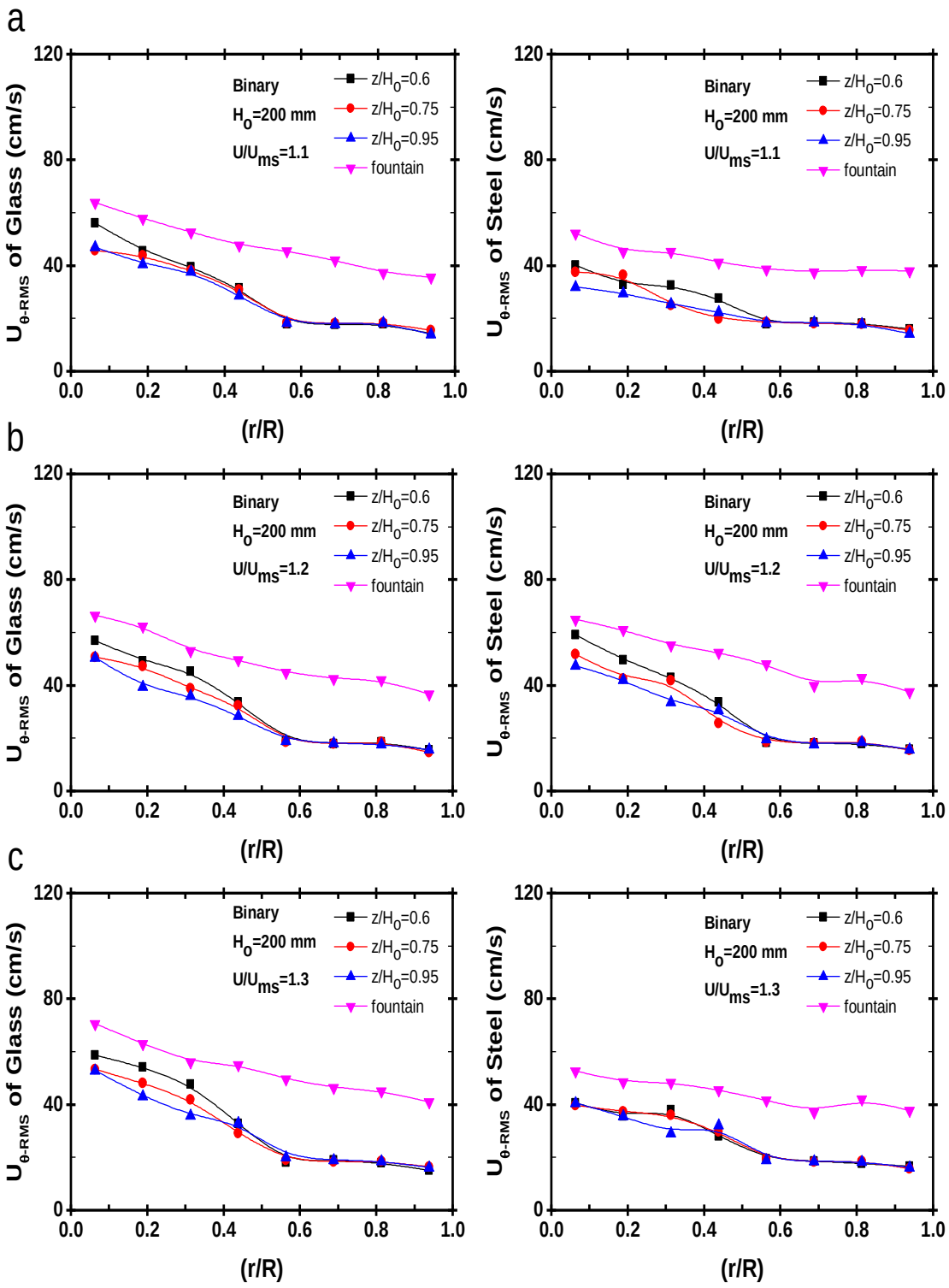

Figure 4.33. Azimuthally averaged radial profiles of the Azimuthal RMS velocity fields of glass (2 mm) and steel (2 mm) particles in gas-solid spouted bed of binary mixture (50% glass 50% steel) at different levels for different U/U_{ms} ratios: (a)1.1, (b)1.2, and (c) 1.3.

4.2.2.4 Turbulent stresses and kinetic energy. Figure 4.34, Figure 4.35, and Figure 4.36, respectively illustrate the azimuthally averaged radial profiles of the axial (τ_{zz}), radial (τ_{rr}), and azimuthal ($\tau_{\theta\theta}$) normal stresses of gas-solid spouted bed for the binary mixture at different z/H_o levels for different U/U_{ms}. As shown in the profiles, the axial normal stresses (τ_{zz}) are much larger than the radial (τ_{rr}), and azimuthal ($\tau_{\theta\theta}$) normal stresses. This is because the high variation in the axial solids velocity as mentioned earlier. Furthermore, the azimuthal and radial solids velocities were small and, therefore, their gradients have also been small. Similar to the RMS solids velocities profiles, the axial (τ_{zz}) and radial (τ_{rr}) solids normal stresses profiles of the glass particles are higher than those of the steel particles. In the spout, the axial normal stress (τ_{zz}) of both glass and steel are higher near the conical-cylindrical conjunction and the middle plane of the bed height than that at the top plane of the bed due to variation in shear rate imported by the gas flow in the spout region. The axial normal stress (τ_{zz}) of both glass and steel particles reach a maximum near the spout axis and then decrease towards the spout-annulus interface. The axial normal stresses (τ_{zz}) are substantially higher than the radial normal stress (τ_{rr}). For example, at $z/H=1.1$ and $U/U_{ms}=1.1$, the axial normal stresses (τ_{zz}) are about 15000 and 8000 cm^2/s^2 for the glass and steel particles, respectively, and the corresponding radial normal stresses (τ_{rr}) are 1500 and 1200 cm^2/s^2, respectively.

The ratios of the axial to the radial normal stresses for the glass and steel particles are 10 and 6.6, respectively. (Clelland and Hrenya, 2002) reported that in granular flow, the ratio of the axial to the radial normal stresses of binary particles of different sizes (but similar density) decreases to unity as the solids holdup increases because of the increase in the impact the particles collisions of granular energy generation

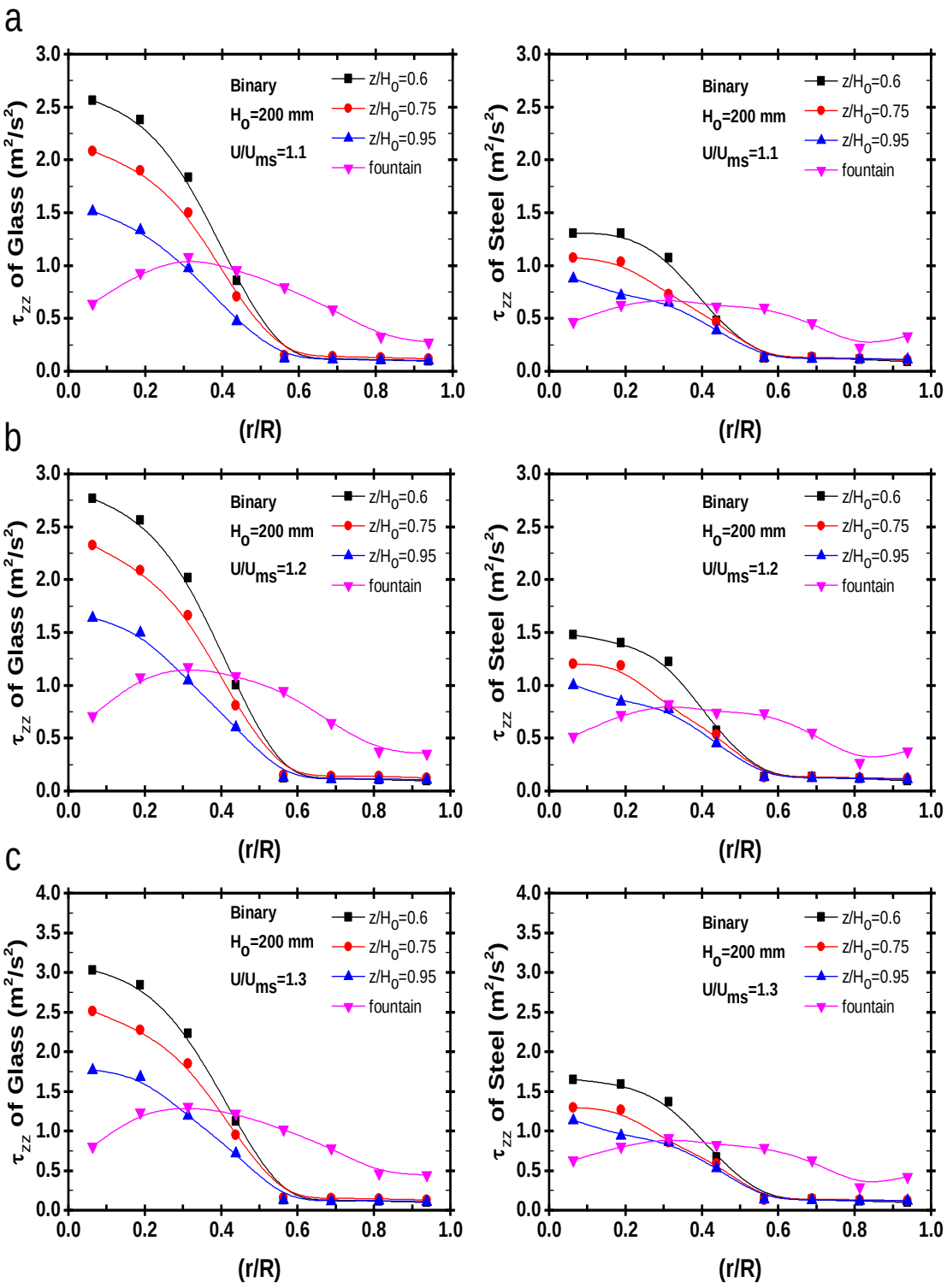

Figure 4.34. Azimuthally averaged radial profiles of the Axial normal stress (τ_{zz}) of glass (2 mm) and steel (2 mm) particles in gas-solid spouted bed of binary mixture (50% glass 50% steel) at different levels for different U/U_{ms} ratios: (a) 1.1, (b) 1.2, and (c) 1.3.

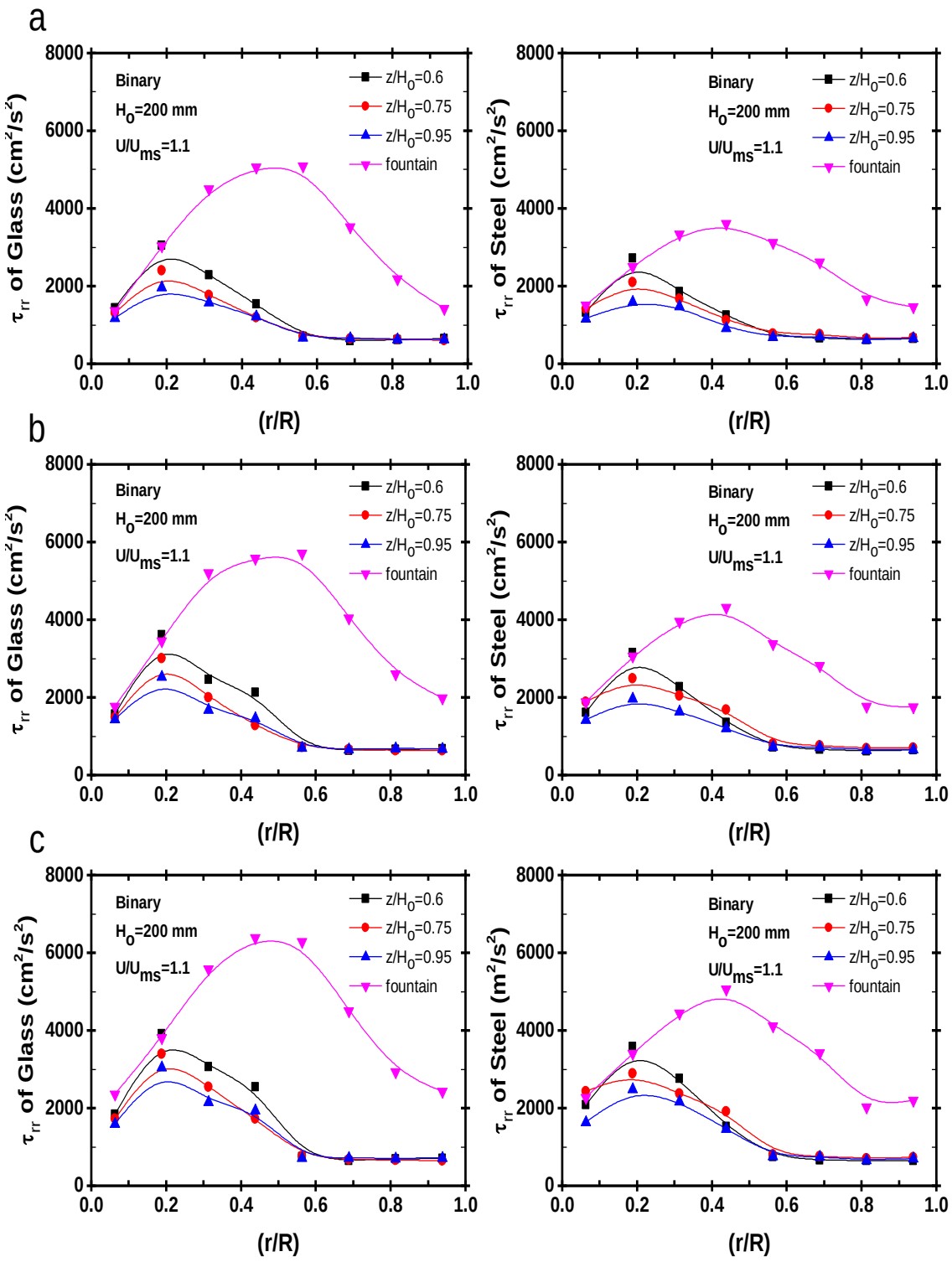

Figure 4.35. Azimuthally averaged radial profiles of the Radial normal stress (τ_{rr}) of glass (2 mm) and steel (2 mm) particles in gas-solid spouted bed of binary mixture (50% glass 50% steel) at different levels for different U/U_{ms} ratios: (a) 1.1, (b) 1.2, and (c) 1.3.

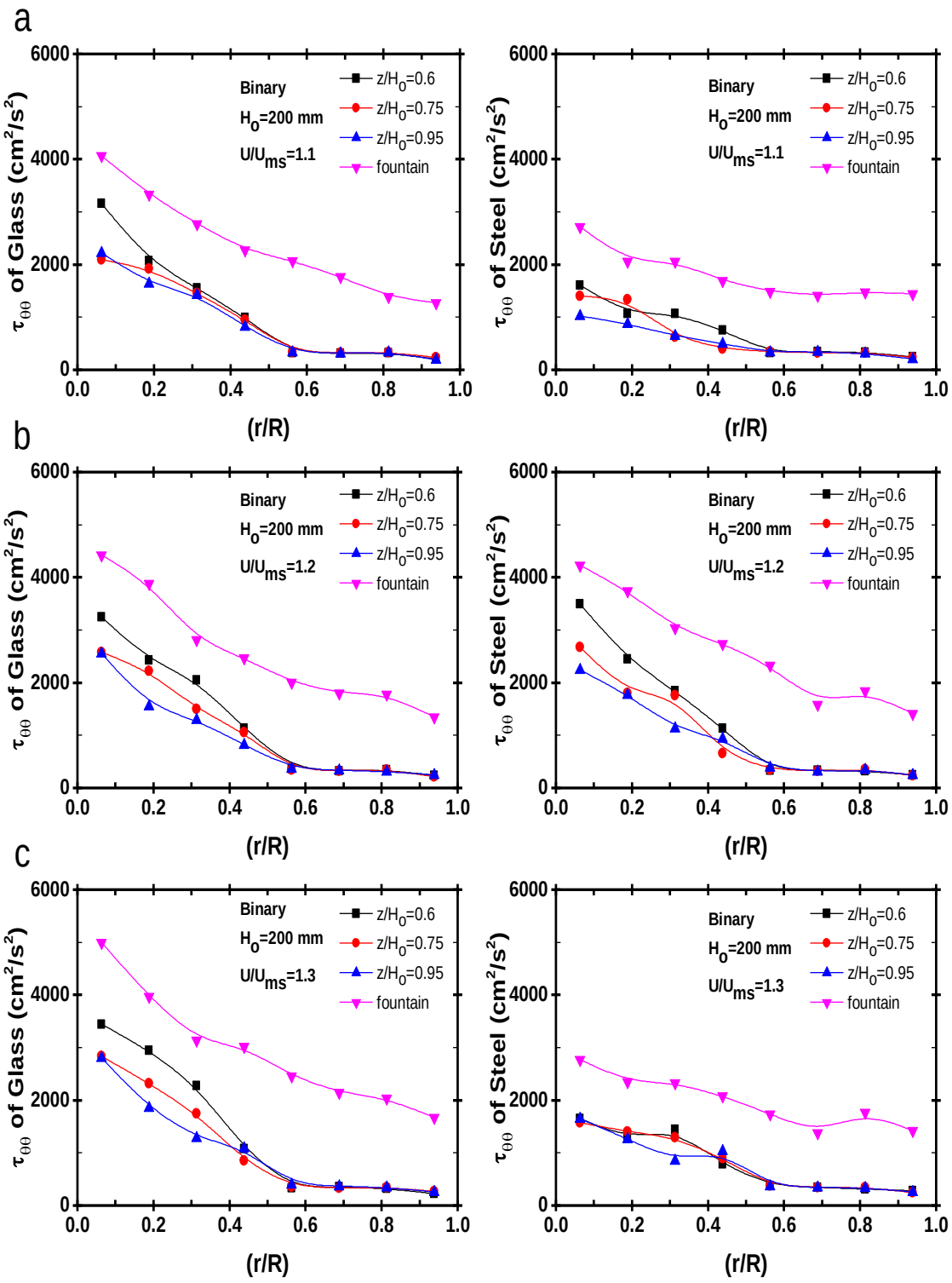

Figure 4.36. Azimuthally averaged radial profiles of the Azimuthal normal stress ($\tau_{\theta\theta}$) of glass (2 mm) and steel (2 mm) particles in gas-solid spouted bed of binary mixture (50% glass 50% steel) at different levels for different U/U_{ms} ratios: (a) 1.1, (b) 1.2, and (c) 1.3.

As explained earlier, the kinetic energy and particles collisions both contribute to the normal stress of the particles. At low gas holdup as the case in the spout region, the particles collisions mode is infrequent, and hence the kinetic mode is the dominant. However, the reason could be due to the high number of the particle collisions binary system, leading to significantly high fluctuating velocities. It stresses that in binary solids mixture spouted beds, the particle-particle interaction takes on an important role however it is not dominating over the fluid-particle interaction. Figure 4.37 shows the shear stress profiles for both glass and steel particles at different levels for different U/U_{ms}. Only the profiles of the shear stress (τ_{rz}) component are presented in this section. The others shear stresses components, $\tau_{z\theta,}$ and $\tau_{r\theta}$, signify the same comparison and therefore they are not reported here. As can be seen in profiles, the Reynolds shear stress (τ_{rz}) of both glass and steel is higher in the spout region with increasing intensities when approaching the conical region. The profiles show that in the spout the shear stresses (τ_{rz}) of same size of glass (density 2600 kg/m^3), are larger than the shear stresses (τ_{rz}) of same size of steel (density 7400 kg/m^3). However, the shear stresses in the spout for both particles are much smaller than the normal stresses meaning that the turbulent of the particles are more controlled by the normal stresses of the particles. In the annulus, the shear stresses of both glass and steel particles are close to balanced. Figure 4.38 illustrates the turbulent kinetic energy profiles for both glass and steel at different levels for different U/Ums ratio. The turbulent kinetic energies of the particles are larger in the center zone of the spout region for the particles and reduce as the spout-annulus interface is approached. This trend is similar to the trend of the τ_{zz} whose values are significant compared to τ_{rr}. At the annulus region, the turbulent kinetic energy levels off and the magnitudes are smaller than those of the spout region are.

In the fountain region, the turbulent kinetic energy magnitudes are comparable to those of the spout region's center zone; the maximum value exists at the region between about r/R=0.4 to r/R=0.5. This is similar to the trends for τ_{zz} and τ_{rr}, whose values are dominating the estimated values of turbulent kinetic energy.

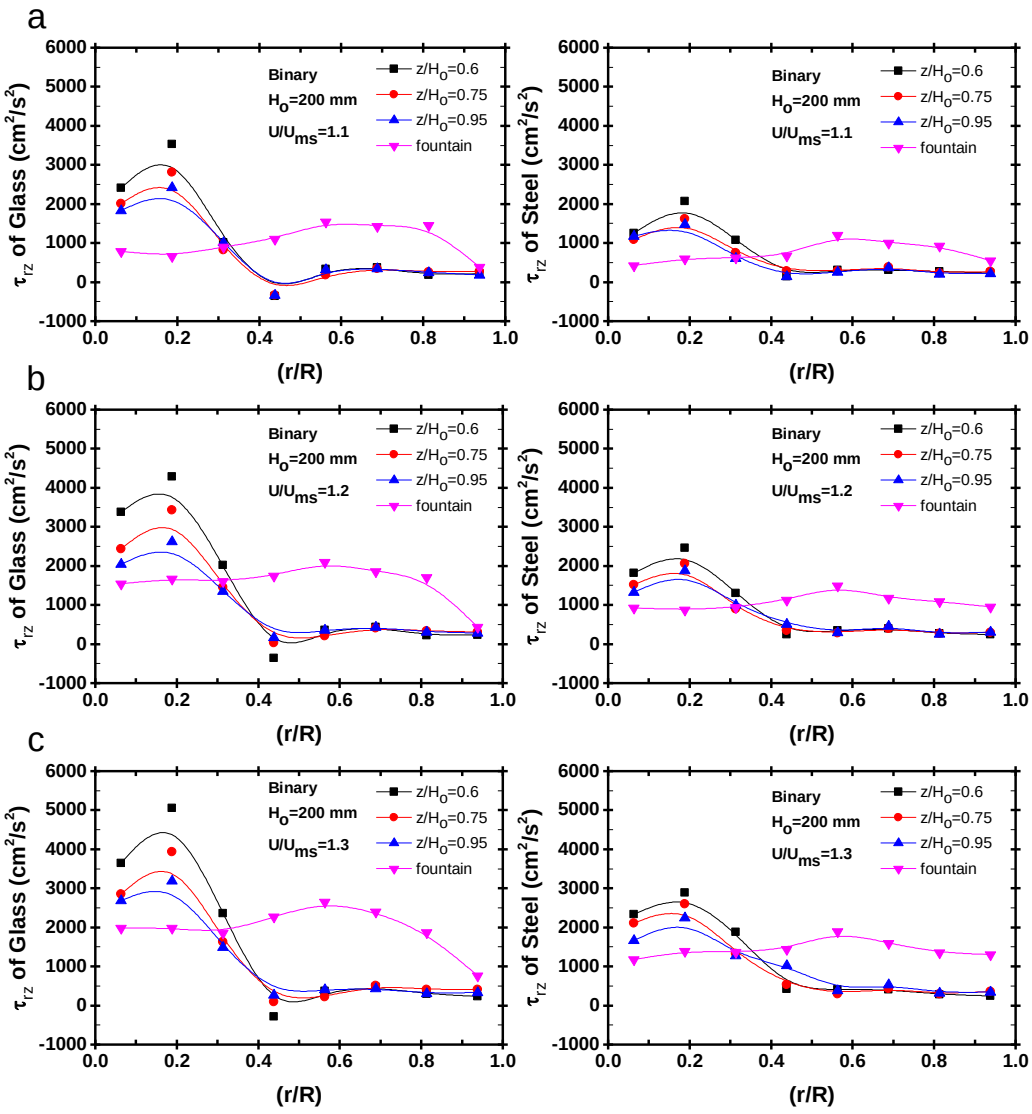

Figure 4.37. Azimuthally averaged radial profiles of the Shear stress (τ_{rz}) of glass (2 mm) and steel (2 mm) particles in gas-solid spouted bed of binary mixture (50% glass 50% steel) at different levels for different U/U_{ms} ratios: (a) 1.1, (b) 1.2, and (c) 1.3.

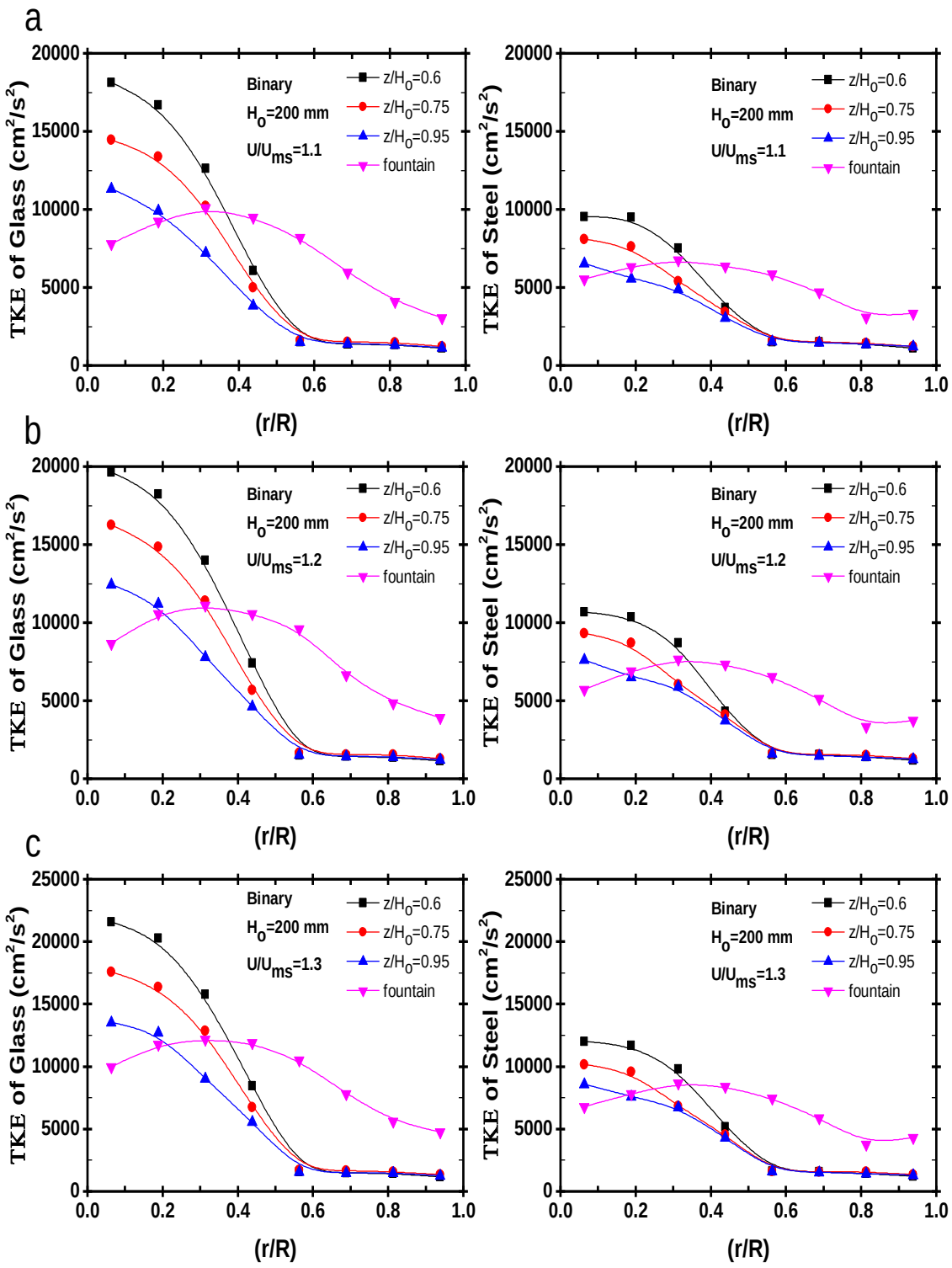

Figure 4.38. Azimuthally averaged radial profiles of the of the turbulent kinetic energy (TKE) of glass (2 mm) and steel (2 mm) particles in gas-solid spouted bed of binary mixture (50% glass 50% steel) at different levels for different U/U_{ms} ratios: (a) 1.1, (b) 1.2, and (c) 1.3.

4.3. SCALE-UP AND HYDRODYNAMICS OF SPOUTED BEDS TRISO NUCLEAR FUEL PARTICLES COATERS USING ADVANCED RADIOACTIVE PARTICLE TRACKING (RPT) TECHNIQUE

4.3.1. Spout Diameter. As explained earlier, (Aradhya et al., 2016) determined a set of conditions of similar and dissimilar gas holdup profiles and implemented these conditions to evaluate the newly-developed mechanistic scale-up methodology using an optical probe. The identified conditions have been verified and validated using gamma-ray computed tomography (CT) by measuring the cross-sectional distribution of the gas holdup at selected levels for both lab, and pilot plant scales spouted beds (Ali et al., 2018). The demonstration of this validation is repeated here in Figure 4.39 and Figure 4.40, where the cross-sectional distributions of the gas holdup and the radial profile gas holdup of the pilot plant and lab scales spouted beds are similar at a selected dimensionless height of both beds. The results signify the very similar gas holdup distributions in term of mean and standard deviation between the conditions of the reference case and the conditions of the similar gas holdup profile. Correspondingly, the next step is to evaluate the investigated hydrodynamics parameters in this study (the spout diameter, cumulative probability distribution of the solids particles penetration into the spout, fraction of cycle time in each region of the bed, the radial profiles of the dimensionless values of the root-mean-square particle velocities and solids eddy diffusivity) and to see whether or not hydrodynamics similarity is obtained between the pilot plant and laboratory scales spouted beds.

Before proceeding, comparison of the spout diameter profiles derived from the RPT and CT techniques is made. The CT is a powerful technique as it can capture the time-averaged cross-sectional distributions of the phases holdups of multiphase flow systems such as spouted beds without being invasive to the flow (see for more details (Al-Juwaya, Ali et al. 2017)). Given that the CT is more accurate to visualize and identified the spout

shape of spouted beds with less than 1% error in spout boundary (Ali et al., 2016a), the CT will stand as a reference here in this comparison. A typical comparison of the dimensionless spout diameter profiles derived from the RPT and CT for the pilot plant-scale of spouted beds at the reference conditions is shown in Figure 4.41. As can be seen in Figure 4.41, close spout diameter is obtained from the RPT to that of CT. The larger deviation deviations were noticed near the gas inlet at the conical part. However, deviations between points of the profiles fall within $\pm 2.5\ mm$ which is fair close from the spatial resolution of the RPT technique reported earlier $\pm 2\ mm$. Similar trends were found for the lab scale spouted beds for all the operating conditions under investigation. Considering the fact that the profiles were derived from two independent experimental techniques, this comparison serves as a validation of results for the RPT technique.

Figure 4.42 shows the dimensionless spout diameters for the conditions of reference case, similar gas holdup profiles, and dissimilar gas holdup profiles. For the convenience of comparison between the beds, the spout radius (R_s) of each condition was non-dimensionalized by dividing them by the column diameter (D_c) of the corresponding bed. The dimensionless spout diameters are presented as a function of dimensionless height (z/H), where z refers to the axial height from the gas distributor and H refers to the height of the bed. As can be seen in Figure 4.42, near similarity in the dimensionless spout diameters between those of the reference case and the case of similar gas holdup profile is achieved. When the gas holdup radial profiles are dissimilar, the dissimilarity in the dimensionless spout diameters is achieved. Dimensionless spout diameters for the case of dissimilar gas holdup profile were smaller than in the reference case. The average deviation for the profile of the similar gas holdup case from that of the reference case as

found to be 4.32% and for the similar gas holdup case were 19.64%. These results are strongly in line with the reported results of matched cross-sectional gas holdup distributions for the conditions of reference case and similar gas holdup profile (Ali et al., 2018). The results signify that when gas holdup profiles are systematically matched between two different scaled spouted beds, small deviations in the dimensionless spout diameter are obtained.

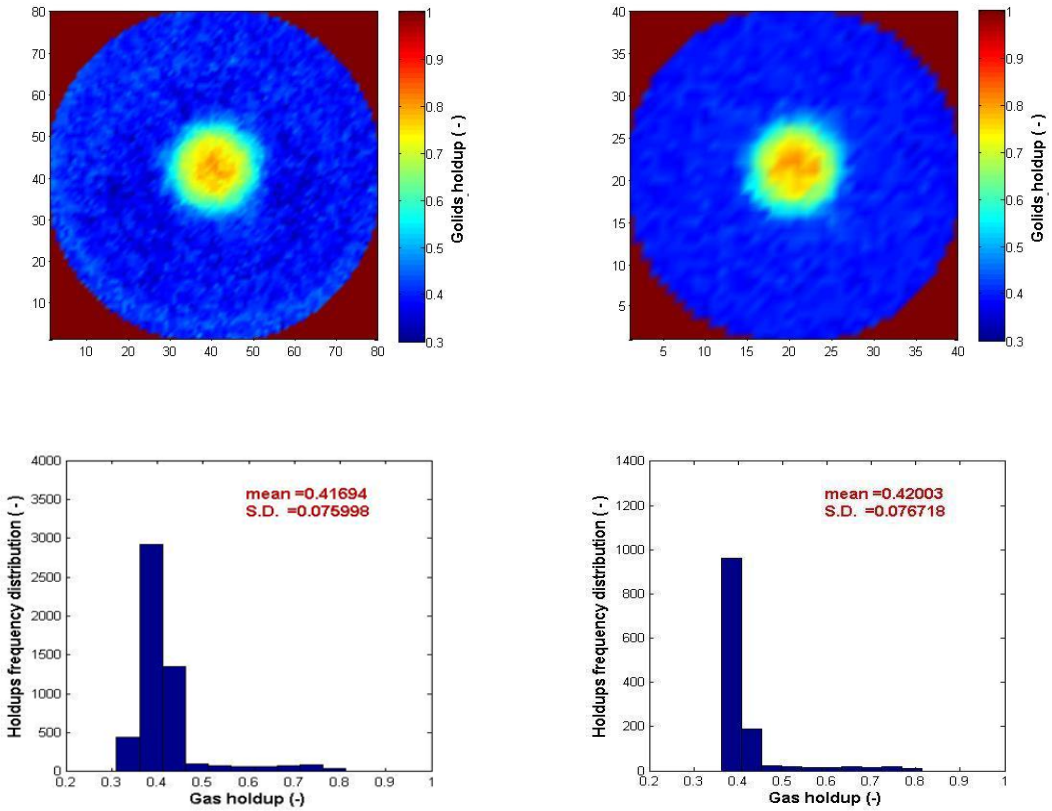

(a) (b)

Figure 4.39. Cross-sectional distribution and corresponding frequency distribution of gas holdup for the conditions of (a) reference case of pilot plant-scale spouted beds at z/D_c=1.8 and (b) similar gas holdup radial profile of lab-scale spouted beds at z/D_c=1.8.

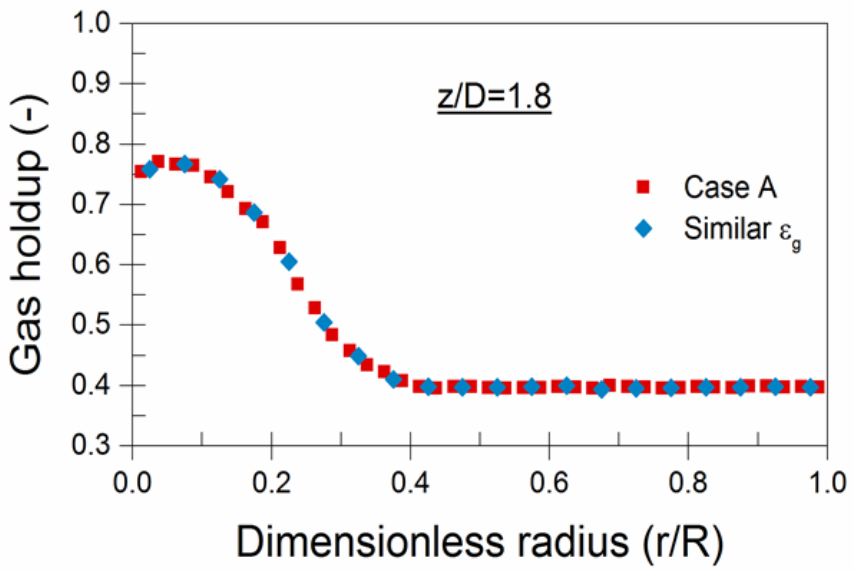

Figure 4.40. Comparison of gas holdup radial profiles at z/D = 1.8, for the conditions of reference case in the 0.152 m spouted bed, and for the conditions that give a similar radial profile of gas holdup (called similar ε_g) in the 0.076 m spouted beds.

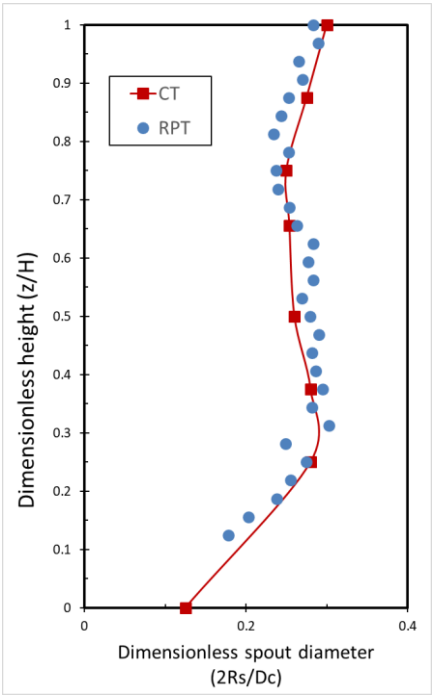

Figure 4.41. Comparison of the dimensionless spout diameter profiles derived from CT and RPT for the pilot plant-scale spouted beds at the condition of the reference case listed in Table 3.5.

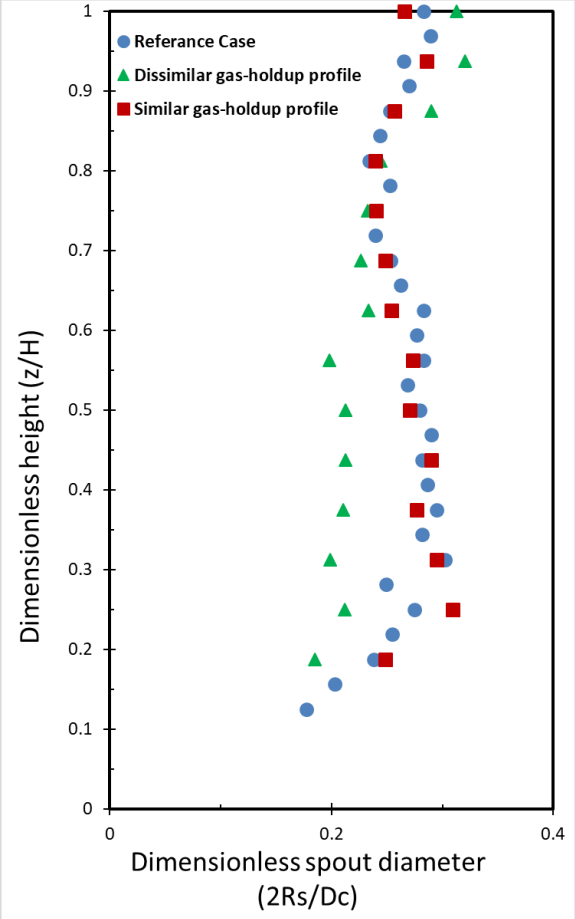

Figure 4.42. Dimensionless spout diameters (or penetration of the solids in the spout) as a function of dimensionless height for the conditions of the reference case, similar gas holdup profiles and dissimilar gas holdup profile.

4.3.2. Probability of Solids Transition Between Adjacent Regions of The Bed.

Figure 4.43 illustrates the cumulative probability distributions of the penetration of solids particles into the spout (***P***) along the spout region for the Cases reference, similar gas holdup profile, and dissimilar gas holdup profile. The appropriate distance coordinate is vertical and non-dimensionalized as z/H to have basis comparison between the pilot plant and lab scale spouted beds. At each level, the spout-annulus boundary is delimited by the spout dimeters presented in Figure 4.42. The solids particle entry levels into the spout is an

important parameter because the dissimilar distribution of entry between the beds would results into dissimilar solids flow in the spout. In Figure 4.43, the penetration levels of the solids particles into the spout are characterized by three regions from bottom to top. The first region is form the gas inlet to a point located between 0.15 and 0.2 dimensionless height above the gas distributor. The second region is from the latter to the height of the conical part and the third one is for the cylindrical part. The profiles for all Cases share the characterization of the three regions, while the magnitudes between these profiles are different. For the pilot plant spouted beds, the solids had 62.66% probability to enter the spout from the conical region at the conditions of the reference case. This value is very close from the 61% value obtained from RPT measurements in a spouted bed dimensionally (i.e. ,geometrical dimensions) similar to the pilot plant spouted beds by (Roy et al., 1994), and the 67 % value obtained from wall measurements in a half column spouted bed by (Thorley et al., 1959). Hence, should the probability value for the condition of similar or dissimilar gas holdup profile is close from the 62.66% value, sthe imilarity is achieved at least from this parameter point of view. As seen from Figure 4.43 less deviation is observed between the profiles of the conditions of similar gas holdup profile from those of the reference case. The solids had 57.45% to enter the spout from the conical region, and 42.54% to enter from the cylindrical part in the lab scale spouted beds at the conditions of the similar gas-holdup profile. These results are strongly in line with the reported results of matched cross-sectional gas holdup distributions for the conditions of reference case and similar gas holdup profile (Ali et al., 2018), and demonstrated in Figure 4.39. On the other hand, for the conditions of dissimilar gas holdup profile, the solids had 52.87 to enter the spout from the conical region, 10 % lower than the reference case. Obviously, the

probability distributions are very close between the conditions of the reference case and similar gas holdup, revealing the fact that hydrodynamics similarity at both operating conditions is similar and serves as a validation of the scale-up methodolog.

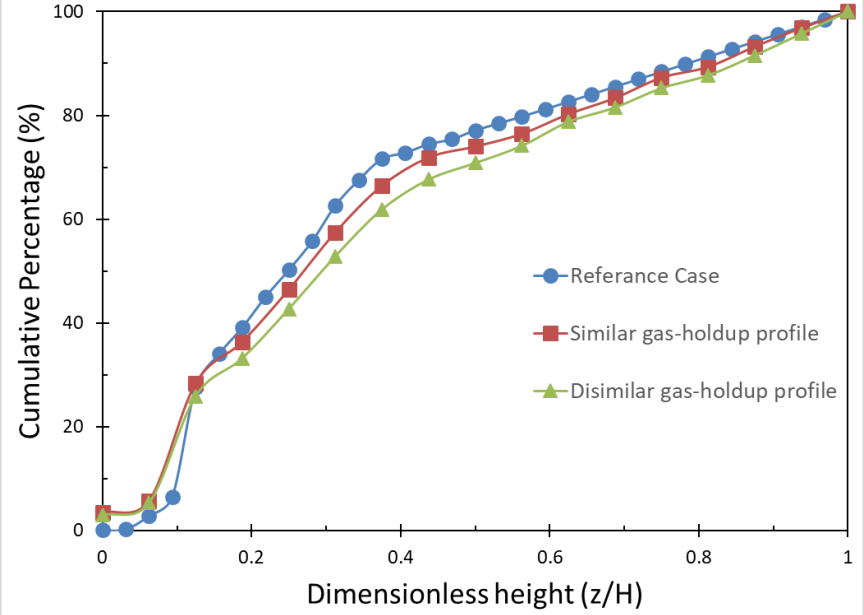

Figure 4.43. Cumulative distribution of particles crossing boundaries between regions for binary spouted bed at U/U_{ms} =1.1. (a) Landing on annulus surface; (b) Being entrained into spout from the annulus; (c) Entering fountain at z = H.

4.3.3. Dimensionless Residence Time Distribution. The distributions of the solids residence time (SRT) in the three regions of spouted beds were obtained by analyzing the trajectory of the tracer particle of each bed at the corresponding applied conditions. Obtaining the similarity in term of solids residence time is an important element for a reliable scale-up of gas-solids spouted beds particularly when chemical vapor deposition (CVD) is taken into consideration as in the coating process of the TRISO particles. The

question then rises how solids residence time should be compared to examine the hydrodynamic similarity between the two different sizes gas-solid spouted beds at the corresponding applied operating conditions. In another word, how the solids residence time should be scaled between differently sized spouted beds to achieve dynamical similarity successfully. The absolute values of the SRT should normally differ due to the differences in the sizes of the beds and the operating conditions (i.e., or even due modification in operating conditions for similar bed geometries). Therefore, the answer to the mentioned question is to represent the solids residence time in the form of dimensionless values using a predictable or measurable parameter. In this study, the solids residence time were non-dimensionalized using the values of the minimum spouting velocity (U_{ms}) and the inner column diameter (D_c) of the corresponding beds and the applied conditions, as follow;

$$Dimensionless\ solids\ residence\ time\ (\acute{T_q}) = T_q.\frac{U_{ms}}{D_c} \qquad q = sp, fo, an \quad (34)$$

The minimum spouting velocity (U_{ms}) is described as the minimum superficial gas velocity necessary to have the onset external spouting state in spouted beds, and less than this velocity, solids circulation is absent, as well as the three regions in spouted beds are not entirely developed. Certainly, such critical velocity is a crucial hydrodynamic parameter in the design and operation of spouted beds processes (Bi, 2004). The minimum spouting velocity can be obtained experimentally (Aradhya et al., 2017) or estimated by correlations such as (Bi et al., 1997; Fane and Mitchell, 1984; Grbavčíc et al., 1976; Wang et al., 2004; Zhou and Bruns, 2012). It is a function of the physical properties of the particles (density, size, and shape), bed geometry (column diameter, inlet diameter, and

cone angle), static bed height, and gas properties (density, viscosity). In this work, the minimum spouting velocity (U_{ms}) was measured experimentally for the pilot plant, and lab spouted beds for all the cases of operating conditions in Table 3.5. The height of the static bed particles (i.e., H, bed height) was fixed at a fixed bed position using a length scale attached to the wall of the column. The gas flow rate was then slowly increased with small increment while the bed surface is monitored. The velocity at which the spouting initiated was measured and identified as the minimum spouting velocity. The measurement of the U_{ms} was repeated five times, and the average value was taken. The average measurement values of U_{ms} for each set of conditions were compared with the predictions of the correlation of (Mathur and Epstein, 1974a) for deep spouted beds ($H_o/D_c > 1$). H_o refers to the initial static beds height, and D_c refers to the column diameter. The estimated values by the correlation are found close to the measured ones. The minimum spouting velocity for the 0.076 m (lab scale) and a 0.152 m (pilot plant scale) spouted beds are listed Table 3.5.

Figure 4.44 shows the distribution of the dimensionless solids residence time in the three regions of spouted beds for the Cases reference, similar gas holdup profile, dissimilar gas holdup profile. For all Cases, the distributions of the dimensionless solids residence time in the spout, in the annulus, and in the fountain of spouted beds are different. The distribution of the dimensionless SRT in the fountain pretty much represent a Gaussian normal distribution, even though the distribution in the spout signify a lognormal distribution. At the same time, different scales of the dimensionless SRTs are obtained because of the presence of the three regions of spouted beds each with a specific flow. For example, for the reference case, the dimensionless SRTs in the spout region range between

0 and 4 s; while in the fountain and annulus regions, the dimensionless SRTs goes from 0 to 8 s and 0 to 60 s, respectively.

The distributions indicate small residence time of solids in the spout region in comparison with the fountain and the annulus regions. Moreover, the residence time elapsed by the solids in the annulus region is much higher than that elapsed in the spout and fountain regions together. This divergence is pronounced in the mean values of the distributions of the dimensionless SRT in the three regions of spouted beds. However, when comparing the means of the dimensionless SRT between the cases, less deviation is observed for the condition of similar gas holdup profiles from those of the reference case, indicating that matching gas holdup profiles can lead hydrodynamics similarity between the two beds. In another word, matching the gas holdup profiles between the two beds can lead to predicting the solids residence time. The absolute relative deviation between the means of the dimensionless SRT in the spout was found to be 1. 9% and 57.67% for the conditions of similar and dissimilar gas holdup profiles, respectively with respect to the reference case. In the fountain, the absolute relative deviation between the means of the dimensionless SRT spent in the fountain was found to be 3.8% and 54.65% for the conditions of similar and dissimilar gas holdup profiles, respectively with respect to the reference case. In another word, matching the gas holdup profiles between the two beds can lead to predicting the solids residence time. It is clear that when the gas holdup radial profiles are not similar the non-similarity in the dimensionless SRT was obtained. In the annulus, the absolute relative deviation between the means of the dimensionless SRT spent in the annulus was found to be 9.14% and 27.24% for the conditions of similar and dissimilar gas holdup profiles, respectively with respect to the reference case.

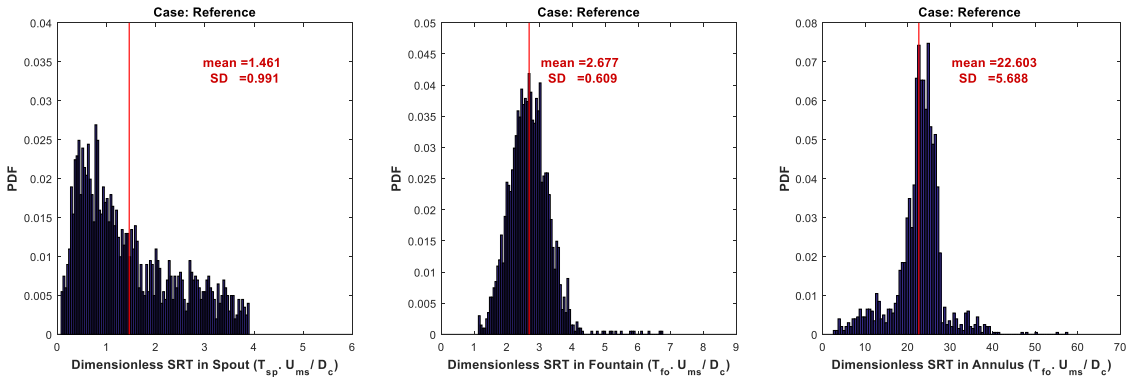

(a)

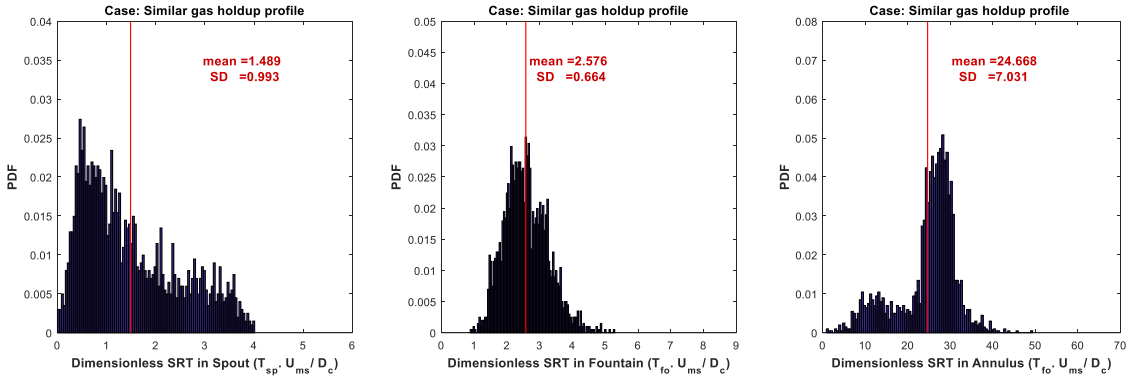

(b)

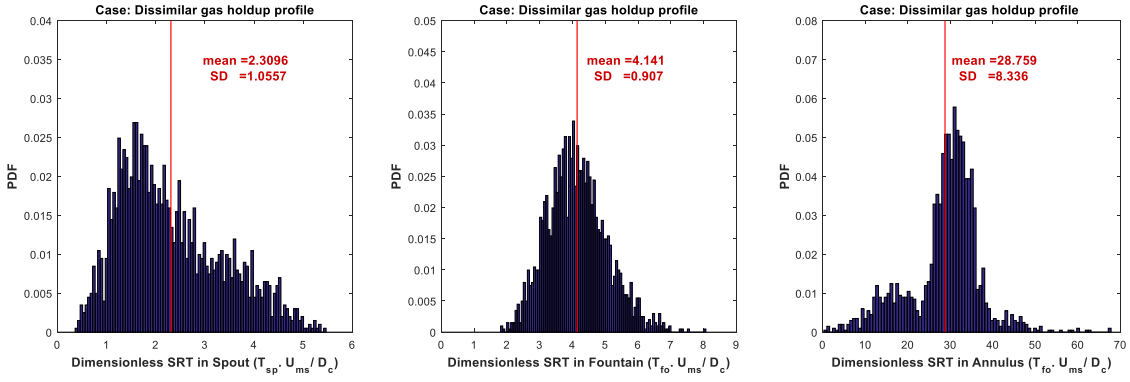

(c)

Figure 4.44. Distribution of the dimensionless solids residence ($T_{sp,fo,an}. U_{ms}/D_c$)in the three different regions of the spouted beds for the conditions of Cases (a) reference, (b) similar, and (c) dissimilar gas holdup radial profiles.

The deviations are smaller, and the similarity is attained in the dimensionless SRT for the reference case and the case of the similar gas holdup. However, the deviations exist and are larger between for the reference case and the case of the dissimilar gas holdup. Accordingly, these results confirm that the gas dictates the dynamics of the gas-solid spouted beds and the radial profile of the gas holdup can properly represent the key role of dynamics of the gas phase on the solids flow field of the spouted beds.

4.3.4. Particle Cycle Time in The Spout, in The Annulus, and The Fountain.

The particle cycle time elapsed by the solids particles in the spout, the annulus, and the fountain were calculated from the RPT data for the conditions of reference case, similar gas holdup profile, and dissimilar gas holdup profile. For the convenience of comparison between the two scales spouted beds and the studied conditions, these cycle times were non-dimensionalized by calculating the contribution of each cycle time of each region to the mean particle cycle time of each bed at the corresponding studied conditions. Figure 4.45 shows the distribution of the fraction of solids cycle time of each region in the bed for the conditions of reference case, similar gas holdup radial profiles, and dissimilar gas holdup radial profiles (Table 3.5). For all the cases studied and as expected, the contribution of time elapsed by the particle in the annulus is much higher than that elapsed in the spout and fountain regions together. This result is qualitatively in agreement with measurements of particle cycle time in spouted beds reported in the literature (Cassanello et al., 1999). However, when comparing the results between the cases, less deviation is observed for the condition of similar gas holdup profiles from those of the reference case, indicating that matching gas holdup profiles can lead hydrodynamics similarity between the two beds. The absolute relative deviation between the fractions of time spent in the spout was found to be

5.36% and 18.26% for the conditions of similar and dissimilar gas holdup profiles, respectively with respect to the reference case.

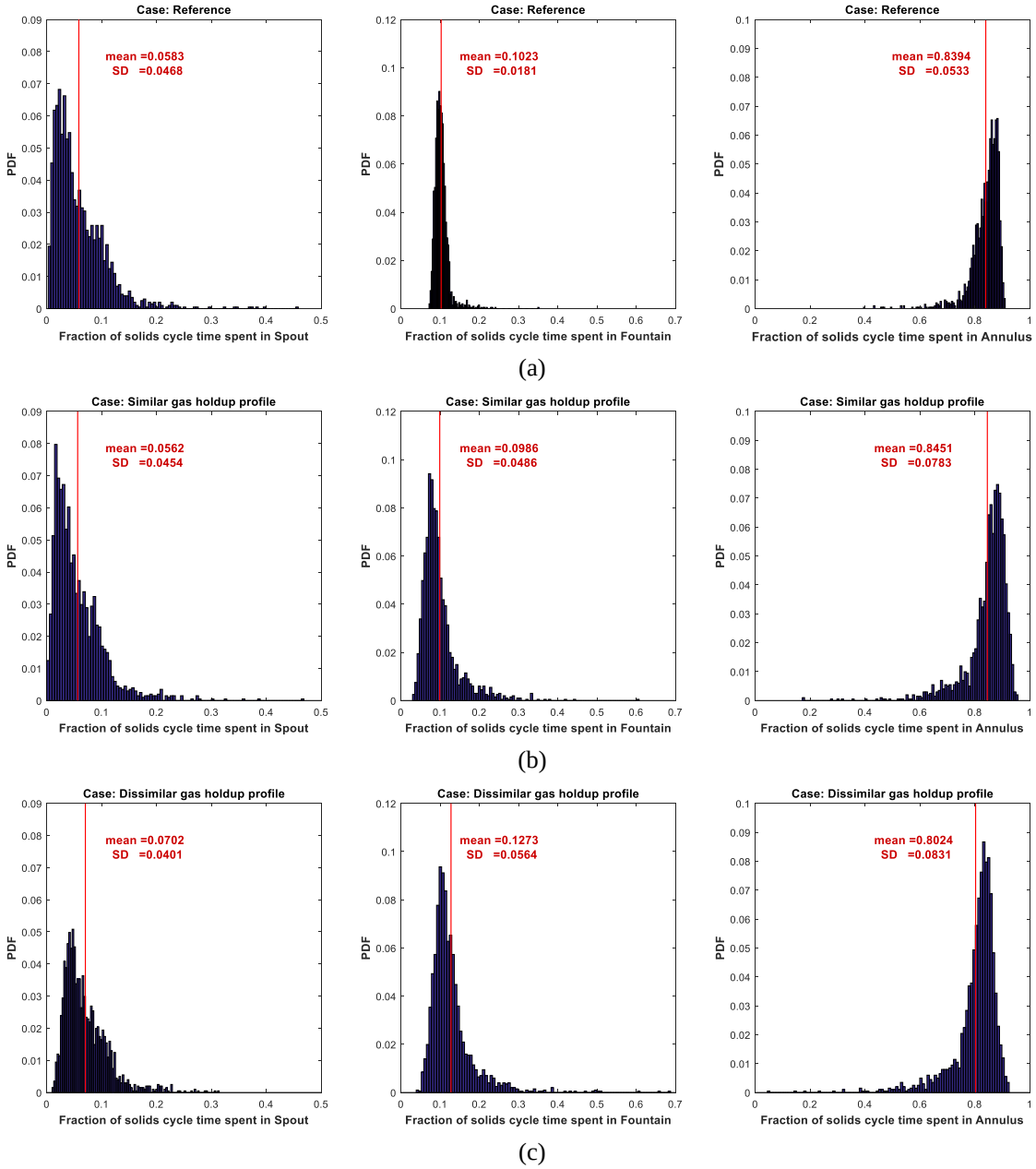

Figure 4.45. Distribution of fraction of solids cycle time of each region in the bed for the conditions of Cases (a) reference, (b) similar, and (c) dissimilar gas holdup radial profiles.

In the fountain, the absolute relative deviation between the fractions of time spent in the fountain was found to be 3.38% and 24.83% for the conditions of similar and dissimilar gas holdup profiles, respectively with respect to the reference case. In the annulus, the absolute relative deviation between the absolute relative deviation between the fractions of time spent in the annulus was found to be 0.79% and 4.29% for the conditions of similar and dissimilar gas holdup profiles, respectively with respect to the reference case. Consequently, these findings provide further confirmation of the relevant role of the gas holdup in the scale-up of spouted beds and how properly can be used to represent the gas dynamics influence in gas-solid spouted beds.

4.3.5. Root Mean Square (RMS) Solids Velocity. Solids mixing and circulation properties are essential when considering optimization and performance purposes of spouted beds. In gas-solids spouted beds, mixing properties originate from the interaction between either gas and particles or particle and particle that take place in the three regions of the spouted bed; the spout, fountain, and annulus. However, such interactions could be controlled by four mechanisms 1) gross solids circulation, 2) solids exchange between annulus and spout regions, 3) dispersive mixing, and 4) segregation. The gross solids circulation is the convective mixing due to the circulation of the particles from the bed base towards the fountain via the spout in addition to their returning to the bed base via the downward motion of the annulus. The exchange mechanism is the movement of solids between from the annulus (dense region) to the spout (dilute region) due to the jet of the gas phase, the solids holdup difference between the two regions, and turbulence of the solids. The dispersive mixing represents the movements of the particles in a diffusion mechanism. At last, the segregation stands for the tendency of dissimilar behavior of solid

materials, when solids are differing in density, size, or shape present in the bed. The solid mixing and diffusion of particles in spouted beds to some extent are mirrored by the axial and radial fluctuation velocities and turbulent eddy diffusivities. Each one of these parameters is a factor that affects mass and heat transfer, and contacting between gas and solids, and hence the performance of the spouted bed. Therefore, the RPT technique was used to calculate *the axial and radial root mean squares (RMS) velocities and turbulent eddy diffusivities of particles* for the conditions of the reference case, similar and dissimilar gas holdup profile. In the following, the evaluation of the new scale-up methodology for hydrodynamics similarity of spouted beds is further assessed by comparing the root mean squares (RMS) velocities and turbulent eddy diffusivities of solids particles for the cases listed in Table 3.5.

Figure 4.46 shows the azimuthally and axially averaged radial profiles of the axial RMS velocity (U_{z_RMS}) for the Cases reference, similar gas holdup profile, dissimilar gas holdup profile for dimensional values (magnitude) in cm/s. The results show the pattern and magnitude of the U_{z_RMS} for all cases in each region of the spouted beds. The fluctuation movements of the particles that are to some extent in charge for the local particle mixing is mainly controlled in the axial component of the fluctuation movements. The U_{z_RMS} profiles showed the same trend for all the different cases. In the spout, the magnitude of the U_{z_RMS} is much larger than in the other regions. The U_{z_RMS} of the particle is high wherever there is a great deal of motion of particles. The maximum value is detected at the center zone of the spout region. This is because the axial particle velocities and its fluctuations velocities are also maximal in the central zone of the spout (Ali et al., 2017b). The axial particle velocities and its fluctuations velocities in the spout reduce radially

outwards to the annulus region (Ali et al., 2017b), and hence the same trends are found for the U_{z_RMS}. However, the U_{z_RMS} magnitudes for all cases are not the same. In the spout, the average absolute relative deviation between the profiles is 30.86% and 36.86% for the Cases of similar and dissimilar gas holdup profiles, respectively with respect to the reference case. In the annulus region, the U_{z_RMS} values are small with small deviations between the profiles of the cases. In the fountain, the average absolute relative deviation between the profiles is 24.67% and 41.77% for the Cases of similar and dissimilar gas holdup profiles, respectively with respect to the reference case. However, to have a basis of comparison between the two different scaled beds for hydrodynamics similarity, the profiles of the U_{z_RMS} were non-dimensionalized for the pilot plant and lab scale beds and the studied conditions by dividing them by the corresponding minimum spouting velocity (U_{ms}). The minimum spouting velocity for the 0.076 m (lab scale) and a 0.152 m (pilot plant scale) spouted beds are listed Table 3.5. The radial profiles of dimensionless U_{z_RMS} in both spouted beds for the studied conditions are presented in Figure 4.46. It is obvious that the tendency between the profiles changes and the similarity between those of the reference case and the case of similar gas holdup profile is achieved. When the gas holdup radial profiles are not similar the non-similarity in the dimensionless U_{z_RMS} was obtained. In the spout, the average absolute relative deviation for the radial profiles of dimensionless axial RMS velocity between cases is 6.19% and 29.76% for the Cases of similar and dissimilar gas holdup profiles, respectively with respect to the reference case. In the fountain, the average absolute relative deviation for the radial profiles of dimensionless axial RMS velocity between cases is 13.64% and 35.21% for the conditions of similar and dissimilar gas holdup profiles, respectively with respect to the reference case. The results

signify that when gas holdup profiles are systematically matched between the lab and pilot plant scale spouted beds, a small deviation in the dimensionless axial RMS velocity is obtained. The reversal of the previous finding takes place when gas holdup profiles are mismatched between the two spouted beds.

Figure 4.47 shows the azimuthally and axially averaged radial profiles of the radial RMS velocity (U_{r_RMS}) for the Cases reference, similar gas holdup profile, dissimilar gas holdup profile for dimensional values (magnitude) in cm/s. The results illustrate the pattern and magnitude of the U_{r_RMS} for all cases in each region of the spouted beds. As can be seen in the profiles, the magnitudes of U_{r_RMS} (Figure 4.47) are much smaller than those of U_{z_RMS} (Figure 4.46) in all the three regions of the studied spouted beds. This is due to insignificance magnitudes of the solids velocity and its fluctuations in the r-direction. However, in the fountain region due to the flow structure of the fountain and the freely fallen particles, noticeable radial velocity and its fluctuations exist. This is in agreement with results reported by (Djeridane et al., 1998). Hence, the magnitudes of U_{r_RMS} in the fountain are much larger than those in the spout and annulus region. Similar to the U_{z_RMS} trends and profiles, there are maxima of the U_{r_RMS} in the region between r/R = 0.4 to 0.6 which indicate that larger fluctuations and magnitudes of the radial particles velocity at this zone. This is consistent with the trend and profiles of the particles radial velocity reported by (Ali et al., 2017b). The deviations between the profiles U_{r_RMS} of all cases were calculated. In the spout, the reference case deviates by 33.9% and 44.72% from the Cases of similar and dissimilar gas holdup profiles, respectively. In the annulus region, the deviations between the profiles of the different cases are small due to the nature of the flow in such region despite differences in the scale of beds or the operating conditions.

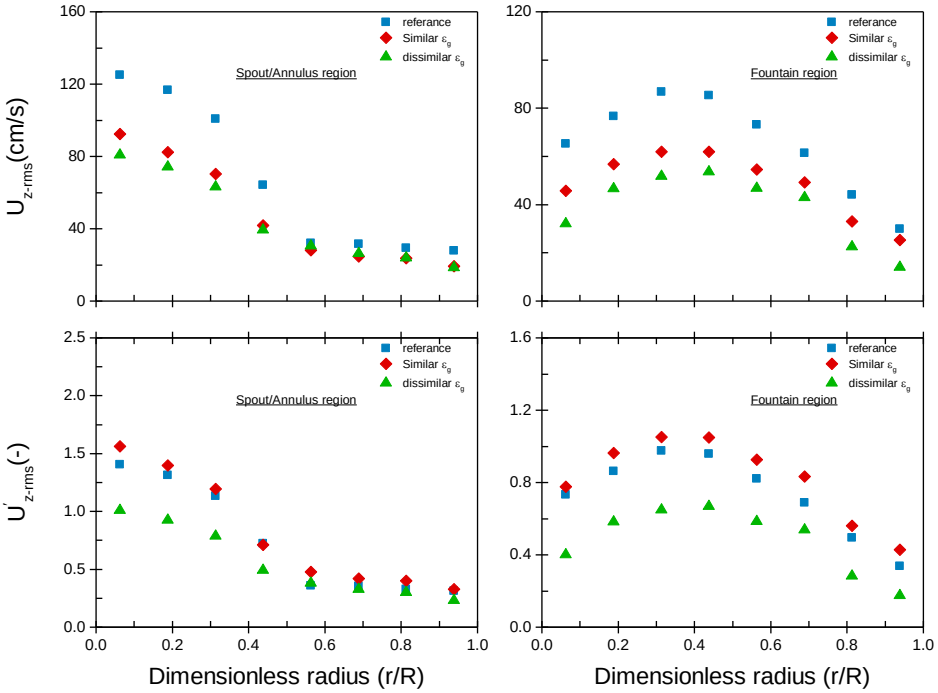

Figure 4.46. Azimuthally and axially averaged radial profiles of (a) the axial RMS particle velocity and (b) the dimensionless axial RMS particle velocity for the conditions of Cases reference, similar, and dissimilar gas holdup radial profiles.

In the fountain, the reference case deviates by 43.68% and 66.38% from the Cases of similar and dissimilar gas holdup profiles, respectively. However, such deviations in dimensional values are expected due to differences in size of beds and applied operating conditions between the cases. Therefore, to examine similarity, the U_{r_RMS} are converted to dimensionless values by dividing them by the minimum spouting velocity (U_{ms}) (cm/s). The dimensionless values are compared between the cases, and less deviation is observed for the Case of similar gas holdup profiles from those of the reference case (Figure 4.47), indicating that matching gas holdup profiles can lead to hydrodynamics similarity between the two beds.

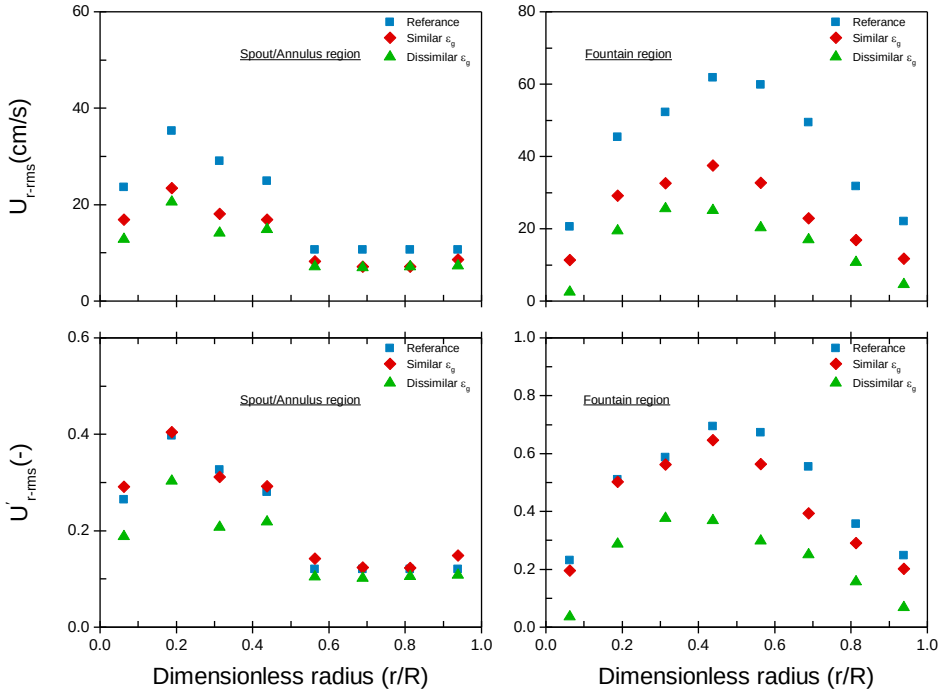

Figure 4.47. Azimuthally and axially averaged radial profiles of (a) the radial RMS particle velocity and (b) the dimensionless radial RMS particle velocity for the conditions of Cases reference, similar, and dissimilar gas holdup radial profiles.

In the spout, the radial profiles of dimensionless U_{r_RMS} for the reference case and the case of similar gas holdup profile deviate from each other by 5.15%; while the difference between Cases reference and dissimilar gas holdup profiles in their dimensionless U_{r_RMS} is more obvious, of about 27.64%. In the fountain, the average absolute relative deviation for the radial profiles of dimensionless axial RMS velocity between cases was found to be 13.58% and 56% for the conditions of similar and non-similar gas holdup profiles, respectively with respect to Case A (reference case). As a result, the above findings present additional verification of the related role of the gas holdup radial profiles in the scale-up of spouted beds and in what way it could be employed to

signify the gas dynamics impact in gas-solid spouted beds. Consequently, these findings provide further confirmation of the relevant role of the gas holdup radial profiles in the scale-up of spouted beds and how properly can be used to represent the gas dynamics influence in gas-solid spouted beds.

4.3.6. Solids Eddy Diffusivity. Figure 4.48 shows the azimuthally and axially averaged radial profiles of the axial eddy diffusivity (D_{zz}) for dimensional values (magnitude) in cm^2/s^2 for the Cases reference, similar gas holdup profile, dissimilar gas holdup profile). The results show the pattern and magnitude of the D_{zz} for all cases in each region of the spouted beds. As expected, the axial diffusivities are larger in the spout for all cases than those in the annulus or the fountain regions. However, the D_{zz} profiles showed the same trend for all cases, but their magnitudes are different. The average absolute relative deviation for the radial profiles of axial eddy diffusivity between cases is 54.82% and 69.53% for the conditions of similar and dissimilar gas holdup profiles, respectively with respect to Case A (reference case). In the fountain, the D_{zz} is higher near the core of the fountain and smaller at the outer region. The same trends are found for all the cases. However, the average absolute relative deviation for the radial profiles of axial eddy diffusivity in the fountain between cases is 57.62% and 68.85% for the conditions of similar and dissimilar gas holdup profiles, respectively with respect to Case A (reference case). Such differences in the absolute magnitudes are expected due to the differences in sizes of the spouted beds and the applied operating conditions. To have a basis of comparison between the two beds for hydrodynamics similarity, the profiles of the D_{zz} were non-dimensionalized for both beds and the studied conditions by dividing them by the square of the corresponding minimum spouting velocity (U_{ms}^2) (cm^2/s^2) (Table 3.5).

The radial profiles of dimensionless D_{zz} in both spouted beds for the studied conditions are presented in Figure 4.48. It is obvious that when the gas holdup profiles are similar between the two beds, the profiles of the dimensionless D_{zz} between the two beds get closer as depicted by the reduction in the average absolute relative deviation. In the spout, the average absolute relative deviation for the radial profiles of dimensionless D_{zz} between cases is 10.75% and 62.28% for the Cases of similar and dissimilar gas holdup profiles, respectively with respect to Case A (reference case). In the fountain, the average absolute relative deviation for the radial profiles of dimensionless D_{zz} between cases is 11.15% and 61.44% for the conditions of similar and non-similar gas holdup profiles, respectively with respect to the reference case. The results signify that when gas holdup profiles are systematically matched between two different scaled spouted beds, a small deviation in the dimensionless D_{zz} is obtained. The reverse of the previous finding is true for dissimilar gas holdup profiles.

Figure 4.49 shows the azimuthally and axially averaged radial profiles of the radial eddy diffusivity (D_{rr}) of the particles for the Cases reference, similar gas holdup profile, dissimilar gas holdup profile for dimensional values (magnitude) in cm^2/s^2. The results show the pattern and magnitude of the D_{rr} for all cases in each region of the spouted beds. The radial eddy diffusivity profiles followed the same trend as the shear stress profiles reported in (Ali et al., 2017b). As can be seen from the profiles, the magnitudes of D_{rr} (Figure 4.49) are much smaller than those of D_{zz} (Figure 4.48) in all the three regions of the studied spouted beds following the trend of the U_{z_RMS}.

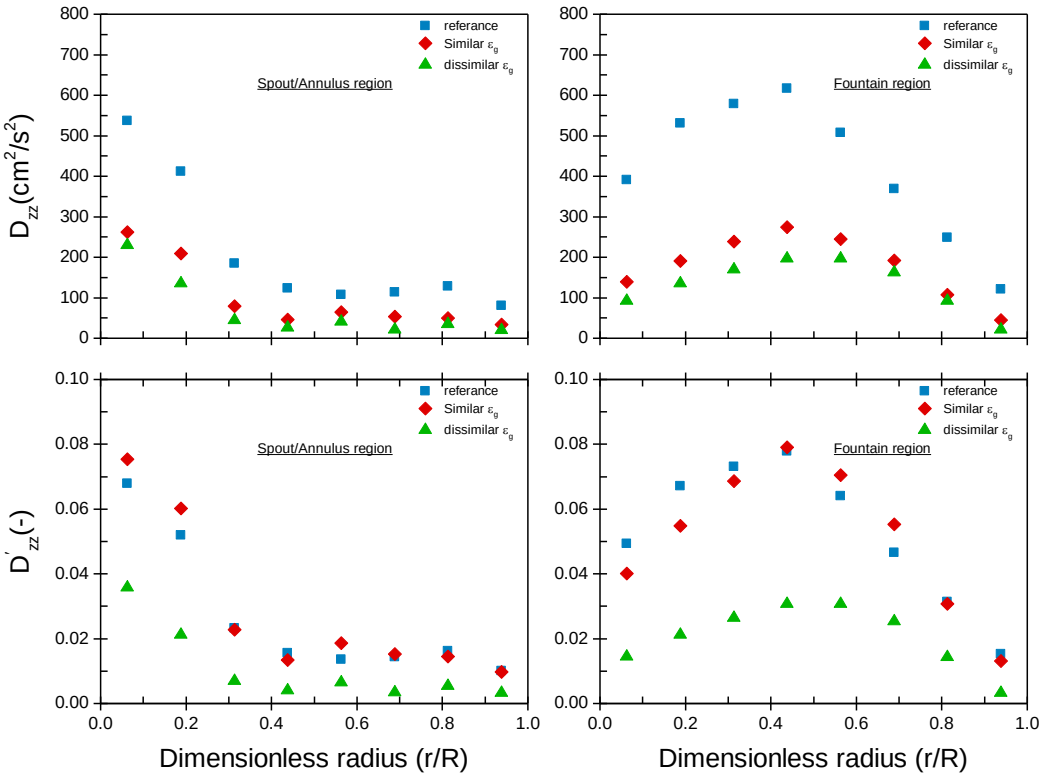

Figure 4.48. Azimuthally and axially averaged radial profiles of (a) the particle axial eddy diffusivity and (b) the dimensionless particle axial eddy diffusivity for the conditions of Cases reference, similar, and dissimilar gas holdup radial profiles.

The D_{rr} magnitudes for all different cases are compared. In the spout, the profiles of the Cases similar and dissimilar gas holdup profiles deviates, respectively, by 61.34% and 78.15% from that of the reference case. However, in the annulus region, the deviations between the profiles of the different cases are small due to the slow moving nature of the flow in such region despite differences in the scale of beds or operating conditions. In the fountain, the maximum radial eddy diffusivity occurred at $r/R \approx 5.6$, where the particles where the particles are less confined, while at the center of the fountain and the wall of the column, they were minimal.

In the fountain, the profiles of the Cases similar and dissimilar gas holdup profiles deviates, respectively, by 47.12% and 57.75% from that of the reference case. However, such deviations in dimensional values are expected due to differences in size of beds and applied operating conditions between the cases. Therefore, to examine similarity, the D_{rr} were converted to dimensionless values by dividing them by the square of the corresponding minimum spouting velocity (U_{ms}^2) (cm^2/s^2). The dimensionless values are compared between the cases, and less deviation is observed for the Case of similar gas holdup profiles from those of the reference case, indicating that matching gas holdup profiles can lead to hydrodynamics similarity between the two beds. In the spout, the radial profiles of dimensionless D_{rr} for the reference case and the case of similar gas holdup profile deviate from each other by 20.49%; while the difference between the reference case and dissimilar gas holdup profiles in their dimensionless radial D_{rr} is more obvious, about 72.96%.

In the fountain, the average absolute relative deviation for the radial profiles of dimensionless D_{rr} between cases was found to be 31.39% and 47.39% for the conditions of similar and dissimilar gas holdup profiles, respectively with respect to that of the reference case. As a result, the above findings present additional verification of the related role of the gas holdup in the scale-up of spouted beds and in what way it could be employed to confirm that the gas dynamics impact the dynamics of the gas-solid spouted beds. Consequently, these findings provide further confirmation of the relevant role of matching the gas holdup radial profile in the scale-up of spouted beds and how properly can be used in scale-up to obtain hydrodynamics similarity.

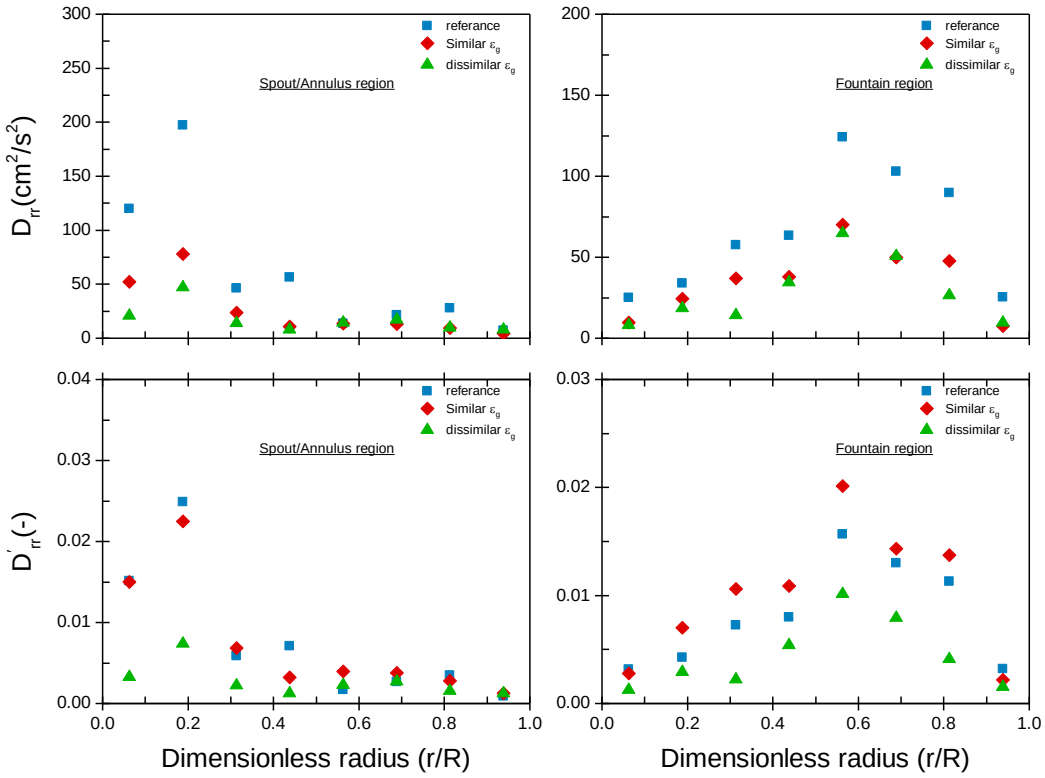

Figure 4.49. Azimuthally and axially averaged radial profiles of (a) the particle radial eddy diffusivity and (b) the dimensionless particle radial eddy diffusivity for the conditions of Cases reference, similar, and dissimilar gas holdup radial profiles.

4.3.7. Our New Scale-Up Methodology Implementation. Our new scale-up methodology can be implemented for scaling lab and pilot plant spouted beds by carrying out the following steps:

I. Performing measurements of the gas holdup radial profile at selected heights in the lab or pilot plant spouted beds that are needed to be scaled up or down. The measurements step can be performed without disturbing the flow using our method of non-invasive measurement techniques such as the gamma-ray densitometry (GRD), and gamma-ray computed tomography (CT). The selected heights in the spouted bed have to include the spout-annulus regions in the cylindrical part of the bed.

II. Applying validated computational fluid dynamics (CFD) simulation to seek out the similar or closer gas holdup radial profile in larger or smaller sizes spouted beds and different operating conditions. The implementation of CFD will allow defining the scale-up or scale-down sizes and the conditions that will provide similar or closer gas-holdup radial profile of that of the bed under investigation measured in step 1. Note that the first condition in the scale-up approach "*when spouted beds with different sizes and/or conditions are geometrically similar"* has to be met in the larger or smaller sizes of spouted beds when performing the CFD.

III. Designing, constructing and operating the newly identified size and conditions of the gas-solid spouted bed.

IV. Evaluating the radial profile of the gas holdup of the constructed and operated spouted bed of step 3 using our method of gamma-ray densitometry technique which is an on-line monitoring technique that has been developed in our laboratory to measure radial/diameters profiles of gas and solids holdups and flow regimes in a non-invasive manner and at both laboratory and pilot plant conditions. Also, the optical fiber probe technique that has been implemented in our laboratory can be applied to large-scale and pilot plant condition to measure radial profiles of gas and solids holdup and solids velocity. The measurements can be utilized to provide benchmarking data to refine the validation of the validated CFD used in step 2.

V. If needed, refining and tuning the operating conditions that are possible to adjust during the operation of the constructed and operated spouted bed in step 3 to ensure as close as possible to the radial profile of gas holdup to that of the bed under investigation of step 1.

The above steps can be implemented on the larger spouted bed of those studied in this work and at pilot plant conditions as well. Furthermore, for liquid-solid spouted beds where the hydrodynamics, in this case, is dictated by the dynamics of the liquid, same steps and methodology can be applied.

5. CONCLUDING REMARKS AND RECOMMENDATIONS

This section presents the conclusion and contribution of this research as well as recommendations of future works.

5.1. CONCLUSION AND PERSPECTIVES

Gamma-ray computed tomography has been successfully used to determine the gas-solid cross-sectional distributions of spouted beds. The quality of the TRISO nuclear fuel particles is strongly impacted by the hydrodynamics, flow field, and flow regime characteristics of the spouted beds. The gas-solid distributions of spouted beds are important from the TRISO fuel coating perspective, as the deposition of the coating layers on the particles depend on how and where the particles are present in the bed, which, in turn, is impacted by the design parameters and operating variables. Experiments that studied the effect of particle density and size and bed size on the solids holdup distributions were performed at different operating conditions. The results lead to further discussion about the influence of the U/U_{ms} on the gas and solids holdups distributions of spouted beds. On the basis of the results obtained, some of the important conclusions are the following:

- The results of the solids holdup of particles of different densities and sizes revealed that the assumption that stable spouting mode would result in uniform coating layers for the particles in the TRISO fuel coating process is not adequate. The results showed that even though the particles were operated at stable spouting state and same U/U_{ms} and H_o, differences were obtained in the solids holdup distributions in the spout and the fountain regions. Hence, the changes in the properties of the particles must be accompanied by appropriate

changes in the input process of the spouting conditions to produce particles with uniform coating layers. This finding needs to be considered for the practical process of the TRISO fuel coating.

The Radioactive Particle Tracking (RPT) Technique has been successfully used to determine to advance the understanding of advanced nuclear fuel particles manufacturing coater and other process mentioned earlier where different types of particles present. In line with the results presented in this part of the study and their analysis, some of the important conclusions are the following:

- It has been found that the gas holdup values in the annulus are higher than the mean gas holdup value at the loose-packed bed state when the gas flow rate increases much the U/U_{ms}. The common assumption that the gas holdup in the annulus is equal to the loose-packed bed value is not proven, especially with increasing the gas flow rate. Therefore, findings, measurements techniques, CFD models, and the reported closures for simulating spouted beds based on this assumption can be challenged due to accuracy.
- The originality of the results and analysis presented in this contribution provides the basis for the assessment of the design of the TRISO fuel coater and its modeling to achieve the proper distribution of the phases and to obtain uniform coating layers.
- At last, successful implementation of the CT as a non-invasive technique on the cold-flow coater will lay the ground for its implementation on hot pilot plant and industrial units.

- It is obvious that for the hydrodynamics of binary solids mixture spouted beds having particles of same size, but different densities, particle collisions by the particle-particle interaction plays a key role but it is not dominating over the gas-particle interaction, and each contribute to the extent of the mixing and segregation phenomena inside the bed of the mixture.
- In the spout region, segregation always takes place due to the unlike behavior between the different solids phases in terms in terms of mean velocities, fluctuating velocities, turbulent stresses and kinetic energy which are determined by particle-particle interaction and other forces exerted on the different solids phases.
- The results also have shown that the fountain region plays a role in the segregation phenomena of the binary solids mixture where such phenomena in this region are more related to interparticle collisions.
- The spreading of the particles out from the core of the fountain is mainly controlled by the interparticle collisions where particles could be spreading out due to colliding with particles of their kind or by the other phases. In this study, the steel particles have a mass that is approximately three times greater than that of the glass particles. Hence collisions between the particles of the two phases resulted in a larger radial deflection of the glass than of the steel particles. Consequently, the lighter glass particles are, in an average sense, spread in the radial direction of the fountain more than the heavier steel particles land, and hence land at the outer region of the annulus surface.

- At the top of the annulus, rolling and bouncing mechanisms are found playing minor or no role. In addition, the results have shown that increasing the U/U_{ms} contributed to counter the extent of segregation of the binary solids mixture in the bed. The solids in spouted beds could be existing simultaneously with particles of different size, density, and shape and hence affect the entrainment and transition of the solids which essentially drive the mixing, residence time, and circulation of the solids.
- The originality of the results and analysis presented in this contribution provides the basis for the assessment of the design of the TRISO fuel spouted bed coaters and its modeling for successfully coating the TRISO nuclear fuel particles.

An advanced non-invasive radioactive particle tracking (RPT) technique has been implemented to validate further the newly developed scale-up methodology of gas-solid spouted beds that is based on matching the gas holdup radial profile between two different sizes of beds and to study the hydrodynamics of gas-solid spouted beds.

- The results confirm that when the radial profiles of the gas holdup are similar or get closer to each other, hydrodynamics similarity has been obtained between the lab-scale and larger scale spouted beds. The hydrodynamics similarity was obtained in terms of the dimensionless values of the spout diameter, cumulative probability distribution of the solids particles penetration into the spout, fraction of cycle time in each region of the bed, the radial profiles of the dimensionless values of the root-mean-square particle velocities and solids eddy diffusivity.

- On the other hand, when the gas holdup radial profiles are dissimilar between the lab and larger scales spouted beds, dissimilarity in the aforementioned parameters were obtained. The reported findings in this study further confirm the findings of (Al-Dahhan et al., 2014; Ali et al., 2017b; Aradhya et al., 2016).
- In addition, the findings demonstrate that the gas phase dictates the dynamics of gas-solid spouted beds and the radial profile of the gas holdup can represent the role of the gas phase on the solids dynamics of the bed. The knowledge and the data obtained also offer a valuable understanding of the solids dynamics of spouted bed and provide benchmarking data to validate computational fluid dynamics (CFD) codes and models.
- It is recommended that this new scale-up methodology can be enabled and applied in practice as outlined earlier by implementing computational fluid dynamics (CFD) as evaluating tool to search for the conditions that can provide similar gas holdup profiles measured at the desired conditions of either lab or larger scales spouted beds.
- Finally, gamma-ray densitometry which is used in industry as nuclear gauge densitometry for liquid or slurry level monitoring and control can be used on site to evaluate and to refine the operating conditions for enabling the pilot plant implementation of our newly developed scale-up methodology for gas-solid spouted beds.

5.2. RECOMMENDATION FOR FUTURE WORKS

Recommendation for future works are the following:

1. The results of the gas and solid cross-sectional distributions have shown that even though the particles were operated at stable spouting state differences were obtained in the solids holdup distributions in the spout and the fountain regions. This suggests that in the actual process of coating TRISO particles, the changes in the properties of the particles must be accompanied by appropriate changes in the input process of the spouting conditions to produce particles with uniform coating layers.
2. It is also suggested to investigate further the effect of particles density that represent the range of particles densities (including the density of the kernel UO_2 ($\rho_p \sim 10.80$ g/cm^3)) used in the actual TRISO spouted beds coaters on the solids and gas hydrodynamics of spouted beds at different velocities, different bed sizes, different solids loadings (the initial solids height before the gas is introduced) using CT, RPT, GRD, gas tracer technique, and pressure transducers.
3. The findings of binary solids mixture spouted beds demonstrates that when solids exist simultaneously with particles of different densities in gas-solid spouted beds, unlike behavior and segregation of the solids present in the bed. This suggests that such behaviors should be considered in the process of the TRISO fuel coating to avoid the failure of the process design and to produce particles with uniform coating layers.
4. The findings of binary solids mixture spouted beds demonstrates that in binary solids mixture gas-solid spouted beds particle-particle interaction plays an important role. Therefore, to understand the effect of particle-particle interaction in greater detail discrete element method (DEM) modeling could be used. Such a

study must be coupled with an investigation of particle collision properties and their role in determining the behavior of larger scale gas-solid spouted beds.

5. The experimental results of the RMS velocities and turbulent parameters per unit volume for binary solid mixture spouted beds indicate that there is frequent cross-over of eddy when the particles near the axis in the spout region and at the wall when particles are in the fountain region. Therefore, this suggests that such behavior cannot be observed when modeling 2D spouted beds and hence a full three-dimensional model would be necessary to model the transient flow of binary solids mixture spouted beds.
6. Demonstrating the CFD as an enabling tool to facilitate the implementation of our new scale-up methodology.
7. Implementing gamma-ray densitometry (GRD) as enabling tool to assess and tune the new scale-up methodology by measuring the radial profile of the gas holdup at the scaled-up gas-solid spouted bed coater and tune the conditions to ensure closer gas holdup radial profile be achieved with respect to the one measured and computed in the scaled down spouted bed.
8. Evaluating the new scale-up methodology for conditions representing the industrial applications of the spouted beds and using larger diameters such as the TRISO nuclear fuel particles coating and other industrial processes such as coal/biomass gasification, drying, coating, etc. Augmenting this with the implementation of the validated CFD and gamma-ray densitometry (GRD) as enabling tools.
9. It is also suggested to use the results reported in this work to validate computational fluid dynamics (CFD) simulations and select proper combinations of the models

and closures. The results reported in this work can be used as a benchmark against computational fluid dynamics codes such as the open-source MFIX code which is used at the Oak Ridge National Laboratory (ORNL) to track particle mixing and circulation beds as functions of operating conditions and bed design in gas-solid spouted beds for TRISO nuclear fuel particles coating.

REFERENCES

Abram, T., Ion, S., 2008. Generation-IV nuclear power: A review of the state of the science. Energy Policy 36, 4323-4330.

Al-Dahhan, M., Aradhya, S., Zaid, F., Ali, N., Aljuwaya, T., 2014. Scale-up and On-line Monitoring of Gas-solid Systems Using Advanced and Non-invasive Measurement Techniques. Procedia Engineering 83, 469-476.

Al-Dahhan, M.H., 2009. Radioisotopes applications in industry: an overview. Atoms for Peace: an International Journal 2, 324-337.

Al-Dahhan, M.H., Kemoun, A., Cartolano, A.R., Roy, S., Dobson, R., Williams, J., 2007. Measuring gas–liquid distribution in a pilot scale monolith reactor via an Industrial Tomography Scanner (ITS). Chemical Engineering Journal 130, 147-152.

Al-Juwaya, T., Ali, N., Al-Dahhan, M., 2017. Investigation of cross-sectional gas-solid distributions in spouted beds using advanced non-invasive gamma-ray computed tomography (CT). Experimental Thermal and Fluid Science 86, 37-53.

Al Mesfer, M.K., Sultan, A.J., Al-Dahhan, M.H., 2016. Impacts of dense heat exchanging internals on gas holdup cross-sectional distributions and profiles of bubble column using gamma ray Computed Tomography (CT) for FT synthesis. Chemical Engineering Journal 300, 317-333.

Al Mesfer, M.K., Sultan, A.J., Al-Dahhan, M.H., 2017. Study the effect of dense internals on the liquid velocity field and turbulent parameters in bubble column for Fischer–Tropsch (FT) synthesis by using Radioactive Particle Tracking (RPT) technique. Chemical Engineering Science 161, 228-248.

Ali, N., Al-Juwaya, T., Al-Dahhan, M., 2016a. Demonstrating the non-similarity in local holdups of spouted beds obtained by CT with scale-up methodology based on dimensionless groups. Chemical Engineering Research and Design 114, 129-141.

Ali, N., Al-Juwaya, T., Al-Dahhan, M., 2017a. An advanced evaluation of spouted beds scale-up for coating TRISO nuclear fuel particles using Radioactive Particle Tracking (RPT). Experimental Thermal and Fluid Science 80, 90-104.

Ali, N., Al-Juwaya, T., Al-Dahhan, M., 2017b. An advanced evaluation of the mechanistic scale-up methodology of gas–solid spouted beds using radioactive particle tracking. Particuology 34, 48-60.

Ali, N., Al-Juwaya, T., Al-Dahhan, M., 2017c. An advanced evaluation of the mechanistic scale-up methodology of gas–solid spouted beds using radioactive particle tracking. Particuology.

Ali, N., Al-Juwaya, T., Al-Dahhana, M., 2016b. An advanced evaluation of the new mechanistic scale-up methodology of gas-solid spouted beds using radioactive particle tracking (RPT). Particuology ##, *"Accepted with minor revision"*.

Ali, N., Al-Juwaya, T., Al-Dahhana, M., 2016c. Demonstrating the non-similarity in local holdups of gas-solid spouted beds obtained by CT with scale-up methodology based on dimensionless groups. Chemical Engineering Research and Design ##, *"Submitted" or "under consideration"*.

Ali, N., Al-Juwaya, T., Al-Dahhana, M., 2018. Evaluating the new mechanistic scale-up methodology of gas-solid spouted beds using gamma ray computed tomography (CT). Experimental Thermal and Fluid Science ##, *"Submitted" or "under consideration"*.

Aradhya, S., Taofeeq, H., Al-Dahhan, M., 2016. A new mechanistic scale-up methodology for gas-solid spouted beds. Chemical Engineering and Processing: Process Intensification 110, 146-159.

Aradhya, S., Taofeeq, H., Al-Dahhan, M., 2017. Evaluation of the dimensionless groups based scale-up of gas–solid spouted beds. International Journal of Multiphase Flow 94, 209-218.

Aradhya, S.B., 2013. Scaleup and hydrodynamics study of gas-solid spouted beds, Chemical and Biochemical Engineering. Missouri University of Science and Technology, pp. xxiv, 301 pages.

Bahramian, A., Olazar, M., 2011. Profiling solid volume fraction in a conical bed of dry micrometric particles: Measurements and numerical implementations. Powder Technology 212, 181-192.

Benkrid, A., Caram, H.S., 1989. Solid flow in the annular region of a spouted bed. AIChE Journal 35, 1328-1336.

Béttega, R., Corrêa, R.G., Freire, J.T., 2009. Scale-up study of spouted beds using computational fluid dynamics. The Canadian Journal of Chemical Engineering 87, 193-203.

Bhusarapu, S., Al-Dahhan, M., Dudukovic, M.P., 2004. Quantification of solids flow in a gas–solid riser: single radioactive particle tracking. Chemical Engineering Science 59, 5381-5386.

Bhusarapu, S., Al-Dahhan, M.H., Duduković, M.P., 2006. Solids flow mapping in a gas–solid riser: Mean holdup and velocity fields. Powder Technology 163, 98-123.

Bhusarapu, S.B., 2005. Solids flow mapping in gas-solid risers.

Bi, H., Macchi, A., Chaouki, J., Legros, R., 1997. Minimum spouting velocity of conical spouted beds. The Canadian Journal of Chemical Engineering 75, 460-465.

Bi, H.T., 2004. A Discussion on Minimum Spout Velocity and Jet Penetration Length. The Canadian Journal of Chemical Engineering 82, 4-10.

Bridgwater, J., Mathur, K.B., 1972. Prediction of spout diameter in a spouted bed—a theoretical model. Powder Technology 6, 183-187.

Burov, S., Jeon, J.-H., Metzler, R., Barkai, E., 2011. Single particle tracking in systems showing anomalous diffusion: the role of weak ergodicity breaking. Physical Chemistry Chemical Physics 13, 1800-1812.

Cassanello, M., Larachi, F., Guy, C., Chaouki, J., 1996. Solids mixing in gas-liquid-solid fluidized beds: Experiments and modelling. Chemical Engineering Science 51, 2011-2020.

Cassanello, M., Larachi, F.ç., Legros, R., Chaouki, J., 1999. Solids dynamics from experimental trajectory time-series of a single particle motion in gas-spouted beds. Chemical Engineering Science 54, 2545-2554.

Chandnani, P.P., Epestein, N., 1986. Spoutability and spout detabilization of fine particles with a gas. Engineering Foundation, United States.

Chen, J., Kemoun, A., Al-Dahhan, M.H., Duduković, M.P., Lee, D.J., Fan, L.-S., 1999. Comparative hydrodynamics study in a bubble column using computer-automated radioactive particle tracking (CARPT)/computed tomography (CT) and particle image velocimetry (PIV). Chemical Engineering Science 54, 2199-2207.

Chen, R.C., Reese, J., Fan, L.S., 1994. Flow structure in a three-dimensional bubble column and three-phase fluidized bed. AIChE Journal 40, 1093-1104.

Clelland, R., Hrenya, C.M., 2002. Simulations of a binary-sized mixture of inelastic grains in rapid shear flow. Physical Review E 65, 031301.

Cook, H.H., Bridgwater, J., 1978. Segregation in spouted beds. The Canadian Journal of Chemical Engineering 56, 636-638.

Csiszar, I., 1991. Why least squares and maximum entropy? An axiomatic approach to inference for linear inverse problems. The annals of statistics, 2032-2066.

Csiszár, I., 1975. I-divergence geometry of probability distributions and minimization problems. The Annals of Probability, 146-158.

Djeridane, T., Larachi, F., Roy, D., Chaovki, J., Legros, R., 1998. Investigation of the mean and turbulent particle velocity fields in a spouted bed using radioactive particle tracking. The Canadian Journal of Chemical Engineering 76, 190-195.

Du, W., Bao, X., Xu, J., Wei, W., 2006a. Computational fluid dynamics (CFD) modeling of spouted bed: Assessment of drag coefficient correlations. Chemical Engineering Science 61, 1401-1420.

Du, W., Bao, X., Xu, J., Wei, W., 2006b. Computational fluid dynamics (CFD) modeling of spouted bed: Influence of frictional stress, maximum packing limit and coefficient of restitution of particles. Chemical Engineering Science 61, 4558-4570.

Du, W., Xu, J., Ji, Y., Wei, W., Bao, X., 2009. Scale-up relationships of spouted beds by solid stress analyses. Powder Technology 192, 273-278.

Du, W., Zhang, J., Bao, S., Xu, J., Zhang, L., 2016. Numerical investigation of particle mixing and segregation in spouted beds with binary mixtures of particles. Powder Technology 301, 1159-1171.

Du, W., Zhang, L., Zhang, B., Bao, S., Xu, J., Wei, W., 2015a. Pressure drop and pressure fluctuations in spouted beds with binary mixtures of particles. Powder Technology 276, 134-143.

Du, W., Zhang, L., Zhang, B., Bao, S., Xu, J., Wei, W., Bao, X., 2015b. Flow regime transition and hydrodynamics of spouted beds with binary mixtures. Powder Technology 281, 138-150.

Duarte, C.R., Murata, V.V., Barrozo, M.A.S., 2005. Simulation of Spouted Bed Using a Eulerian Multiphase Model. Materials Science Forum 498-499, 270-277.

Duarte, C.R., Olazar, M., Murata, V.V., Barrozo, M.A.S., 2009. Numerical simulation and experimental study of fluid–particle flows in a spouted bed. Powder Technology 188, 195-205.

Duduković, M.P., 2003. Use of gamma Ray computed tomography (CT) and computer aided radioactive particle tracking (CARPT) in multiphase reactors. Hemijska industrija 57, 249-261.

Epstein, N., Lim, C.J., Mathur, K.B., 1978. Data and models for flow distribution and pressure drop in spouted beds. The Canadian Journal of Chemical Engineering 56, 436-447.

Fane, A.G., Mitchell, R.A., 1984. Minimum spouting velocity of scaled-up beds. The Canadian Journal of Chemical Engineering 62, 437-439.

Fütterer, M.A., Fu, L., Sink, C., de Groot, S., Pouchon, M., Kim, Y.W., Carré, F., Tachibana, Y., 2014. Status of the very high temperature reactor system. Progress in Nuclear Energy 77, 266-281.

Ge, W., Han, Y., Wang, J., Wang, L., Liu, X., Zhou, J., Li, J., Liu, M., Liu, R., Liu, B., Shao, Y., 2015. New Paradigm of Particle Science and Technology Proceedings of The 7th World Congress on Particle TechnologyPreparation of the Coated Nuclear Fuel Particle Using the Fluidized Bed-chemical Vapor Deposition (FB-CVD) Method. Procedia Engineering 102, 1890-1895.

GIF, 2002. The Generation IV International Forum (GIF), A Technology Roadmap for Generation IV Nuclear Energy Systems 2002.

GIF, 2014. The Generation IV International Forum, Annual Report 2014.

GIF, 2016. The Generation IV International Forum, Annual Report 2016.

Glicksman, L.R., 1984. Scaling relationships for fluidized beds. Chemical Engineering Science 39, 1373-1379.

Godfroy, L., Larachi, F., Kennedy, G., Grandjean, B., Chaouki, J., 1997. On-line flow visualization in multiphase reactors using neural networks. Applied Radiation and Isotopes 48, 225-235.

Grbavčíc, Ž.B., Vukovíc, D.V., Zdanski, F.K., Littman, H., 1976. Fluid flow pattern, minimum spouting velocity and pressure drop in spouted beds. The Canadian Journal of Chemical Engineering 54, 33-42.

Gryczka, O., Heinrich, S., Miteva, V., Deen, N.G., Kuipers, J.A.M., Jacob, M., Mörl, L., 2008. Characterization of the pneumatic behavior of a novel spouted bed apparatus with two adjustable gas inlets. Chemical Engineering Science 63, 791-814.

Guoxin, H., Yanhong, L., Xiwu, G., 2008. Spoutable bed height and pressure fluctuation of a novel annular spouted bed with V-shaped deflector. Powder Technology 185, 152-163.

He, A.-L., Lim, C.J., Grace, J.R., Qin, S.-Z., 1998. Spout diameters in full and half spouted beds. The Canadian Journal of Chemical Engineering 76, 702-706.

He, Y.L., Lim, C., Grace, J., Zhu, J.X., Qzn, S.Z., 1994a. Measurements of voidage profiles in spouted beds. The Canadian Journal of Chemical Engineering 72, 229-234.

He, Y.L., Lim, C.J., Grace, J.R., 1992. Spouted bed and spout-fluid bed behaviour in a column of diameter 0.91 m. The Canadian Journal of Chemical Engineering 70, 848-857.

He, Y.L., Lim, C.J., Grace, J.R., 1997. Scale-up studies of spouted beds. Chemical Engineering Science 52, 329-339.

He, Y.L., Lim, C.J., Grace, J.R., 2000. Pressure gradients, voidage and gas flow in the annulus of spouted beds. The Canadian Journal of Chemical Engineering 78, 161-167.

He, Y.L., Qin, S.Z., Lim, C.J., Grace, J.R., 1994b. Particle velocity profiles and solid flow patterns in spouted beds. The Canadian Journal of Chemical Engineering 72, 561-568.

Heath, P.G., Corkhill, C.L., Stennett, M.C., Hand, R.J., Meyer, W.C.H.M., Hyatt, N.C., 2013. Encapsulation of TRISO particle fuel in durable soda-lime-silicate glasses. Journal of Nuclear Materials 436, 139-149.

Hosseini, S.H., Ahmadi, G., Olazar, M., 2013. CFD simulation of cylindrical spouted beds by the kinetic theory of granular flow. Powder Technology 246, 303-316.

Huddle, R., Mayr, K., Jones, K., 1969. INFLUENCE OF FABRICATION PARAMETERS ON THE INCIDENCE OF SPEARHEAD ATTACK IN COATED PARTICLE FUEL. OECD High Temperature Reactor Project, Winfrith, Eng.

Huilin, L., Yunhua, Z., Ding, J., Gidaspow, D., Wei, L., 2007. Investigation of mixing/segregation of mixture particles in gas–solid fluidized beds. Chemical Engineering Science 62, 301-317.

Huilin, L., Yurong, H., Wentie, L., Ding, J., Gidaspow, D., Bouillard, J., 2004. Computer simulations of gas–solid flow in spouted beds using kinetic–frictional stress model of granular flow. Chemical Engineering Science 59, 865-878.

Ishikura, T., Shinohara, H., Tanaka, I., 1983. Behavior of fine particles in a spouted bed consisting of fine and coarse particles. The Canadian Journal of Chemical Engineering 61, 317-324.

José, M.J.S., 2013. A Novel Technology to Segregate Binary Mixtures of Different Density in a Conical Spouted Bed.

Juhn, P.E., Kupitz, J., Cleveland, J., Cho, B., Lyon, R.B., 2000. IAEA activities on passive safety systems and overview of international development. Nuclear Engineering and Design 201, 41-59.

Karim, K., Varma, R., Vesvikar, M., Al-Dahhan, M.H., 2004. Flow pattern visualization of a simulated digester. Water Research 38, 3659-3670.

Kemoun, A., Cheng Ong, B., Gupta, P., Al-Dahhan, M.H., Dudukovic, M.P., 2001. Gas holdup in bubble columns at elevated pressure via computed tomography. International Journal of Multiphase Flow 27, 929-946.

Khane, V., Said, I.A., Al-Dahhan, M.H., 2016a. Experimental investigation of pebble flow dynamics using radioactive particle tracking technique in a scaled-down Pebble Bed Modular Reactor (PBMR). Nuclear Engineering and Design 302, Part A, 1-11.

Khane, V., Taha, M.M., Al-Dahhan, M.H., 2016b. Experimental investigation of the overall residence time of pebbles in a pebble bed reactor (PBR) using radioactive pebble. Progress in Nuclear Energy 93, 267-276.

Khane, V.B., 2014. Experimental and computational investigation of flow of pebbles in a pebble bed nuclear reactor.

Kim, W.K., Lee, Y.W., Cho, M.S., Park, J.Y., Ra, S.W., Park, J.B., 2008. Nondestructive measurement of the coating thickness for simulated TRISO-coated fuel particles by using phase contrast X-ray radiography. Nuclear Engineering and Design 238, 3285-3291.

Konduri, R.K., Altwicker, E.R., Morgan Iii, M.H., 1999. Design and scale-up of a spouted-bed combustor. Chemical Engineering Science 54, 185-204.

Krzywanski, R.S., Epstein, N., Bowen, B.D., 1992. Multi-dimensional model of a spouted bed. The Canadian Journal of Chemical Engineering 70, 858-872.

Kumar, S.B., Moslemian, D., Duduković, M.P., 1995. A γ-ray tomographic scanner for imaging voidage distribution in two-phase flow systems. Flow Measurement and Instrumentation 6, 61-73.

Kutluoglu, E., Grace, J.R., Murchie, K.W., Cavanagh, P.H., 1983. Particle segregation in spouted beds. The Canadian Journal of Chemical Engineering 61, 308-316.

Lan, X., Xu, C., Gao, J., Al-Dahhan, M., 2012. Influence of solid-phase wall boundary condition on CFD simulation of spouted beds. Chemical Engineering Science 69, 419-430.

Larachi, F., Chaouki, J., Kennedy, G., Dudukovic, M.P., 1997. Chapter 11 - Radioactive particle tracking in multiphase reactors: Principles and applications, in: Duduković, J.C.L.P. (Ed.), Non-Invasive Monitoring of Multiphase Flows. Elsevier Science B.V., Amsterdam, pp. 335-406.

Larachi, F.ç., Grandjean, B.P.A., Chaouki, J., 2003. Mixing and circulation of solids in spouted beds: particle tracking and Monte Carlo emulation of the gross flow pattern. Chemical Engineering Science 58, 1497-1507.

Lee, Y.-W., Park, J.-Y., Kim, Y.K., Jeong, K.C., Kim, W.K., Kim, B.G., Kim, Y.M., Cho, M.S., 2008. Development of HTGR-coated particle fuel technology in Korea. Nuclear Engineering and Design 238, 2842-2853.

Lim, C.J., Grace, J.R., 1987. Spouted bed hydrodynamics in a 0.91 m diameter vessel. The Canadian Journal of Chemical Engineering 65, 366-372.

Lin, J.S., Chen, M.M., Chao, B.T., 1985. A novel radioactive particle tracking facility for measurement of solids motion in gas fluidized beds. AIChE Journal 31, 465-473.

Liu, G.Q., Li, S.Q., Zhao, X.L., Yao, Q., 2008. Experimental studies of particle flow dynamics in a two-dimensional spouted bed. Chemical Engineering Science 63, 1131-1141.

Liu, M., Shao, Y., Liu, B., 2012. Pressure analysis in the fabrication process of TRISO UO2-coated fuel particle. Nuclear Engineering and Design 250, 277-283.

Liu, M., Wen, Y., Liu, R., Liu, B., Shao, Y., 2015a. Investigation of fluidization behavior of high density particle in spouted bed using CFD–DEM coupling method. Powder Technology 280, 72-82.

Liu, X., Zhong, W., Jiang, X., Jin, B., 2015b. Spouting behaviors of binary mixtures of cylindroid and spherical particles. AIChE Journal 61, 58-67.

Liu, Y.-J., Li, W., Han, L.-C., Cao, Y., Luo, H.-a., Al-Dahhan, M., Dudukovic, M.P., 2011. γ-CT measurement and CFD simulation of cross section gas holdup distribution in a gas–liquid stirred standard Rushton tank. Chemical Engineering Science 66, 3721-3731.

López-Honorato, E., Meadows, P.J., Xiao, P., Marsh, G., Abram, T.J., 2008. Structure and mechanical properties of pyrolytic carbon produced by fluidized bed chemical vapor deposition. Nuclear Engineering and Design 238, 3121-3128.

López-Honorato, E., Tan, J., Meadows, P.J., Marsh, G., Xiao, P., 2009. TRISO coated fuel particles with enhanced SiC properties. Journal of Nuclear Materials 392, 219-224.

Luo, H.-P., Al-Dahhan, M.H., 2010. Local gas holdup in a draft tube airlift bioreactor. Chemical Engineering Science 65, 4503-4510.

Luo, H.-P., Kemoun, A., Al-Dahhan, M.H., Sevilla, J.M.F., Sánchez, J.L.G.a., Camacho, F.G.a., Grima, E.M., 2003. Analysis of photobioreactors for culturing high-value microalgae and cyanobacteria via an advanced diagnostic technique: CARPT. Chemical Engineering Science 58, 2519-2527.

Madonna, L.A., 1966. Void Fraction Variation in Spouted Bed Annulus. An Approximation. Industrial & Engineering Chemistry Process Design and Development 5, 47-50.

Mathur, K.B., Epstein, N., 1974a. 1 - Introduction, in: Mathur, K.B., Epstein, N. (Eds.), Spouted Beds. Academic Press, pp. 1-13.

Mathur, K.B., Epstein, N., 1974b. 6 - Spouting Stability, in: Mathur, K.B., Epstein, N. (Eds.), Spouted Beds. Academic Press, pp. 112-124.

Mathur, K.B., Epstein, N., 1974c. Spouted Beds. Academic Press.

Mathur, K.B., Gishler, P.E., 1955. A technique for contacting gases with coarse solid particles. AIChE Journal 1, 157-164.

Matsen, J.M., 1968. Void Fraction Variation in Spouted Bed Annulus. Industrial & Engineering Chemistry Process Design and Development 7, 159-160.

McNab, G., 1972. The Pattern of Change of Spout Diameter in a Spouting Bed. Brit. Chem. Eng. & Proc. Tech 17, 532.

Mesfer, M.K.A., 2013. Effect of Dense Heat Exchanging Internals on the Hydrodynamics of Bubble Column Reactors Using Non-invasive Measurement Techniques, Department of Chemical and Biochemical Engineering. Missouri University of Science and Technology, Rolla, Missouri.

Miller, G.K., Petti, D.A., Maki, J.T., 2004. Consideration of the effects of partial debonding of the IPyC and particle asphericity on TRISO-coated fuel behavior. Journal of Nuclear Materials 334, 79-89.

Miller, G.K., Petti, D.A., Maki, J.T., Knudson, D.L., 2006. An evaluation of the effects of SiC layer thinning on failure of TRISO-coated fuel particles. Journal of Nuclear Materials 355, 150-162.

Minato, K., Kikuchi, H., Tobita, T., Fukuda, K., Kaneko, M., Suzuki, N., Yoshimuta, S., Tomimoto, H., 1997. Improvements in quality of as-manufactured fuels for high-temperature gas-cooled reactors. Journal of nuclear science and technology 34, 325-333.

Nickel, H., Nabielek, H., Pott, G., Mehner, A.W., 2002. Long time experience with the development of HTR fuel elements in Germany. Nuclear Engineering and Design 217, 141-151.

O'Sullivan, J.A., Benac, J., 2007. Alternating minimization algorithms for transmission tomography. Medical Imaging, IEEE Transactions on 26, 283-297.

Olazar, M., Alvarez, S., Aguado, R., San José, M.J., 2003. Spouted Bed Reactors. Chemical Engineering & Technology 26, 845-852.

Olazar, M., San Jose, M.J., Aguayo, A.T., Arandes, J.M., Bilbao, J., 1992. Stable operation conditions for gas-solid contact regimes in conical spouted beds. Industrial & Engineering Chemistry Research 31, 1784-1792.

Olazar, M., San José, M.J., Alvarez, S., Morales, A., Bilbao, J., 1998. Measurement of particle velocities in conical spouted beds using an optical fiber probe. Industrial & engineering chemistry research 37, 4520-4527.

Olazar, M., San Jose, M.J., Penas, F.J., Aguayo, A.T., Bilbao, J., 1993. Stability and hydrodynamics of conical spouted beds with binary mixtures. Industrial & Engineering Chemistry Research 32, 2826-2834.

Pannala, S., Daw, C.S., Finney, C.E.A., Boyalakuntla, D., Syamlal, M., O'Brien, T.J., 2007. Simulating the Dynamics of Spouted-Bed Nuclear Fuel Coaters. Chemical Vapor Deposition 13, 481-490.

Pianarosa, D.L., Freitas, L.A.P., Lim, C.J., Grace, J.R., Dogan, O.M., 2000. Voidage and particle velocity profiles in a spout-fluid bed. The Canadian Journal of Chemical Engineering 78, 132-142.

Piccinini, N., 1980. Particle Segregation in Continuously Operating Spouted Beds, in: Grace, J.R., Matsen, J.M. (Eds.), Fluidization. Springer US, Boston, MA, pp. 279-286.

Piccinini, N., Bernhard, A., Campagna, P., Vallana, F., 1977. Segregation phenomenon in spouted beds. The Canadian Journal of Chemical Engineering 55, 122-125.

Piskova, E., Mörl, L., 2008. Characterization of spouted bed regimes using pressure fluctuation signals. Chemical Engineering Science 63, 2307-2316.

Pissinati, R., Oliveira, W.P., 2003. Enteric coating of soft gelatin capsules by spouted bed: effect of operating conditions on coating efficiency and on product quality. European Journal of Pharmaceutics and Biopharmaceutics 55, 313-321.

Porter, I.E., Knight, T.W., Dulude, M.C., Roberts, E., Hobbs, J., 2013. Design and fabrication of an advanced TRISO fuel with ZrC coating. Nuclear Engineering and Design 259, 180-186.

Prasser, H.M., Baldauf, D., Fietz, J., Hampel, U., Hoppe, D., Zippe, C., Zschau, J., Christen, M., Will, G., 2003. Time resolving gamma-tomography for periodically changing gas fraction fields and its application to an axial pump. Flow Measurement and Instrumentation 14, 119-125.

Rados, N., Al-Dahhan, M.H., Dudukovic, M.P., 2003. Modeling of the Fischer–Tropsch synthesis in slurry bubble column reactors. Catalysis Today 79–80, 211-218.

Rados, N., Shaikh, A., Al-Dahhan, M.H., 2005. Solids flow mapping in a high pressure slurry bubble column. Chemical Engineering Science 60, 6067-6072.

Rammohan, A.R., Kemoun, A., Al-Dahhan, M.H., Dudukovic, M.P., 2001a. Characterization of Single Phase Flows in Stirred Tanks via Computer Automated Radioactive Particle Tracking (CARPT). Chemical Engineering Research and Design 79, 831-844.

Rammohan, A.R., Kemoun, A., Al-Dahhan, M.H., Dudukovic, M.P., 2001b. A Lagrangian description of flows in stirred tanks via computer-automated radioactive particle tracking (CARPT). Chemical Engineering Science 56, 2629-2639.

Ren, B., Shao, Y., Zhong, W., Jin, B., Yuan, Z., Lu, Y., 2012. Investigation of mixing behaviors in a spouted bed with different density particles using discrete element method. Powder Technology 222, 85-94.

Ren, B., Zhong, W., Jin, B., Yuan, Z., Lu, Y., 2011. Computational Fluid Dynamics (CFD)–Discrete Element Method (DEM) Simulation of Gas–Solid Turbulent Flow in a Cylindrical Spouted Bed with a Conical Base. Energy & Fuels 25, 4095-4105.

Robinson, T., Waldie, B., 1978. Particle cycle times in a spouted bed of polydisperse particles. The Canadian Journal of Chemical Engineering 56, 632-635.

Roy, D., Larachi, F., Legros, R., Chaouki, J., 1994. A study of solid behavior in spouted beds using 3-D particle tracking. The Canadian Journal of Chemical Engineering 72, 945-952.

Roy, S., Al-Dahhan, M., 2005. Flow distribution characteristics of a gas–liquid monolith reactor. Catalysis Today 105, 396-400.

Roy, S., Kemoun, A., Al-Dahhan, M.H., Dudukovic, M.P., Skourlis, T.B., Dautzenberg, F.M., 2005. Countercurrent flow distribution in structured packing via computed tomography. Chemical Engineering and Processing: Process Intensification 44, 59-69.

San José, M.a.J., Alvarez, S., de Salazar, A.O., Olazar, M.n., Bilbao, J., 2005a. Influence of the particle diameter and density in the gas velocity in jet spouted beds. Chemical Engineering and Processing: Process Intensification 44, 153-157.

San José, M.J., Alvarez, S., Morales, A., Olazar, M., Bilbao, J., 2006. Solid Cross-Flow into the Spout and Particle Trajectories in Conical Spouted Beds Consisting of Solids of Different Density and Shape. Chemical Engineering Research and Design 84, 487-494.

San José, M.J., Olazar, M., Aguayo, A.T., Arandes, J.M., Bilbao, J., 1993. Expansion of spouted beds in conical contactors. The Chemical Engineering Journal 51, 45-52.

San José, M.J., Olazar, M., Alvarez, S., Bilbao, J., 1998. Local Bed Voidage in Conical Spouted Beds. Industrial & Engineering Chemistry Research 37, 2553-2558.

San José, M.J., Olazar, M., Alvarez, S., Morales, A., Bilbao, J., 2005b. Local porosity in conical spouted beds consisting of solids of varying density. Chemical Engineering Science 60, 2017-2025.

San José, M.J., Olazar, M., Alvarez, S., Morales, A., Bilbao, J., 2005c. Spout and Fountain Geometry in Conical Spouted Beds Consisting of Solids of Varying Density. Industrial & Engineering Chemistry Research 44, 193-200.

Santos, K.G., Santos, D.A., Duarte, C.R., Murata, V.V., Barrozo, M.A.S., 2012. Spouting of Bidisperse Mixture of Particles: A CFD and Experimental Study. Drying Technology 30, 1354-1367.

Sari, S., Kulah, G., Koksal, M., 2012. Characterization of gas–solid flow in conical spouted beds operating with heavy particles. Experimental Thermal and Fluid Science 40, 132-139.

Sawa, K., 2012. 3.06 - TRISO Fuel Production, in: Konings, R.J.M. (Ed.), Comprehensive Nuclear Materials. Elsevier, Oxford, pp. 143-149.

Scott, A.M., Bridgwater, J., 1975. Interparticle Percolation: A Fundamental Solids Mixing Mechanism. Industrial & Engineering Chemistry Fundamentals 14, 22-27.

Şentürk Lüle, S., Colak, U., Koksal, M., Kulah, G., 2015. CFD Simulations of Hydrodynamics of Conical Spouted Bed Nuclear Fuel Coaters. Chemical Vapor Deposition 21, 122-132.

Shaikh, A., Al-Dahhan, M., 2003. Development of an artificial neural network correlation for prediction of overall gas holdup in bubble column reactors. Chemical Engineering and Processing: Process Intensification 42, 599-610.

Shaikh, A., Al-Dahhan, M., 2005. Characterization of the hydrodynamic flow regime in bubble columns via computed tomography. Flow Measurement and Instrumentation 16, 91-98.

Shuyan, W., Xiang, L., Huilin, L., Long, Y., Dan, S., Yurong, H., Yonglong, D., 2009. Numerical simulations of flow behavior of gas and particles in spouted beds using frictional-kinetic stresses model. Powder Technology 196, 184-193.

Shuyan, W., Yongjian, L., Yikun, L., Lixin, W., Qun, D., Chunsheng, W., 2010. Simulations of flow behavior of gas and particles in spouted bed with a porous draft tube. Powder Technology 199, 238-247.

Spreutels, L., Chaouki, J., Bertrand, F., Haut, B., Legros, R., 2016a. Gas residence time distribution in a conical spouted bed. Powder Technology 290, 62-71.

Spreutels, L., Haut, B., Legros, R., Bertrand, F., Chaouki, J., 2016b. Experimental investigation of solid particles flow in a conical spouted bed using radioactive particle tracking. AIChE Journal 62, 26-37.

Takeda, H., Yamamoto, Y., 1976. Mixing of Particles in a Spouted Bed. Journal of Nuclear Science and Technology 13, 372-381.

Takeuchi, S., Wang, S., Rhodes, M., 2008. Discrete element method simulation of three-dimensional conical-base spouted beds. Powder Technology 184, 141-150.

Tang, C., Tang, Y., Zhu, J., Zou, Y., Li, J., Ni, X., 2002. Design and manufacture of the fuel element for the 10 MW high temperature gas-cooled reactor. Nuclear Engineering and Design 218, 91-102.

Thanit, T., Wiwut, W., Tawatchai, T., Toshihiro, T., Toshitsugu, T., Yutaka, Y., 2005. Prediction of gas-particle dynamics and heat transfer in a two-dimensional spouted bed. Advanced Powder Technology 16, 275-293.

Thorley, B., Mathur, K.B., Klassen, J., Gishler, P.E., National Research Council of, C., Division of Applied, C., 1955. The Effect of design variables on flow characteristics in a spouted bed. Division of Applied Chemistry, National Research Council, Ottawa.

Thorley, B., Saunby, J.B., Mathur, K.B., Osberg, G.L., 1959. An analysis of air and solid flow in a spouted wheat bed. The Canadian Journal of Chemical Engineering 37, 184-192.

Tsoulfanidis, N., 2010. Measurement and detection of radiation. CRC press.

Upadhyay, R.K., Roy, S., 2010. Investigation of hydrodynamics of binary fluidized beds via radioactive particle tracking and dual-source densitometry. The Canadian Journal of Chemical Engineering 88, 601-610.

Varma, R., 2008. Characterization of anaerobic bioreactors for bioenergy generation using a novel tomography technique. ProQuest.

Varma, R., Bhusarapu, S., Sullivan, J.A.O., Al-Dahhan, M.H., 2008. A comparison of alternating minimization and expectation maximization algorithms for single source gamma ray tomography. Measurement Science and Technology 19, 015506.

Verfondern, K., Nabielek, H., Kendall, J.M., 2007. Coated particle fuel for high temperature gas cooled reactors. Nuclear Engineering and Technology 39, 603.

Waldie, B., Wilkinson, D., McHugh, T.G.P., 1986. Measurement of voidage in the fountain of a spouted bed. The Canadian Journal of Chemical Engineering 64, 950-953.

Wang, S., Zhao, L., Wang, C., Liu, Y., Gao, J., Liu, Y., Cheng, Q., 2014. Numerical simulation of gas–solid flow with two fluid model in a spouted-fluid bed. Particuology 14, 109-116.

Wang, Z., Bi, H.T., Lim, C.J., Su, P., 2004. Determination of Minimum Spouting Velocities in Conical Spouted Beds. The Canadian Journal of Chemical Engineering 82, 11-19.

Wang, Z.G., Bi, H.T., Lim, C.J., 2006. Numerical simulations of hydrodynamic behaviors in conical spouted beds. China Particuology 4, 194-203.

Wu, Y., Cheng Ong, B., Al-Dahhan, M.H., 2001. Predictions of radial gas holdup profiles in bubble column reactors. Chemical Engineering Science 56, 1207-1210.

Yang, M., Zhang, J., Song, S.-J., Li, X., Meng, F., Kang, T., Liu, W., Wei, D., 2013. Imaging and measuring methods for coating layer thickness of TRISO-coated fuel particles with high accuracy. NDT & E International 55, 82-89.

Zhang, F., Zhong, Y., Yang, X., Lin, J., Zhu, Z., 2017. Encapsulation of metal-based phase change materials using ceramic shells prepared by spouted bed CVD method. Solar Energy Materials and Solar Cells 170, 137-142.

Zhang, Y., Zhong, W., Jin, B., 2011. New method for the investigation of particle mixing dynamic in a spout-fluid bed. Powder Technology 208, 702-712.

Zhang, Y., Zhong, W., Jin, B., Xiao, R., 2012. Mixing and Segregation Behavior in a Spout-Fluid Bed: Effect of Particle Size. Industrial & Engineering Chemistry Research 51, 14247-14257.

Zhang, Y., Zhong, W., Jin, B., Xiao, R., 2013. Mixing and Segregation Behavior in a Spout-Fluid Bed: Effect of the Particle Density. Industrial & Engineering Chemistry Research 52, 5489-5497.

Zhonghua, W., Mujumdar, A.S., 2008. CFD modeling of the gas–particle flow behavior in spouted beds. Powder Technology 183, 260-272.

Zhou, J., Bruns, D.D., 2012. Minimum spouting velocity of dense particles in shallow spouted beds. The Canadian Journal of Chemical Engineering 90, 558-564.

Zhu, R.R., Zhu, W.B., Xing, L.C., Sun, Q.Q., 2011. DEM simulation on particle mixing in dry and wet particles spouted bed. Powder Technology 210, 73-81.

VITA

Thaar M. Aljuwaya joined the research group of Dr. Muthanna Al-Dahhan in 2013 at Missouri University of Science and Technology in Rolla, MO, USA to pursue his Ph.D. degree in Nuclear Engineering. He received his M.S. degree in nuclear engineering from Missouri University of Science and Technology in 2012. During his Ph.D. studies, Thaar worked on the project of Advancing the Fundamental Understanding and Scale-up of TRISO Nuclear Fuel Coaters via Advanced Measurement and Computational Techniques. This work has been supported by U.S. Department of Energy (DOE) – Nuclear Energy University Program (NEUP).

Thaar has been a member of the American Nuclear Society since 2012. He has attended several conferences related to his research interests and published five peer-reviewed journal papers, several proceeding papers and several oral presentations at national and international conferences. In May 2018, he received his PhD degree in Nuclear Engineering from Missouri University of Science and Technology .